# Variational Multi-Task Models for Image Analysis

## Applications to Magnetic Resonance Imaging

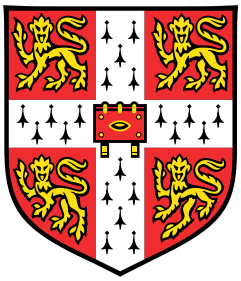

**Veronica Corona**

Department of Applied Mathematics and Theoretical Physics
University of Cambridge

This dissertation is submitted for the degree of
*Doctor of Philosophy*

Jesus College

August 2019

# Declaration

I hereby declare that except where specific reference is made to the work of others, the contents of this dissertation are original and have not been submitted in whole or in part for consideration for any other degree or qualification in this, or any other university. This dissertation is my own work and contains nothing which is the outcome of work done in collaboration with others, except as specified in the text.

Veronica Corona
August 2019

# Acknowledgements

During these years, I have been very fortunate to work with amazing, inspiring people. Here, I would like to briefly thank the most important people in this journey, knowing that words can not convey the immense gratitude I have for all of them.

First of all, I would like to thank Carola-Bibiane Schönlieb for being an exceptional mentor throughout this PhD. I am eternally grateful for everything you have taught me and for always showing your support and encouragement. Your passion for research has been truly inspiring and contagious and I can not begin to express how valuable your advise and guidance has been.

I warmly would like to thank Prof. Pietro Lio' and Prof. Samuli Siltanen for proof-reading the thesis and for the interesting and fruitful discussion we had during my viva examination.

My deepest gratitude goes to my colleagues and friends Angelica Aviles-Rivero and Noémie Debroux. Thank you for being a dream team, for your constant support and positive attitude. Your enthusiasm has inspired me to do better every day and I feel so lucky to have had the opportunity to work with you.

I am forever thankful to Martin Benning, who has been an incredible colleague and friend in the past years. Thank you for always being available every time I needed help and for making work so much fun.

I would like to thank Matthias Ehrhardt, for his brilliant support and guidance. Working with you has been an honour.

I have been very lucky to work with colleagues from different departments and universities. I would like to thank Carole Le Guyader for interesting and stimulating discussions as well as her kind and positive comments. I am grateful to Martin Graves and Guy Williams for their time and helpful discussions and for giving me new insights in the context of MRI. I would like to deeply thank Lynn Gladden, Andi Reci and Andrew Sederman for an amazing collaboration and for introducing me to new exciting problems. I am also grateful to Yehuda Dar for fruitful and fun discussions during his brief stay in Cambridge that led to a very interesting project. I am also thankful to all the lovely people at the Cancer Research UK that helped me acquiring data and showed me the

practical side of MRI during our experiments. Also thank you to Kevin Brindle and Stefanie Reichelt for their help at the institute.

I am so grateful to Joana Grah, for being an amazing colleague and a caring office mate. Moreover, I thank you for being my friend through all the ups and downs in these years. I couldn't have done it without your support! Thank you, Tamara Großmann for being a super office mate. I am going to miss our coffee breaks very much! But more than anything, thank you for always reminding me of my strength and for always being on my side. I would also like to thank Simone Parisotto, for his moral and technical help, but more importantly, for his honest friendship and for bringing Vera into my life.

I would like to thank all the colleagues at the Cambridge Image Analysis group for creating the most collaborative and stimulating environment, for all the lunch breaks together and the beautiful memories. In particular, I would like to thank Sebastian Lunz, Lukas Lang and Kasia Targonska-Hadzibabic for their sincere support and encouragement, especially during some tough moments this year.

I also greatly acknowledge the funding of my PhD fellowship by the Cambridge Cancer Centre and CRUK that made this research possible and gave me the means to present it at conferences around the world.

Last but definitely not least, I am infinitely thankful to my family. My parents, for always being there for me, every day. I couldn't have written this thesis without your support. Thank you to my sisters, Roberta and Francesca, for being my rock and my best friends and for giving me the most precious gift I could ever ask for, Lorenzo and Mattias, who make every day brighter.

# Abstract

This thesis deals with the study and development of several variational multi-task models for solving inverse problems in imaging, with a particular focus on Magnetic Resonance Imaging (MRI). In most image processing problems, one usually deals with the reconstruction task, i.e., the task of reconstructing an image from indirect measurements, and then performs various operations, one after the other (i.e. sequentially), to improve the quality of the reconstruction and to extract useful information.

However, recent developments in a variational context, have shown that performing those tasks jointly (i.e. in a multi-task framework) offers great benefits, and this is the perspective that we follow in this thesis. We go beyond traditional sequential approaches and set a new basis for variational multi-task methods for MRI analysis. We demonstrate that by sharing representation between tasks and carefully interconnecting them, one can create synergies across challenging problems and reduce error propagation.

More precisely, firstly we propose a multi-task variational model to tackle the problems of image reconstruction and image segmentation using non-convex Bregman iteration. We describe theoretical and numerical details of the problem and its optimisation scheme. Moreover, we show that our multi-task model achieves better results in several examples and MRI applications than existing approaches in the same context.

Secondly, we show that our approach can be extended to a multi-task reconstruction and segmentation model for the nonlinear inverse problem of velocity-encoded MRI. In this context, the aim is to estimate not only the magnitude from MRI data, but also the phase and its flow information, whilst simultaneously identify regions of interest through the segmentation task.

Finally, we go beyond two-task frameworks and introduce for the first time a variational multi-task model to handle three imaging tasks. To this end, we design a variational multi-task framework addressing reconstruction, super-resolution and registration for improving the quality of MRI reconstruction. We demonstrate that our model is theoretically well-motivated and it outperforms sequential models whilst requiring less computational cost. Furthermore, we show through experimental results the potential of this approach for clinical applications.

**Keywords:** medical imaging, joint models/multi-tasking, image reconstruction, image segmentation, image registration, super-resolution, hyperelastic regularisation, inverse problems, total variation, non-convex optimisation, Bregman distances.

# Contents

# List of Figures

# List of Tables

# List of Algorithms

# Notation and Acronyms

| | |
|---|---|
| $\mathbb{N}$ | Set of natural numbers |
| $\mathbb{R}$ | Set of real numbers |
| $\mathbb{R}^+$ | Set of positive real numbers |
| $\mathbb{R}_{\geq 0}$ | Set of nonnegative real numbers |
| $\overline{\mathbb{R}}$ | Set of extended real numbers |
| $\mathbb{Z}$ | Set of integers |
| $\mathbb{Z}_{\geq 0}$ | Set of nonnegative integers |
| $A \cap B$ | Intersection of sets $A$ and $B$ |
| $A \cup B$ | Union of sets $A$ and $B$ |
| $C^n$ | Space of continuous functions with continuous first $n$ derivatives |
| $C_c^n$ | Space of continuous functions with continuous first $n$ derivatives and compact support |
| $L^p$ | Lebesgue space of functions for which the $p$th power of the absolute value is Lebesgue integrable; mostly $p \in \{1, 2\}$ |
| $W^{k,p}$ | Sobolev space of $L^p$ functions with $k$ weak derivatives |
| $\lvert \cdot \rvert$ | Absolute value |
| $\lVert \cdot \rVert_1$ | $L^1$-norm |
| $\lVert \cdot \rVert_2$ | $L^2$-norm |
| $\lVert \cdot \rVert_\infty$ | $L^\infty$-norm |

| | |
|---|---|
| $\|\cdot\|_F$ | Frobenius-norm |
| $\langle\cdot,\cdot\rangle$ | Inner product |
| $\frac{\partial F}{\partial x}$ | Partial derivative of $F$ with respect to $x$ |
| $\partial F(x)$ | Subdifferential of $F$ at $x$ |
| $\nabla u$ | Gradient of $u$ |
| $\operatorname{div} u$ | Divergence of $u$ |
| $\mathcal{F}$ | Fourier transform |
| $\mathcal{A}, \mathcal{K}, \mathcal{S}$ | Linear operators |
| $\mathcal{K}^*$ | Adjoint of operator $\mathcal{K}$ |
| $\Delta u$ | Laplacian of $u$ |
| $\imath_A$ | Indicator function of the set A |
| $\ell$ | Number of partitions for segmentation |
| $F^*$ | Convex conjugate of function $F$ |
| $\Omega \subset \mathbb{R}^2$ | Image domain |
| $\partial\Omega$ | Boundary of $\Omega$ |
| BV | Space of functions of Bounded Variation |
| l.s.c. | Lower semi-continuous |
| CS | Compressed Sensing |
| MSE | Mean Squared Error |
| PSNR | Peak Signal-to-Noise Ratio |
| SSIM | Structure SIMilarity index |
| TV | Total Variation |

# Chapter 1

# Introduction

Imaging refers to the process of representing visual perception through the formation of an image. In the past decades, digital images and videos have become an integral part of everyone's life at a global scale. They are generated at a pace that is far beyond what any human or teams of humans can possibly view and analyse. This calls for more powerful machines but more importantly for more powerful algorithms in the context of image processing and analysis. As images are a representation of the analogue world, they usually contain very complicated geometrical structures of different shapes, scales and textures. Thus, processing this information requires sophisticated mathematical methods and algorithms.

Most image processing problems, and in particular the ones we encounter in this thesis, can be formulated as *inverse problems*. The general task is to find an image $u$ from some acquired measurements $f$ that possibly live in a transformed domain and are likely corrupted by noise and artefacts. That is the case for any imaging device: they operate on specific physical principles and are usually concerned with the acquisition of some indirect signal that needs to be transformed into the quantity of interest. Additionally, due to system defects, quantisation and/or poor condition, the measurement may contain several undesirable artefacts such as noise and blur.

We typically write an inverse problem to estimate a quantity of interest $u$ as follows

$$f = \mathcal{A}u + \eta \tag{1.1}$$

where $\mathcal{A}$ is the so-called *forward operator* describing the physical system, $f$ is the given measurements and $\eta$ denotes some additive noise that follows a certain statistical distribution. The forward operator $\mathcal{A} : X \to Y$ is usually a bounded and linear operator mapping one vector-space to another and describes the degrading/transforming process

of our sought image $u$. For example, when this process introduces noise in the solution, $\mathcal{A}$ is modelled as the identity operator; when blurring artefacts are present, $\mathcal{A}u$ denotes the convolution with a blurring kernel; in image reconstruction problems, $\mathcal{A}$ models the physics of the specific modalities, e.g. Fourier transform in MRI where the operator maps the image to the frequency domain.

In order to retrieve the original image $u$, we need to invert the operator $\mathcal{A}$. However, most of the time $\mathcal{A}$ is not invertible or its inversion is ill-conditioned. Furthermore, the presence of noise and incomplete data makes the problem even harder. In these cases, problems of the form (1.1) are said to be *ill-posed* [Had02, Had23]. An approach to solve ill-posed inverse problems is to incorporate in the mathematical model some *prior* information to favour a specific type of solutions, based on what we know about the quantity of interest. In this way, one can *regularise* the solution to be meaningful. In this context, *variational approaches* have been proposed to recover $u$ by solving a family of well-posed problems through regularisation and suitable optimisation schemes [Tik63, Ter86].

Variational methods have become very popular in the context of image processing and analysis, as many imaging tasks can be formulated as an optimisation problem and this is the mathematical perspective we follow in this thesis. In this context, the main challenges lie in designing specific priors and functionals that accurately model the relevant features for the specific problem. In general, the first problem concerns the image acquisition or sensing, where a physical sensor converts some signal emitted from the object of interest into digital form. This is usually called *raw data* (see left side of Figure 1.1b for an example) and requires a reconstruction task to form the final image. Secondly, image processing is required and this includes all those operations that aim at improving the quality of the image, such as denoising and deblurring. Then, image analysis is carried out on the processed images, where one seeks to extract useful information from the images, such as detecting tumours in medical imaging, counting cells in microscopy, assessing the mineral content of a rock sample in material sciences. Finally, based on the previous analysis, the goal is to achieve a better image understanding for the specific application with the aim of aiding the decision-making process of the user.

Most of the time, all of the steps above are necessary to obtain the desired output of the specific imaging application. Furthermore, they are usually performed in a serial fashion, that is to say one task after the other, in what we will refer to as *sequential approach* (e.g. [BSW+11, UAO+13]). This classical pipeline is illustrated in Figure 1.1a, emphasising the dependency of a successive task on the output of the previous one. For

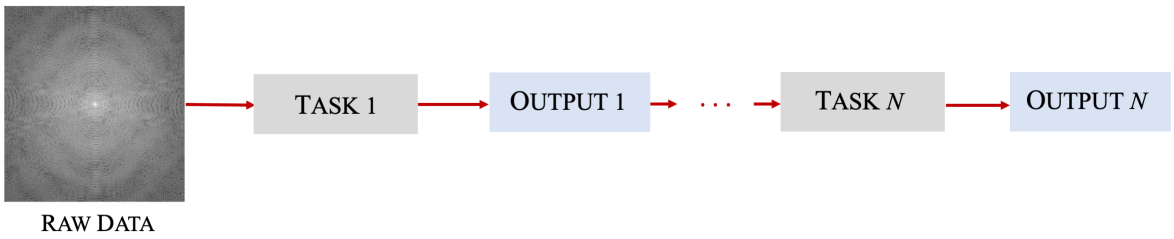


**(a)** A sequential approach.

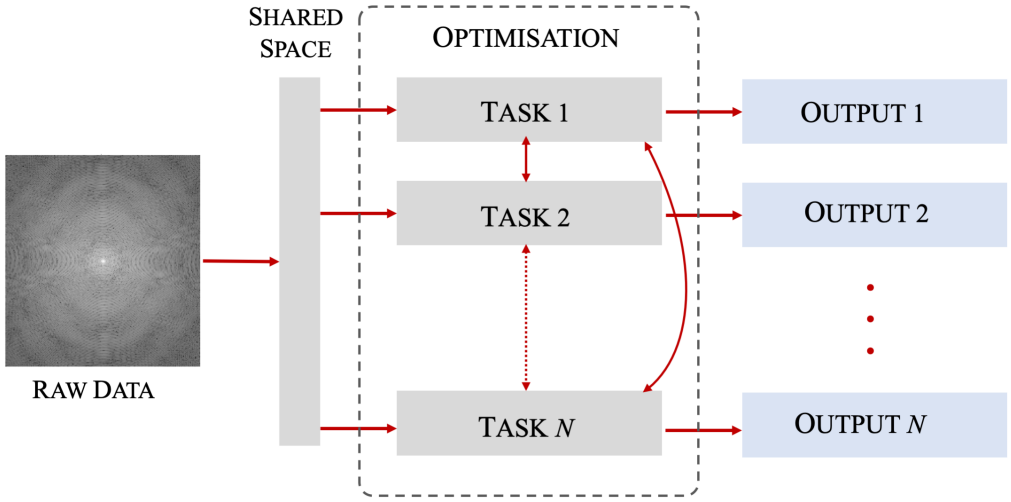


**(b)** A joint approach.

**Figure 1.1:** Illustration of sequential and joint approaches. (a) In the classical sequential pipeline, each task is solved separately and only starts when the previous one is finished. In this way, errors get more easily propagated in every step. (b) In joint models, all tasks are intertwined through a mathematical model that exploits correlation and complementary information in the data. The optimisation scheme makes possible to connect each output. In these examples, the raw data is the measurement in frequency domain, typical of MRI. In the rest of the thesis, we will see different examples of possible tasks in imaging problems.

example, task 1 is the image reconstruction from the raw data and task 2 could be image denoising of the reconstructed image (output 1).

Although this seems logical at first glance, we also observe that each individual step is strongly connected to the previous and next one. Certainly, the quality of the image, whether you can clearly identify edges and textures, will affect for example the detection of cancer regions, and in fact, the accuracy of these detected regions will then determine pre-surgical planning for the clinician. This sequential pipeline is intrinsically subject to error propagation from one step to the next: the further we go from the raw data of the physical sensor, the more mistakes we introduce in the process. Moreover, the classical

sequential approach can be seen as a sub-optimal configuration [LMGCCV12]: each task is treated separately without exploiting relevant information and outcomes at different stages to improve performance towards the final goal.

More recent developments in the variational context have shown that performing those tasks *jointly* (i.e. in a multi-task framework) offers great benefits, and this is the perspective of this thesis. Examples of variational joint models can be found for different purposes, such as joint reconstruction and motion estimation [JF03, SMF09, BMMK+10, OME+16, BDF+17, ARWGS18, BDS18], joint reconstruction and segmentation [RR07, Kla11, CBP+14, BRZ16], joint segmentation and registration [OGLG15, DG18, DOLG17, SPSM18], to name a few. The conceptual idea of *joint models* is depicted in Figure 1.1b, illustrating that all imaging tasks are interconnected through modelling and optimisation to boost each output.

Our research hypothesis is that solving multiple processes - jointly - will yield overall performance improvement compared to the classical sequential case. In this thesis, we demonstrate that by sharing representation between tasks and carefully interconnecting them, one can create synergies across challenging problems and reduce error propagation. This results in boosting the accuracy of the outcomes whilst achieving better generalisation capabilities than sequential models.

The main motivation is that one single model may neglect a potentially rich source of information hidden in other related tasks [Car97]. And especially when tasks are correlative and complementary at a certain level, exploiting the correlation between them is beneficial for improving the final outcome. By carefully intertwining and sharing information across the different imaging processing tasks, we can exploit relevant features and each individual output and finally refine them through a suitable optimisation scheme.

While there has been a growing set of research exploring multi-task frameworks in the context of machine learning, this is not the focus of this work. Although, certainly, those approaches deserve attention, this thesis is concerned with variational methods for which we have a solid interpretability of the model and various theoretical guarantees. However, we will demonstrate in Section 6.2 how we can integrate algorithms from machine learning in our proposed variational framework, resulting in a *hybrid model*.

Certainly, designing relevant functionals and models to interconnect multiple tasks in such a way that they positively affect each other to boost performance in the final outcome, is not a trivial task. In this thesis, we go beyond current approaches and set a new basis for variational multi-task methods, with a particular focus on magnetic resonance

imaging (MRI). We propose several joint models and demonstrate the effectiveness of multi-task frameworks for different applications.

## 1.1 Contribution

This thesis is a contribution to variational multi-task models for inverse imaging problems. Through three research projects, we go beyond existing solutions and demonstrate that by carefully sharing information across different imaging tasks, we improve overall performance and reduce error propagation compared to state of the art methods. While this is an important part of the thesis, our specific contributions are discussed next.

### 1.1.1 Multi-Task Model for Reconstruction and Segmentation with Non-Convex Bregman Iteration

In Chapter 3 we present a research project in collaboration with Martin Benning, Matthias J. Ehrhardt, Lynn F. Gladden, Richard Mair, Andi Reci, Stephanie Reichelt, Andrew Sederman and Carola-Bibiane Schönlieb that was published in [CBE+19]. In this work we deal with the *problem of connecting image reconstruction and segmentation in a unified framework* and we propose a novel joint variational model to tackle both tasks simultaneously using non-convex Bregman iteration. Typically, segmentation is performed in the reconstructed image, that is after the reconstruction task is finished. In this way, one may lose complementary information (i.e., edge and object localisation) that is embedded in the raw data, leading to sub-optimal solutions. Those errors are then propagated to the next task, i.e. segmentation in this case. We explore a new approach that combines reconstruction and segmentation in a unified framework. We derive a variational model that consists of a total variation regularised reconstruction from undersampled measurements and a Chan-Vese based segmentation. We extend the variational regularisation scheme to a Bregman iteration framework to improve the reconstruction and therefore the segmentation. We develop a novel alternating minimisation scheme that solves the non-convex optimisation problem with provable convergence guarantees. Our results for synthetic and real data show that both reconstruction and segmentation are improved compared to the classical sequential approach. Our main contributions are:

- In our proposed joint method, we obtain an image reconstruction that preserves its intrinsic structures and edges, possibly enhancing them, thanks to the joint segmentation, and simultaneously we achieve an accurate segmentation. In this unified Bregman iteration framework, we have the advantage of improving the

reconstruction by reducing the contrast bias in the TV formulation, which leads to more accurate segmentation. In addition, the segmentation constitutes another prior for the reconstruction by enhancing edges of the regions of interest.

- We propose a non-convex alternating direction algorithm in a Bregman iteration scheme for which we prove global convergence.
- We evaluate the performance of our joint approach throughout an exhaustive set of experimental results on synthetic and real MRI data. We provide a thorough comparison with classical sequential approach and with another joint model from the literature.

### 1.1.2 Multi-Task Model for Phase Reconstruction and Magnitude Segmentation in Velocity-Encoded MRI

In Chapter 4 we extend our joint model for reconstruction and segmentation described in Chapter 3 to the problem of estimating not only the magnitude image from MRI data, but also the phase image, and simultaneously identify regions of interest through the segmentation task. This extension is not trivial as estimating velocity through phase images involve a non-convex and non-linear problem. This project is in collaboration with Martin Benning, Lynn F. Gladden, Andi Reci, Andrew Sederman and Carola-Bibiane Schönlieb and resulted in [CBG+19]. In this work, we consider the *problem of estimating flow, magnitude and segmentation of regions of interest from undersampled velocity-encoded MRI data*. The problem is of great interest in different areas including cardiovascular blood flow analysis in medical imaging and rheology of complex fluids in industrial applications. To this end, we propose a joint variational model for undersampled velocity-encoded MRI. The significance of our approach is that by tackling the phase and magnitude reconstruction *jointly*, we can exploit their strong correlation. This is further assisted by the introduction of a segmentation term as additional prior to enhance edges of the regions of interest. Our main contributions are

- A description of the forward and inverse problem of velocity-encoded MRI in the setting of bubbly flow estimation.
- A joint variational framework for the approximation of the non-linear inverse problem of velocity estimation. We show that by exploiting the strong correlation in the data, our joint method yields an accurate estimation of the underlying flow, alongside a magnitude reconstruction that preserves and enhances intrinsic

structures and edges, thanks to the joint segmentation approach. Moreover, we achieve an accurate segmentation to discern between different areas of interest, e.g. fluid and air.

- An alternating Bregman iteration method for non-convex optimisation problems.
- Numerical experiments on synthetic and real data in which we demonstrate the suitability and potential of our approach and provide a comparison with sequential approach.

### 1.1.3 Multi-Task Model for MRI Reconstruction: Joint Reconstruction, Registration and Super-Resolution

In Chapter 5 we present a research project to improve MRI reconstruction from dynamic motion-corrupted MRI data. This is a collaboration with Angelica I. Aviles-Rivero, Noémie Debroux, Martin J. Graves, Carole Le Guyader, Guy Williams and Carola-Bibiane Schönlieb and resulted in [CDAR+19], [CARD+19a] and [CARD+19b].
Motion degradation is a central problem in MRI. This work addresses the problem of *how to obtain higher quality, super-resolved motion-free, reconstructions from highly undersampled MRI data*. In this work, we present for the first time a variational multi-task framework that allows joining three relevant tasks in MRI: reconstruction, registration and super-resolution. Our framework takes a set of multiple undersampled MR acquisitions corrupted by motion into a novel multi-task optimisation model, which is composed of an $L^2$ fidelity term that intertwines the different tasks, super-resolution foundations and hyperelastic deformations to model biological tissue behaviours. We demonstrate that this combination yields to significant improvements over sequential models and other bi-task methods. Our results exhibit fine details and compensate for motion producing sharp and highly textured images compared to state of the art methods. Our main contributions are:

- We propose a computationally tractable and mathematically well-motivated variational multi-task framework for motion correction in MRI, in which our novelties largely rely on:
  - An original optimisation model that is composed of an $L^2$ fidelity term that allows sharing representations between three tasks (reconstruction, super-resolution and registration); a weighted total variation (TV) ensuring robustness of our method to intensity changes; a TV regulariser of the highly resolved

reconstruction; and a hyperelasticity-based regulariser. We demonstrate that this combination yields to significant improvements over sequential models and existing multi-task methods.

  - We show that our optimisation problem can be solved efficiently by using auxiliary variables and then splitting it into sub-problems. We show that this requires lower CPU time than several methods from the body of literature.

- We extensively evaluate our approach using five datasets and different acceleration factors. We also compare our multi-task framework against existing approaches. Our experiments are further validated by interpretations of experts through a user-study.

## 1.2 Thesis Overview

This thesis is organised into three main chapters, i.e. Chapters 3, 4 and 5, covering the main contributions described in the previous section. Additionally, in Chapter 2, we introduce the main mathematical tools used in this thesis, that is variational methods in inverse problems, and describe the various imaging problems we tackle in this work. Finally, we also give a brief overview of our imaging modality of interest, namely MRI.

In Chapter 3, we introduce a novel joint framework for reconstruction and segmentation. First, we describe the problems of MRI reconstruction and region-based segmentation. We then introduce our joint reconstruction and segmentation approach in a Bregman iteration framework. This section also contains a detailed comparison with other joint models in the literature. We study the non-convex optimisation problem and present the convergence analysis for this class of problems. Finally we present numerical results for MRI data for different applications. Here we investigate the robustness of our model by testing the undersampling rate up to its limit and by considering different noise levels.

In Chapter 4, we present the extension of the joint framework for reconstruction and segmentation to the estimation of velocities from MRI velocimetry. Firstly, we describe the derivation of the inverse problem of velocity-encoded MRI from the acquisition process to the spin proton density estimation. Secondly, we present our joint variational model to jointly estimate phase and magnitude reconstruction and its segmentation. We then present the optimisation scheme for the non-convex and non-linear problem using Bregman iteration. Finally, we demonstrate the performance of our proposed joint method in comparison with a sequential approach for synthetic and real MRI data.

In Chapter 5, we introduce for the first time a variational multi-task framework that interconnects three relevant imaging problems, namely image reconstruction, registration and super-resolution, for the central problem of motion-corrupted dynamic MRI. The aim is to produce a high quality image by compensating for motion and acceleration artefacts. After giving an overview of the field, we describe the derivation of the joint model by introducing the relevant tasks and regularisation terms. Here, we provide a theoretical result on the existence of minimisers for such a joint functional. Then, we explain in detail our alternating optimisation scheme. We present an extensive set of results to show the potential of our approach, which was validated by a user-study. Finally, we offer a discussion of the possibilities of our model in terms of a plug-and-play framework.

Finally, in Chapter 6, we conclude the thesis by summarising our contributions and highlighting the possible outcomes and applications for our proposed models. Furthermore, we present a discussion of on-going and future work that arised from the thesis.

# Chapter 2

# Preliminaries

This chapter aims at introducing the main mathematical tools and the imaging processing problems we will consider in this thesis. Finally, we give a brief overview of MRI as this constitutes the main application of the proposed work. We assume that the reader is familiar with basic concepts of mathematical analysis and linear algebra. We provide some notions and definitions which will be useful for this thesis in Appendix A. For any further details that are beyond the scope of this thesis, we refer the reader to [AFP00a, Bre10, EG91, Rud87].

## 2.1 Variational Methods in Inverse Problems

Inverse problems in imaging are highly relevant in different areas of science as they allow us to gain high-level understanding and achieve practical solutions for real-world problems including image segmentation, reconstruction and registration. In particular when dealing with advanced imaging modalities, inverse problems become more challenging and one needs to account for specific modelling hypothesis. Having introduced the general linear operator equation in Chapter 1, we are interested in reconstructing an image $u$ that underwent some kind of degradation through the forward operator $\mathcal{A}$. Most of the time, it is not possible to invert $\mathcal{A}$ and the problem is said to be ill-posed. According to the definition proposed by Hadamard, an inverse problem is said to be well-posed if a solution exists, is unique and depends continuously on the data [Had02, Had23, Joh60, EHN96]. However, most inverse problems in imaging fail to fulfil at least one of these three points and are therefore considered to be ill-posed. In this case, we need to introduce some prior knowledge on $u$, leading to regularisation. Variational methods have been proposed as a way to tackle the ill-posedness of the inverse problems. In a variational approach, the

aim is to minimise an *energy functional* $E$ modelling certain assumptions on the problem

$$u^* := \arg\min_u E(u). \tag{2.1}$$

The energy functional $E$ is usually composed of a *data term* $D(u, f)$ and a *regulariser* $J(u)$

$$E(u) = D(\mathcal{A}u, f) + \alpha J(u). \tag{2.2}$$

The data term or fidelity term depends on the input data $f$, which is usually distorted, and it ensures that the solution $u$ is close to the measurement $f$. This is usually formulated by minimising a norm of the distance between $f$ and $Au$, where the norm depends on the given problem. For example, if we have additive Gaussian noise, this results in $D$ being the squared $L^2$-norm, as we will see later in the thesis. The regulariser encodes prior knowledge about the characteristics of the desired output, not depending on the observed data. In many practical problems, it is reasonable to assume sparsity of the solution in a particular transformed domain. For example, using the $L^1$-norm, sparsity can be enforced by penalising $\|u\|_1$, which means that the components of $u$ are sparse, or by penalising its gradient $\|\nabla u\|_1$, leading to piecewise constant reconstructions with sparse edges. The parameter $\alpha > 0$ balances the data fidelity term against the regularisation.

We refer the reader to [EHN96, SGG+09, CP16, BB18] for classical regularisation approaches in inverse problems with application to imaging.

A particular type of regularisation that we are going to consider in this thesis is the **total variation**, introduced in 1992 by Rudin, Osher and Fatemi in [ROF92] for image denoising. In its rigorous mathematical formulation, the total variation is defined as

$$\mathrm{TV}(u) := \sup\left\{ \int_\Omega u \operatorname{div} \Psi \, \mathrm{d}\mathbf{x} \,\middle|\, \Psi \in \mathrm{C}_c^1(\Omega, \mathbb{R}^d),\ \|\Psi\|_\infty \leq 1 \right\} \tag{2.3}$$

where $u \in L^1(\Omega)$ and $\Omega$ is an open subset in $\mathbb{R}^n$ representing the image domain. Since in image analysis we require discontinuities in $u$ such as intensity jumps at edges, we define a more suitable function space, that is the **space of functions of bounded variations**:

$$BV(\Omega) = \{u \in L^1(\Omega) \mid \mathrm{TV}(u) < \infty\}. \tag{2.4}$$

If we assume that $u$ is sufficiently smooth, i.e. $u \in W^{1,1}(\Omega)$, then the total variation simplifies to

$$\mathrm{TV}(u) = \int_\Omega |\nabla u| \, dx. \tag{2.5}$$

Then in the discrete setting where $\Omega = \{1, \dots, n_1\} \times \{1, \dots, n_2\}$, it corresponds to the 1-norm penalty on a discrete finite difference approximation of the two-dimensional gradient $\nabla : \mathbb{R}^n \to (\mathbb{R}^2)^n$, that is $\nabla u(i,j) = (\nabla_1 u(i,j), \nabla_2 u(i,j))^T$, with:

$$\begin{aligned} \nabla_1 u(i,j) &= \begin{cases} u(i+1,j) - u(i,j) & \text{if } i < n_1 \\ 0 & \text{if } i = n_1 \end{cases} \\ \nabla_2 u(i,j) &= \begin{cases} u(i,j+1) - u(i,j) & \text{if } j < n_2 \\ 0 & \text{if } j = n_2 \end{cases} \end{aligned} \tag{2.6}$$

with $n = n_1 n_2$ being the total number of pixels. Finally the discrete total variation is

$$\mathrm{TV}(u) = \|\nabla(u)\|_{2,1} = \sum_{(i,j)\in\Omega} \sqrt{|\nabla_1 u(i,j)|^2 + |\nabla_2 u(i,j)|^2}, \tag{2.7}$$

for the isotropic case.

Since its introduction, TV has been investigated and used extensively in the context of image processing thanks to its edge preserving properties. Some of these applications include image denoising [CL97, BC98, CKS01, Nik04, VO04, LV08b], image deblurring [Ves01, CC98, WYZ07, BT09], image inpainting [SC02, CS05], image decomposition [Mey01, VO03, BLMV10], image segmentation [LKY+09] and motion estimation [ZPB07], to name a few.

## 2.2 Imaging Problems

In the following, we will give a brief introduction of the imaging problems we encounter in this thesis, namely image reconstruction, segmentation, registration and super-resolution.

### 2.2.1 Reconstruction

Recent years have seen the development of a variety of imaging modalities in many areas including biology, medicine, engineering and physics, to name a few. All these techniques such as magnetic resonance imaging (MRI), X-ray computed assisted tomography (CT), positron emission tomography (PET) are based on different physical principles and are usually concerned with the acquisition of some indirect signal that needs to be transformed into an interpretable quantity of interest. This problem is called image reconstruction and it is usually modelled depending on the underlying physics of the specific imaging modality. The basic limitation is that during acquisition several sources of noise coming

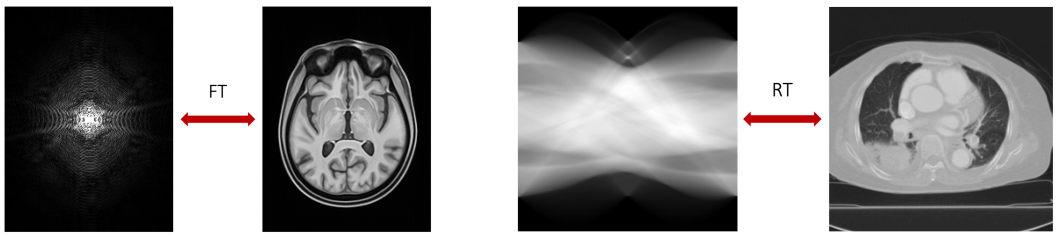


**(a)** MRI **(b)** CT

**Figure 2.1:** Examples of image reconstruction. Left: MRI reconstruction is related to the Fourier transform and the raw data is in the frequency domain. Right: CT reconstruction is modelled using the Radon transform and the raw data is called sinogram.

from both the hardware and the object that we want to image, will affect the signal. Additionally, due to sampling and discretisation of the signal, we only observe incomplete data which leads to artefacts in the reconstruction due to missing information. Based on the theory of compressed sensing (CS) [CRT06a, CRT06b, Don06, LDP07, EK12], it is possible to tackle these problems by exploiting sparsity in some transformed domain of the signal, while acquiring significantly fewer measurements than the classical sampling theorem.

The reconstruction can be seen as an inversion model to map some given noisy measurements into the corresponding image and it is modelled as the classical formulation for inverse problems (1.1). The operator $\mathcal{A}$ will model the physical acquisition process of the specific imaging system and it is in general a trade-off between accuracy of the model itself and computational complexity.

For example, in MRI, the signal is encoded in the frequency domain, in the so-called $k$-space, and mathematically this is related to the Fourier transform [BCH+14] (see Figure 2.1a). Additionally, the MRI forward operator can account for undersampling and coil sensitivities. In X-ray CT, the data is collected in the sinogram as a collection of line integrals and this process is characterised by the Radon transform [Buz08] (see Figure 2.1b). In both MRI and CT the noise is assumed to be additive Gaussian noise with zero mean and standard deviation $\sigma$ [GP95, Mac96, DRR+07]. Therefore, the discrepancy measure for the reconstruction problem in a variational formulation is the squared $L^2$-norm. In PET, the operator is again related to the Radon transform, however, the noise in this case follows a Poisson distribution [BMTV05, BLZ+08, OF97], thus, the fidelity term is now the Kullback-Leibler divergence.

Finally, by modelling the discrepancy measure and forward operator according to the specific application, we solve a variational problem of the form (2.2). In this case, different sparsity-promoting regularisation functionals can be chosen, including total

**(a)** Original photo **(b)** Segmentation (finer) **(c)** Segmentation (coarser)

**Figure 2.2:** Example of image segmentation. From left to right: original frame and two segmentation results showing different numbers of regions. There segmentations were generated following the model in [SWFU15].

variation (e.g.[LDP07, BUF07, LKS+09, Blo08]), wavelets (e.g. [GC11, GKHPU11, GDC05, QGN+12]) or dictionary learning (e.g. [AEB06, RB10, XYM+12]), to name a few.

### 2.2.2 Segmentation

Image segmentation refers to the task of partitioning an image into meaningful non-overlapping regions (e.g. see Figure 2.2). While humans are naturally very good at distinguishing different objects in a picture, the mathematical formulation that leads to the same partition is not easy to obtain. Some assumptions need to be made: e.g. pixels belonging to the same region have similar intensities, and/or sharp intensity changes identify interface between different structures.

Image segmentation has found a large number of applications in different fields, such as medical imaging (e.g. tumour detection, surgery planning, surgery navigation), object detection in satellite images (e.g. to identify roads, trees, crops), traffic control systems (e.g. to detect vehicles, planes, pedestrians) and video surveillance (e.g. to monitor and detect specific activities in public places).

Although in the recent years machine learning has proposed numerous successful segmentation algorithms [LSD14, RFB15, Gir15, PCD15, LDG+17, GDDM16], in the following we are only giving an overview of unsupervised methods relying on low-level features, such as pixel intensities, texture, curvature, without relying on any explicit object model. Indeed, these approaches are more similar to the methods encountered in the rest of the thesis. Following [ZMCL16], we can distinguish between

1. discrete methods: the image is treated as a fixed discrete grid. These methods include image thresholding, e.g. Otsu [Ots79]; filtering approaches, e.g. the Canny edge detection algorithm. This method uses first a Gaussian filter to reduce noise, then it applies filters (e.g. Sobel mask) to find intensity gradient and finally threshold

the image to keep only the edges. Other approaches are clustering methods, e.g. K-means, Fuzzy K-means, C-means [Mac67, Ste56, Llo06], where the aim is to group pixels or object based on proximity, similarity, continuation, closure and symmetry. Finally graph-based methods consider an image as a graph, where each pixel typically corresponds to a node and is connected to the other nodes by edges whose value respects some similarities [SM00, BVZ01a, BVZ01b, FH04, BK04].

2. continuous methods: based on variational techniques, the image is seen as a continuous surface. These can be subdivided into two categories:

   - edge-based methods, often referred to as active contours or "snakes", detect different objects by evolving and deforming a snake/contour curve $C$ to match object boundaries. First introduced by Kass [KWT88], a spline curve is parametrised and evolves by minimising an energy functional composed of an internal regularisation force to ensure smoothness and an external data-driven energy based on the image gradient. However, this functional is non-convex and sensitive to initialisation. To tackle this problem, Osher et al. [OS88] proposed an implicit parametrisation of the curve through the level-set method, allowing an implicit modelling of topological changes of the curve. In 1997 Caselles et al. [CKS97] introduced the geodesic active contour model and showed that the classical energy snakes model is equivalent to finding a geodesic curve in a Riemannian space with a metric derived from the image content. Moreover, by using the zero level line of a level-set function as the evolving curve, topological changes are automatically handled. Since then, several models have been introduced based on active contours, including [LV08a] where a topology-preserving constraint prevents the curves from splitting or merging.
   - region-based methods, based on the assumption that pixels belonging to the same object share some similarities. In contrast to the active contours models, the segmentation is not driven by edges and image gradients. These models are mainly based on the well-known Mumford-Shah model. In [MS89], the authors introduced the following model

$$\inf_{u,K} \mu \int_{\Omega} (u-f)^2 dx + \int_{\Omega \setminus K} |\nabla u|^2 + \mathcal{H}(K) \tag{2.8}$$

   where $\mathcal{H}$ is the 1-D Hausdorff measure, $K$ is the set of discontinuities for a given image $f$. The goal is to find an image $u$ which is a piecewise-smooth

approximation of $f$, based on the idea that $f$ can be partitioned in regions in which it varies smoothly in the interior, and quickly at the boundaries represented by $K$. Since then, a large number of variants of (2.8) have been proposed. A special case is the so-called minimal partition which is obtained by restricting $u$ to be piecewise constant, e.g. [CV01, CCP12a, SW14], and this is what we will use in Chapter 3.

### 2.2.3 Registration

In many applications, e.g. medical imaging, several images of the same patient are acquired using different imaging modalities to provide complementary information, or acquired at different times to assess disease progression or treatment planning. This kind of data is most informative when the images are put into a common space. This process is called image registration.

Image registration is one the most challenging tasks in medical image analysis. It refers to the process of finding the optimal spatial transformation or correspondence between two or more images, achieving the best fitting and overlaying (see Figure 2.3). In general, we can refer to one image as the template $T$ or moving image, and to the other one as the Reference $R$ or fixed image, where $T, R : \Omega \subset \mathbb{R}^d \to [0, 1]$. The idea is that a transformation $\varphi : \mathbb{R}^d \to \mathbb{R}^d$ is applied to the source image, mapping point locations of $T$ to other locations in $R$. Is is modelled as an optimisation problem for estimating the best transformation that minimises an energy of the form:

$$\min_{\varphi} \underbrace{D(T(\varphi), R)}_{\text{distance measure}} + \underbrace{J(\varphi)}_{\text{regulariser}} \tag{2.9}$$

The first term is a similarity measure that quantifies the level of alignment between the two images. A popular example is the $L^2$-norm $D(T(\varphi), R) = \frac{1}{2}\int_\Omega (T(\varphi(x)) - R(x))^2 dx$. The regularisation term provides some prior information in order to enforce specific types of solutions and it is closely related to the deformation model; for example one can consider $L^2$-norm of the derivatives on the displacements to enforce some smoothness. Following [SDP13a], a registration algorithm consists of three main components: a *deformation model*, an *objective function* and an *optimisation method* .

Deformation models can be divided into two broad categories: *linear* models, which include rotation, translation, scaling and shearing, and *elastic* (non-linear, deformable) models. In this last category we can distinguish among:

**(a)** Reference image (R)

**(b)** Template image (T)

**(c)** Difference between R and T before registration

**(d)** Difference between R and T after registration

**Figure 2.3:** Example of image registration. Given a reference image (R) and a moving template (T) that are misaligned (c), the registration task aims at aligning T to R. Images computed using an affine transformation. Result in (d). The differences are displayed as a composite RGB image showing R and T overlaid in different color bands.

1. geometric transformations derived from physical models: elastic body, viscous fluid flow, diffusion, curvature and flows of diffeomorphisms models [SDP13b, CRM+96b].

2. geometric transformations derived from interpolation theory: radial basis functions, elastic body splines, free-form deformations, basis functions from signal processing, piecewise affine models [DKFH97, dVBV+17a].

3. knowledge-based geometric transformations: statistically-constrained, inspired by biomechanical/biophysical models [CSB+05].

In addition to these models, it is often useful to consider task-specific constraints, such as volume [HM04] or topology [KD04, OLG15] preservation, as a way to introduce prior knowledge and tackle the intrinsic ill-posedness of the registration problem. This is relevant in many applications, e.g. to avoid interpenetration of matter, which is physically not possible, or in medical imaging, to preserve volume of anatomical structures.

The choice of a similarity or matching criterion is also important. We can identify three main methods:

1. geometric methods: aim at assessing a correspondence between landmarks and requires user input [CR03].

2. iconic methods (intensity-based methods): aim at quantifying the alignment of the images based on intensity or attribute distances over the whole image domain [DLG14, KBD17].

3. hybrid methods: aim at combining geometric and iconic methods either independently and sequentially or using the additional information as constraints [LL14].

Finally, the choice of the optimisation algorithm will determine the quality of the obtained transformation. Optimisation methods fall into two main categories:

1. continuous methods: gradient descent [BMTY05], conjugate gradient [MY01], Newton-type [WVRE08], stochastic gradient descent [WIVA+96].

2. discrete methods: including graph-based methods [TC07] and belief propagation approaches [HSP+16].

Additionally, in the context of machine learning, several algorithms have been proposed for image registration, including the RegNet convolutional neural network architecture developed in [SdVB+17]. However, these models do not constitute the focus of this thesis.

Following [Mod04], another classification of registration methods distinguishes

1. parametric methods: the set of feasible transformations is restricted to a certain class of mapping (e.g. splines [RSH+99])

$$D(T(\varphi), R) \to \min_{\varphi} \text{ s.t. } \varphi \in Q = \{x + \sum_j w_j q_j, w \in \mathbb{R}^m\}$$

   where the components of $\varphi$ are linear combinations of certain basis functions $q$ and the coefficients are the parameters $w$.

2. non-parametric methods: deformation maps are not restricted to a parametrisable set and thus more degrees of freedom are allowed [SDP13a]

$$\min_{\varphi} D(T(\varphi), R) + \alpha J(\varphi - \varphi_{reg}), \quad \varphi_{reg}(x) = x.$$

In all of these models, the distance measure can be chosen in several ways. Examples are the $L^2$-norm of the difference between the deformed template and the reference intensities, correlation, mutual information, normalised gradient fields. The regulariser can also vary a lot, including the use of the linearised elastic potential [Bro81], viscous fluid flow [Chr94], diffusion [BF02], and curvature models [BF03]. In Chapter 5, we will introduce a regulariser based on hyperelasticity principles to allow for large and smooth deformations.

**(a)** Original image **(b)** Low resolution image **(c)** Super-resolved image

**Figure 2.4:** Example of image super-resolution. From left to right: original image, low resolution version and a super-resolved image obtained from the low resolution.

**Topology preservation.** In many applications, especially in medical imaging, we need to ensure that the deformation we estimate during the registration algorithm are physically feasible. This means that the estimated deformation will not result in penetration of boundaries and overlapped or distorted mesh elements. Therefore, topology preservation is a crucial step to guarantee that structures will avoid distortion and maintain their connectivity and relations between neighbouring structures. This can be done by looking at the Jacobian determinant [DM90]. Generally, values equal to 1 in the Jacobian determinant mean that the topology is preserved. Small positive ($< 1$) or large positive values indicate that the deformations exhibit contractions or expansions, respectively. However, negative numbers in the Jacobian determinant result in distortions, overlapping and creation of new structures. This approach has been adopted in several works involving deformable registration models to guarantee that the estimated deformation are realistic (e.g. [CRM96a, AAF99, OLG15]).

### 2.2.4 Super-Resolution

Super-resolution (SR) is the process of generating an image with a higher resolution than its source. The source can consist of one or more low quality frames [vO06] (see an example in Figure 2.4). This problem finds practical applications in many real-world problems including satellite and aerial imaging, medical image processing, facial image analysis, text image analysis, sign and number plates reading, and biometrics recognition [NM14]. In this thesis, we are mainly interested in a multi-frame setting for which we give a brief introduction in the following section.

### Variational Multi-Frame Super-Resolution

In a classical multi-frame variational framework, super-resolution is the problem of restoring a single high-resolution (HR) image from several low quality images representing the same scene possibly corrupted by motion. This is a highly ill-posed inverse problem which has been extensively studied in the literature both in a variational setting [Tsa89, KBV90, PST94, EF97, EHO01, UPWB10, GDCM17] and more recently in the context of deep learning [WCH19]. The general variational formulation (see e.g. [EHO01]) is given by

$$\min_u \sum_{i=1}^{m} \|\mathcal{D}\mathcal{B}\mathcal{W}_i u - f_i\|_2^2 + \lambda \operatorname{Reg}(u), \tag{2.10}$$

where $\mathcal{D}$ is the downsampling operator, $\mathcal{B}$ is the blurring operator, $\mathcal{W}_i$ corresponds to the geometric warp existing between the $m$ observed images $f_i$ and the restored image $u$ to correct for motion. Finally, $\operatorname{Reg}(u)$ is a generic regulariser and $\lambda$ its regularisation parameter. The downsampling operator defines the way we obtain the low quality images, e.g. this can be modelled as a window average [GDCM17].

The blurring kernel models any blurring affecting the low resolution (LR) observed images. The blurring can be caused by the imaging system, acquisition conditions, and/or motion, which is the case we will encounter in this thesis. Blurring due to the imaging system is modelled by the so-called point spread function (PSF), which is usually a Gaussian kernel. The warping operator aims at compensating temporal or spatial misalignment between the LR images. This can be done through a registration task, to align the different frames to the same coordinate space. Finally, different regularisation functionals can be used, such as TV [CZ00, CZ03, MO08, YSG+10, YZS12], wavelet [LJF08, MY10, CP14], Tikhonov-type [ZM07, MSMM08, TYO08], markov random fields [RC01, GAM02, SF06], to name a few.

Note that, from (2.10), we observe the natural connection between registration and super-resolution. Together with a reconstruction framework, this is what we explore in Chapter 5 of this thesis.

## 2.3 Magnetic Resonance Imaging

In this thesis, we mainly deal with the application of Magnetic Resonance Imaging (MRI). In this section, we provide a brief overview to introduce the related imaging problems.

MRI is a non-ionizing and non-invasive imaging technique widely used in medical and non-medical applications, as we will see in this thesis. MRI uses strong magnetic fields to excite the spin of hydrogen protons in the human body [MRI08]. When a magnetic

field is applied the protons' spins rotate at the so-called Larmor frequency $\omega_0$ around the direction of the magnetic field and create a net magnetic vector.

By the introduction of a radio frequency (RF) pulse, it is possible to tilt the magnetic vector. When the RF pulse is switched off, the magnetic vector realigns with the main magnetic field. This process is called *relaxation* of the magnetic vector. The relaxation of the spin follows an exponential decay with time constants $T_1$ and $T_2$. The two relaxations are independent processes, however $T_1$ is always larger than $T_2$. Relaxation parameters and proton density (PD) are generally different for different tissues, thus they are responsible for the contrast in MR images. In addition, RF excitations known as pulse sequences, influence the contrast by manipulating tissue and relaxations. They are responsible for generating and recording the signals at specific times, and for producing the tomographic images by spatially encoding the underlying object. The (simplified) MRI imaging equation reads as

$$f(t) = \int_\Omega r(x) e^{-i2\pi x \cdot k(t)}\, dx\,, \tag{2.11}$$

where we observe that $f$ is just the Fourier transform of the object $r$ and $k(t) \propto \int_0^T G(\tau) d\tau$. We refer to Chapter 4 (Section 4.1) for the full derivation of the inverse problem. The recorded data are Fourier samples at specific spatial frequencies $k(t_0), k(t_1), \dots$ dictated by the design of the gradient $G$ generated from the gradient coils. We refer to this frequency space of measurements as *k-space*. By appropriately designing the gradient coils, we can control how we cover the $k$-space. We notice that the data is acquired sequentially by travelling the $k$-space, which means that the MRI scans are arbitrarily slow. This constitutes a central limitation in MRI and a large body of research is devoted to the study ways to speed up the acquisition process. Naturally, this is important for a number of reasons: long scanning times highly affect patients' comfort, especially for those with severe pathologies or for paediatric imaging [VMA+11]; motion also becomes an issue, leading to degradation in the signal. This prolonged time is prohibitive when imaging fast changing dynamics such as perfusion in cardiovascular system [GBK08].

**Sparse MRI** A way to partially overcome the limitation of slow acquisition consists in exploiting redundancy in the data, following the theory of CS [LDP07] as mentioned in Section 2.2.1. We refer to this as sparse MRI, where the idea is to acquire far fewer measurements than traditionally imposed by the Nyquist–Shannon sampling theorem. This is achieved by collecting $k$-space samples along continuous trajectories determined by the sampling scheme. Some common patterns (e.g. lines, random, spiral) are illustrated

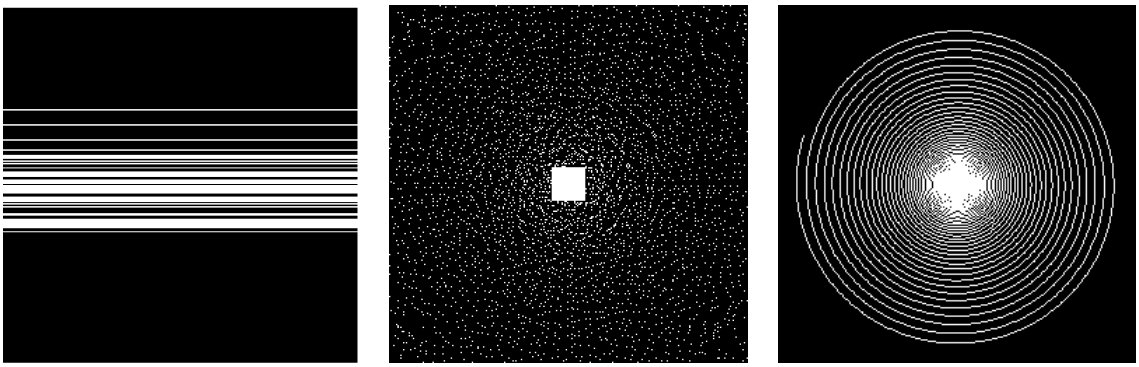

**(a)** Lines **(b)** Random **(c)** Spiral

**Figure 2.5:** Examples of sampling patterns. Note that it is common practice to acquire more samples at the centre of the $k$-space (low frequencies) to be able to recover contrast information.

in Figure 2.5. Note that because the $k$-space is in the frequency domain, it is usual to acquire samples using a variable density, that is more samples are acquired at the centre of the $k$-space (low frequencies) to recover contrast information and thus achieve higher quality reconstructions. Let $\mathsf{S} : \{1, \dots, M\} \to \{1, \dots, N\}$ be the locations of the sampling scheme from the acquisition protocol and let $\mathcal{S} : \mathbb{C}^N \to \mathbb{C}^M$ be the sampling operator with $M << N$ being the total number of acquired samples, much lower than the image size. The sampling operator is defined as

$$(\mathcal{S}x)_m := x_{\mathsf{S}(m)} \tag{2.12}$$

and its adjoint operator $\mathcal{S}^* : \mathbb{C}^M \to \mathbb{C}^N$ as

$$\mathcal{S}^*(f) := \sum_{m=1}^{M} f_m \delta_{n,\mathsf{S}[m]} \tag{2.13}$$

with $\delta_{n,m}$ being the Kronecker delta

$$\delta_{n,m} := \begin{cases} 1, & \text{if } n = m \\ 0, & \text{else} \end{cases}. \tag{2.14}$$

**MRI operator** Finally the MRI forward operator is related to the Fourier transform $\mathcal{F}$ [BCH+14]. Because we mainly work with real-valued images (following the standard assumption that we have negligible phase in many practical cases of interest) but the Fourier transform acts on complex data, we model the MRI forward operator as $\mathcal{A} : \mathbb{R}^n \to \mathbb{C}^m$ and its adjoint $\mathcal{A}^* : \mathbb{C}^m \to \mathbb{R}^n$, see e.g.[EB16], with $\mathcal{A} = \mathcal{S}\mathcal{F}$.

**Parallel MRI** Another approach to speed up the acquisition time consists in acquiring more data at the same time through parallel MRI. In parallel MRI one usually deals with multiple receiver coils with spatially varying sensitivities $\mathcal{P}$ [PWSB99, GJH+02]. These sensitivity maps can then be incorporated in the MRI forward operator, which now reads $\mathcal{A} = \mathcal{S}\mathcal{F}\mathcal{P}$. However, in this thesis, we assume that the coil sensitivities are known and therefore, the problem of how to compute them is not addressed here.

# Chapter 3

# Multi-Task Model for Reconstruction and Segmentation with Non-Convex Bregman Iteration

In this chapter, we introduce our first joint variational model for image reconstruction and segmentation and it is based on the publication [CBE+19]. This is joint work with Martin Benning, Matthias J. Ehrhardt, Lynn F. Gladden, Richard Mair, Andi Reci, Stephanie Reichelt, Andrew Sederman and Carola-Bibiane Schönlieb.

We have seen in Section 2.2 that all imaging modalities such as computed tomography (CT), emission tomography and magnetic resonance imaging (MRI) require a reconstruction approach to produce an image. A common image processing task for applications that utilise those modalities is image segmentation, typically performed posterior to the reconstruction. Recently, the idea of tackling both problems jointly has been proposed. We explore a new approach that combines reconstruction and segmentation in a unified framework.

Image reconstruction plays a central role in many imaging modalities for medical and non-medical applications. The majority of imaging techniques deal with incomplete data and noise, making the inverse problem of reconstruction severely ill-posed. Based on compressed sensing (CS) it is possible to tackle this problem by exploiting prior knowledge of the signal [CRT06a, Don06, LDP07]. Nevertheless, reconstructions from very noisy and undersampled data will present some errors that will be propagated into further analysis, e.g. image segmentation. Segmentation is an image processing task used to partition the image into meaningful regions. Its goal is to identify objects of interest, based on contours or similarities in the interior. Typically segmentation is performed after reconstruction, hence its result strongly depends on the quality of

the reconstruction. Recently the idea of combining reconstruction and segmentation has become more popular. The main motivation is to avoid error propagations that occur in the sequential approach by estimating edges simultaneously from the data, ultimately improving the reconstruction. In this work, we propose a new model for joint reconstruction and segmentation from undersampled MRI data. The underlying idea is to incorporate prior knowledge about the objects that we want to segment in the reconstruction step, thus introducing additional regularity in our solution. In this unified framework, we expect that the segmentation will also benefit from sharper reconstructions. We demonstrate that our joint approach improves the reconstruction quality and yields better segmentations compared to sequential approaches. In Figure 3.1, we consider a brain phantom from which we simulated the undersampled $k$-space data and added Gaussian noise. Figure 3.1b and 3.1e present reconstructions and segmentations obtained with the sequential approaches, while Figure 3.1c and 3.1f show the results for our joint approach. The reconstruction using our method shows clearly more details and it is able to detect finer structures that are not recovered with the classical separate approach. As a consequence, the joint segmentation is also improved. In the following section we present the mathematical models that we used in our comparison. We investigated the performance of our model for two different applications: bubbly flow and cancer imaging. We show that both reconstruction and segmentation benefit from this method, compared to the traditional sequential approaches, suggesting that error propagation is reduced.

**Contributions.** In this chapter, we introduced a novel mathematical approach to jointly perform image reconstruction and segmentation with application to undersampled MRI data, although our model can be used for different imaging modalities. Our main contributions are summarised in the following:

- In our proposed joint method, we obtain an image reconstruction that preserves its intrinsic structures and edges, possibly enhancing them, thanks to the joint segmentation, and simultaneously we achieve an accurate segmentation. In this unified Bregman iteration framework, we have the advantage of improving the reconstruction by reducing the contrast bias in the TV formulation, which leads to more accurate segmentation. In addition, the segmentation constitutes another prior for the reconstruction by enhancing edges of the regions of interest.

- We propose a non-convex alternating direction algorithm in a Bregman iteration scheme for which we prove global convergence.

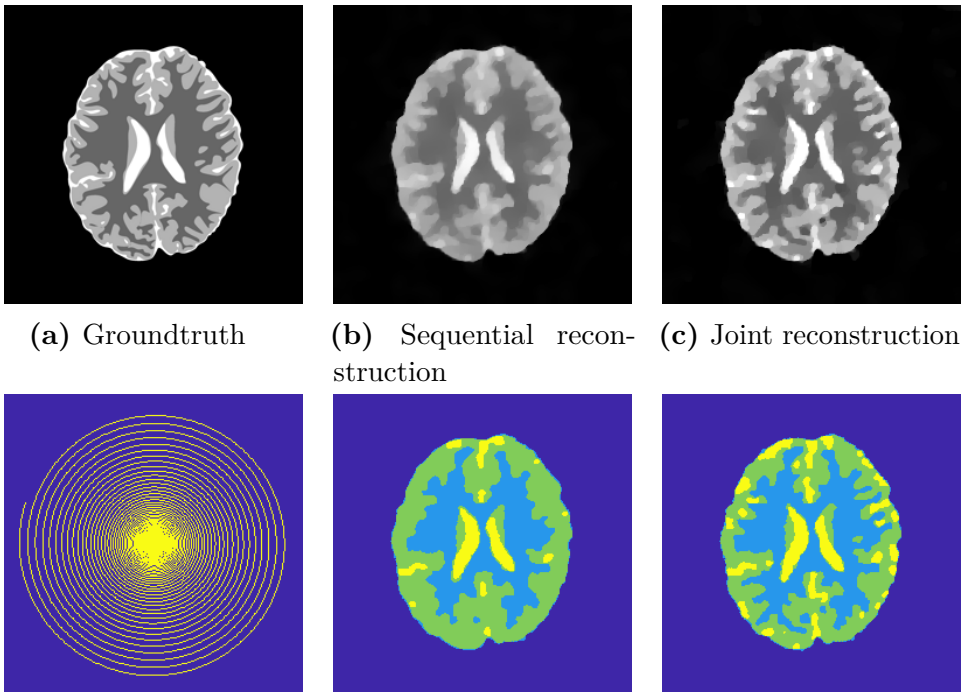

**(a)** Groundtruth **(b)** Sequential reconstruction **(c)** Joint reconstruction

**(d)** Sampling matrix **(e)** Sequential segmentation **(f)** Joint segmentation

**Figure 3.1:** Sequential approach (left) versus unified approach (right). Combining reconstruction and segmentation in a single unified approach improves both the reconstructed image and its segmentation. See Figure 3.2 for more details.

- We evaluate the performance of our joint approach throughout an exhaustive set of experimental results on synthetic and real MRI data. We provide a thorough comparison with classical sequential approach and with another joint model from the literature.

**Organisation of the chapter.** The chapter is organised as follows. In Section 3.1 we describe the problems of MRI reconstruction and region-based segmentation. We then introduce our joint reconstruction and segmentation approach in a Bregman iteration framework. This section also contains a detailed comparison with other joint models in the literature. In Section 3.2 we study the non-convex optimisation problem and present the convergence analysis for this class of problems. Finally in Section 3.3 we present numerical results for MRI data for different applications. Here we investigate the robustness of our model by testing the undersampling rate up to its limit and by considering different noise levels.

## 3.1 MRI Reconstruction and Segmentation

In the following section we recall the mathematical tools to perform image reconstruction and image segmentation (see Section 2.2.1 and Section 2.2.2 for an overview). In this work, we focus on the specific MRI application; however, our proposed joint method can be applied to other imaging problems in which the measured data is connected to the image via a linear and bounded forward operator, cf. Subsection 3.1.1. Finally we present our model that combines the two tasks of reconstruction and segmentation in a unified framework.

### 3.1.1 Reconstruction

In this chapter, we consider the application of MRI and we refer to the measurements $f$ as the $k$-space data. We recall the general reconstruction problem which reads

$$f = \mathcal{A}u + \eta. \tag{3.1}$$

As explained in Section 2.3, the Fourier samples are stored in the k-space sequentially, meaning the scanning time is constrained by physical limitations of the imaging system. One of the most common ways to perform fast imaging consists of undersampling the $k$-space; this, however, only yields satisfactory results if the dimension of the parameter space can implicitly be reduced, for example by exploiting sparsity in certain domains. In the reconstruction, this assumption is incorporated in the regularisation term. Let $\Omega := \{1, \dots, n_1\} \times \{1, \dots, n_2\}$ with $n_1, n_2 \in \mathbb{N}$ be a discrete image domain. Let $f = (f_i)_{i=1}^m \in \mathbb{C}^m$ with $m \ll n = n_1 n_2$ be our given undersampled $k$-space data, where $f_i \in \mathbb{C}$ are the measured Fourier coefficients that fulfil the relationship (3.1) with $\mathcal{A} = \mathcal{S}\mathcal{F}$. The operator $\mathcal{A}$ is now composed by $\mathcal{S} : \mathbb{C}^n \to \mathbb{C}^m$, which is a sampling operator (defined in Section 2.3) that selects $m$ measurements from the $\mathcal{F}u$ data according to the locations provided by a binary sampling matrix (see e.g. Figure 3.1d), where $\mathcal{F}$ is the discrete Fourier transform. In MRI, the noise $\eta$ is drawn from a complex-valued Gaussian distribution with zero mean and standard deviation $\sigma$ [Mac96].

In the formulation of problem (3.1) for MRI, the aim is to recover the image $u \in \mathbb{C}^n$ from the data. However, in this chapter we follow the standard assumption that in many applications we have negligible phase, i.e. we are working with real valued, non-negative images. Therefore, we are only interested in $u \in \mathbb{R}^n$; hence we consider the MRI forward operator as $\mathcal{A} : \mathbb{R}^n \to \mathbb{C}^m$ and its adjoint $\mathcal{A}^* : \mathbb{C}^m \to \mathbb{R}^n$ as modelled in [EB16]. Problem (3.1) is ill-posed due to noise and incomplete measurements. The easiest approach to

approximate (3.1) is to compute the so-called *zero-filling solution*, for which the missing entries are replaced with zero

$$u_z = \mathcal{A}^* f.$$

However, images reconstructed with this approach will suffer from aliasing artefacts because undersampling the $k$-space violates the Nyquist–Shannon sampling theorem. Therefore, we consider a mathematical model that incorporates prior knowledge by using a variational regularisation approach. A popular model is to find an approximate solution for $u$ as a minimiser of the Tikhonov-type regularisation approach

$$u^* \in \arg\min_u \left\{ \frac{1}{2} \|\mathcal{A}u - f\|_2^2 + \alpha J(u) \right\}, \tag{3.2}$$

where the first term is the data fidelity that forces the reconstruction to be close to the measurements and the second term is the regularisation, which imposes some regularity on the solution. The parameter $\alpha > 0$ is a regularisation parameter that balances the two terms in the variational scheme. In this setting, different regularisation functionals $J$ can be chosen (see [BGH+14] for a survey of variational regularisation approaches). Although problems of the form (3.2) are very effective, they also lead to a systematic loss of contrast [Mey01, SC03, BB01]. This is typically observed for common choices of the regulariser $J$, i.e., convex functional. To overcome this problem, [OBG+05] proposed an iterative regularisation method based on the generalised **Bregman distance** [Bre67, Kiw97]. The Bregman distance with respect to $J$ is defined as

$$D_J^{p^k}(u, u^k) = J(u) - J(u^k) - \langle p^k, u - u^k \rangle \tag{3.3}$$

with $p^k \in \partial J(u^k)$, where $\partial J(u^k)$ is called sub-differential and it is a generalisation of the classical differential for convex functions. We replace problem (3.2) with a sequence of minimisation problems

$$u^{k+1} \in \arg\min_u \left\{ \frac{1}{2} \|\mathcal{A}u - f\|_2^2 + \alpha D_J^{p^k}(u, u^k) \right\}. \tag{3.4}$$

The update on the subgradient can be conveniently computed by the optimality condition of (3.4)

$$p^{k+1} = p^k - \frac{1}{\alpha} \mathcal{A}^* (\mathcal{A}u^{k+1} - f). \tag{3.5}$$

In this work, we will focus on one particular choice for $J$, namely the isotropic total variation (TV) regularisation, introduced in Section 2.1.

We then consider the Bregman iteration scheme in (3.4) for $J(u) = \mathrm{TV}(u)$. This approach is usually carried on by initialising the regularisation parameter $\alpha$ with a large value, producing overregularised initial solutions. At every step $k$, finer details are added. A suitable criterion to stop iterations (3.4) and (3.5) (see [BGH+14]), is the Morozov's discrepancy principle [Mor66]. The discrepancy principle suggests to choose the smallest $k \in \mathbb{N}$ such that $u^{k+1}$ satisfies

$$\|f - \mathcal{A}u^{k+1}\|_2 \leq \sigma\sqrt{m} \tag{3.6}$$

where $m$ is the number of samples and $\sigma$ is the standard deviation of the noise in the data. Note that using Bregman iterations, the contrast is improved and in some cases even recovered exactly, compared to the variational regularisation model. In addition, it makes the regularisation parameter choice less challenging. Note that for different choices of $J$ in (4.18), e.g., the Mumford-Shah/Potts model [MS89, AT90, Cha95, BKL+09, PCCB09], we do not have loss of contrast, but we deal with a non-convex NP hard problem, algorithmically more challenging.

### 3.1.2 Segmentation

Image segmentation refers to the process of automatically dividing the image into meaningful regions. Mathematically, one is interested in finding a partition $\{\Omega_i\}_{i=1}^{\ell}$ of the image domain $\Omega$ subject to $\cup_{i=1}^{\ell}\Omega_i = \Omega$ and $\cap_{i=1}^{\ell}\Omega_i = \emptyset$. One way to do this is to use *region-based* segmentation models, which identify regions based on similarities of their pixels. The segmentation model we are considering was originally proposed by Chan and Vese in [CV01] and it is a particular case of the piecewise-constant Mumford-Shah model [MS89]. Given an image function $u : \Omega \to \mathbb{R}$, the goal is to divide the image domain $\Omega$ in two separated regions $\Omega_1$ and $\Omega_2 = \Omega \setminus \Omega_1$ by minimising the following energy function

$$\int_{\Omega_1} (u(x) - c_1)^2\, dx + \int_{\Omega_2} (u(x) - c_2)^2\, dx + \beta \cdot Length(C) \to \min_{c_1, c_2, C}$$

where $C$ is the desired contour separating $\Omega_1$ and $\Omega_2$, and the constants $c_1$ and $c_2$ represents the average intensity value of $u$ inside $C$ and outside $C$, respectively. The parameter $\beta$ penalises the length of the contour $C$, controlling the scale of the objects in the segmentation. From this formulation we can make two observations: first, the

regions $\Omega_1$ and $\Omega \setminus \Omega_1$ can be represented by the characteristic function

$$v(x) = \begin{cases} 0, & \text{if } x \in \Omega_1 \cup C \\ 1, & \text{if } x \in \Omega_2, \end{cases}$$

second, the perimeter of the contour identified by the the characteristic function corresponds to its total variation, as shown by the Coarea formula [AFP00b]. This leads to the new formulation

$$\int_\Omega v(x)(u(x) - c_1)^2 dx + (1 - v(x))(u(x) - c_2)^2 \, dx + \beta \, \mathrm{TV}(v) \to \min_{c_1, c_2, v \in \{0,1\}}.$$

Even assuming fixed constants $c_1$, $c_2$ the problem is non-convex due to the binary constraint. In [CEN06] the authors proposed to relax the constraint, allowing $v(x)$ to assume values in the interval $[0, 1]$. They showed that for fixed constants $c_1$, $c_2$, global minimisers can be obtained by minimising the following energy

$$\int_\Omega v(x)(u(x) - c_1)^2 dx + (1 - v(x))(u(x) - c_2)^2 \, dx + \beta \, \mathrm{TV}(v) \to \min_{v \in [0,1]} \tag{3.7}$$

followed by thresholding, setting $\Sigma = \{x : v(x) \geq \mu\}$ for a.e. $\mu \in [0, 1]$. As the problem is convex but not strictly convex, the global minimiser may not be unique. In practice we obtain solutions which are almost binary, hence the choice of $\mu$ is not crucial.
Setting

$$s(x) = (u(x) - c_1)^2 - (u(x) - c_2)^2$$

the energy (3.7) can be written in a more general form as

$$\int_\Omega v(x) s(x) \, dx + \beta \, \mathrm{TV}(v) \to \min_{v \in [0,1]}.$$

In this work, we are interested in the extension of the two-class problem to the multi-class formulation [LLWS13]. Following the simplex-constrained vector function representation for multiple regions and its convex relaxation proposed in [LKY+09], we obtain as a special case a convex relaxation of the Chan-Vese model for arbitrary number of regions, which reads

$$\int_\Omega \sum_{i=1}^{\ell} v_i(x)(c_i - u(x))^2 \, dx + \beta \, \mathrm{TV}(v) \to \min_{v \in \mathscr{C}}, \tag{3.8}$$

where $\mathscr{C} := \{v : \Omega \to \mathbb{R}^\ell \,|\, v(x) \geq 0, \sum_{i=1}^{\ell} v_i(x) = 1\}$ is a convex set which restricts $v(x)$ to lie in the standard probability simplex. As in the binary case, the constants $c_i$ describe

the average intensity value inside region $i$. In this case we consider the vector-valued formulation of TV

$$\mathrm{TV}(v) = \int_\Omega \sqrt{\|\nabla v_1\|^2 + \cdots + \|\nabla v_\ell\|^2}\, dx.$$

### 3.1.3 Joint Reconstruction and Segmentation

MRI reconstructions from highly undersampled data are subject to errors, even when prior knowledge about the underlying object is incorporated in the mathematical model. It is often required to find a trade-off between filtering out the noise and retrieving the intrinsic structures while preserving the intensity configuration and small details. As a consequence, segmentations in the presence of artefacts are likely to fail.

In this chapter, we propose to solve the two image processing tasks of reconstruction and segmentation in a unified framework. The underlying idea is to inform the reconstruction with prior knowledge of the regions of interest, and simultaneously update this belief according to the actual measurements. Mathematically, given the under-sampled and noisy $k$-space data $f$, we want to recover the image $u\colon \Omega \to \mathbb{R}$ and compute its segmentation $v$ in $\ell$ disjoint regions, by solving the following problem

$$\begin{aligned}(u, v) = \arg\min_{u,v} \underbrace{\frac{1}{2}\|\mathcal{A}u - f\|_2^2 + \alpha\,\mathrm{TV}(u)}_{\text{reconstruction}} \\ \underbrace{+\,\delta \sum_{i=1}^{n}\sum_{j=1}^{\ell} v_{ij}(c_j - u_i)^2 + \beta\,\mathrm{TV}(v) + \iota_{\mathscr{C}}(v)}_{\text{segmentation}}\,.\end{aligned} \tag{3.9}$$

where $\iota_{\mathscr{C}}(v)$ is the characteristic function over $\mathscr{C} := \{v : \mathbb{R}^n \to \mathbb{R}^\ell \,|\, v_{ij} \geq 0, \sum_{j=1}^{\ell} v_{ij} = 1, \forall i \in \{1, \ldots, n\}\}$, and $\alpha$, $\beta$, $\delta > 0$ are some regularisation parameters. However, instead of solving (3.9), we consider the iterative regularisation procedure using Bregman distances. The main motivation is to exploit the contrast enhancement aspect for the reconstruction thanks to the Bregman iterative scheme. By improving the reconstruction, the segmentation is in turn refined. Therefore, we replace (3.9) with the following

sequence of minimisation problems for $k = 0, 1, 2, \ldots$

$$u^{k+1} = \arg\min_u \frac{1}{2}\|\mathcal{A}u - f\|_2^2 + \alpha D_{\mathrm{TV}}^{p^k}(u, u^k) + \delta \sum_{i=1}^{n}\sum_{j=1}^{\ell} v_{ij}(c_j - u_i)^2 \tag{3.10a}$$

$$p^{k+1} = p^k - \frac{1}{\alpha}\left(\mathcal{A}^*(\mathcal{A}u^{k+1} - f) - 2\delta \sum_{j=1}^{\ell} v_j^k (u^{k+1} - c_j)\right) \tag{3.10b}$$

$$v^{k+1} \in \arg\min_v \delta \sum_{i=1}^{n}\sum_{j=1}^{\ell} v_{ij}(c_j - u_i^{k+1})^2 + \imath_{\mathscr{C}}(v) + \beta D_{\mathrm{TV}}^{q^k}(v, v^k) \tag{3.10c}$$

$$q^{k+1} = q^k - \frac{\delta}{\beta}(c_j - u^{k+1})^2. \tag{3.10d}$$

Note that (3.10) solves a problem different from (3.9). Assuming that a minimiser exists, the model (3.10) converges to a minimiser of

$$\frac{1}{2}\|\mathcal{A}u - f\|_2^2 + \delta \sum_{i=1}^{n}\sum_{j=1}^{\ell} v_{ij}(c_j - u_i^{k+1})^2\,,$$

as we will show in Subsection 3.2.1. In case of noisy data $f$ this is not desirable, so that we combine the iteration with a stopping criterion in order to form a regularisation method.

This model combines the reconstruction approach described in (3.4) and the discretised multi-class segmentation in (3.8) with a variation in the regularisation term, which is now embedded in the Bregman iteration scheme. In [ZvDT+17] the authors used Bregman distances for the Chan-Vese formulation (3.7), combined with spectral analysis, to produce multiscale segmentations.

As described in the previous subsection, the parameters $\alpha$ and $\beta$ describe the scale of the details in $u$ and the scale of the segmented objects in $v$. By integrating the two regularisations into the same Bregman iteration framework, we obtain that these scales are now determined by the iteration $k+1$. At the first Bregman iteration $k = 0$, when $\alpha$ is very large, we obtain an over-smoothed $u^1$, and the value of $\beta$ is not very important. Intuitively, $u^1$ is almost piecewise constant with small total variation and a broad range of values of $\beta$ may lead to very similar segmentations $v^1$. However, at every iteration $k+1$, finer scales are added to the solution with the update $p^{k+1}$. Accordingly, with the update $q^{k+1}$, which is independent of $v^{k+1}$, the segmentation keeps up with the scale in the reconstructed image $u^{k+1}$.

The novelty of this approach is also represented by the role of the parameter $\delta > 0$. This parameter weighs the effect of the segmentation in the reconstruction, imposing

regularity in $u$ in terms of sharp edges in the regions of interest. In Section 3.3 we show how different ranges of $\delta$ affects the reconstruction (see Figure 3.12). Intuitively, large values of $\delta$ force the solution $u$ to be close to the piecewise constant solution described by the constants $c_i$. This is beneficial in applications where MRI is a means to extract shapes and sizes of underlying objects, (e.g. bubbly flow in Subsection 3.3.1). On the other hand, with very small $\delta$, the segmentation has little impact and the solutions for $u$ are close to the ones obtained by solving the individual problem (3.4). Instead, intermediate values of $\delta$ impose sharper boundaries in the reconstruction while preserving the texture.

Obviously, we need to stop the iteration before the residual brings back noise from the data $f$. As we cannot use Morozov discrepancy principle in this case (due to the fact that $\|\mathcal{A}u^k - f\|_2$ will rather increase due to the effect of the coupling term controlled by the parameter $\delta$), we stop when the difference between two consecutive iterates in $v$ is smaller than a certain tolerance, $\|v^{k+1} - v^k\| < tol$, following the observation that the rate at which $u^{k+1}$ changes close to the optimal solution is low, in contrary to more abrupt changes at the beginning of the Bregman iteration and later on when it starts to add noise.

Clearly, problem (3.10) is non-convex in the joint argument $(u, v)$ due to the coupling term. However, it is convex in each individual variable. We propose to solve the joint problem by iteratively alternating the minimisation with respect to $u$ and to $v$ (see Section 3.2 for numerical optimisation and convergence analysis).

### 3.1.4 Comparison to other Joint Reconstruction and Segmentation Approaches

In this section we will provide an overview of some existing simultaneous reconstruction and segmentation (SRS) approaches with respect to different imaging applications.

**CT/SPECT.** Ramlau and Ring [RR07] first proposed a simultaneous reconstruction and segmentation model for CT, that was later extended to SPECT in [EKR11] and to limited data tomography [Kla11]. In these works, the authors aim to simultaneously reconstruct and segment the data acquired from SPECT and CT. CT measures the mass density distribution $\mu$, that represents the attenuation of x-rays through the material; SPECT measures the activity distribution $f$ as the concentration of the radio tracer injected in the material. Given the two measurements $z^\delta$ and $y^\delta$, from CT and SPECT,

they consider the following energy functional

$$E(f,\mu,\Gamma^f,\Gamma^\mu) = \|\mathcal{A}(f,\mu) - y^\delta\|^2 + \beta\|\mathcal{R}\mu - z^\delta\|^2 + \alpha(Length(\Gamma^f) + Length(\Gamma^\mu)).$$

They propose a joint model based on a Mumford-Shah like functional, in which the reconstructions of $\mu$ and $f$ and the given data are embedded in the data term in a least squares sense. The operators $\mathcal{A}$ and $\mathcal{R}$ are the attenuated Radon transform (SPECT operator) and the Radon transform (CT operator), respectively. The penalty term is considered to be a multiple of the lengths of the contours of $\mu$, $\Gamma^\mu$ and the contours of $f$, $\Gamma^f$. These boundaries are modelled using level set functions. In these segmented partitions of the domain, $\mu$ and $f$ are assumed to be piecewise constant. The optimisation problem is then solved alternatively with respect to the functional variables $f$ and $\mu$ with fixed geometric variables $\Gamma^\mu$ and $\Gamma^f$ and the other way around.

In [BRZ16] the simultaneous reconstruction and segmentation is applied to dynamic SPECT imaging, which solves a variational framework consisting of a Kullback-Leibler (KL) data fidelity and different regulariser terms to enforce sharp edges and sparsity for the segmentation and smoothness for the reconstruction. The cost function is

$$E(u,c) = KL\Big(\mathcal{R}(u\cdot c), g\Big) + \alpha\sum_{k=1}^{K}\|\nabla u_k\| + \beta\sum_{k=1}^{K}\|u_k\|_1 + \frac{\delta}{2}\sum_{k=1}^{K}\|\frac{\partial}{\partial t}c_k\|_2^2.$$

Given the data $g$, they want to retreive the concentration curves $c_k(t)$ in time for K disjoint regions and their indication functions $u_k(x)$ in space. The optimisation is carried out alternating the minimisation over $u$ having $c$ fixed and then over $c$ having $u$ fixed.

In [LQP17] they propose a variational approach for reconstruction and segmentation of CT images, with limited field of view and occluded geometry. The cost function

$$E(u,c,v) = \frac{1}{2}\|\mathcal{A}x - y\|^2 + \alpha\|\nabla u\| + \frac{\beta}{2}\left(\lambda\sum_{i=1}^{n}\sum_{k=1}^{K}v_{ik}(u_i - c_k)^2 + \frac{1}{2}\|Dv\|_2^2\right)$$

s.t. a box constraint on the image values $x$ and the simplex constraint on the labelling function $v$. The operator $A$ is the undersampled Radon transform modelling the occluded geometry and $y$ is the given data. The second term is the edge-preserving regularisation term for $u$, the third term is the segmentation term which aims at finding regions in $u$ that are close to the value $c_k$ in region $k$. The operator $D$ is the finite difference approximation

of the gradient. The non-convex problem is solved by alternating minimisation between updates of $u, v, c$.

**PET and Transmission Tomography.** In [VdSB08], the authors propose a maximum likelihood reconstruction and doubly stochastic segmentation for emission and transmission tomography. In their model they use a Hidden Markov Measure Field Model (HMMFM) to estimate the different classes of objects from the given data $r$. They want to maximise the following cost function

$$E(u, p, \theta) = \log P(r|u) + \log P(u|p, \theta) + \log P(p).$$

The first term is the data likelihood which will be modelled differently for emission and transmission tomography. The second term is the conditional probability or class fitting term, for which they use HMMFM. The third term is the regularisation on the HMMFM. The optimisation is carried out in three steps, where first they solve for $u$ (image update) fixing $p, \theta$, then for $p$, holding $u, \theta$ (measure field update) and finally for $\theta$ (parameter update) having $u, p$ fixed.

A variant of this method has been presented in [RDDH15], in which they incorporate prior information about the segmentation classes through a HMMFM. Here, the reconstruction is the minimisation over a constrained Bayesian formulation that involves a *data fidelity term* as a classical least squares fitting term, a *class fitting term* as a Gaussian mixture for each pixel given $K$ classes and dependent of the class probabilities defined by the HMMFM, and a *regulariser* also dependent of the class probabilities. The model to minimise is

$$\begin{aligned} E(u, \delta) =& \lambda_{noise} \|\mathcal{A}u - b\|_2^2 - \sum_{j=1}^{N} \log \left( \sum_{k=1}^{K} \frac{\delta_{jk}}{\sqrt{2\pi}\sigma_k} \exp\left( -\frac{(u_j - \mu_k)^2}{2\sigma_k^2} \right) \right) + \lambda_{class} \sum_{k=1}^{K} R(\delta_k) \\ \text{s.t.} \quad & \sum_{k=1}^{K} \delta_{jk} = 1, \quad \delta_{jk} \geq 0, \quad j = 1, \ldots, N, \quad k = 1, \ldots, K. \end{aligned}$$

The operator $\mathcal{A}$ will be modelled as the Radon transform in case of CT and $b$ represents the measured data; $N$ is the number of pixels in the image; $\lambda_{noise}$ and $\lambda_{class}$ are the regularisation parameters; $\mu_k, \sigma_k$ are the class parameters. The cost function is non convex and they solve the problem in an alternating scheme where they either update the pixel values or the class probabilities for each pixel.

Storath and others [SWFU15] model the joint reconstruction and segmentation using the Potts Model with applications to PET imaging and CT. They consider the variational formulation of the Potts model for the reconstruction. Since the solution is piecewise constant, this directly induces a partition of the image domain, thus a segmentation. Given the data $f$ and an operator $\mathcal{A}$ (e.g. Radon transform), the energy functional is in the following form

$$E(u) = \lambda \|\nabla u\|_0 + \|\mathcal{A}u - f\|_2^2$$

where the first term is the jump penalty enforcing piecewise constant solutions and the second term is the data fidelity. As the Potts model is NP hard, they propose a discretisation scheme that allows to split the Potts problem into subproblems that can be solved efficiently and exactly.

**MRI.** In [CBP+14], the authors proposed a joint model with applications to MRI. Their reconstruction-segmentation model consists of a fitting term and a patch-based dictionary to sparsely represent the image, and a term that models the segmentation as a mixture of Gaussian distributions with mean, standard deviation and mixture weights $\mu$, $\sigma$, $\pi$. Their model is

$$E(u, \Gamma, \mu, \sigma, \pi) = \|\mathcal{A}u - y\|^2 + \lambda \sum_{n=1}^{N} \|R_n u - D\gamma_n\|^2 - \beta \, \mathrm{P}(u|\mu, \sigma, \pi) \quad \text{s.t. } \|\gamma_n\|_0 \leq T \;\; \forall n \,,$$

where $\mathcal{A}$ is the undersampled Fourier transform, $y$ is the given data, $R_n$ is a patch extraction operator, $\lambda$ is a weighting parameter, $T$ is the sparsity threshold, and $\gamma_n$ is the sparse representation of patch $R_n u$ organised as column $n$ of the matrix $\Gamma$. The problem is highly non-convex and it is solved iteratively using conjugate gradient on $u$, orthogonal matching pursuit on $\Gamma$ and Expectation-Maximisation algorithm on $(\mu, \sigma, \pi)$.

**Summary.** Recently, the idea to solve the problems of reconstruction and segmentation simultaneously has become more popular. The majority of these joint methods have been proposed for CT, SPECT and PET data. Mainly they differ in the way they encode prior information in terms of regularisers and how they link the reconstruction and segmentation in the coupling term. Some impose smoothness in the reconstruction [BRZ16], others sparsity in the gradient [RR07, LQP17, SWFU15], others consider a patch-dictionary sparsifying approach [CBP+14]. In [SWFU15] they do not explicitly obtain a segmentation, but they force the reconstruction to be piecewise constant. Depending on the application, the coupling term is the data fitting term itself (e.g.

SPECT), or the segmentation term. In [VdSB08, RDDH15, CBP+14] the authors model the segmentation as a mixture of Gaussian distribution, while [LQP17] has a a region-based segmentation approach similar to what we propose. However, [LQP17] penalises the squared 2-norm of segmentation, imposing spatial smoothness.

In our proposed joint approach, we perform reconstruction and segmentation in a unified Bregman iteration scheme, exploiting the advantage of improving the reconstruction, which results in a more accurate segmentation. Furthermore, the segmentation constitutes another prior imposing regularity in the reconstruction in terms of sharp edges in the regions of interest. We propose a novel numerical optimisation problem in a non-convex Bregman iteration framework for which we present a rigorous convergence result in the following section.

## 3.2 Optimisation

The cost function (3.10) is non-convex in the joint argument $(u, v)$, but it is convex in each individual variable. To solve this problem we derive a splitting approach where we solve the two minimisation problems in an alternating fashion with respect to $u$ and $v$. We present the general algorithm and its convergence analysis in the next subsection. First, we describe the solution of each subproblem.

**Problem in $u$.** The problem in $u$ reads

$$u^{k+1} = \arg\min_u \frac{1}{2}\|\mathcal{A}u - f\|_2^2 + \alpha(\mathrm{TV}(u) - \langle p^k, u\rangle) + \delta \sum_{i=1}^{n}\sum_{j=1}^{\ell} v_{ij}^k (c_j - u_i)^2.$$

We solve the optimisation for $u$, fixing $v$, using the primal-dual algorithm proposed in [CP11a, CP16, EZC10, PCBC09]. We write $F(u) = \|u\|_1$, $\mathcal{K}(u) = \nabla u$ and $G(u) = \frac{1}{2}\|\mathcal{A}u - f\|_2^2 - \alpha\langle p^k, u\rangle + \delta \sum_{i=1}^{n}\sum_{j=1}^{\ell} v_{ij}^k (c_j - u_i)^2$ and obtain the following iterates for $\theta = 1$ and step sizes $\sigma = \tau = 0.99/\|\nabla\|$

$$\begin{aligned} y^{n+1} &= \frac{y^n + \sigma\nabla\bar{u}^n}{\max(1, \|y^n + \sigma\nabla\bar{u}^n\|)} \\ u^{n+1} &= \frac{u^n + \tau\nabla\cdot y^{n+1} + 2\tau\delta\sum_{j=1}^{\ell} v_j^k c_j + \tau\alpha p^k + \tau\mathcal{A}^* f}{1 + 2\tau\delta + \tau\mathcal{A}^*\mathcal{A}} \\ \bar{u}^{n+1} &= 2u^{n+1} - u^n. \end{aligned}$$

After sufficiently many iterations we set $u^{k+1} = u^{n+1}$ and compute the update $p^{k+1}$ from the optimality condition of (3.2) as (3.10b).

**Problem in $v$.** The problem in $v$ reads

$$v^{k+1} = \arg\min_{v \in C} \langle v, \delta g - \beta q^k \rangle + \beta \, \mathrm{TV}(v)$$

with $g = \Big((c_1 - u^{k+1})^2, \dots, (c_\ell - u^{k+1})^2\Big)^T$. We now solve a variant of the primal-dual method [CP11a] as suggested in [PCBC09, CCP12b]. They consider the general problem including pointwise linear terms of the form

$$\min_{x \in C} \max_{y \in B} \langle \mathcal{K}x, y \rangle + \langle g, x \rangle - \langle h, y \rangle$$

where $C \subseteq X$, $B \subseteq Y$ are closed, convex sets.
Setting $\mathcal{K} = \nabla$ and $h = 0$, $\theta = 1$ and step sizes $\sigma = \tau = 0.99/\|\nabla\|$, the updates are

$$\begin{aligned} w^{n+1} &= \Pi_B\Big(w^n + \sigma(\nabla \bar{v}^n - h)\Big) \\ v^{n+1} &= \Pi_C\Big(v^n + \tau \nabla \cdot (v^{n+1} - \delta g + \beta q^k)\Big) \\ \bar{v}^{n+1} &= 2v^{n+1} - v^n. \end{aligned}$$

At the end, we set $v^{k+1} = v^{n+1}$ and obtain the update $q^{k+1}$ as (3.10d).

### 3.2.1 Convergence Analysis

The proposed joint approach (3.10) is an optimisation problem of the form

$$\min_{u,v} E(u, v) + D_{J_1}^{p^k}(u, u^k) + D_{J_2}^{q^k}(v, v^k) \tag{3.11}$$

in the general Bregman distance framework for (nonconvex) functions $E : \mathbb{R}^n \times \mathbb{R}^m \to \mathbb{R} \cup \{\infty\}$, for $k \in \{0, \dots, N\}$ and some positive parameters $\alpha$ and $\beta$. The functions $J_1 : \mathbb{R}^n \to \mathbb{R} \cup \{\infty\}$ and $J_2 : \mathbb{R}^m \to \mathbb{R} \cup \{\infty\}$ impose some regularity in the solution. In this work we consider a finite dimensional setting and we refer to the next section for the required definitons. To prove global convergence of (3.11), we consider functions that satisfy the Kurdika-Łojasiewicz property, defined below, and we make the following assumptions.

**Definition 3.1** (Kurdyka-Łojasiewicz (KL) property)**.** *Let $F : \mathbb{R}^d \to \mathbb{R}$ be a proper and lower semicontinuous function.*

- *Then the function $F$ is said to have the KL property at $\bar{u} \in dom(\partial F) := \{u \in \mathbb{R}^d | \partial F \neq \emptyset\}$ if there exists a constant $\eta \in (0, \infty]$, a neighbourhood $N$ of $\bar{u}$ and a*

*concave function* $\varphi : [0, \eta) \to \mathbb{R}_{>0}$ *that is continuous at* 0 *and satisfies* $\varphi(0) = 0$, $\varphi \in C^1(]0, \eta[)$, *and* $\varphi'(s) > 0$ *for all* $s \in ]0, \eta[$, *such that for all* $u \in N \cap \{u \in \mathbb{R}^d | F(\bar{u}) < F(u) < F(\bar{u}) + \eta\}$ *the inequality*

$$\varphi'(F(u) - F(\bar{u}))\, dist(0, \partial F(u)) \geq 1 \tag{KL}$$

*holds.*

- *If* $F$ *satisfies the KL property at each point of* $dom(\partial F)$, $F$ *is called a KL function.*

**Lemma 3.2.** *The function* $E(u, v) = \frac{1}{2}\|\mathcal{A}u - f\|_2^2 + \delta \sum_{i=1}^{n} \sum_{j=1}^{\ell} v_{ij}(c_j - u_i)^2$ *in our joint problem* (3.10) *satisfies the KL property over* $\mathbb{R}^n \times \mathbb{R}^m$.

*Proof.* It has been proved in [Loj63] that real-analytic functions satisfy the KL property. The function $E(u, v)$ is polynomial and therefore it is a real-analytic function. □

**Assumption 1.**

1. $E$ *is a* $C^1$ *function*
2. $E > -\infty$
3. $E$ *is a KL function*
4. $J_i : \mathbb{R}^n \to \mathbb{R}$, $i = 1, 2$, *are proper, lower semi-continuous (l.s.c.) and strongly convex*
5. $J_i$, $i = 1, 2$, *are KL function*
6. *for any fixed* $v$, *the function* $u \to E(u, v)$ *is convex. Likewise for any fixed* $u$, *the function* $v \to E(u, v)$ *is convex.*
7. *for any fixed* $v$, *the function* $u \to E(u, v)$ *is* $C^1_{L_1(v)}$, *hence the partial gradient is* $L_1(v)$*-Lipschitz continuous*

$$\|\nabla_u E(u_1, v) - \nabla_u E(u_2, v)\| \leq L_1(v)\|u_1 - u_2\| \qquad \forall u_1, u_2 \in \mathbb{R}^n.$$

*Likewise for any fixed* $u$, *the function* $v \to E(u, v)$ *is* $C^1_{L_2(u)}$.

**Algorithm 1:** Alternating splitting method with Bregman iteration

**Input:** $(u^0, v^0)$, $p^0 \in \partial J_1(u^0)$, $q^0 \in \partial J_2(v^0)$, $N \in \mathbb{N}$
**for** $k = 0, 1, \ldots, N$ **do**
  $u^{k+1} = \arg\min_u \left\{ E(u, v^k) + D_{J_1}^{p^k}(u, u^k) \right\}$
  $p^{k+1} = p^k - \nabla_u E(u^{k+1}, v^k)$
  $v^{k+1} = \arg\min_v \left\{ E(u^{k+1}, v) + D_{J_2}^{q^k}(v, v^k) \right\}$
  $q^{k+1} = q^k - \nabla_v E(u^{k+1}, v^{k+1})$
  $k = k + 1$
**end for**
**Output:** $(u^N, v^N)$

We want to study the convergence properties of the alternating scheme

$$u^{k+1} = \arg\min_u \left\{ E(u, v^k) + D_{J_1}^{p^k}(u, u^k) \right\} \tag{3.12a}$$

$$p^{k+1} = p^k - \nabla_u E(u^{k+1}, v^k) \tag{3.12b}$$

$$v^{k+1} = \arg\min_v \left\{ E(u^{k+1}, v) + D_{J_2}^{q^k}(v, v^k) \right\} \tag{3.12c}$$

$$q^{k+1} = q^k - \nabla_v E(u^{k+1}, v^{k+1}) \tag{3.12d}$$

for initial values $(u^0, v^0)$, $p^0 \in \partial J_1(u^0)$ and $q^0 \in \partial J_2(v^0)$.
We want to show that the whole sequence generated by (3.12) and depicted in Algorithm 1 converges to a critical point of $E$.

In order for the updates (3.12a) and (3.12c) to exist, we want $J$ to be of the form $J = R + \varepsilon G$ (e.g. $R = \|\nabla u\|_1$ and $G = \|u\|_2^2$, see [BBES17]) where $R$ and $G$ fulfil the following assumptions. In practice, we verify that $G$ does not significantly change the reconstruction and segmentation performance for the examples we consider in the next section, for sufficiently small parameter (e.g. $\varepsilon = 10^{-3}$). Therefore, in our model (3.10) and in the numerical results we omit it.

**Assumption 2.**

1. *The functions $G_1 : \mathbb{R}^n \to \mathbb{R}$ and $G_2 : \mathbb{R}^m \to \mathbb{R}$ are strongly convex with constants $\gamma_1$ and $\gamma_2$, respectively. They have Lipschitz continuous gradient $\nabla G_1$ and $\nabla G_2$ with Lipschitz constant $\delta_1$ and $\delta_2$, respectively.*

2. *The functions* $R_1 : \mathbb{R}^n \to \mathbb{R}$ *and* $R_2 : \mathbb{R}^m \to \mathbb{R}$ *are proper, l.s.c. and convex.*

For $J_i = \alpha_i R_i + \varepsilon_i G_i$, $i \in \{1, 2\}$, we can write (3.12) as

$$u^{k+1} = \arg\min_u \left\{ E(u, v^k) + \alpha_1 D_{R_1}^{p^k}(u, u^k) + \varepsilon_1 D_{G_1}(u, u^k) \right\} \tag{3.13a}$$

$$p^{k+1} = p^k - \frac{1}{\alpha_1}\Big( \nabla_u E(u^{k+1}, v^k) + \varepsilon_1 \big( \nabla G_1(u^{k+1}) - \nabla G_1(u^k) \big) \Big) \tag{3.13b}$$

$$v^{k+1} = \arg\min_v \left\{ E(u^{k+1}, v) + \alpha_2 D_{R_2}^{q^k}(v, v^k) + \varepsilon_2 D_{G_2}(v, v^k) \right\} \tag{3.13c}$$

$$q^{k+1} = q^k - \frac{1}{\alpha_2}\Big( \nabla_v E(u^{k+1}, v^{k+1}) + \varepsilon_2 \big( \nabla G_2(v^{k+1}) - \nabla G_2(v^k) \big) \Big). \tag{3.13d}$$

**Theorem 3.3** (Global convergence)**.** *Suppose* $E$ *is a KL function for any* $z^k = (u^k, v^k) \in \mathbb{R}^n \times \mathbb{R}^m$ *and* $r^k = (p^k, q^k)$ *with* $p^k \in \partial R_1(u^k)$, $q^k \in \partial R_2(v^k)$. *Assume Assumptions 1 and 2 hold. Let* $\{z^k\}_{k\in\mathbb{N}}$ *and* $\{r^k\}_{k\in\mathbb{N}}$ *be sequences generated by (3.13), which are assumed to be bounded. Then*

1. *The sequence* $\{z^k\}_{k\in\mathbb{N}}$ *has finite length, that is*

$$\sum_{k=0}^{\infty} \|z^{k+1} - z^k\| < \infty. \tag{3.14}$$

2. *The sequence* $\{z^k\}_{k\in\mathbb{N}}$ *converges to a critical point* $\bar{z}$ *of* $E$

### 3.2.2 Proof of Theorem 3.3

In the following we are going to show global convergence of this algorithm. The first step in our convergence analysis is to show a sufficient decrease property of a surrogate of the energy function (3.11) and a subgradient bound of the norm of the iterates gap. We first recall the following definitions.

**Definition 3.4** (Convex Conjugate)**.** *Let* $G$ *be a proper, l.s.c. and convex function. Then its convex conjugate* $G^* : \mathbb{R}^n \to \mathbb{R} \cup \{\infty\}$ *is defined as*

$$G^*(p) := \sup_{u\in\mathbb{R}^n} \{\langle u, p\rangle - G(u)\},$$

*for all* $p \in \mathbb{R}^n$.

**Lemma 3.5.** *Let* $G$ *be a proper, l.s.c. and convex function and* $G^*$ *its convex conjugate. Then for all arguments* $u \in \mathbb{R}^n$ *with corresponding subgradients* $p \in \partial G(u)$ *we know*

- $\langle u, p\rangle = G(u) + G^*(p)$,
- $p \in \partial G(u)$ *is equivalent to* $u \in \partial G^*(p)$.

From Lemma 3.5 we can rewrite the Bregman distance in (3.3) as follows

$$D_J^{p^k}(u, u^k) = J(u) + J^*(p^k) - \langle u, p^k\rangle, \tag{3.15}$$

where we can see that now it does not depend on $u^k$ anymore, but it can be defined as a function of $u$ and $p^k$ only, $D_J(u, p^k)$.

**Definition 3.6** (Strong convexity)**.** *Let $G$ be a proper, l.s.c. and convex function. Then $G$ is said to be $\gamma$-strongly convex if there exists a constant $\gamma$ such that*

$$D_G^p(u, v) \geq \frac{\gamma}{2}\|u - v\|^2$$

*holds true for all $u, v \in \mathrm{dom}(G)$ and $q \in \partial G(v)$.*

**Definition 3.7** (Symmetric Bregman distance)**.** *Let $G$ be a proper, l.s.c. and convex function. Then the symmetric generalised Bregman distance $D_G^{symm}(u, v)$ is defined as*

$$D_G^{symm}(u, v) := D_G^p(u, v) + D_G^q(v, u) = \langle p - q, u - v\rangle$$

*for $u, v \in \mathrm{dom}(G)$ with $p \in \partial G(u)$ and $q \in \partial G(v)$. We also observe that in case $G$ is $\gamma$-strongly convex we have*

$$D_G^{symm}(u, v) \geq \gamma\|u - v\|^2.$$

**Definition 3.8** (Lipschitz continuity)**.** *A function $G : \mathbb{R}^n \to \mathbb{R}$ is (globally) Lipschitz-continuous if there exists a constant $L > 0$ such that*

$$\|G(u) - G(v)\| \leq L\|u - v\|$$

*is satisfied for all $u, v \in \mathbb{R}^n$.*

Before we show global convergence, we first define the surrogate functions.

**Definition 3.9** (Surrogate objective)**.** *Let $E, R_i, G_i, i \in \{1, 2\}$ satisfy Assumption 1 and Assumption 2, respectively. For any $(u^k, v^k) \in \mathbb{R}^n \times \mathbb{R}^m$ and subgradients $p^k \in \partial R_1(u^k)$*

*and $q^k \in \partial R_2(v^k)$, we define the following surrogate objectives $F$, $F_1$ and $F_2$*

$$\begin{aligned} F(u^{k+1}, v^{k+1}, p^k, q^k) = E(u^{k+1}, v^{k+1}) &+ \alpha_1 \underbrace{\Big(R_1(u^{k+1}) + R_1^*(p^k) - \langle u^{k+1}, p^k\rangle\Big)}_{= D_{R_1}^{p^k}(u^{k+1}, u^k)} \\ &+ \alpha_2 \underbrace{\Big(R_2(v^{k+1}) + R_2^*(q^k) - \langle v^{k+1}, q^k\rangle\Big)}_{= D_{R_2}^{q^k}(v^{k+1}, v^k)}, \end{aligned} \tag{3.16}$$

$$F_1(u^{k+1}, p^k) = E(u^{k+1}, v^{k+1}) + \alpha_1\Big(R_1(u^{k+1}) + R_1^*(p^k) - \langle u^{k+1}, p^k\rangle\Big), \tag{3.17}$$

$$F_2(v^{k+1}, q^k) = E(u^{k+1}, v^{k+1}) + \alpha_2\Big(R_2(v^{k+1}) + R_2^*(q^k) - \langle v^{k+1}, q^k\rangle\Big). \tag{3.18}$$

*For convenience we will use the following notations*

$$\begin{aligned} z^k &:= (u^k, v^k) \qquad \forall k \geq 0 \\ r^k &:= (p^k, q^k) \qquad p^k \in \partial R_1(u^k),\ q^k \in \partial R_2(v^k). \end{aligned}$$

*The surrogate function $F$ will then read*

$$F(z^{k+1}, r^k) = F(u^{k+1}, v^{k+1}, p^k, q^k).$$

We can now show the sufficient decrease property of (3.16) for subsequent iterates.

**Lemma 3.10** (Sufficient decrease property)**.** *The iterates generated by (3.13) satisfy the descent estimate*

$$F(z^{k+1}, r^k) + \rho_2 \|z^{k+1} - z^k\|^2 \leq F(z^k, r^{k-1}) \tag{3.19}$$

*In addition we observe*

$$\begin{aligned} \lim_{k\to\infty} D_{R_1}^{symm}(u^{k+1}, u^k) &= 0 \qquad \lim_{k\to\infty} D_{R_2}^{symm}(v^{k+1}, v^k) = 0 \\ \lim_{k\to\infty} D_{G_1}^{symm}(u^{k+1}, u^k) &= 0 \qquad \lim_{k\to\infty} D_{G_2}^{symm}(v^{k+1}, v^k) = 0. \end{aligned}$$

*Proof.* From (3.11) we consider the following step for $J_1 = \alpha_1 R_1 + \varepsilon_1 G_1$

$$\begin{aligned} u^{k+1} &= \arg\min_u \Big\{E(u, v^k) + \alpha_1 D_{R_1}^{p^k}(u, u^k) + \varepsilon_1 D_{G_1}(u, u^k)\Big\} \\ &= \arg\min_u \Big\{E(u, v^k) + \alpha_1 R(u) + \varepsilon_1 G(u) - \langle \alpha_1 p^k + \varepsilon_1 \nabla G(u^k), u - u^k\rangle\Big\}. \end{aligned}$$

Computing the optimality condition we obtain

$$\alpha_1(p^{k+1} - p^k) + \nabla_u E(u^{k+1}, v^k) + \varepsilon_1(\nabla G(u^{k+1}) - \nabla G(u^k)) = 0$$

Taking the dual product with $u^{k+1} - u^k$ yields

$$\alpha_1 \underbrace{\langle p^{k+1} - p^k, u^{k+1} - u^k \rangle}_{= D_{R_1}^{symm}(u^{k+1}, u^k)} + \underbrace{\langle \nabla_u E(u^{k+1}, v^k), u^{k+1} - u^k \rangle}_{\geq E(u^{k+1}, v^k) - E(u^k, v^k)}$$
$$+\varepsilon_1 \underbrace{\langle \nabla G_1(u^{k+1}) - \nabla G_1(u^k), u^{k+1} - u^k \rangle}_{= D_{G_1}^{symm}(u^{k+1}, u^k)} = 0.$$

Using the convexity estimate $E(u^{k+1}, v^k) - E(u^k, v^k) \leq -\langle \nabla_u E(u^{k+1}, v^k), u^{k+1} - u^k \rangle$ we obtain the inequality

$$\alpha_1 D_{R_1}^{symm}(u^{k+1}, u^k) + \varepsilon_1 D_{G_1}^{symm}(u^{k+1}, u^k) + E(u^{k+1}, v^k) - E(u^k, v^k) \leq 0$$

$$\alpha_1 \Big( D_{R_1}^{p^k}(u^{k+1}, u^k) + D_{R_1}^{p^{k+1}}(u^k, u^{k+1}) \Big) + \varepsilon_1 D_{G_1}^{symm}(u^{k+1}, u^k) + E(u^{k+1}, v^k)$$
$$\leq E(u^k, v^k).$$

Adding $\alpha_1 D_{R_1}^{p^{k-1}}(u^k, u^{k-1})$ to both sides, using the strong convexity of $G_1$ and the surrogate function notation, we get

$$F_1(u^{k+1}, p^k) + \alpha_1 \Big( D_{R_1}^{p^{k+1}}(u^k, u^{k+1}) + D_{R_1}^{p^{k-1}}(u^k, u^{k-1}) \Big) + \varepsilon_1 \gamma_1 \|u^{k+1} - u^k\|^2 \leq F_1(u^k, p^{k-1}).$$

Using the trivial estimate for the Bregman distances, we get the decrease property

$$F_1(u^{k+1}, p^k) + \varepsilon_1 \gamma_1 \|u^{k+1} - u^k\|^2 \leq F_1(u^k, p^{k-1}).$$

Similarly for $v$, we obtain

$$F_2(v^{k+1}, q^k) + \varepsilon_2 \gamma_2 \|v^{k+1} - v^k\|^2 \leq F_2(v^k, q^{k-1}).$$

Summing up these estimates, we verify the sufficient decrease property (3.19), with positive

$\rho_2 = \max\{\varepsilon_1\gamma_1, \varepsilon_2\gamma_2\}$. We also observe

$$0 \leq \Delta^k \leq E(z^k) - E(z^{k+1}).$$

with

$$\Delta^k := \alpha_1 D_{R_1}^{symm}(u^{k+1}, u^k) + \alpha_2 D_{R_2}^{symm}(v^{k+1}, v^k) + \varepsilon_1 D_{G_1}^{symm}(u^{k+1}, u^k) + \varepsilon_2 D_{G_2}^{symm}(v^{k+1}, v^k).$$

Summing over $k = 0, \ldots, N$

$$\sum_{k=0}^{N} \Delta^k \leq \sum_{k=0}^{N} E(z^k) - E(z^{k+1}) = E(z^0) - E(z^{N+1}) \leq E(z^0) - \inf_z E(z) < \infty.$$

Taking the limit $N \to \infty$ implies

$$\sum_{k=0}^{\infty} \Delta^k < \infty$$

thus $\lim_{k\to\infty} D_{R_1}^{symm}(u^{k+1}, u^k) = 0$ , $\lim_{k\to\infty} D_{G_1}^{symm} = 0$, $\lim_{k\to\infty} D_{R_2}^{symm}(v^{k+1}, v^k) = 0$, $\lim_{k\to\infty} D_{G_2}^{symm}(v^{k+1}, v^k) = 0$, due to $\alpha_1$, $\alpha_2$, $\varepsilon_1$, $\varepsilon_2 > 0$. □

In order to show that the sequences generated by (3.13) approach the set of critical point we first estimate a bound for the subgradients of the surrogate functions and verify some properties of the limit point set. We first write the subdifferential of the surrogate function as

$$w^{k+1} := \begin{pmatrix} \nabla_u E(u^{k+1}, v^{k+1}) + \alpha_1(p^{k+1} - p^k) \\ \nabla_v E(u^{k+1}, v^{k+1}) + \alpha_2(q^{k+1} - q^k) \\ u^k - u^{k+1} \\ v^k - v^{k+1} \end{pmatrix} \in \partial F(z^{k+1}, r^k) \tag{3.20}$$

with $p^k \in \partial R_1(u^k)$ and $q^k \in \partial R_2(v^k)$ being equivalent to $u^k \in \partial R_1^*(p^k)$ and $v^k \in \partial R_2^*(q^k)$, respectively.

**Lemma 3.11** (A subgradient lower bound for the iterates gap)**.** *Suppose Assumptions 1 and 2 hold. Then the iterates* (3.13) *satisfy*

$$\|w^{k+1}\| \leq \rho_1 \|z^{k+1} - z^k\| \tag{3.21}$$

$w^{k+1} \in \partial F(z^{k+1}, r^k)$ *as defined in* (3.20) *and* $\rho_1 = \max\{1 + \varepsilon_1\delta_1, 1 + \varepsilon_2\delta_2 + L_2\}$.

*Proof.* From (3.20) we know

$$\begin{aligned}\|w^{k+1}\| \leq\ & \|\nabla_u E(u^{k+1}, v^{k+1}) + \alpha_1(p^{k+1} - p^k)\| + \|\nabla_v E(u^{k+1}, v^{k+1}) + \alpha_2(q^{k+1} - q^k)\| \\ & + \|u^k - u^{k+1}\| + \|v^k - v^{k+1}\|\end{aligned}$$

From the optimality conditons of (3.13b) and (3.13d), we compute

$$\begin{aligned}\|w^{k+1}\| \leq\ & \|\nabla_u E(u^{k+1}, v^{k+1}) + \alpha_1(p^{k+1} - p^k)\| + \|\nabla_v E(u^{k+1}, v^{k+1}) + \alpha_2(q^{k+1} - q^k)\| \\ & + \|u^k - u^{k+1}\| + \|v^k - v^{k+1}\| \\ =\ & \varepsilon_1 \underbrace{\|\nabla G_1(u^{k+1}) - \nabla G_1(u^k)\|}_{\leq \delta_1\|u^{k+1} - u^k\|} + \underbrace{\|\nabla_u E(u^{k+1}, v^{k+1}) - \nabla_u E(u^{k+1}, v^k)\|}_{\leq L_2\|v^{k+1} - v^k\|} \\ & + \varepsilon_2 \underbrace{\|\nabla G_2(v^{k+1}) - \nabla G_2(v^k)\|}_{\leq \delta_2\|v^{k+1} - v^k\|} + \|u^{k+1} - u^k\| + \|v^{k+1} - v^k\| \\ \leq\ & (1 + \varepsilon_1\delta_1)\|u^{k+1} - u^k\| + (1 + \varepsilon_2\delta_2 + L_2)\|v^{k+1} - v^k\| \\ \leq\ & \rho_1\|z^{k+1} - z^k\|.\end{aligned}$$

with $\rho_1 = \max\{1 + \varepsilon_1\delta_1, 1 + \varepsilon_2\delta_2 + L_2\}$. Here we used the Lipschitz-continuity of $\nabla G_i$ and $\nabla E$. □

Following [BBES17, BST14], we verify some properties of the limit point set. Let $\{z^k\}_{k\in\mathbb{N}}$ and $\{r^k\}_{k\in\mathbb{N}}$ be sequences generated by (3.13). The set of limit points is defined as

$$\begin{aligned}\omega(z^0, r^0) := \Big\{ & (\bar{z}, \bar{r}) \in \mathbb{R}^n \times \mathbb{R}^n : \exists \text{ an increasing sequence of integers } \{k_j\}_{j\in\mathbb{N}} \\ & \text{such that } \lim_{j\to\infty} z^{k_j} = \bar{z} \text{ and } \lim_{j\to\infty} r^{k_j} = \bar{r} \Big\}.\end{aligned}$$

As in [BBES17, Definition 5.4, Proposition 5.5], we are going to assume that $R_i$, $i = 1, 2$ has locally bounded subgradients.

**Lemma 3.12.** *Suppose Assumptions 1 and 2 hold. Let $\{z^k\}_{k\in\mathbb{N}}$ be a sequence generated by (3.13) which is assumed to be bounded. Let $(\bar{z}, \bar{r}) \in \omega(z^0, r^0)$. Then the following assertion holds*

$$\lim_{k\to\infty} F(z^{k+1}, r^k) = F(\bar{z}, \bar{r}) = E(\bar{z}). \tag{3.22}$$

*Proof.* Since $(\bar{z}, \bar{r})$ is a limit point of $\{(z^k, r^k)\}_{k\in\mathbb{N}}$, $\{(z^k, r^k)\}_{k\in\mathbb{N}}$, there exist subsequences $\{z^{k_j}\}_{j\in\mathbb{N}}$ and $\{r^{k_j}\}_{j\in\mathbb{N}}$ such that $\lim_{j\to\infty} z^{k_j} = \bar{z}$ and $\lim_{j\to\infty} r^{k_j} = \bar{r}$, respectively. We

immediately obtain

$$\begin{aligned}\lim_{j\to\infty} F(z^{k_j}, r^{k_j-1}) &= \lim_{j\to\infty} \left\{E(z^{k_j}) + \alpha_1 D_{R_1}^{p^{k_j-1}}(u^{k_j}, u^{k_j-1}) + \alpha_2 D_{R_2}^{q^{k_j-1}}(v^{k_j}, v^{k_j-1})\right\} \\ &= E(\bar{z})\end{aligned}$$

due to the continuity of $E$ and $\lim_{j\to\infty} D_{R_1}^{p^{k_j-1}}(u^{k_j}, u^{k_j-1}) = 0$ and $\lim_{j\to\infty} D_{R_2}^{q^{k_j-1}}(v^{k_j}, v^{k_j-1}) = 0$. From the sufficient decrease property we conclude (3.22). □

**Lemma 3.13** (Properties of limit point set)**.** *The limit point set $w(z^0)$ is a non empty, compact and connected set, the objective function $E$ is constant on $w(z^0)$ and we have $\lim_{k\to\infty} dist(z^k, w(z^0)) = 0$.*

*Proof.* This follows steps as in [BST14, Lemma 5]. □

To finally prove global convergence of (3.13), we will use the following Kurdyka-Łojasiewicz property defined and the result from [BST14]. Before recalling the definition, we introduce the notion of distance between any subset $S \subset \mathbb{R}^d$ and any point $x \in \mathbb{R}^d$ defined as

$$\operatorname{dist}(x, S) := \begin{cases} \inf\{\|y - x\| : y \in S\} & S \neq \emptyset \\ \infty & S = \emptyset \end{cases},$$

where $\|\cdot\|$ denotes the Euclidean norm.

**Lemma 3.14** (Uniformised KL property)**.** *Let $\Omega$ be a compact set and let $E : \mathbb{R}^n \times \mathbb{R}^m \to \mathbb{R} \cup \{\infty\}$ be a proper and l.s.c. function. Assume that $E$ is constant on $\Omega$ and satisfy the KL property at each point in $\Omega$. Then there exists $\varepsilon > 0$, $\eta > 0$ and $\varphi \in C^1((0, \eta))$ that satisfies the same conditions as in Definition KL, such that for all $\bar{u} \in \Omega$ and all $u$ in*

$$\{u \in \mathbb{R}^n \mid dist(u, \Omega) < \varepsilon\} \cap \{u \in \mathbb{R}^n \mid E(\bar{z}) < E(z) < E(z) + \eta\} \tag{3.23}$$

*condition KL is satisfied.*

*Proof.* Follows from [BST14]. □

With these results we can now show global convergence of (3.13).

*Proof of Theorem 1.* By the boundedness assumption on $\{(z^k, r^k)\}_{k\in\mathbb{N}}$, there exist converging subsequences $\{z^{k_j}\}_{j\in\mathbb{N}}$ and $\{r^{k_j}\}_{j\in\mathbb{N}}$ such that $\lim_{j\to\infty} z^{k_j} = \bar{z}$ and $\lim_{j\to\infty} r^{k_j} = \bar{r}$, respectively. We know from Lemma 3.12 that (3.22) is satisfied.

1. KL property holds for $E$ and therefore for $E^k$ and we write

$$\varphi'\Big(F(z^k, r^{k-1}) - E(\bar{z})\Big)\mathrm{dist}\Big(0, \partial F(z^k, r^{k-1})\Big) \geq 1.$$

From Lemma 3.11 we obtain

$$\varphi'\Big(F(z^k, r^{k-1}) - E(\bar{z})\Big) \geq \rho_1^{-1}\|z^k - z^{k-1}\|^{-1},$$

and from the concavity of $\varphi$ we know that

$$\begin{aligned}&\varphi\Big(F(z^k, r^{k-1}) - E(\bar{z})\Big) - \varphi\Big((F(z^{k+1}, r^k) - E(\bar{z})\Big)\\ &\geq \varphi'\Big(F(z^k, r^{k-1}) - E(\bar{z})\Big)\Big(F(z^k, r^{k-1}) - F(z^{k+1}, r^k)\Big).\end{aligned}$$

Thus, we obtain

$$\frac{\varphi\Big(F(z^k, r^{k-1}) - E(\bar{z})\Big) - \varphi\Big(F(z^k, r^{k-1}) - E(\bar{z})\Big)}{F(z^k, r^{k-1}) - F(z^k, r^{k-1})} \geq \rho_1^{-1}\|z^k - z^{k-1}\|^{-1}.$$

From (3.19) with Lemma 3.10 and using the abbreviation

$$\varphi^k := \varphi(F(z^k, r^{k-1}) - E(\bar{z})),$$

it follows

$$\frac{\|z^{k+1} - z^k\|^2}{\|z^k - z^{k-1}\|} \leq \frac{\rho_1}{\rho_2}(\varphi^k - \varphi^{k+1}).$$

Multiplying by $\|z^k - z^{k-1}\|$ and using Young's inequality ($2\sqrt{ab} \leq a + b$ )

$$2\|z^{k+1} - z^k\| \leq \frac{\rho_1}{\rho_2}(\varphi^k - \varphi^{k+1}) + \|z^k - z^{k-1}\|.$$

Summing up from $k = 1, \ldots, N$ we get

$$\begin{aligned}\sum_{k=1}^{N}\|z^{k+1} - z^k\| &\leq \frac{\rho_1}{\rho_2}(\varphi^1 - \varphi^{N+1}) + \|z^1 - z^0\| + \|z^{N+1} - z^N\|\\ &\leq \frac{\rho_1}{\rho_2}\varphi^1 + \|z^1 - z^0\| < \infty.\end{aligned}$$

In addition we observe that the finite length property implies that the sequence $\{z^k\}_{k\in\mathbb{N}}$ is a Cauchy sequence and hence is a convergent sequence. For each $z^r$ and $z^s$ with $s > r > l$ we have

$$\|z^r - z^s\| = \|\sum_{k=r}^{s-1} z^{k+1} - z^k\| \leq \sum_{k=r}^{s-1} \|z^{k+1} - z^k\|.$$

2. The proof follows in a similar fashion as in [BBES17, Lemma 5.9]

□

**Remark 3.15** (Extension to $d$ blocks)**.** *The analysis described above holds for the general setting of $d$ blocks*

$$\min_{\{u_1,\dots,u_d\}} E(u_1,\dots,u_d) + \sum_{i=1}^{n} \alpha_i^k D_{J_i}^{p_i^k}(u_i, u_i^k). \tag{3.24}$$

*The update for each of the $d$ blocks then reads*

$$u_i^{k+1} = \arg\min_{u_i} \left\{ E(u_1^{k+1}, u_2^{k+1}, \dots, u_{i-1}^{k+1}, u_i^k, u_{i+1}^k, \dots, u_d^k) + \alpha_i D_{J_i}^{p_i^k}(u_i, u_i^k) \right\}$$
$$p_i^{k+1} = p_i^k - \frac{1}{\alpha_i} \Big( \nabla_{u_i} E(u_1^{k+1}, u_2^{k+1}, \dots, u_{i-1}^{k+1}, u_i^{k+1}, u_{i+1}^k, \dots, u_d^k) \Big).$$

## 3.3 Numerical Results

In this section we present numerical results for our joint reconstruction and segmentation model described in (3.10). We demonstrate its advantages and limitations, as well as a discussion on the parameter choice. In the first part, we focus on bubbly flow segmentation for simulated data. In the second part, we show results for real data acquired at the Cancer Research UK, Cambridge Institute, for tumour segmentation.

**Quality measure.** To assess the performance of the reconstruction we will compare our solutions $u$ with respect to the groundtruth $u^{gt}$. As quality measure we use the relative reconstuction error (RRE) and the peak signal to noise ratio (PSNR) defined as

- $\text{RRE}(u, u^{gt}) = \|u^{gt} - u\|_2 / \|u^{gt}\|_2$
- $\text{PSNR}(u, u^{gt}) = 10 \log_{10} \left( \frac{\max(u)}{\|u^{gt} - u\|_2 / N} \right)$

For the segmentation quality, we will use the relative segmentation error (RSE) to compare our segmentations $v$ with respect to the true segmentations $v^{gt}$

- $\text{RSE}(v, v^{gt}) = \frac{1}{N} \sum_{i=1}^{N} \delta_{v_i^{gt}, v_i}$

where $N$ is the number of pixels in the image, $\delta$ is the Kronecker delta function that will count the number of mis-classified pixels.

Before we present our two applications, we show a more detailed result of the phantom brain in Figure 3.1. In this example, we show the TV reconstruction 3.2b, where the parameter $\alpha$ has been optimised with respect to PSNR and its sequential segmentation 3.2f with optimal $\beta$ with respect to RSE. In 3.2c and 3.2g we present Bregman reconstruction and sequential segmentation where the Bregman iteration has been stopped according to the discrepancy principle Equation 3.6 and $\beta$ has been optimised with respect to RSE. These parameter choices for the sequential approaches will be used in the whole chapter. In this first result, we clearly see that the joint approach performs much better compared to the separate steps in Figures 3.2b, 3.2f and 3.2c, 3.2g. Both reconstruction and segmentation are improved and more details are recovered. We refer to B for more simulated examples.

### 3.3.1 Bubbly Flow

The first application considered is the characterisation of bubbly flows using MRI. Bubbly flows are two-phase flow systems of liquid and gas trapped in bubbles, which are common in industrial applications such as bioreactors [Cha94] and hydrocarbon processing units [DF92]. MRI has been successfully used to characterise the bubble size distribution [HBT+12, THSG12a] and the liquid velocity field of bubbly flows [HMB+10, THSG12b]; these properties govern the heat and mass transfer between the bubbles and the liquid which ultimately determine the efficiency of these industrial systems. However, when studying fast flowing systems, the acquisition time for fully sample $k$-space is too long to resolve the temporal changes; the most common method of breaking the temporal resolution barrier is through under-sampling. It is therefore critical to develop reconstruction techniques for highly under-sampled $k$-space data for the accurate reconstruction of the MRI images which would be subsequently used in calculating the bubble size distribution or in studying the hydrodynamics of the system.

We apply our joint reconstruction and segmentation approach to simulated bubbly flow imaging. In Figure 3.3 we present some results for synthetic data, where Figure 3.3a represents the groundtruth magnitude image, from which we simulate its $k$-space following the forward model described in (3.1). From the full $k$-space we collect 8% of the samples using the sampling matrix in Figure 3.3e and we corrupt the data with Gaussian noise of standard deviation $\sigma = 0.35$. In Figure 3.3b and 3.3f we show the results for the total variation regularised reconstruction and its segmentation performed

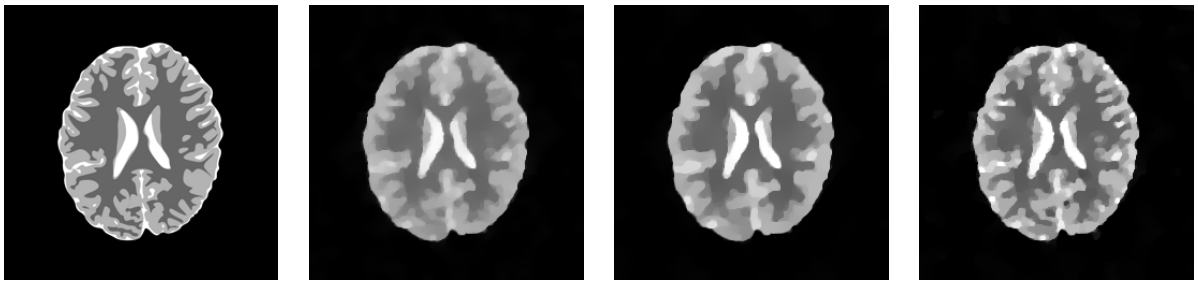

**(a)** Groundtruth

**(b)** TV reconstruction, $\alpha = 0.2$, RRE=0.046, PSNR=24.87

**(c)** Bregman reconstruction, $\alpha = 1$, RRE=0.044, PSNR=24.98

**(d)** Joint reconstruction, $\alpha = 0.8$, RRE=0.036, PSNR=26.04

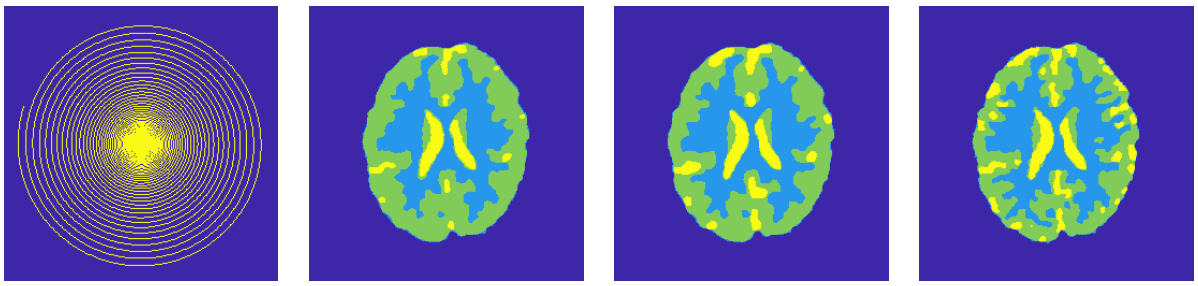

**(e)** Sampling matrix, 15%

**(f)** Segmentation, $\beta = 0.001$, RSE=0.061

**(g)** Bregman segmentation, $\beta = 0.001$, RSE=0.065

**(h)** Joint segmentation, $\beta = 0.001$, $\delta = 0.01$, RSE=0.057

**Figure 3.2:** We consider 15% of the simulated $k$-space for the brain phantom, where Gaussian noise ($\sigma = 0.25$) was added. We compare results for the total variation reconstruction and total variation based Bregman iterative reconstruction and their segmentation in a sequential approach with our joint model. We show that both reconstruction and segmentation are improved.

sequentially. In the same sequential way, we show the results for the Bregman iterative regularization in Figure 3.3c and 3.3g. In the last column in Figure 3.3d and 3.3h, we finally show the results for our joint approach. Although the TV and the Bregman approaches are already quite good, we can see that both RRE and PSNR are improved using our model in the reconstruction and the segmentation. Smaller details, such as the top right bubble contour, are better detected when solving the joint problem. As the goal of the bubbly flow application is to detect bubble size distribution, this improvement is really advantageous.

We tested the robustness of our approach by corrupting the data with different signal to noise ratio (SNR) and by considering different amount of sampling. In Figure 3.5 we show in the top row the reconstructions obtained with the joint model for different SNR (which corresponds to different standard deviation $\sigma$) and in the bottom

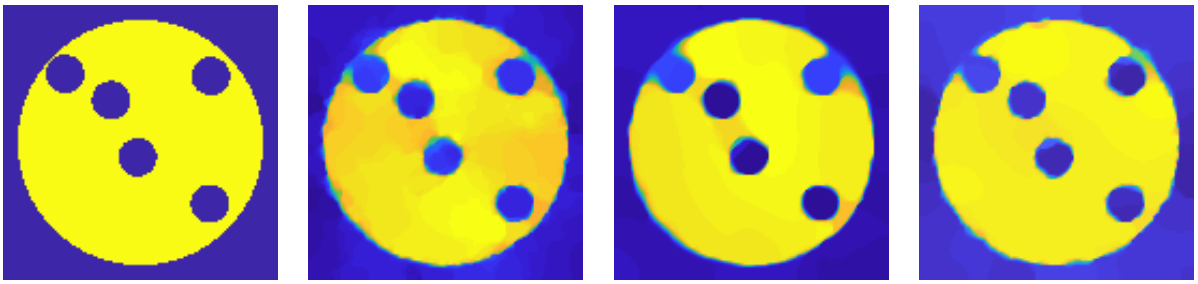

**(a)** Groundtruth

**(b)** TV reconstruction, $\alpha = 0.1$, RRE=0.081, PSNR=18.42

**(c)** Bregman reconstruction, $\alpha = 2$, RRE=0.069, PSNR=18.83

**(d)** Joint reconstruction, $\alpha = 0.8$,RRE=0.058, PSNR=20.7105

**(e)** Sampling matrix, 8%

**(f)** Segmentation, $\beta = 0.001$, RSE=0.0093

**(g)** Bregman segmentation, $\beta = 0.001$, RSE=0.017

**(h)** Joint segmentation, $\beta = 0.001$, $\delta = 1$, RSE=0.0102

**Figure 3.3:** Results of the TV reconstruction and Bregman iterative reconstruction and their segmentation in the sequential approach are compared with our joint model. Both MSE and SSIM are improved in the joint approach. The data was corrupted with Gaussian noise with $\sigma = 0.35$.

row the corresponding segmentation obtained by the joint approach. To complement this information, we show in Figure 3.6 how the PSNR, RRE and RSE are affected, for the joint approach (blue lines) and for the separate approaches, TV (red dotted lines) and Bregman TV (green dotted lines). As expected, with the SNR increasing the error decreases. We can see that the joint approach performs better than the sequential approach for any SNR. The improvement is even more significant for very noisy data. As in practice we often observe high levels of noise, the joint approach is able to takle this problem better than the traditional sequential approaches.

It is also interesting to investigate how the joint approach performs with very low undersampling rates. In Figure 3.3e we show joint reconstructions (top row) and corresponding segmentations (bottom row) for decreasing sampling rates. We can see that up to 5% results are still very good. Using 3 and 2% of the samples the results are less clean but it is possible to identify the main structures. In contrast, 1% sampling is not enough

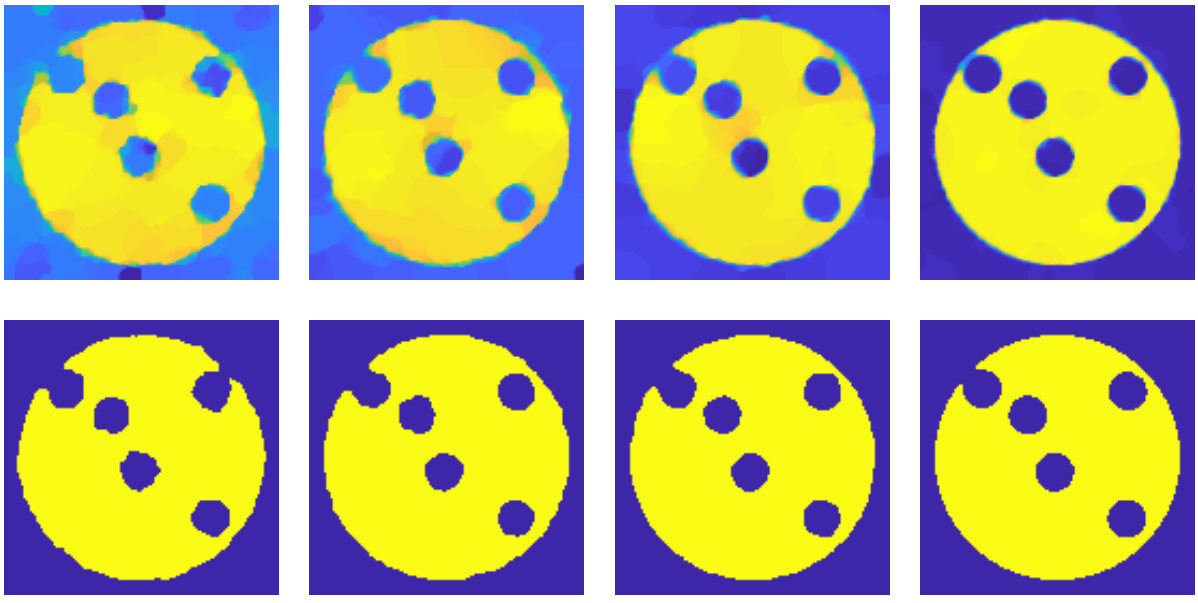

**(a)** SNR=10.56, $\sigma$=0.70 **(b)** SNR=12.69, $\sigma$=0.56 **(c)** SNR=16.68, $\sigma$=0.35 **(d)** SNR=32.83, $\sigma$=0.06

**Figure 3.4:** Top row: reconstructions obtained by the joint model with different SNR. Bottom row: corresponding segmentations.

to retrieve a good image reconstruction and consequently its segmentation. In Figure 3.7, we plot PSNR , RRE and RSE for different sampling rates. The blue lines represent the error for our joint approach, while the red and green dotted lines are for the sequential TV and sequential Bregman TV approaches. We can see that up to 5% sampling the error measures do not change significantly. However, for lower rates, the improvement is more significant. This is highly beneficial for the bubbly flow application as increasing the temporal resolution is really important to keep track of the gas flowing in the pipe.

### 3.3.2 Cancer Imaging

In this subsection, we illustrate the performance of the joint model for real cancer data. At the Cancer Research UK, Cambridge Institute, researchers acquire every day a huge amount of MRI scans to assess tumour progression and response to therapy [RSK+14]. For this reason, it is very convenient to have fast sampling through compressed sensing, and automatic segmentation methods. Furthermore, reconstructions with enhanced edges are advantageous to facilitate clinical analysis.

Here we show our results for MRI data of a rat bearing a glioblastoma. The MR image represents the rat head where the brain is the gray area in the top half of the image. Inside this gray region, a tumour is clearly visible appearing as a brighter area. For this

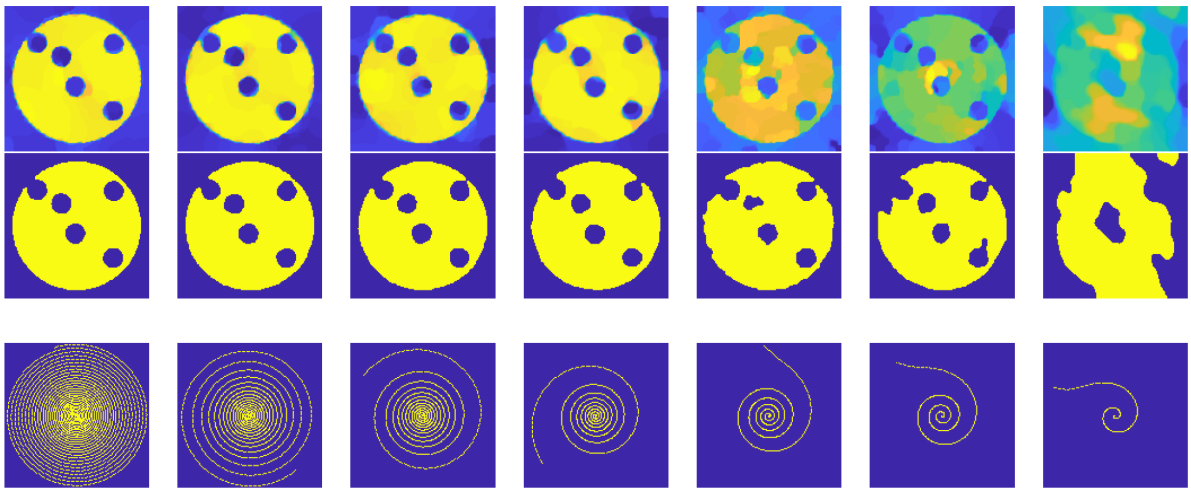

(a) 25% (b) 12.5% (c) 8% (d) 5% (e) 3% (f) 2% (g) 1%

**Figure 3.5:** Top row: reconstructions obtained by the joint model with different sampling rates. Bottom row: corresponding segmentations. The joint reconstruction and segmentation is able to detect the main structures down to 5% of the samples. Up to 2% the results are less clean but still acceptable. Using only 1% of the data is not enough to produce the image and segmentation.

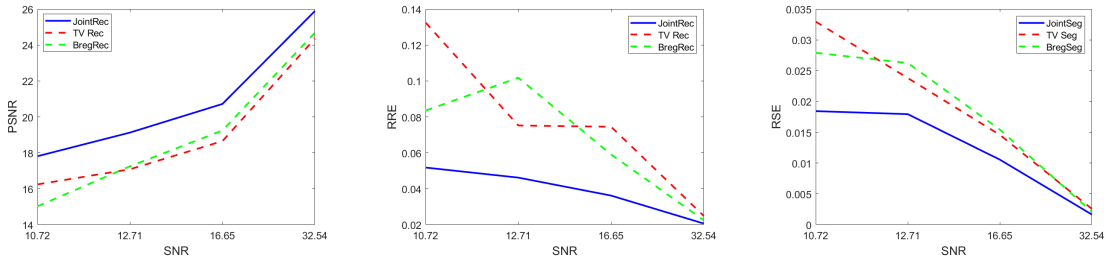


**(a)** PSNR **(b)** RRE **(c)** RSE

**Figure 3.6:** Error plots for different SNR. From left to right, we show the PSNR, RRE and RSE, respectively, for different levels of noise in the measurements. The blue lines represent the error for our joint approach, while the red and green dotted lines are for the sequential TV and sequential Bregman TV approaches. For each SNR, the joint model performs better than the separate methods. This improvement is even more significant for noisier data, which is highly advantageous as in practice we often observe lower SNR.

experiment, we acquired the full $k$-space and present the zero-filling reconstruction in Figure 3.8a and the sequential segmentation in Figure 3.8e. As discussed already in the previous section, the zero-filled reconstruction presents noise and artefact which may complicate the segmentation. We want to show that the compressed sensing approach and in particular the joint model can improve this reconstruction. Given the full $k$-space, we select 15% of the samples using a spiral mask. In Figure 3.8b, 3.8f and Figure 3.8c,

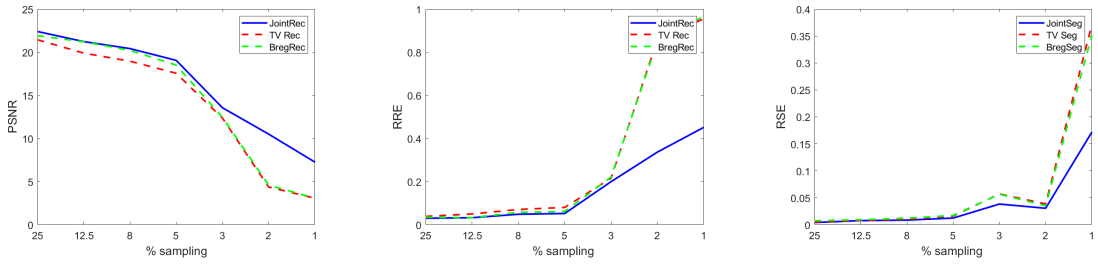


**(a)** PSNR **(b)** RRE **(c)** RSE

**Figure 3.7:** Error plots varying sampling rate. From left to right, we show the PSNR, RRE and RSE, respectively, for different levels of noise in the measurements. The blue lines represent the error for our joint approach, while the red and green dotted lines are for the sequential TV and sequential Bregman TV approaches. The joint appraoch performs better than the sequential cases. The gain is not very significant for higher sampling rates, but it becomes more important for lower rates, starting from 3%.

3.8g we show the results for the sequential approaches. In Figure 3.8d and 3.8h we show the joint reconstruction and the joint segmentation obtained for the same data. The regularised approaches perform better that the zero-filled reconstruction, producing less noisy results. However, our joint model is able to produce a cleaner reconstruction where the edges that defines the tumour and the brain are very well detected. In Figure 3.9, we show a zoomed section where it is easy to assess that the joint model tackle the noise and detect the region of interest. We can see that we are able to improve the reconstruction and automatically identify the tumour in the brain. The degree of enhancement of the edges in the reconstruction is controllable by the parameter $\delta$ in the model (3.10). In the next subsection we present a discussion on how to tune this parameter.

### 3.3.3 Parameter Reasoning

In the model proposed in (3.10), the parameters that we need to choose are $\alpha$, $\beta$ and $\delta$. In this section we discuss a rule to choose them depending on the desired results. Some examples will clarify these empirical choices.

- $\alpha$ balances the total variation regularization term in the reconstruction for the magnitude. The higher the $\alpha$, the more piecewise constant the reconstruction will be. See Figure 3.10.

- $\beta$ defines the scale of the objects that will be detected in the segmentation. Smaller values of $\beta$ will allow for smaller objects. See Figure 3.11.

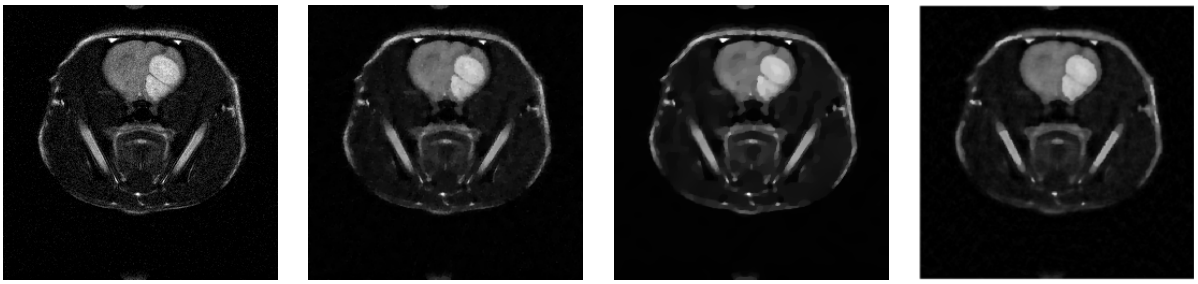

**(a)** Zero-filled reconstruction **(b)** TV reconstruction, $\alpha = 0.01$ **(c)** Bregman reconstruction, $\alpha = 1$ **(d)** Joint reconstruction, $\alpha = 0.5$

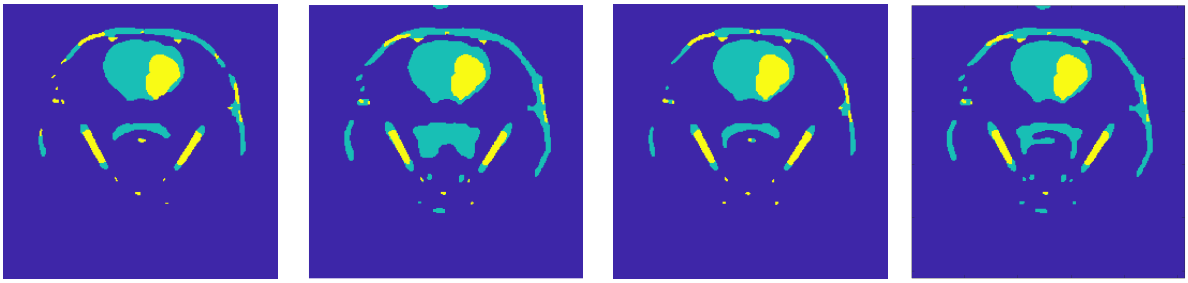

**(e)** Segmentation **(f)** Segmentation, $\beta = 0.07$ **(g)** Bregman segmentation, $\beta = 0.07$ **(h)** Joint segmentation, $\beta = 0.01$, $\delta = 0.01$

**Figure 3.8:** Reconstructions and segmentation for real MRI data. We select 15% of the samples using a spiral mask. The image show a rat brain bearing a tumour (brighter region). The zero-filled reconstruction 3.8a and the TV regularised reconstruction 3.8b are shown together with their sequential segmentation 3.8e and 3.8f respectively. In the last column 3.8d and 3.8h we show the results for our model. The parameter $\alpha$ for the TV reconstruction and for the joint reconstruction has been chosen such that it achieves visually optimal in the sense that it resolve all the details (e.g. the darker line cutting the tumour transversally).

- $\delta$ is the parameter linking the reconstruction and the segmentation. To better illustrate its role, let us consider a zero-filling like reconstruction and segmentation:

$$\imath_{\mathcal{SF}\cdot=f}(u) + \delta \sum_{i\in\Omega} \sum_{j=1}^{\ell} v_{ij}(c_j - u_i)^2 dx + \beta\|\nabla v\| \to \min_{u,v} \tag{3.25}$$

where $\imath(u) = \begin{cases} +\infty, & \text{if } \mathcal{SF}u \neq f \\ 0, & \text{if } \mathcal{SF}u = f \end{cases}$. This problem is solving the zero-filled reconstruction and segmentation jointly. For $\delta = 0$, the reconstruction is the zero-filling solution. In Figure 3.12 we can see the impact of the segmentation term on the reconstruction for increasing values of $\delta$. We can see that for very small $\delta$ the result is close to the zero-filling solution. For $\delta = 1$ the noise from the model is present as

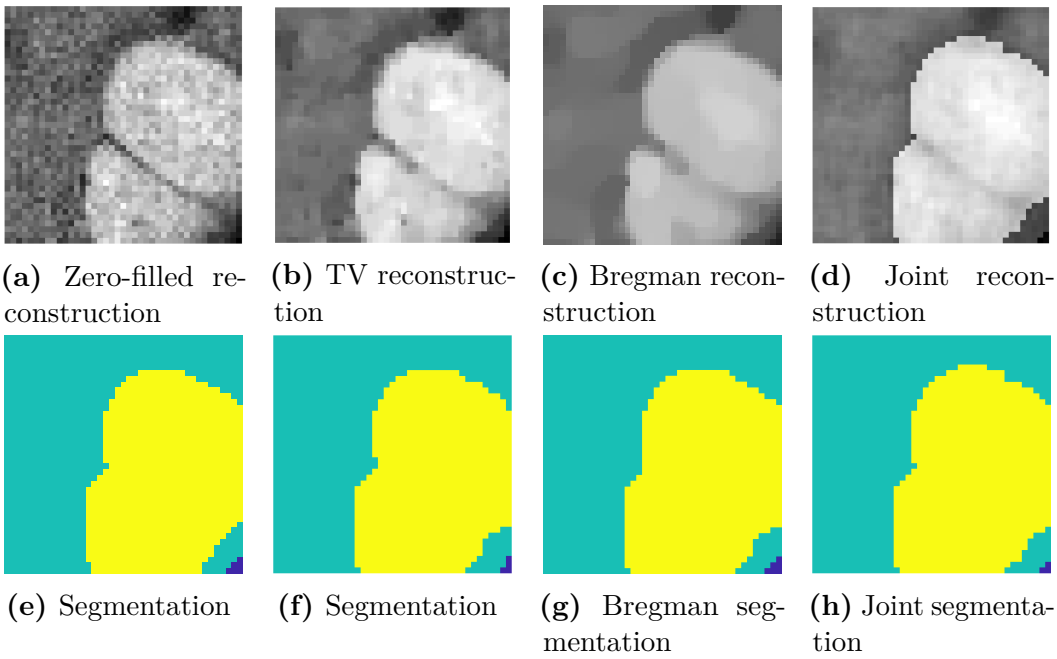

**(a)** Zero-filled reconstruction **(b)** TV reconstruction **(c)** Bregman reconstruction **(d)** Joint reconstruction

**(e)** Segmentation **(f)** Segmentation **(g)** Bregman segmentation **(h)** Joint segmentation

**Figure 3.9:** Zoomed section on the tumour for the different approaches.

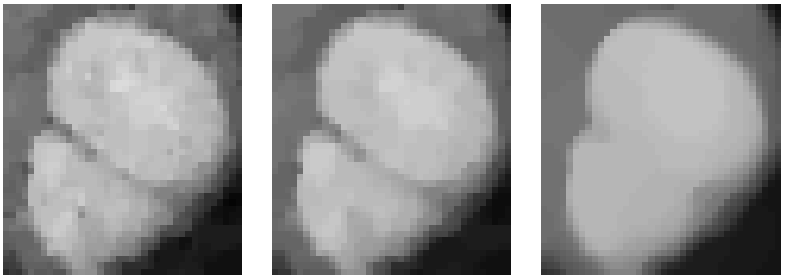

**(a)** $\alpha = 0.001$ **(b)** $\alpha = 0.01$ **(c)** $\alpha = 0.1$

**Figure 3.10:** The parameter $\alpha$ balances the data fidelity term and the total variation regularisation for the reconstruction. Smaller values of $\alpha$ produce a reconstruction closer to the data fitting term, hence less smooth as in 3.10a. As $\alpha$ increases in 3.10b the solution gets smoother and less noisy. Finally for large values it tends to become more piecewise constant as in 3.10c.

expected but in addition the boundaries are enhanced. For large $\delta$ the boundaries are still very pronounced and the noise is also amplified.

### 3.3.4 Comparison with another Joint Approach

We present a comparison of our joint model with another non-convex method, namely the Potts model approach by [SWFU15], described in Subsection 3.1.4. The major advantage of the joint reconstruction and segmentation using the Potts model is that it does not

**(a)** $\beta = 0.1$ **(b)** $\beta = 1$ **(c)** $\beta = 3$

**Figure 3.11:** The parameter $\beta$ determines the scale of the objects that we are segmenting. Smaller values of $\beta$ can detect smaller objects 3.11a, which are lost for intermediate values 3.11b. Finally very large values only detect main structures 3.11c.

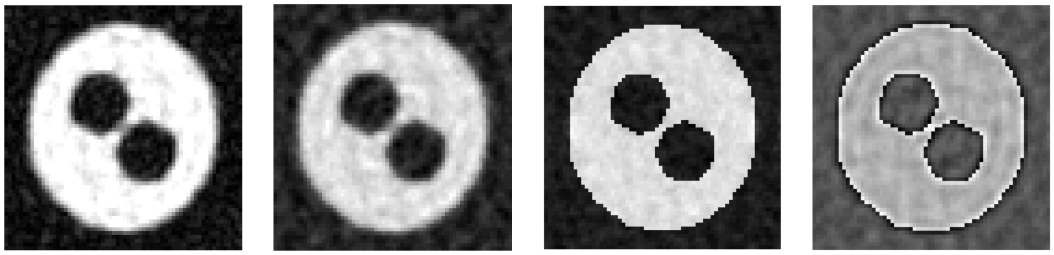

**(a)** $\delta = 0$ **(b)** $\delta = 0.1$ **(c)** $\delta = 1$ **(d)** $\delta = 2.5$

**Figure 3.12:** We show the reconstructions obtained solving (3.25) for different values of $\delta$. For $\delta = 0$ we get the zero-filling solution. For small $\delta$ we expect the solution to be similar to the zero-filling reconstruction. For $\delta = 1$ we see the effect of the joint term on the reconstruction. The solution presents the same noise artefacts but having in addition very sharp boundaries. Finally, for very large $\delta$ we still have enhanced boundaries but we also amplify the noise.

require to select explicitely the number of regions to segment, although this depends on the choice of the regularisation parameter. However, by definition, it only produces a piecewise constant image, therefore a segmentation, and not a reconstruction. This is useful in some applications where one is only interested in the segmentation. In contrast, our model produces both reconstruction and segmentation. In Figure 3.13, we show the results for some examples. Note that because the results of the Potts model are in the range of the groundtruth image, while our segmentation are in label space, we can not directly use the RSE as before, or common metrics that compare actual intensities such as PSNR and structure similarity index measure (SSIM), for comparison. For example, for some tissue in class 1, to label it class 2 is as wrong as to label it class 3. However in this case, the SSIM and PSNR will favour the label class 2.

We therefore focus on a visual assessment and show the results of the Potts model for two different choices of the regularisation parameter $\gamma$. We recall that the proposed model requires to determine the number of classes in advance, while the model for comparison

estimates the number of regions but this depends on the choice of the regularisation parameter. In the top row, we can see that the Potts model, although it retrieves the shape of the main structures for the brain phantom example, it overestimates the number of classes. By increasing the parameter $\gamma$, this issue is not resolved as it assigns different intensities to objects of the same category. In contrast, our approach is able to identify the desired classes as in the groundtruth. For the bubble case (middle row), we can see that our method works better and our segmentation is more accurate, while the Potts model fails to capture shape details (e.g., outer circle is distorted) and again overestimates the number of regions. We can also see that, when slightly decreasing $\gamma$, the Potts model is very sensitive to artefacts. For the real MR data (bottom row), we see that both methods identify the tumour quite well. Because we were only interested in identifying three classes as tumour, brain and background, we do not segment the outer region (rat's head), captured insted by the Potts model. However, the Potts model only produces the segmentation, while our method, as shown in Figure 3.8, also produces an enhanced reconstruction with sharp edges.

## 3.4 Conclusion and Outlook

In this chapter, we have investigated a novel mathematical approach to perform simultaneously reconstruction and segmentation from undersampled MRI data. Our motivation was to include in the reconstruction prior knowledge of the objects we are interested in. By interconnecting the reconstruction and the segmentation terms, we can achieve sharper reconstructions and more accurate segmentations. We derived a variational model based on Bregman iteration and we have verified its convergence properties. With our approach we show that by solving the more complicated joint model, we are able to improve both reconstruction and segmentation compared to the traditional sequential approach. This suggests that with the joint model it is possible to reduce error propagations that occur in sequential analysis, when the segmentation is separate and posterior to the reconstruction.

We have tested our method for two different application, which are bubbly flow and cancer imaging. In both cases, the reconstructions are sharper and finer structures are detected. Additionally, the segmentations also benefit from the improvement in the reconstructions. We have found that the joint model outperforms the sequential approach by exploiting prior information on the objects that we want to segment. In addition, we also show that our method performs better than the well-known Potts model. We also presented a discussion on the parameter choice rule that offer some insight on how

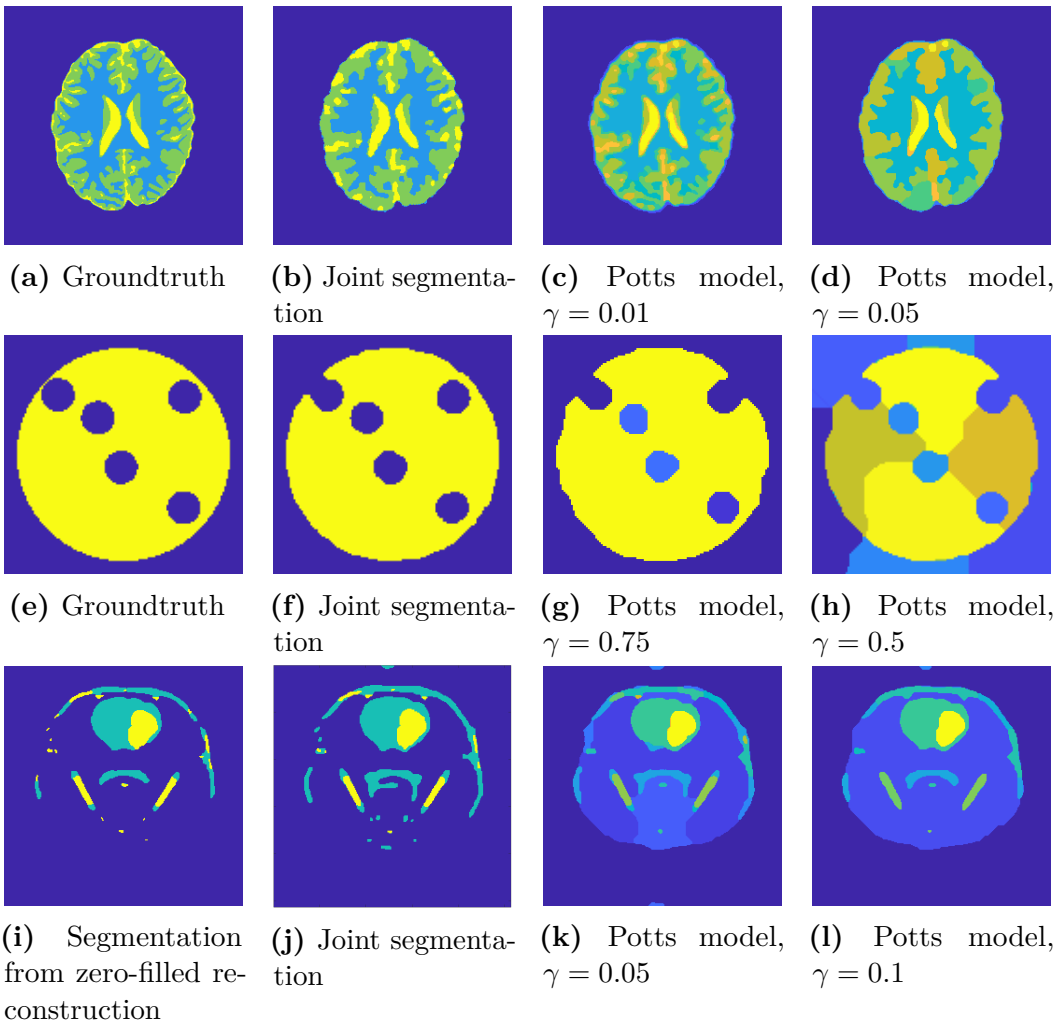

**(a)** Groundtruth **(b)** Joint segmentation **(c)** Potts model, $\gamma = 0.01$ **(d)** Potts model, $\gamma = 0.05$

**(e)** Groundtruth **(f)** Joint segmentation **(g)** Potts model, $\gamma = 0.75$ **(h)** Potts model, $\gamma = 0.5$

**(i)** Segmentation from zero-filled reconstruction **(j)** Joint segmentation **(k)** Potts model, $\gamma = 0.05$ **(l)** Potts model, $\gamma = 0.1$

**Figure 3.13:** Comparison of our joint approach with the Potts model. Noise level and undersampling rate are described in Figure 3.2, 3.3 and 3.8. The results are presented for three different examples and for two different choices of the regularisation parameter $\gamma$. We can see that the Potts model tends to overestimate the number of regions to segment.

to tune the parameters according to the desired result. It is interesting to notice that, with our model, we are able to control the segmentation effect on the reconstruction. Furthermore, when the final analysis of the MR image is indeed the segmentation, it is possible to bias the reconstruction towards the piecewise constant solution, yet preserving finer details in the structure.

In our set-up, we have specified the intensity constants characteristic of the region of interests, which were known a priori for our applications. However, it is possible to also include the optimisation with respect to $c_j$ in our joint model, where the same convergence guarantees hold (see Remark 3.15). Nevertheless, one limitation of the model is the need to specify the number of regions to be segmented.

In the next chapter, we will study the extension of this model for the bubbly flow to the reconstruction of the magnitude image as well as the phase image. The goal is not only to extract the structure of the bubble, but also to estimate velocity information, which is encoded in the phase image.

# Chapter 4

# Multi-Task Model for Phase Reconstruction and Magnitude Segmentation in Velocity-Encoded MRI

In this chapter, we deal with velocity-encoded MRI where now we are not only interested in the magnitude image, as in Chapter 3, but also to the phase image which encodes velocity information. Here we present the extension of our joint reconstruction and segmentation model for the application of velocity-encoded MRI which can be found in [CBG+19]. This is joint work with Martin Benning, Lynn F. Gladden, Andi Reci, Andrew Sederman and Carola-Bibiane Schönlieb.

We have seen in the previous chapters that MRI is a very powerful imaging technique that allows to visualise the chemical composition of patients or materials in a non-invasive fashion. However, besides resolving in great detail the morphology of the object under consideration, MRI is intrinsically sensitive to motion, flow and diffusion [Bur82, Axe84]. This means that in a single experiment, MRI can produce both structural and functional information. By designing the acquisition protocol appropriately, MRI can provide flow and motion estimation. This technique is known as MR velocimetry or phase-encoded MR velocity imaging [Cal11, Fuk99, EA07, GS13]. In this work, we will focus on the dynamic inverse problem involved in recovering velocities from this kind of data.

In many MRI applications, the goal is not only to extract the structure of the object of interest, but also to estimate some functional features. An example is flow imaging, in which the aim is to reconstruct the velocity of the fluid that is moving in some structure. In order to acquire the velocity information and assess flow motion, phase-encoded MR

velocity imaging is widely used in different areas. In medical imaging, this is used for example in cardiovascular blood flow studies to assess the distribution and variation in flow in blood vessels around the heart [GKC+05]. Other industrial applications include the study the rheology of complex fluids [Cal99], liquids and gases flowing through packed beds [SJAG98, SHSG09, HMB+10], granular flows [Fuk99, HMD+08] and multiphase turbulence [THSG12a].

MRI scanners use strong magnetic fields and radio waves to excite subatomic particles (like protons) that subsequently emit radio frequency signals which can be measured by the radio frequency coils. Because the local magnetisation of the spins is a vector quantity, it is possible to derive both magnitude and phase images from the signal. Furthermore, for appropriately designed experiments, the velocity information can be estimated from the phase image. The problem of retrieving magnitude and phase (and therefore velocities) from such measurements is non-linear. Many standard approaches reduce this inverse problem to a complex but linear inverse problem, where magnitude and phase are estimated subsequently. With this strategy, however, it is impossible to impose regularity on the velocity information. In this work, we therefore propose a joint framework to simultaneously estimate magnitude and phase from undersampled velocity-encoded MRI. Based on [CBE+19] and Chapter 3, we additionally introduce a third task, that is the segmentation on the magnitude, to improve the overall reconstruction quality. The main motivation is that by estimating edges simultaneously from the data, both magnitude and segmentation are reconstructed more accurately. By enhancing the magnitude reconstruction, we expect in turn to improve the corresponding phase image and therefore the final velocity estimation.

**Contributions.** In this work we consider the problem of estimating flow, magnitude and segmentation of regions of interest from undersampled velocity-encoded MRI data. The problem is of great interest in different areas including cardiovascular blood flow analysis in medical imaging and rheology of complex fluids in industrial applications. To this end, we propose a joint variational model for undersampled velocity-encoded MRI. The significance of our approach is that by tackling the phase and magnitude reconstruction *jointly*, we can exploit their strong correlation and finally impose regularity on the velocity component. This is further assisted by the introduction of a segmentation term as additional prior to enhance edges of the regions of interest. Our main contributions are

- A description of the forward and inverse problem of velocity-encoded MRI in the setting of bubbly flow estimation.

- A joint variational framework for the approximation of the non-linear inverse problem of velocity estimation. We show that by exploiting the strong correlation in the data, our joint method yields an accurate estimation of the underlying flow, alongside a magnitude reconstruction that preserves and enhances intrinsic structures and edges, due to a joint segmentation approach. Moreover, we achieve an accurate segmentation to discern between different areas of interest, e.g. fluid and air.
- An alternating Bregman iteration method for non-convex optimisation problems.
- Numerical experiments on synthetic and real data in which we demonstrate the suitability and potential of our approach and provide a comparison with sequential approach.

**Organisation of the chapter** This chapter is organised as follows. In Section 4.1 we describe the derivation of the inverse problem of velocity-encoded MRI from the acquisition process to the spin proton density estimation. In Section 4.2 we present our joint variational model to jointly estimate phase and magnitude reconstruction and its segmentation. In Section 4.3 we propose an optimisation scheme to solve the non-convex and non-linear problem using Bregman iteration. To conclude, in Section 4.4 we demonstrate the performance of our proposed joint method in comparison with a sequential approach for synthetic and real MRI data.

## 4.1 Velocity-Encoded MRI

In the following we will briefly describe the mathematics of the acquisition process involved in MRI velocimetry. Subsequently we are going to see that finding the unknown spin proton density basically leads to solving the inverse problem of the Fourier transform. We refer the reader to [Cal93, HBTV99] for more details on MRI.

### 4.1.1 From the Bloch Equations to the Inverse Problem

The magnetisation of a so-called spin isochromat can be described by the Bloch equations

$$\frac{d}{dt}\begin{pmatrix} M_x(t) \\ M_y(t) \\ M_z(t) \end{pmatrix} = \begin{pmatrix} -\frac{1}{T_2} & \gamma B_z(t) & -\gamma B_y(t) \\ -\gamma B_z(t) & -\frac{1}{T_2} & \gamma B_x(t) \\ \gamma B_y(t) & -\gamma B_x(t) & -\frac{1}{T_1} \end{pmatrix} \begin{pmatrix} M_x(t) \\ M_y(t) \\ M_z(t) \end{pmatrix} + \begin{pmatrix} 0 \\ 0 \\ \frac{M_0}{T_1} \end{pmatrix}. \tag{4.1}$$

Here $M(t) = (M_x(t), M_y(t), M_z(t))$ is the nuclear magnetisation (of the spin isochromat), $\gamma$ is the gyromagnetic ratio, $B(t) = (B_x(t), B_y(t), B_z(t))$ denotes the magnetic field experienced by the nuclei, $T_1$ is the longitudinal and $T_2$ the transverse relaxation time and $M_0$ the magnetisation in thermal equilibrium. If we define $M_{xy}(t) = M_x(t) + iM_y(t)$ and $B_{xy}(t) = B_x(t) + iB_y(t)$, we can rewrite (4.1) to

$$\frac{d}{dt}M_{xy}(t) = -i\gamma\left(M_{xy}(t)B_z(t) - M_z(t)B_{xy}(t)\right) - \frac{M_{xy}(t)}{T_2} \tag{4.2a}$$

$$\frac{d}{dt}M_z(t) = i\frac{\gamma}{2}\left(M_{xy}(t)\overline{B_{xy}}(t) - \overline{M_{xy}}(t)B_{xy}(t)\right) - \frac{M_z(t) - M_0}{T_1} \tag{4.2b}$$

with $\bar{\cdot}$ denoting the complex conjugate of $\cdot$.

If we assume for instance that $B = (0, 0, B_0)$ is just a constant magnetic field in $z$-direction, (4.2) reduces to the decoupled equations

$$\frac{d}{dt}M_{xy}(t) = -i\gamma B_0 M_{xy}(t) - \frac{M_{xy}(t)}{T_2}\,, \tag{4.3a}$$

$$\frac{d}{dt}M_z(t) = -\frac{M_z(t) - M_0}{T_1}\,. \tag{4.3b}$$

It is easy to see that this system of equations (4.3) has the unique solution

$$M_{xy}(t) = e^{-t(i\omega_0 + 1/T_2)}M_{xy}(t_j) \tag{4.4a}$$

$$M_z(t) = M_z(t_j)e^{-\frac{t}{T_1}} + M_0\left(1 - e^{-\frac{t}{T_1}}\right) \tag{4.4b}$$

for $\omega_0 := \gamma B_0$ denoting the Lamor frequency, and $M_{xy}(t_j)$, $M_z(t_j)$ being the initial magnetisations at time $t = t_j \geq 0$.

### 4.1.2 Signal Recovery

The key idea to enable spatially resolved nuclear magnetic resonance spectrometry is to add a magnetic field $\hat{B}(t)$ to the constant magnetic field $B_0$ in $z$-direction that varies spatially over time. Then, (4.3a) changes to

$$\frac{d}{dt}M_{xy}(t) = -i\gamma(B_0 + \hat{B}(t))M_{xy}(t) - \frac{M_{xy}(t)}{T_2}\,,$$

which, for initial value $M_{xy}(t_j)$, has the unique solution

$$M_{xy}(t) = e^{-i\gamma\left(B_0 t + \int_{t_j}^{t} \hat{B}(\tau)\, d\tau\right)} e^{-\frac{t}{T_2}} M_{xy}(t_j)\,, \tag{4.5}$$

if we ensure $\hat{B}(t_j) = 0$. If now $x(t)$ denotes the spatial location of a considered spin isochromat at time $t$, we can write $\hat{B}(t)$ as $\hat{B}(t) = x(t) \cdot g(t)$, with a function $g$ that describes the influence of the magnetic field gradient over time.

If a radio-frequency (RF) pulse that has been used to induce magnetisation in the $x$-$y$-plane is subsequently turned off at time $t = t_*$ and thus, $B_x(t) = 0$ and $B_y(t) = 0$ for $t > t_* > t_j$, the same coils that have been used to induce the RF pulse can be used to measure the $x$-$y$ magnetisation. Using (4.4a) and assuming $t_* < t \ll T_2$ for all $x \in \mathbb{R}^3$, this gives rise to the following model-equation:

$$M_{xy}(t) = e^{-i\gamma\left(B_0 t + \int_{t_j}^{t} x(\tau)\cdot g(\tau)\, d\tau\right)} M_{xy}(t_j)\,. \tag{4.6}$$

In the following we assume that $x(t)$ can be approximated reasonably well via its Taylor approximation around a time $t = t_j$, i.e.

$$x(t) = \sum_{n=0}^{\infty} \frac{x^{(n)}(t_j)}{n!} (t - t_j)^n\,,$$

which yields

$$\begin{aligned} \int_{t_j}^{t} x(s) \cdot g(s)\, ds &= \sum_{n=0}^{\infty} \left[ \frac{x^{(n)}(t_j)}{n!} \cdot \int_{t_j}^{t} g(s)\ (s - t_j)^n\ ds \right] \\ &= \sum_{n=0}^{\infty} \left[ \frac{x^{(n)}(t_j)}{n!} \cdot \int_{0}^{t-t_j} g(\tau + t_j)\, \tau^n\, d\tau \right], \end{aligned} \tag{4.7}$$

for $t \geq t_j$. It is well-known that appropriate application of gradients (i.e. appropriate design of $g$) enables the approximation of individual moments of (4.7). If we further assume that the system to be observed does only contain zero- and first-order moments, we can assume

$$\int_{t_j}^{t} x(s) \cdot g(s)\, ds = x_j \cdot \int_{t_j}^{t} g(\tau + t_j)\, d\tau + \varphi_j \cdot \int_{t_j}^{t} g(\tau + t_j)\, \tau\, d\tau\,, \tag{4.8}$$

where $x_j$ is now short for $x(t_j)$ and $\varphi_j := x'(t_j)$ is the corresponding velocity information.

Equation (4.8) allows us to turn (4.6) into a useful mathematical model as we can encode velocity information and remove the temporal dependency of $x$. For notational convenience, we denote

$$\xi_j(t) := \int_{t_j}^{t} g(\tau + t_j)\, d\tau \quad \text{and} \quad \zeta_j(t) := \int_{t_j}^{t} g(\tau + t_j)\, \tau\, d\tau\,.$$

Since the RF-coils measure a volume of the whole $x$-$y$ net-magnetisation, the acquired signal then equals

$$f_j(t) = \int_{\mathbb{R}^3} u(x)\, e^{-i\gamma(B_0(x)\, t + \varphi(x)\cdot\zeta_j(t))}\, e^{-i\gamma x\cdot\xi_j(t)}\, dx\,. \tag{4.9}$$

with $u(x)$ denoting the spin-proton density $M_{xy}(t_j)$ at a specific spatial coordinate $x \in \mathbb{R}^3$. Note that for $r_j(x) := u(x)\, e^{-i\gamma(B_0(x)t + \varphi(x)\cdot\zeta_j(t))}$ we observe that $f$ is just the Fourier transform of the complex signal $r_j$ with magnitude $u$ and phase $-\gamma(B_0 t + \varphi\cdot\zeta_j)$.

### 4.1.3 Removal of Background Magnetic Field

Our goal is to recover the velocity information $\varphi$ from $f$. Assuming that we do not know $B_0$, we can alternatively conduct two experiments, where the setup is identical apart from the velocity-encoding gradients having opposite polarities, i.e. we measure

$$f_+(t) = \int_{\mathbb{R}^3} u(x)\, e^{-i\gamma(B_0(x)t + \varphi(x)\cdot\zeta(t))}\, e^{-i\gamma x\cdot\xi(t)}\, dx\,, \tag{4.10a}$$

$$f_-(t) = \int_{\mathbb{R}^3} u(x)\, e^{-i\gamma(B_0(x)t - \varphi(x)\cdot\zeta(t))}\, e^{-i\gamma x\cdot\xi(t)}\, dx\,. \tag{4.10b}$$

Note that we have omitted the subscript $j$ introduced in the previous section for simplicity of notation. If we denote $\varphi_+(x,t) := B_0(x)t + \varphi(x)\cdot\zeta(t)$ and $\varphi_-(x,t) := B_0(x)t - \varphi(x)\cdot\zeta(t)$, we immediately observe

$$\varphi(x)\cdot\zeta(t) = \frac{1}{2}\left(\varphi_+(x,t) - \varphi_-(x,t)\right)\,.$$

The inverse problem of (4.10) is to recover $u$ and $\varphi$ from $f_+$ and $f_-$.

### 4.1.4 Zero-Flow Experiment

A zero-flow experiment that allows for the removal of additional artifacts is also conducted. This experiment is to account for imperfections in the measurement system which cause an added signal between the positive and negative $\zeta$ experiments even in the absence of

flow, and enables a correction that allows direct quantification of flow and tissue motion. We refer to this technique as flow compensation, which consists of acquiring a reference scan, with any flow switched-off, with vanishing zero and first gradient moments, before the actual velocity encoding scan with added bipolar gradients is performed. In this way, we obtain background phase images from the reference scan, and velocity sensitivity with the second flow-sensitive scan. In practice, this means that in addition to (4.10), the following two measurements are taken:

$$f_{\text{noflow}_+}(t) = \int_{\mathbb{R}^3} u(x)\, e^{-i\gamma\varphi_{\text{noflow}_+}(x,t)}\, e^{-i\gamma x\cdot\xi(t)}\, dx\,, \tag{4.11a}$$

$$f_{\text{noflow}_-}(t) = \int_{\mathbb{R}^3} u(x)\, e^{-i\gamma\varphi_{\text{noflow}_-}(x,t)}\, e^{-i\gamma x\cdot\xi(t)}\, dx\,, \tag{4.11b}$$

so that the actual velocity information can be recovered via

$$\varphi(x)\cdot\zeta(t) = \frac{1}{2}\left((\varphi_+(x,t)-\varphi_-(x,t)) - \left(\varphi_{\text{noflow}_+}(x,t)-\varphi_{\text{noflow}_-}(x,t)\right)\right)\,. \tag{4.12}$$

The inverse problem is to recover $u$ and $\varphi$ from (4.10) and (4.11) via (4.12). More details on phase-encoded MR velocity imaging can be found in [Mar06].

In other words, for a given direction of the velocity to be measured ($x$, $y$ or $z$), the corresponding component velocity map ($v_x$, $v_y$ or $v_z$) is acquired by applying repeatedly a pulse sequence with the velocity-encoding gradient in the respective direction ($x$, $y$ or $z$) and with alternating polarity between consecutive pulse sequences (from $\pm g$ to $\mp g$). The difference between the phase of the MRI image reconstructed from the acquired $k$-space data of consecutive pulse sequences, and the reference to a zero flow experiment, yields the component velocity map.

### 4.1.5 Sampling

The MRI signal is acquired by sampling the continuous signals of $f_+$, $f_-$, $f_{\text{noflow}_+}$ and $f_{\text{noflow}_-}$ at $m$ discrete points in time. Based on the previous model assumptions, the acquisition of an individual sample reads

$$f_{j+1} = \int_0^{t_*} \Psi(t, t_{j+1}) \left[\int_{\mathbb{R}^3} u(x)\, e^{i\,\varphi(x)\cdot\zeta_j(t)}\, e^{-i\gamma x\cdot\xi_j(t)}\, dx\right] dt\,, \tag{4.13}$$

for $j \in \{0,\dots,m-1\}$, and where $\Psi$ denotes the sampling function or distribution. If we for example assume $\Psi(t,t_{j+1}) = \delta(t-t_{j+1})$, where $\delta$ denotes the Dirac delta distribution,

then (4.13) simplifies to

$$f_j = \int_{\mathbb{R}^3} u(x)\, e^{i\,\varphi(x)\cdot\zeta_j}\, e^{-i\gamma x\cdot\xi_j}\, dx\,, \qquad j \in \{1,\dots,m\}\,, \tag{4.14}$$

for

$$\xi_j := \int_{t_{j-1}}^{t_j} g(\tau + t_{j-1})\, d\tau \quad \text{and} \quad \zeta_j := \int_{t_{j-1}}^{t_j} g(\tau + t_{j-1})\, \tau\, d\tau\,.$$

This is our final acquisition model. We record and store all measurements in a vector $f \in \mathbb{C}^m$. For the remainder of this chapter, we assume $\zeta_j$ to be constant during the acquisition, and rewrite (4.14) (in vecotrial form) as

$$f = SF\left(ue^{i\varphi}\right)\,, \tag{4.15}$$

where $SF$ denotes the (sub-sampled) Fourier transform, $f \in \mathbb{C}^m$ denotes the vector of $k$-space samples. We recall that sampling strategies are very important to reduce the acquisition times and therefore to be able to image dynamic systems using velocity-encoded MRI through fast imaging techniques. Thanks to the theory of CS [CRT04, Don06, LDP07], it is possible to exploit redundancy in some specific domain of the measured data, and many image reconstruction techniques have been proposed [HMB+10, THSG12a, JHU+08, PB11, PBP10, PMS+09].
Depending on whether $\gamma\xi$ is sampled on a uniform or non-uniform grid, $\mathcal{SF}$ can be realised via the Fast Fourier Transform (FFT) [CT65] or via a non-uniform Fourier Transform such as NUFFT [FS03].

### 4.1.6 Dynamic Inverse Problem

We want to highlight that (4.15) can easily be extended to studying spin-proton density $u$ and the velocity $\varphi$ in (4.15) over time. To do so, one could take a sequence of $m$ measurements each, at (initial) times $\{\Delta t_j\}_{j=1}^s$, for $0 = \Delta t_1 < \Delta t_2 < \ldots < \Delta t_s$, so that we have a sequence of measurements $\{f_j\}_{j=1}^s$. This way, we would easily introduce a discrete temporal dimension to our inverse problem that potentially allows us to exploit any temporal correlation between frames $\{u_j\}_{j=1}^s$ and $\{\varphi_j\}_{j=1}^s$. In this work, however, we will only consider the reconstruction of individual frames for reasons that we are going to address later. In the following we will refer to an individual frame of the dynamic inverse problem for velocity-encoded MRI in the discrete setting and under the presence of noise making use of the notation of the discrete Fourier transform operator.

## 4.2 Mathematical Modelling

In this section we first present the velocity-encoded MRI reconstruction inverse problem in the presence of noise and discuss a sequential variational regularisation scheme to approximate the solution. Secondly, we introduce our joint reconstruction and segmentation approach in a Bregman iteration framework to jointly estimate phase, magnitude and segmentation.

### 4.2.1 Indirect Phase-Encoded MR Velocity Imaging

The velocity-encoded MRI image reconstruction problem is described as follows. Let $u, \phi \in \mathbb{R}^n$ be the proton density or magnitude image and correspondent phase image, respectively, in a discretised image domain $\Omega := \{1, \dots, n_1\} \times \{1, \dots, n_2\}$, with $n = n_1 n_2$. The vector $f = (f_i)_{i=1}^m \in \mathbb{C}^m$ with $m \ll n$ are the measured Fourier coefficients obtained from (4.15). Based on (4.15) the forward model for noisy data is given by

$$f = \mathcal{S}\mathcal{F}\left(ue^{i\phi}\right) + \eta\,, \tag{4.16}$$

where $i^2 = -1$ and $\eta$ is Gaussian noise with zero mean and standard deviation $\sigma$. For brevity we will follow the notation $\mathcal{A} = \mathcal{S}\mathcal{F}$. As explained in the previous section, velocity information is encoded in the phase image. However, during the acquisition the phase is perturbed by an error due to field inhomogeneity and chemical shift. To account for this error, usually different measurements corresponding to different polarities of encoding flow gradients are acquired. Then the velocity (in one direction) at one particular time will be estimated as in (4.12), where $\zeta$ is a constant known from the acquisition setting.

Given the presence of noise and partial observation of the data due to undersampling, the problem described in (5.1) is ill-posed. We have seen in the previous chapter that a simple strategy to obtain an approximated solution is to compute the zero-filling solution

$$r_z = \mathcal{A}^* f \tag{4.17}$$

where $r = ue^{i\phi}$. However, these reconstructed images will present aliasing artefacts because of the undersampling. Therefore, we will instead compute approximate solutions of (4.16) using a variational regularisation approach. We consider a Tikhonov-type regularisation approach that reads

$$r_j \in \arg\min_r \left\{ \frac{1}{2}\|\mathcal{A}_j r - f_j\|_2^2 + \alpha J(r) \right\}, \tag{4.18}$$

for $j \in \{1, \dots, 4\}$ being the different measurements, where the first term is the data fidelity that imposes consistency between the reconstruction and the given measurements $f$, the second term is the regularisation, which incorporates some prior knowledge of the solution. The parameter $\alpha > 0$ is a regularisation parameter that balances the two terms in the variational scheme. In this setting, the survey proposed in [BGH+14] describes different choices for the regularisation functional $J$, including wavelets and higher-order total variation (TV) schemes. Subsequently, the phases can be extracted from these complex images $r_j = u_j e^{i\phi_j}$ as

$$\phi_j = \arg(r_j). \tag{4.19}$$

More recently, other reconstruction approaches have been proposed to regularise the phase of the image [FN04, ZD10, ZNNF12, Val14, ZP17]. All these methods rely on modelling separately prior knowledge on the magnitude and on phase images and differ on the optimisation schemes involved in the non-convex and non-linear problem. However, while it is possible to exploit information about the velocity from fluid mechanics, it is in general hard to assume specific knowledge on the individual phases. As explained in the previous section and described in (4.12), velocities are computed as phase differences of different MR measurements and therefore the regularisation needs to be imposed on the phase difference rather than individual phases. In this work, we step away from the approach of only regularising individual phases and propose instead to regularise the velocity as difference of phases. In the following we describe our choice of regularisation and algorithmic framework for velocity-encoded MRI.

### 4.2.2 Joint Variational Model

In many industrial applications, velocity-encoded MRI is used to estimate flow of different chemical species in different physical status, such as gas-liquid systems [GS17]. In this case, one aims at recovering a piecewise constant image or an image with sharp edges to facilitate further analysis such as identification of regions of interest. In this context, our joint model proposed in [CBE+19] and Chapter 3 uses a segmentation task as additional regularisation on the reconstruction to impose regularity in terms of sharp edges. Furthermore, we have shown that this is highly beneficial for very low undersampling rates in MRI, which becomes extremely more relevant for fast-changing systems such as the ones we consider in this chapter. In this work, we expand this idea to the phase-encoded MR velocity imaging data, where the idea is to jointly solve for magnitude, segmentation and phase improving performances on the three tasks.

Following our previous model in [CBE+19], we are interested in the *joint model* to recover magnitude $u_j$ and velocity $\varphi$ components through the measured phases $\phi_j$ from undersampled MRI data $f_i$ and to estimate a segmentation $v_j$ on the magnitude images. As described in the previous section, we are dealing with four MRI measurements to obtain one component velocity image. Defining the shorthand notations $u := \{u_j\}_{j=1}^4$, $v := \{v_j\}_{j=1}^4$ and $\phi := \{\phi_j\}_{j=1}^4$, this joint model reads as

$$E(u,v,\phi) = \sum_{j=1}^{4} \Bigg\{ \frac{1}{2} \underbrace{\|\mathcal{A}(u_j e^{i\phi_j}) - f_j\|_2^2}_{\text{reconstruction}} + \delta \underbrace{\sum_n v_{nj}(c_1 - u_{nj})^2 + (1 - v_{nj})(c_2 - u_{nj})^2}_{\text{segmentation}} \Bigg\} . \tag{4.20}$$

The first term in (3.10) describes the reconstruction fidelity term for the magnitudes $u$ and phases $\phi$ for the given data $f := \{f_j\}_{j=1}^4$. The second term represents the segmentation problem to find partitions $v$, with $v_n \in [0,1]$, of the images $u$ in two disjoint regions that have mean intensity values close to the constants $c_1$ and $c_2$ [CV01, CEN06]. The parameter $\delta$ weighs the effect of the segmentation onto the reconstruction. The underlying idea is to exploit structure and redundancy in the data, estimating edges simultaneously from the data, ultimately improving the reconstruction. By incorporating prior knowledge of the regions of interest we impose additional regularity of the solution.

The joint cost function (4.20) is non-convex. While sub-problems in $u$ and $v$ (leaving the other parameters fixed) are convex, the sub-problems in $\phi$ are non-linear and non-convex. In the next section we present a unified framework based on non-convex Bregman iterations to solve the joint model.

## 4.3 Optimisation

There are many ways of minimising (3.10). We want to pursue a strategy that guarantees smooth velocity-components, piecewise-constant segmentations and magnitude images with sharp transitions in an inverse scale-space fashion. In order to achieve those features, we aim to approximate minimisers of (3.10) via an alternating Bregman proximal method

or Bregman iteration of the form

$$u_l^{k+1} \in \arg\min_u \left\{ E(u_1^{k+1}, \dots, u_{l-1}^{k+1}, u, u_{l+1}^k, \dots, u_d^k, v^k, \phi^k) + D_{J_u}^{p_l^k}(u, u_l^k) \right\}, \tag{4.21a}$$

$$p_l^{k+1} = p_l^k - \frac{\partial}{\partial u_l} E(u_1^{k+1}, \dots, u_{l-1}^{k+1}, u_l^{k+1}, u_{l+1}^k, \dots, u_d^k, v^k, \phi^k), \tag{4.21b}$$

$$v_l^{k+1} = \arg\min_v \left\{ E(u^{k+1}, v_1^{k+1}, \dots, v_{l-1}^{k+1}, v, v_{l+1}^k, \dots, v_d^k, \phi^k) + D_{J_v}^{q_l^k}(v, v_l^k) \right\}, \tag{4.21c}$$

$$q_l^{k+1} = q_l^k - \frac{\partial}{\partial v_l} E(u^{k+1}, v_1^{k+1}, \dots, v_{l-1}^{k+1}, v_l^{k+1}, v_{l+1}^k, \dots, v_d^k, \phi^k), \tag{4.21d}$$

$$\phi^{k+1} = \arg\min_\phi \left\{ \langle \partial_\phi E(u^{k+1}, v^{k+1}, \phi^k), \phi \rangle + D_{J_\phi}^{w^k}(\phi, \phi^k) \right\}, \tag{4.21e}$$

$$w^{k+1} = w^k - \frac{\partial}{\partial \phi} E(u^{k+1}, v^{k+1}, \phi^k). \tag{4.21f}$$

for $l = 1, \dots, d := 4$, $u := (u_l)_{l=1}^d$, $v := (v_l)_{l=1}^d$ and $\phi := (\phi_l)_{l=1}^d$. Here $J_u$, $J_v$ and $J_\phi$ are proper, lower semi-continuous and convex functions and $D_{J_u}^{p_l^k}(u, u_l^k)$, $D_{J_v}^{q_l^k}(v, v_l^k)$ and $D_{J_\phi}^{w^k}(\phi, \phi^k)$ are the corresponding generalised Bregman distances [Bre67, Kiw97] with arguments and corresponding subgradients $p_l^k$, $q_l^k$ and $w^k$. We recall here that a generalised Bregman distance is the distance between a function $J$ evaluated at argument $u$ and its linearisation around argument $v$, i.e.

$$D_J^q(u, v) = J(u) - J(v) - \langle q, u - v \rangle,$$

for a subgradient $q \in \partial J(v)$. Note that algorithm (4.21) has update rules for the subgradients, as $J_u$, $J_v$ and $J_\phi$ are allowed to be non-smooth, which makes the selection of particular subgradients necessary.

The algorithm is a hybrid of the our algorithm described in Chapter 3 and the one proposed in [BBES17]. For both algorithms global convergence results, motivated by [XY13, BST14], have been established. Since we deal with imperfect data potentially corrupted by measurement noise and numerical errors, we will, however, use (4.21) in combination with an early-stopping criterion in order not to converge to a minimiser of (3.10) but to approximate the solution of (5.1) via iterative regularisation.

The crucial part for the application of (4.21) are the choices of the underlying functions $J_u$, $J_v$ and $J_\phi$ of the corresponding Bregman distances. We want both the magnitude images and the segmentations to maintain sharp discontinuities and therefore want to penalise their discretised, isotropic, total variation. On the other hand, we want to guarantee smooth components of our velocity field, which is why we penalise them with

the two-norm of a discretised gradient. In particular, we choose

$$J_u(u) = \alpha\,\mathrm{TV}(u) := \alpha\||\nabla u|\|_1\,, \qquad J_v(v) := \beta\,\mathrm{TV}(v), \tag{4.22}$$

to be the isotropic total variation with weights $\alpha > 0$ and $\beta > 0$. Further, we choose $J_\phi$ in a way that allows to enable an $H^1$-norm-type smoothing on the difference of the phases, i.e.

$$J_\phi^{k+1}(\phi) = \frac{1}{2\tau}\left(\eta\||\nabla\left((\phi_1-\phi_2)-(\phi_3-\phi_4)\right)|\|^2 + \sum_{l=1}^{d}\|\phi_l\|^2\right),$$

where $\eta > 0$ denotes another weight. Note that all convex sub-optimisation-problems in (4.21) are solved numerically with a primal-dual hybrid gradient (PDHG) method [ZC08, PCBC09, EZC10, CP11b] (cf. Appendix A). Once we have approximated the magnitudes, labels and phases with this iterative regularisation strategy, we can compute the velocity components via (4.12).

## 4.4 Numerical Results

In this section we present numerical results of our method for the specific application of bubble burst hydrodynamics using MR velocimetry. The hydrodynamics of bursting bubbles is important in many different areas such as geophysical processes and bioreactor design. We refer to [Rec19] for an overview on the field and the description of results on the first experimental measurement of the liquid velocity field map during the burst of a bubble at the liquid surface interface.

### 4.4.1 Case-Study on Simulated Dataset

To quantitatively evaluate our method, we consider the simulated k-space data of a rising spherical bubble in an infinite fluid during Stoke's flow regime. The simulated data consists of 32 time frames, but for the sake of compactness we will show some visual outputs for one time step $t = 19$.

We assess the performance of our approach for velocity and magnitude estimation by comparing our solutions with respect to the groundtruth and using the mean squared error (MSE) defined as $\|x^{\mathrm{groundtruth}} - x\|_2^2/n$, where $n$ is the number of pixels in the image.

We also present a comparison with a sequential approach, where the magnitude is obtained with a classic CS TV-regularised approach and the phase is subsequently

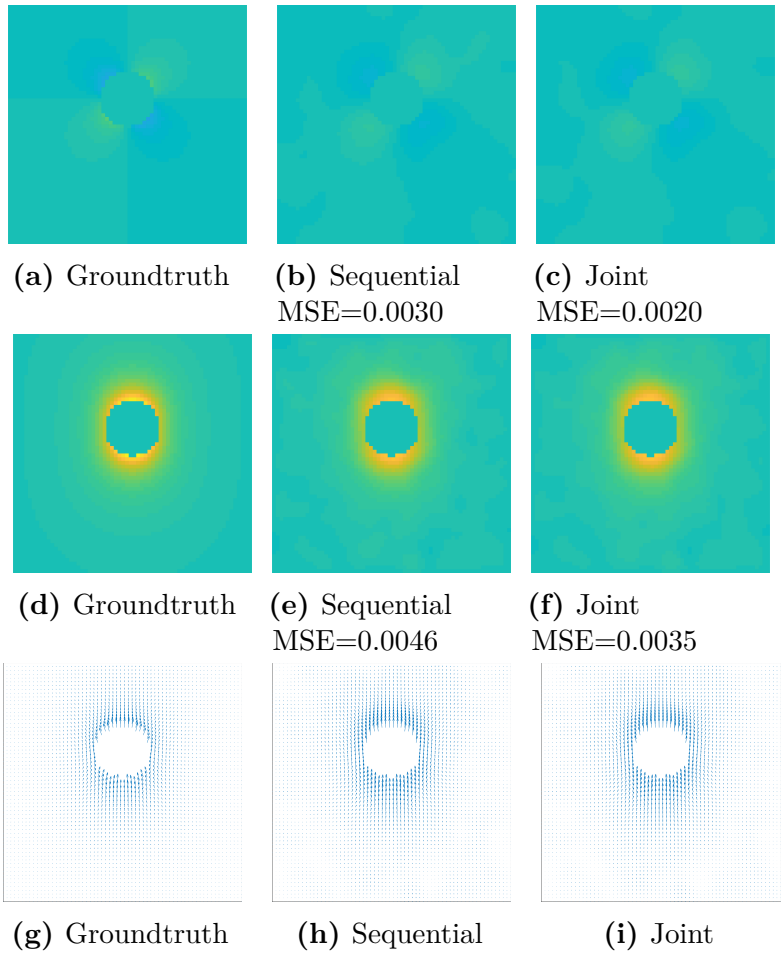

**(a)** Groundtruth **(b)** Sequential MSE=0.0030 **(c)** Joint MSE=0.0020

**(d)** Groundtruth **(e)** Sequential MSE=0.0046 **(f)** Joint MSE=0.0035

**(g)** Groundtruth **(h)** Sequential **(i)** Joint

**Figure 4.1:** Phase reconstructions for the sequential approach and our joint approach compared to the ground truth. Top row: $x$ direction, middle row: $z$ direction, bottom row: velocity plots. We sampled 11% of the $k$-space data.

estimated using the method proposed in [BBES17] and presented in [Rec19] for the evaluation of bubbly flow estimation.

In Fig. 4.1 we can see the results for the sequential approach compared to the joint approach when sampling only 11% of the $k$-space data. Although visually there is not significant change, the MSE shows a big improvement for the joint approach. This confirms that using our joint model is relevant for the problem of velocity-encoded MRI. For the 32 frames, we report the average MSE for magnitude and phase in Table 4.1 where can see a drastic improvement compared to the sequential approach.

**Table 4.1:** MSE for phase ($\phi_1$ and $\phi_2$) and magnitude ($u_1$ and $u_2$) images for the sequential and joint approaches. The error is significantly decreased using our proposed joint approach.

| | $u_1$ | $u_2$ | $\phi_1$ | $\phi_2$ |
|---|---|---|---|---|
| Sequential | 0.0019 | 0.0028 | 0.0032 | 0.0059 |
| Joint | **0.0011** | **0.0012** | **0.0018** | **0.0051** |

### 4.4.2 Real Dataset

In this section we present our model performance on real data acquired with the following protocol described in [Rec19] and briefly reported here.

**Acquisition protocol** The experiments were conducted on an AV-400 Bruker magnet, operating at a resonant frequency of 400.25 MHz for $^1$H observation with an RF coil of 25 mm diameter. The maximum magnetic field gradient amplitude available in each spatial direction is 146 Gcm$^{-1}$. The velocity images were acquired with a 2D MR spiral imaging technique developed and published in [THSG12b]. Images were acquired with 64 $\times$ 64 pixels over a field of view of 17 mm $\times$ 17 mm resulting in an image resolution of 265 mm $\times$ 265 mm. Data in k-space were acquired along a spiral trajectory at a sampling rate corresponding to 25% of full Nyquist sampling over a time of 2.05 ms for the entire image. We acquire the three velocity components for a transverse slice (perpendicular to the axis of the pipe) and a longitudinal slice (parallel to the axis of the pipe), cutting through approximately the centre of the bubble. For a given slice direction (transverse or longitudinal) and a given direction of the velocity, four measurements corresponding to the application of the velocity-encoding gradient with alternating polarity and to the flow compensation, are taken, as discussed in Section 4.1 (see Figure 4.2(b)). The final velocity for each component is then obtained as the difference between the phase of the MRI images reconstructed from the acquired k-space data of consecutive pulse sequences with flow on, and the reference to the zero flow experiment (see Sections 4.1.3 and 4.1.4, respectively).

**Experimental results on real data** For the real data acquired with protocol described above, we present the results for our joint model in comparison with the zero-filling solution and the corresponding sequential approach also used in the previous subsection. In Figure 4.3 we show the result for a specific time frame for a bubble in a transversal and longitudinal view. At this specific time, the bubble is bursting which corresponds to an upward jet being ejected. As we can see, the zero-filling solution gives an indication

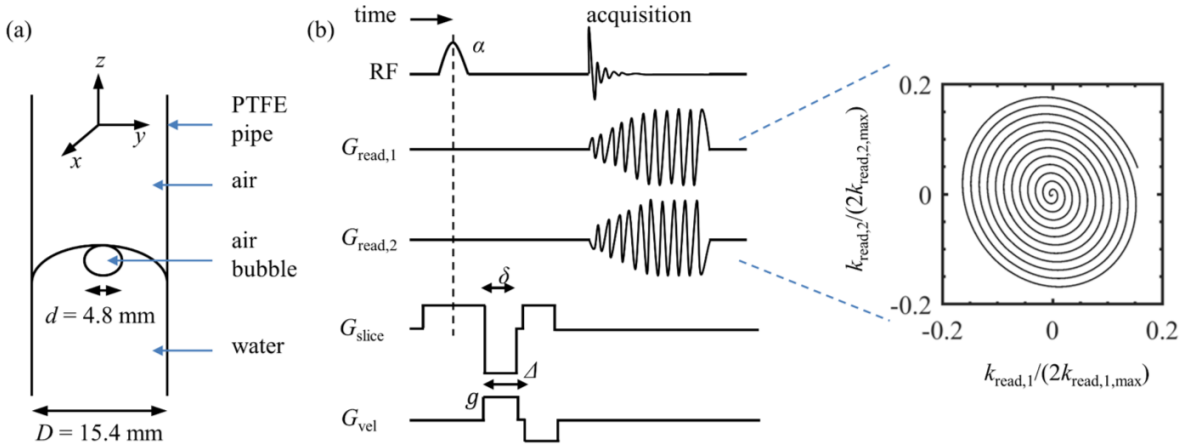


**Figure 4.2:** Experimental setup. (a) Schematic of experimental setup. (b) Pulse sequence used for MR velocimetry acquisitions and the corresponding k-space traversal. Taken from [Rec19].

of the flow velocity but it is very noisy and imprecise. In contrast, the joint approach removes noise and successfully estimate the velocity flow. The sequential approach on the other hand, although it produces a smoother reconstruction, results in small errors (see e.g. Figure 4.3e on the left). In Figure 4.6 we observe similar results for a different time frame. We refer to the Appendix for the full dynamic sequence result.

We also present the results for the magnitude and segmentation for the zero-filling solution, sequential approach and joint approach. We can see in Figure 4.4 and 4.5 that the joint approach exploits the structure in the data and present more accurate magnitude reconstructions and segmentations. It is clear that, even in this rather simple segmentation problem, the joint approach is able to improve the results of both tasks. This gain is significant in Figure 4.5f. Additionally, the joint magnitudes present very sharp edges distinguishing air and fluid thanks to the segmentation coupling term in the model, which acts as additional prior to reconstruct images exploiting prior knowledge on the region of interest.

### Full dynamic sequence

In this section we show the full dynamic sequence of a bubble burst event in Figure 4.8 and 4.7. At time $t = 1$ the bubble resting at the air-liquid interface. When the thin liquid film breaks, the bubble bursts, causing the formation of an upward and downward jet. The upward jet moves in the empty space left by the bubble and reached its maximum

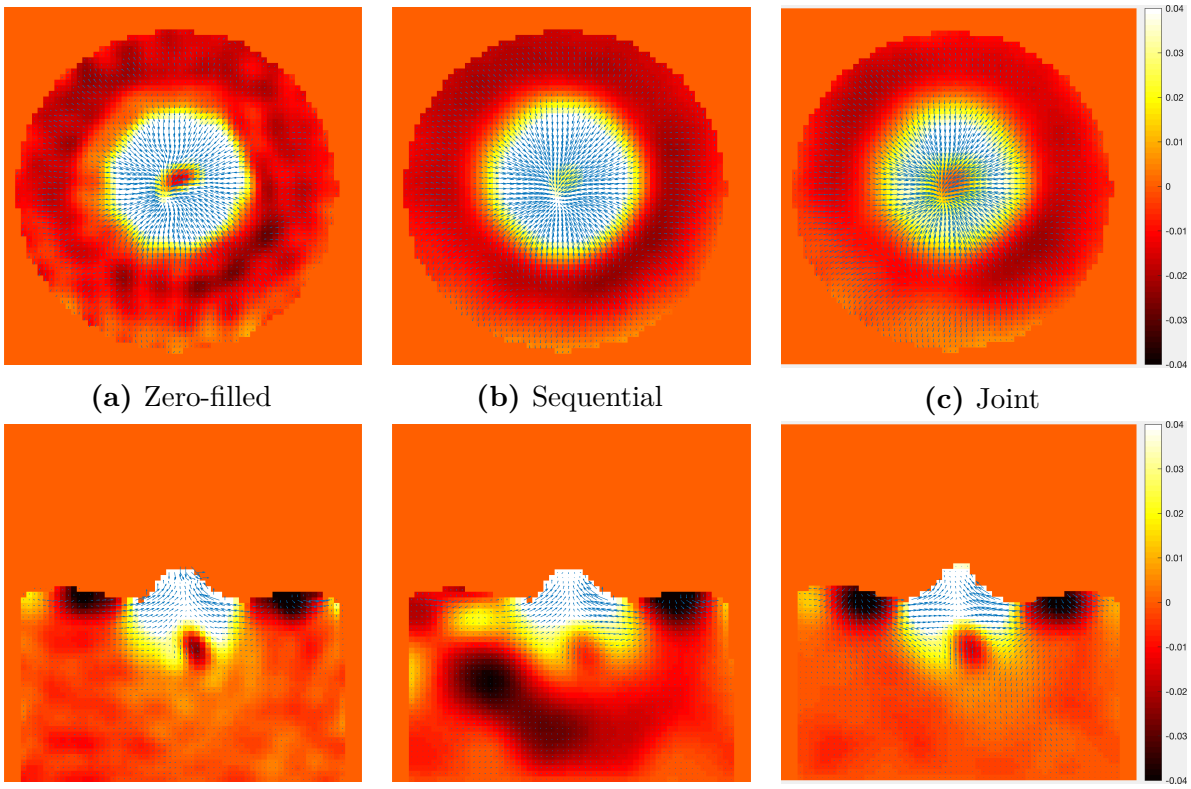


**(a)** Zero-filled **(b)** Sequential **(c)** Joint

**(d)** Zero-filled **(e)** Sequential **(f)** Joint

**Figure 4.3:** Phase reconstructions for the sequential approach and our joint approach compared to the zero-filling solution. Results for a bursting bubble from a transversal view (top row) and longitudinal view (bottom row).

at $t = 4$. After that, the jet falls down into the liquid pool, causing a downward jet and some oscillation. At around $t = 8$ the liquid motion stops.

## 4.5 Conclusion and Outlook

In this chapter we have presented a joint framework for flow estimation, magnitude reconstruction and segmentation from undersampled velocity-encoded MRI data. After having described the corresponding dynamic inverse problem, we have presented a joint variational model based on a non-convex Bregman iteration. We have demonstrated that by imposing regularity on the individual components (in contrast to the sequential approach), our joint method achieves accurate estimations of the velocities, as well as an enhanced magnitude reconstruction with sharp edges, thanks to the joint segmentation. Furthermore, we assessed the performance of our joint approach on synthetic and real

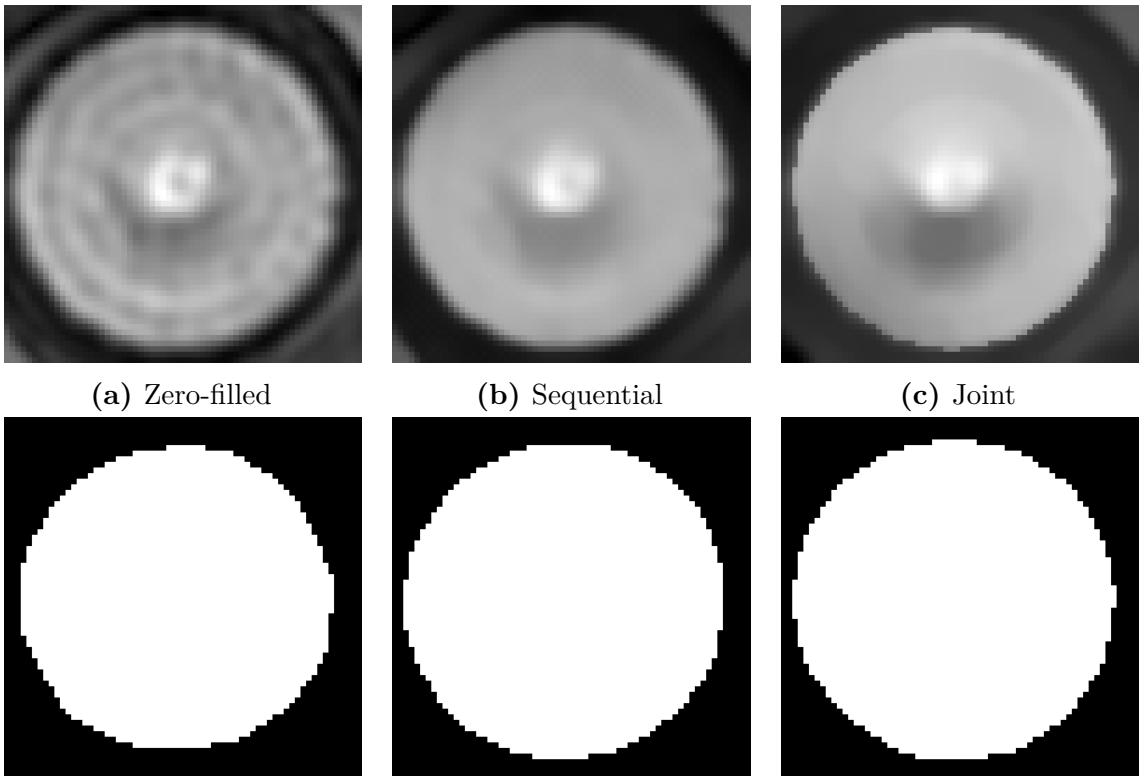

**(a)** Zero-filled **(b)** Sequential **(c)** Joint

**(d)** Zero-filled **(e)** Sequential **(f)** Joint

**Figure 4.4:** Magnitude reconstructions (top row) and corresponding segmentations (bottom row) for the sequential approach and our joint approach compared to the zero-filling solution. Transversal view.

data. In this context, we have shown that the joint model improves the performances of the different imaging tasks compared to the classical sequential approaches.

Future work includes the investigation of the full joint temporal and spatial optimisation. By extending the model to the full 4D setting, we believe the performance will be enhanced further, as temporal correlation e.g. in the segmentation can be exploited. The current limitation is the lack of such 4D dataset. Indeed, as described in the acquisition protocol, the velocity data was acquired separately for each spatial component to speed up the acquisition.

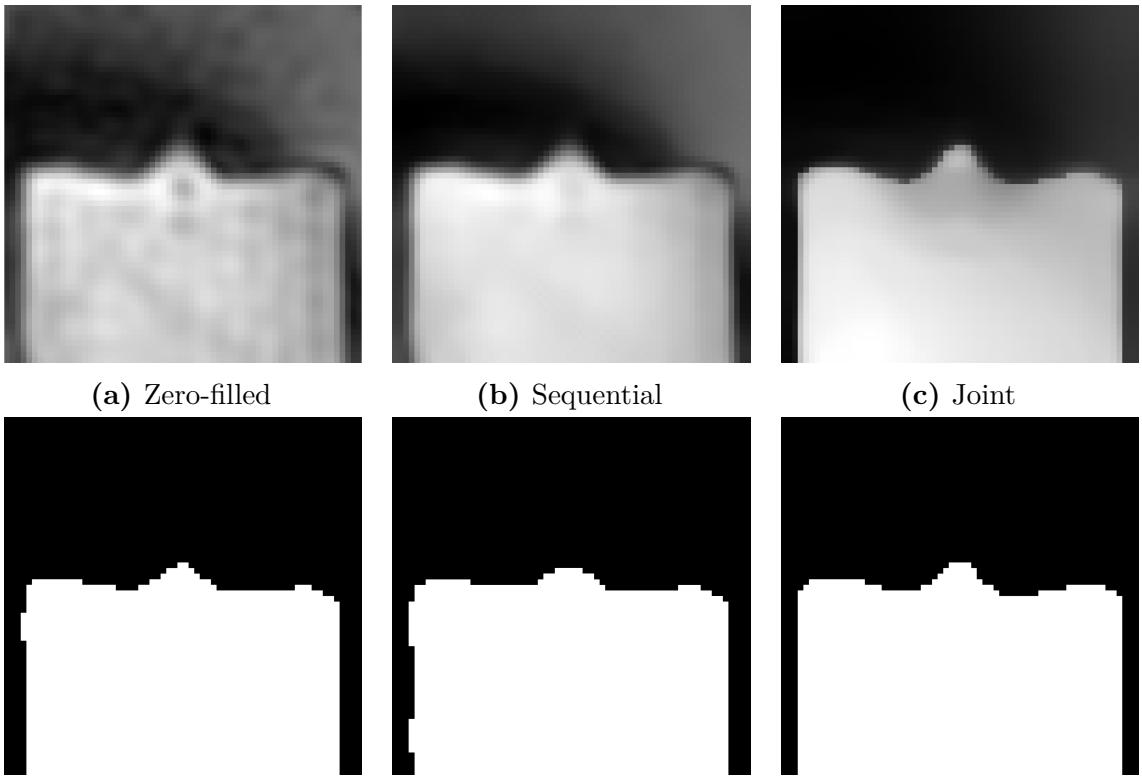

**(a)** Zero-filled **(b)** Sequential **(c)** Joint

**(d)** Zero-filled **(e)** Sequential **(f)** Joint

**Figure 4.5:** Magnitude reconstructions (top row) and corresponding segmentations (bottom row) for the sequential approach and our joint approach compared to the zero-filling solution. Longitudinal view.

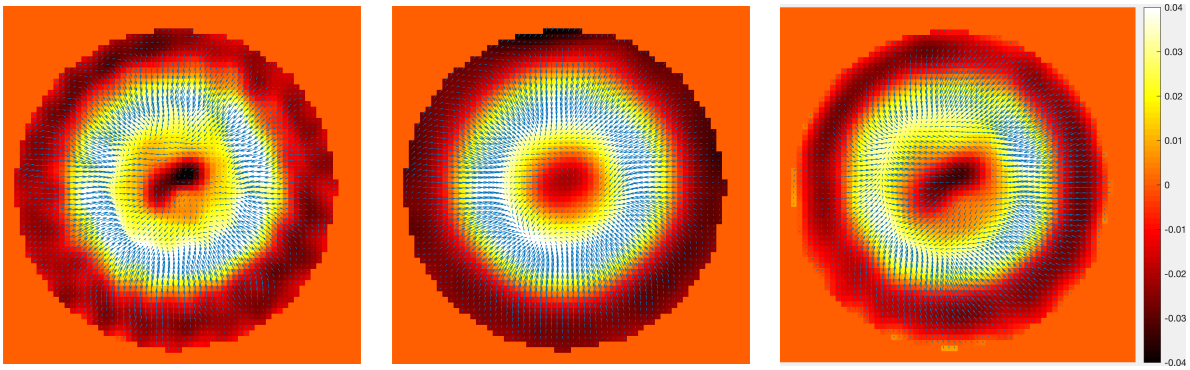


**(a)** Zero-filled **(b)** Sequential **(c)** Joint

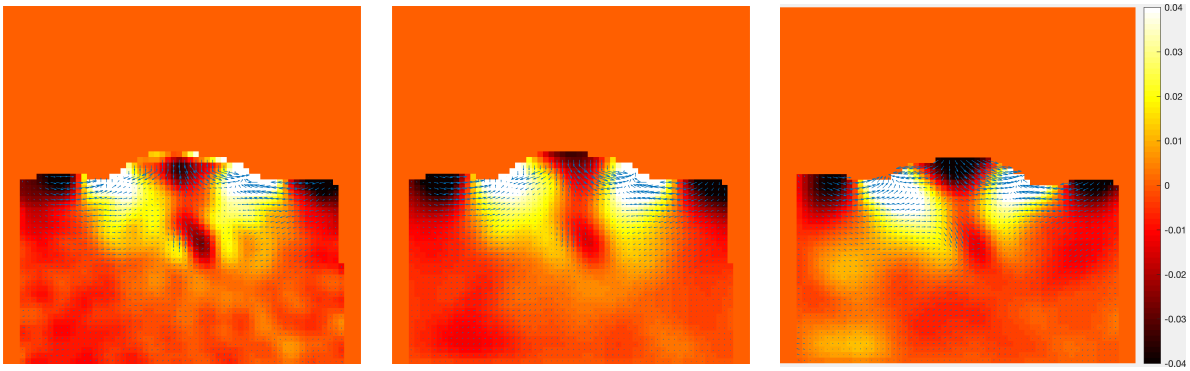


**(d)** Zero-filled **(e)** Sequential **(f)** Joint

**Figure 4.6:** Phase reconstructions for the sequential approach and our joint approach compared to the zero-filling solution. Top row: transversal view. Bottow row: longitudinal view.

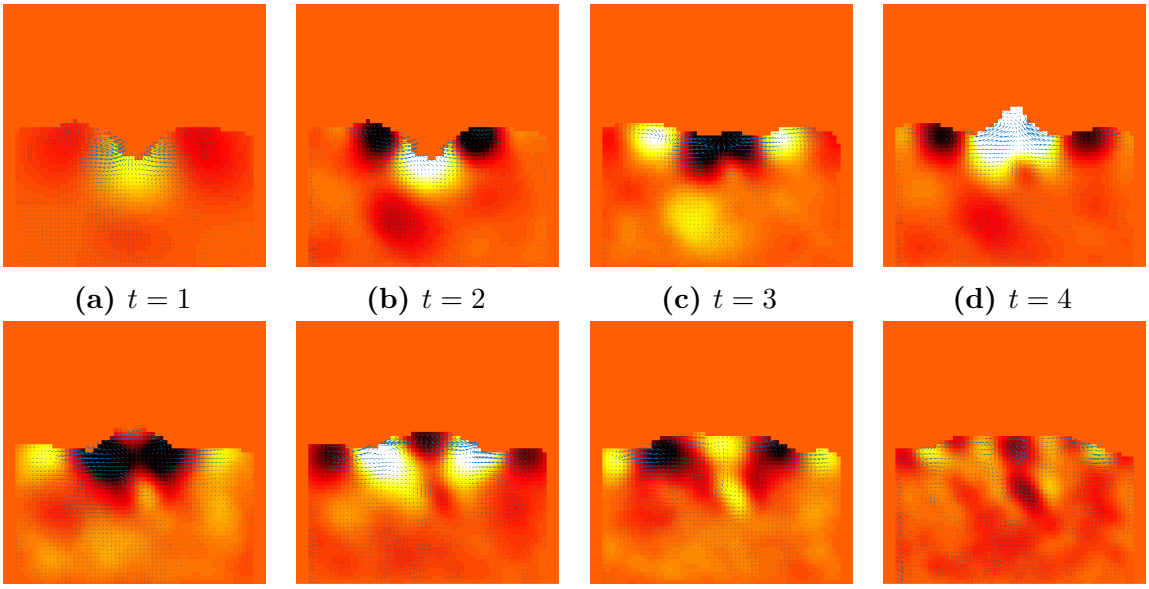

**(a)** $t = 1$ **(b)** $t = 2$ **(c)** $t = 3$ **(d)** $t = 4$

**(e)** $t = 5$ **(f)** $t = 6$ **(g)** $t = 7$ **(h)** $t = 8$

**Figure 4.7:** Full time sequence. Longitudinal view. The bubble burst event sees the bubble resting at the interface between liquid and air, before this film is finally broken. The bursting causes an upward jet that moves the liquid at its highest position at $t = 4$. Subsequently, the jet drops into a downward jet, causing oscillation in the liquid, until it finally dies out at $t = 8$.

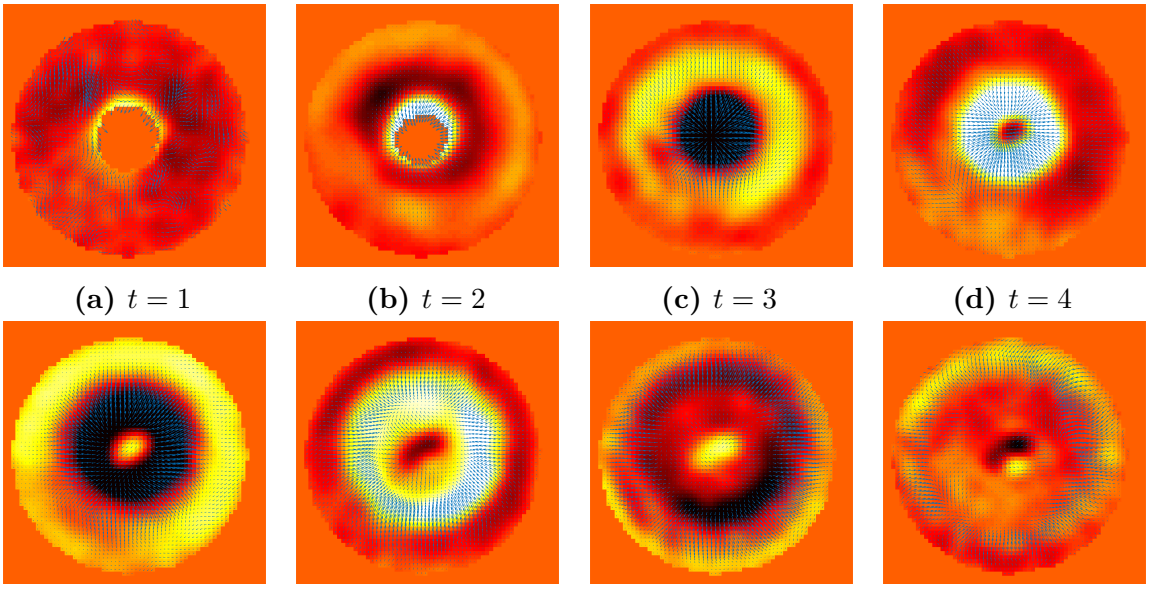

**(a)** $t = 1$ **(b)** $t = 2$ **(c)** $t = 3$ **(d)** $t = 4$

**(e)** $t = 5$ **(f)** $t = 6$ **(g)** $t = 7$ **(h)** $t = 8$

**Figure 4.8:** Full time sequence. Transversal view through the middle of the bubble. We can see the bubble burst event and the upward/inward jet caused by the empty space left by the bubble. Subsequently, the jet falls down into the liquid pool causing a downward/outward jet, until it dies out at $t = 8$.

# Chapter 5

# Multi-Task Model for Motion-Compensated MRI: Joint Reconstruction, Registration and Super-Resolution

In this chapter, we present a variational multi-task framework to solve three relevant tasks, namely image reconstruction, registration and super-resolution for the application of motion correction in MRI. This is joint work with Angelica I. Aviles-Rivero, Noémie Debroux, Martin J. Graves, Carole Le Guyader, Guy Williams and Carola-Bibiane Schönlieb and resulted in [CDAR+19, CARD+19a, CARD+19b]. Here, we focus on motion corrupted undersampled MRI data, which requires explicit motion compensation techniques to improve the image quality and provide clinically relevant information that can be used for diagnosis.

MRI is a widely used and non-invasive modality that creates detailed images of the anatomical structures of the human body, including undergoing physiological events. It allows radiologists to examine MRI for diagnosis, treatment monitoring and abnormality/disease detection [BSD15]. However, a central limitation of MRI is the prolonged acquisition period needed to reconstruct an image [ZMH15]. This constraint is reputed to be a major contributor to image quality degradation, and therefore, compromising the expert interpretation.

Image degradation appears as motion artefacts including blurring effects and geometric distortions [SMI+95, ZMH15]. Therefore, the problem of how to reduce the acquisition time whilst producing high quality images, super-resolved and motion-free, is of a great interest in the community, and it is the problem that we address in this chapter.

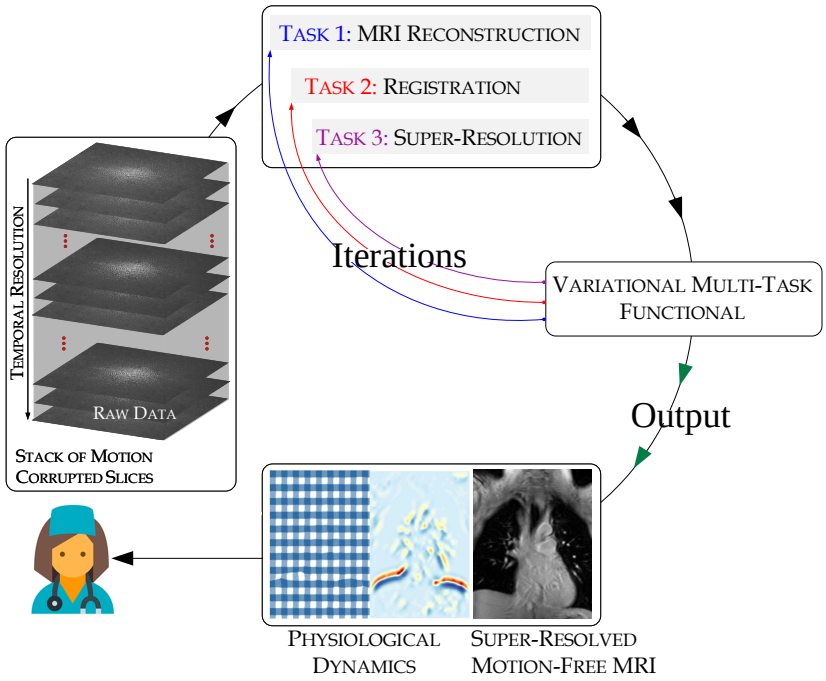


**Figure 5.1:** The proposed variational multi-task framework. A set of higly undersampled MRI measurements are taken as input to our three-tasks framework: reconstruction, registration and super-resolution. We then jointly address them using a proposed functional that has as input a super-resolved motion-free MRI and the physiological dynamics.

In particular, in a dynamic MRI setting, acquisitions with low signal-to-noise ratios or small anatomical structures might be severely degraded, affecting the final expert's outcome [HOM+17]. These small structures can appear smeared or blurred, and discerning whether these are artefacts or lesions is very challenging for the expert, leading to potential false positive or negative findings [ABMB+15]. Moreover, movement distortions are most prominent at contrast edges [BCB04].

Although, it is possible to reduce the artefacts by performing breath-holding techniques, there is still residual motion to be compensated. This is mainly produced because the timescale of physiological motion is shorter than the required time to form an image. Likewise, gating strategies [SFL00, PSR+01, KYK+01, GEO06, JIA06, KKVM00], which track either the breathing or cardiac cycles, have been also widely explored. However, they are mainly effective for perpetual breathing motion disregarding all other involuntary physiological motion and therefore only partially accurate. Furthermore, it is challenging to precisely co-register these signals to the corresponding MRI data [HST+06].

As an alternative to the aforementioned techniques, a body of research has developed several algorithmic approaches based on the conceptual definition of Compressed Sensing (CS) which has demonstrated promising results since the seminal paper of Lustig et

al. [LDP07]. The main idea of using CS is to reconstruct signals from low-dimensional measurements through iterative optimisation relying on sparsity of the image in a transformed domain. Since then, several promising results have been reported in the body of literature e.g. [Lia07], [LHDJ11a], [LHDJ11b], [OCS15], [ZPL15]. However, there is still a need for improving the quality of the MRI reconstruction whilst decreasing the number of measurements.

A commonality of previous techniques is that they perform a single task (just reconstruction). However in most recent years, there has been a great interest for improving medical image reconstruction [LDJ15, RdVCGSW+16, ARWGS18] by using what is called multi-tasking models (also known as joint models). The central idea of this perspective is that by sharing representation between tasks and carefully intertwining them, one can create synergies across challenging problems and reduce error propagation, which results in boosting the accuracy of the outcomes whilst achieving better generalisation capabilities.

Following the multi-task perspective, different works have been presented e.g. [LDJ15, RdVCGSW+16, OME+16, ARWGS18, BMMK+10, JF03]. Unlike existing approaches from the literature, and to the best of our knowledge, we are presenting for the first time a model that considers more than two tasks. In this work, we introduce a new variational multi-tasking framework that integrates, in a single model, three relevant tasks in MRI: reconstruction, registration and super-resolution (see Figure 5.1). Our contributions are described below:

**Contributions.** In this chapter, we present a new variational multi-tasking framework that combines, in a single model, three important tasks in MRI: reconstruction, registration and super-resolution. Whilst this is a relevant part of this work, our contributions are:

- We propose a computationally tractable and mathematically well-motivated variational multi-task framework for motion correction in MRI, in which our novelties largely rely on:
  - An original optimisation model that is composed of an $L^2$ fidelity term that allows sharing representations between three tasks (reconstruction, super-resolution and registration); a weighted total variation (TV) ensuring robustness of our method to intensity changes; a TV regulariser of the highly resolved reconstruction; and a hyperelasticity-based regulariser. We demonstrate that this combination yields to significant improvements over sequential models and existing multi-task methods.

  - We show that our optimisation problem can be solved efficiently by using auxiliary variables and then splitting it into sub-problems. We show that this requires lower CPU time than several methods from the body of literature.

- We extensively evaluate our approach using five datasets and different acceleration factors. We also compare our multi-task framework against existing approaches. Our experiments are further validated by interpretations of experts.

## 5.1 Related Work

There have been different attempts to improve motion correction in MRI from undersampled data. Besides motion prevention techniques such as breath-holding, another set of of algorithmic approaches has been devoted to do motion correction based on image-based motion tracking, where one needs an explicit estimation of the motion in between scans. The predominant scheme, in this context, is image registration which aims at finding a mapping aligning a moving image to a reference one. Following this perspective, the body of literature can be roughly classified on rigid (translations, rotations) and deformable registration.

In the first category, several approaches have been proposed including [GSB+03, ADS, WYW+08, JBC18]. However, physiological motion, such as cardiac and respiratory, can hardly be characterised by a simple combination of rotations and translations. To mitigate this limitation, motion correction methods based on deformable registration have been proposed such as [LCM07, LCKAM, LTC+15, JKV+17]. However, in a closer look on the aforementioned approaches, a commonality between them is that the algorithmic approaches are performed sequentially. That is - the motion estimation task is executed only after the image reconstruction is computed (from now we refer to this perspective as sequential model). A clear drawback of using this perspective is that the motion estimation highly depends on the quality of the reconstruction as well as on the selection of the reference image.

More recently, a body of research has solved jointly multiple tasks (the so-called multi-task approach) such as image reconstruction and registration in a unified framework. In particular, in the medical domain and following a variational perspective [BDS18], different works have been reported using multi-task approaches. These include SPECT imaging [MGS06, SMF09], PET [BMMK+10] and MRI [LDJ15, RdVCGSW+16, ARWGS18]- to name a few. The works with a closer aim to ours are discussed next.

Authors in [JF03] and [BMMK+10] proposed a joint model composed of a motion-aware likelihood function and a smoothing term for a simultaneous image reconstruction

and motion estimation for PET data. Schumacher et al. [SMF09] presented an algorithmic approach that combines reconstruction and motion correction for SPECT imaging. The authors proposed a variational approach that includes a regulariser that penalises an offset of motion parameter - to favour a mean location of the target object. However, the major limitation is that they only consider rigid motions. In the same spirit, authors of [SYC09, Fes10] proposed a generic joint reconstruction/registration framework. That model is based on a penalised-likelihood functional, which use a weighted least square fidelity term along with a spatial and a motion regulariser.

In the work of that Odille et al. [OME+16] proposed a joint model for MRI image reconstruction and motion estimation. This approach allows for an estimate of both intra and inter-image motion, meaning that, not only the misalignment problem is addressed but also it allows correcting for blurring/ghosting artefacts. More recently in the context of deep learning (DL), a number of methods has been investigated for image registration - e.g. [YKSN17, dVBV+17b]. Although, certainly, those approaches deserve attention, their review goes beyond the scope of this chapter.

## 5.2 Proposed Model

In this section, we introduce our joint variational framework which addresses simultaneously the following three tasks: MRI reconstruction, registration and super-resolution. We introduce the mathematical formulation as separated tasks and then we show how our novel optimisation model judiciously intertwines them. Finally, we describe the numerical realisation of our approach.

**Problem statement.** We remark to the reader the focus of this work. Given a set of multiple undersampled MR acquisitions $\{x_t\}_{t=1}^{T}$ of low resolution and corrupted by motion, we seek to recover a single high resolved, static and motion-corrected image that represents the true underlying anatomy along with the estimation of the breathing dynamics through deformation maps.

### 5.2.1 Task 1: CS MRI reconstruction

The first task in our multi-task framework is MRI reconstruction. In particular, in standard dynamic MRI, the acquired data is in a time-spatial-frequency space, i.e. *k,t*-space, which is composed of $x = (x_{m,t})_{m=1,t=1}^{M,T} \in \mathbb{C}^{M\times T}$ measurements. Therefore, the

task of MRI reconstruction, from those samples, reads:

$$x = \mathcal{A}u + \eta \tag{5.1}$$

where $\mathcal{A} : \mathbb{R}^{N\times T} \to \mathbb{C}^{M\times T}$ is the undersampled MRI forward operator. More precisely, $\mathcal{A} = \mathcal{S}\mathcal{F}$ where $\mathcal{S}$ is a subsampling operator, $\mathcal{F}$ the Fourier operator, and $\mathcal{A}^* : \mathbb{C}^{M\times T} \to \mathbb{R}^{N\times T}$ its adjoint. Moreover, $u \in \mathbb{R}^{N\times T}$ is the stack of reconstructed images, $\eta$ an additive Gaussian noise inherent to the acquisition, and $t$ the temporal coordinate.

The MRI reconstruction task is thus highly ill-posed due to the noise and incomplete measurements. However, (5.1) can be solved by adding prior information and then casting the problem as an CS-based optimisation problem as:

$$u^* \in \arg\min_u \|\mathcal{A}u - x\|_2^2 + \delta\|\Phi(u)\|_1, \tag{5.2}$$

where the first term, i.e. data fidelity term, ensures consistency in the observed data $x$ whilst $\|.\|_1$ enforces sparsity in the transformed domain given by $\Phi$, and $\delta$ is a parameter balancing the influence of each term.

In this work, we focus on the Total Variation (TV) regulariser [ROF92], which, imposing edge sparsity, leads to piecewise constant reconstructions. However one can easily replace this regulariser by any other one in a plug-and-play fashion.

Although a large body of literature has showed potential results in the context of undersampled MRI reconstruction using CS or its extended philosophies including [LHDJ11a, MW12, OCS15], there is a still room for improvement, and in particular, with the problem of reconstruction a single high quality image that reflects the true underlying anatomy.

In this context, our initial hypothesis was to model image reconstruction and registration in a unified framework, with the goal of obtaining a single, motion-corrected image from dynamic MRI. We published our first findings in [CDAR+19] and [CARD+19a]. The main idea was that by computing the reconstruction and registration tasks jointly one can exploit their strong correlation thus reducing error propagation and resulting in a significant motion correction. We use this as our basis to propose our model in [CARD+19a], which now exploits the natural correlation between motion estimation and super-resolution. This motivate the use of two more tasks − image registration and super-resolution, which are described next.

### 5.2.2 Task 2&3: When Image Registration Meets Image Super-Resolution

In a dynamic MRI setting, there are two tasks that show a natural strong correlation: motion estimation and super-resolution. Therefore, our hypothesis is that by unifying these two tasks, one can create synergies leading to error propagation reduction, and therefore, an increase of the image quality.

In a multi-frame variational framework, super-resolution is the problem of restoring a high-resolution image from several low quality images that are corrupted by motion. From a variational perspective, it can be expressed as:

$$\min_{u} \sum_{i=1}^{m} \| \mathcal{D}\mathcal{B}\mathcal{W}_{\mathrm{i}}\, u - f_i \|_2^2 + \lambda\, \mathrm{Reg}(u), \tag{5.3}$$

where $\mathcal{D}$ and $\mathcal{B}$ are the downsampling and blurring operators correspondingly. Moreover, $\mathcal{W}_{\mathrm{i}}$ models the geometric warp existing between the $m$ observed images $f_i$ and the restored image $u$ to correct for motion. Finally, $\mathrm{Reg}(u)$ is a generic regulariser. In this work, the dowsampling operator is modelled as an averaging window, the blurring kernel is assumed to be Gaussian, and the warping operator is viewed as the deformations from a registration task. Whilst for the regulariser we adopt the TV option, our approach is well-suited for the plug-and-play setting. That is- one can easily replace the TV regulariser with other options (some examples are mentioned in Subsection 2.2.4).

In particular, for our registration method we have the following. Let $\Omega$ be the image domain, i.e. a connected bounded open subset of $\mathbb{R}^2$, and $u : \Omega \to \mathbb{R}$ be the sought single reconstructed image depicting the true underlying anatomy. We introduce the unknown deformations, between the $t$-th acquisition and the image $u$, as $\phi_t : \bar{\Omega} \to \mathbb{R}^2$. We remark that the deformations are smooth mappings with topology preserving and injectivity properties. Moreover, let $v_t$ be the associated displacements such that $\phi_t = \mathrm{Id} + v_t$, where Id is the identity function. At the practical level, these deformations should be with values in $\bar{\Omega}$, and Ball's results [Bal81a] guarantee this property theoretically for our model. We also consider $\nabla\phi_t : \Omega \to M_2(\mathbb{R})$ to be the gradient of the deformation, where $M_2(\mathbb{R})$ is the set of real square matrices of order two.

As MRI images biological soft tissues well-modelled by hyperelastic materials, which allows for large and smooth deformations while keeping an elastic behavior, we propose to view the shapes to be matched in the registration process as isotropic, homogeneous and hyperelastic materials of Ogden type. For more details on this kind of materials, we

refer to [**?** ]. This is reflected in our formulation as a regularisation on the deformations $\phi_t$ based on the stored energy function of such a material.

In two dimensions, the stored energy function of an Ogden material, in its general form, is given by the following expression:

$$W_O(F) = \sum_{i=1}^{M} a_i \|F\|_F^{\gamma_i} + \Gamma(\det F), \tag{5.4}$$

with $a_i > 0$, $\gamma_i \geq 1$ for all $i = 1, \cdots, M$ and $\Gamma : ]0; \infty[ \to \mathbb{R}$ a convex function satisfying $\lim_{\delta \to 0^+} \Gamma(\delta) = \lim_{\delta \to +\infty} \Gamma(\delta) = +\infty$, $\|.\|_F$ designating the Frobenius matrix norm.

Following [CBE+19], we consider the particular energy:

$$W_{Op}(F) = \begin{cases} a_1 \|F\|_F^4 + a_2 \left(\det F - \frac{1}{\det F}\right)^4 & \text{if } \det F > 0, \\ +\infty \text{ otherwise,} \end{cases} \tag{5.5}$$

with $a_1 > 0$, and $a_2 > 0$. The first term penalises the changes in length, whilst the second term enforces small changes in area. We check that this function falls within the general formulation of the stored energy function of an Ogden material:

$$W_{Op}(F) = \tilde{W}(\xi, \delta) = \begin{cases} a_1 \|\xi\|^4 + a_2 \left(\delta - \frac{1}{\delta}\right)^4 & \text{if } \delta > 0, \\ +\infty & \text{otherwise,} \end{cases}$$

$\tilde{W} : M_2(\mathbb{R}) \times \mathbb{R} \to \mathbb{R}$ is continuous since $\lim_{\delta \to 0^+} \tilde{W}(\xi, \delta) = \lim_{\delta \to +\infty} \tilde{W}(\xi, \delta) = +\infty$, and is convex with respect to $\delta \left( g : \left| \begin{array}{c} \mathbb{R}_*^+ \to \mathbb{R} \\ x \mapsto \left(x - \frac{1}{x}\right)^4 \end{array} \right. \right.$ and $\left. g'' : \left| \begin{array}{c} \mathbb{R}_*^+ \to \mathbb{R} \\ x \mapsto 4\left(x - \frac{1}{x}\right)^2 \left(\frac{3x^4+4x^2+5}{x^4}\right) \geq 0 \end{array} \right. \right)$. The design of the function $\Gamma$ is driven by Ball's results [Bal81b] guaranteeing the deformation to be a bi-Hölder homeomorphism, and therefore, preserving the topology. It also controls that the Jacobian determinant remains close to one to avoid expansions or contractions that are too large.

### 5.2.3 Variational Multi-Task Model: Reconstruction, Registration and Super-Resolution

In the body of literature, there have been different attempts of using reconstruction, registration and super-resolution. However, they tackled the tasks separately or jointly but up to two tasks. In this part, we describe, for the first time, how these three tasks can be jointly computed to benefit the final reconstruction. The main idea is to exploit

temporal redundancy in the data to compensate for motion artefacts due to breathing and/or involuntary movements whilst increasing the resolution to retrieve finer details in the reconstruction. In particular, we now turn to describe how (5.2) and (5.3) can be solved in a multi-task framework.

Our variational multi-task framework takes three key factors: firstly the hyperelastic regulariser (5.5), secondly a discrepancy measure that joins the reconstruction, super-resolution and the registration tasks, and the TV-based regularisers for reconstruction and super-resolution. Moreover, our model accounts for intensity changes, this, by modifying the CS-classical TV regulariser for the weighted TV to enforce edge alignment. From now $\mathcal{A}$ is acting on one single frame. We thus introduce weights $g_t$ as the Canny edge detector applied to $G_\sigma * \mathcal{A}^* x_t$ - for each $t = 1, \cdots, T$ - where $G_\sigma$ is a Gaussian filter of variance $\sigma$. We follow Baldi's arguments ([Bal01]) to introduce the weighted $BV$-space and the associated weighted total variation related to the weight $g_i$, for each $i = 1, \cdots, T$. Let $w$ be a weight function satisfying some properties (defined in [Bal01] and fulfilled here by $g_i$). We denote by $\mathrm{BV}_w(\Omega)$ the set of functions $u \in L^1(\Omega, w)$, which are integrable with respect to the measure $w(x)dx$, such that:

$$\sup \left\{ \int_\Omega u \mathrm{div}(\varphi)\, dx \ : \ |\varphi| \leq w \text{ everywhere }, \ \varphi \in Lip_0(\Omega, \mathbb{R}^2) \right\} < +\infty,$$

with $Lip_0(\Omega, \mathbb{R}^2)$ the space of Lipschitz continuous functions with compact support. We denote by $TV_w$ the previous quantity.

Given $A$ a bounded open set in $\mathbb{R}^2$, with boundary of class $\mathscr{C}^2$, then we have $\mathrm{TV}_{g_i}(\xi_A) = |\partial A|(\Omega, g_i) = \int_{\Omega \cap \partial A} g_i \, dH^1$, where $\xi_A$ is the characteristic function of the set $A$. This quantity can be viewed as a new definition of the curve length- with a metric depending on the observations $x_i$. Minimising it is equivalent to locating the curve on the edges of $\mathcal{A}^* x_i$ where $g_i$ is close to 0. We thus consider the following fidelity term and regulariser for our high-resolved image:

$$\begin{aligned} E(u, (\phi_t)_{t=1,\cdots,T}) &= \frac{1}{T} \sum_{t=1}^{T} \delta \, \mathrm{TV}_{g_t}((\mathcal{C}u) \circ \phi_t^{-1}) \\ &+ \alpha \, \mathrm{TV}(u) + \frac{1}{2} \| \mathcal{A}((\mathcal{C}u \circ \phi_t^{-1})) - x_t \|_2^2, \end{aligned} \tag{5.6}$$

where $\mathcal{C} = \mathcal{D}\mathcal{B}$ comes from the super-resolution formulation. The first term of $E$ seeks to align the edges of the deformed reconstruction $((\mathcal{C}u) \circ \phi_t^{-1}))$ with the ones of the different acquisitions, whilst regularising it. The second quantity aims to get $\mathcal{A}((\mathcal{C}u) \circ \phi_t^{-1})$ close to the acquisitions $x_t$, and thus $\mathcal{A}^*(x_t)$ close to $\mathcal{C}u \circ \phi_t^{-1}$ to correct for motion.

Our variational multi-task framework is then defined as a combination of (5.5) and (5.6), which leads to the following minimisation problem:

$$\begin{aligned} &\inf_{u,(\phi_t)_{t=1,\cdots,T}} G(u,(\phi_t)_{t=1,\cdots,T}) = E(u,(\phi_t)_{t=1,\cdots,T}) \\ &+ \frac{1}{T}\sum_{t=1}^{T}\int_\Omega W_{Op}(\nabla\phi_t)\,dx, \\ \Leftrightarrow &\inf_{u,(\phi_t)_{t=1,\cdots,T}} \frac{1}{T}\sum_{t=1}^{T}\frac{1}{2}\|\mathcal{A}((\mathcal{C}u)\circ\phi_t^{-1}) - x_t\|_2^2 + \alpha\,\mathrm{TV}(u) \\ &+ \delta\,\mathrm{TV}_{g_t}((\mathcal{C}u)\circ\phi_t^{-1}) + \int_\Omega W_{Op}(\nabla\phi_t)\,dx, \end{aligned} \tag{5.7}$$

We now introduce the next theorem to set the well-posedness of our model.

**Theorem 5.1** (Existence of minimisers)**.** *Let $\mathcal{A} = \mathcal{SF} : L^2(\mathbb{R}^2) \to L^2(\mathbb{R}^2)$, $\mathcal{C} : L^1(\Omega') \to L^p(\Omega)$, be linear bounded and continuous for the strong topology operators with $p \in ]1, \frac{8}{5}[$, and $\Omega \subset \Omega'$, $\Omega$ and $\Omega'$ connected bounded open subsets of $\mathbb{R}^2$ with boundaries of class $\mathcal{C}^1$ (verified by the chosen operators). With $\delta$, $\alpha$, $a_1$, $a_2 > 0$, problem (5.7) admits minimisers $(\bar{u}, (\bar{\phi}_t)_{t=1,\cdots,T})$ on $\mathscr{U} = \{u \in BV(\Omega'),\ \phi_t \in \mathscr{W},\ \forall t = 1,\cdots,T \,|\, (\mathcal{C}u)\circ\phi_t^{-1} \in BV_{g_t,0}(\Omega),\ \forall t \in \{1,\cdots,T\}\}$, with $\mathscr{W} = \{\psi \in Id + W_0^{1,4}(\Omega,\mathbb{R}^2) \,|\, \det\nabla\psi \in L^4(\Omega),\ \frac{1}{\det\nabla\psi} \in L^4(\Omega),\ \det\nabla\psi > 0$ a.e. on $\Omega\}$.*

*Proof.* The proof can be found in Section C.3. □

In the next section, we detail how the proposed model (5.7) can be solved in a computational tractable form.

## 5.3 Optimisation

The numerical realisation of (5.7) imposes different challenges due to the nonlinearity and nonconvexity in $\nabla\phi_t$ and the composition $(\mathcal{C}u)\circ\phi_t^{-1}$ in the fidelity term. In this work, we overcome this difficulties by introducing three auxiliary variables $z_t$, $h_t$, $f_t$, this, to mimic $\nabla\phi_t$, $(\mathcal{C}u)\circ\phi_t^{-1}$ and $h_t$. We then relax our problem using quadratic penalty terms. This leads to the following discretised decoupled problem:

$$\begin{aligned}\min_{u,\phi_t,z_t,h_t,f_t} \frac{1}{T}\sum_{t=1}^{T}\sum_{x\in\Omega} & W_{Op}(z_t(x)) + \frac{\gamma_1}{2}\|z_t - \nabla\phi_t\|_2^2 \\ & + \frac{\gamma_3}{2}\|\mathcal{A}h_t - x_t\|_2^2 + \alpha\,\mathrm{TV}(u) \\ & + \frac{\gamma_2}{2}\|(h_t - (\mathcal{C}u)\circ\phi_t^{-1})\sqrt{\det\nabla(\phi_t)^{-1}}\|_2^2 \\ & + \frac{1}{2\theta}\|f_t - h_t\|_2^2 + \mathrm{TV}_{g_t}(f_t).\end{aligned} \tag{5.8}$$

We now can solve our minimisation problem by splitting (5.8) into five more computational tractable problems. We now turn to give more details on each sub-problem.

**Sub-problem 1: Optimisation over $z_t$.** In practice, $z_t = (z_{t,1}, z_{t,2})^T$ simulates the gradient of the displacements $v_t = (v_{t,1}, v_{t,2})^T$ associated to the deformations $\phi_t$. For every $z_t$, we have $z_t = \begin{pmatrix} z_{11} & z_{12} \\ z_{21} & z_{22}\end{pmatrix}$. For the sake of readability, we drop here the dependency on $t$. We solve the Euler-Lagrange equation with an $L^2$ gradient flow and a semi-implicit finite difference scheme and update $z_t$ as:

$$\begin{aligned}
z_{11}^{k+1} &= \frac{1}{1+dt\gamma_1}\left(z_{11}^k + dt(-4a_1\|I + z_t^k\|_F^2(z_{11}^k+1) - 4a_2(1+z_{22}^k)c_0c_1 + \gamma_1\frac{\partial v_{t,1}^k}{\partial x}\right),\\
z_{12}^{k+1} &= \frac{1}{1+dt\gamma_1}\left(z_{12}^k + dt(-4a_1\|I + z_t^k\|_F^2 z_{12}^k + 4a_2 z_{21}^k c_0c_1 + \gamma_1\frac{\partial v_{t,1}^k}{\partial y}\right),\\
z_{21}^{k+1} &= \frac{1}{1+dt\gamma_1}\left(z_{21}^k + dt(-4a_1\|z_t^k + I\|_F^2 z_{21}^k + 4a_2 z_{12}^k c_0c_1 + \gamma\frac{\partial v_{t,2}^k}{\partial x}\right),\\
z_{22}^{k+1} &= \frac{1}{1+dt\gamma_1}\left(z_{22}^k + dt(-4a_1\|I + z_t^k\|_F^2(z_{22}^k+1) - 4a_2(1+z_{11}^k)c_0c_1 + \gamma_1\frac{\partial v_{t,2}^k}{\partial y}\right),
\end{aligned}$$

with $c_0 = \left(\det(I+z_t^k) - \frac{1}{\det(I+z_t^k)}\right)^3$ and $c_1 = 1 + \frac{1}{(\det(I+z_t^k))^2}$.

**Sub-problem 2: Optimisation over $\phi_t$.** We solve the Euler-Lagrange equation in $\phi_t$, after making the change of variable $y = \phi_t^{-1}(x)$ in the $L^2$ penalty term, for all $t$, using an $L^2$ gradient flow scheme with a semi-implicit Euler time stepping.

$$0 = -\gamma_1\Delta\phi_t^{k+1} + \gamma_1\begin{pmatrix}\operatorname{div} z_{t,1}^{k+1} \\ \operatorname{div} z_{t,2}^{k+1}\end{pmatrix} + \gamma_2(h_t^k\circ\phi_t^k - \mathcal{C}u^k)\nabla h_t^k(\phi_t^k),$$

**Sub-problem 3: Optimisation over $h_t$.** The update in $h_t$, for all $t$, has a closed form solution using the subsampling operator $\mathcal{S}$ and the Fourier operator $\mathcal{F}$ along with their adjoints $\mathcal{S}^*$ and $\mathcal{F}^* = \mathcal{F}^{-1}$:

$$h_t^{k+1} = \mathcal{F}^* \Bigg\{ (\gamma_2 \det \nabla (\phi_t^{-1})^{k+1} \mathrm{Id} + \gamma_3 \mathcal{S}^* \mathcal{S} + \frac{1}{\theta} \mathrm{Id})^{-1} \\ \left( \mathcal{F} \Big( \gamma_2 \det \nabla (\phi_t^{-1})^{k+1} (\mathscr{C} u^k) \circ (\phi_t^{-1})^{k+1} + \frac{f_t^k}{\theta} \Big) + \gamma_3 \mathcal{S}^* x_t \right) \Bigg\}.$$

**Sub-problem 4: Optimisation over $f_t$.** This is solved via Chambolle projection algorithm [Cha04]. For an inner loop over $n = 1, \cdots, M$:

$$f_t^{n+1} = h_t^{k+1} - \theta \operatorname{div} p_t^n, \\ p_t^{n+1} = \frac{p_t^n + \delta_t \nabla (\operatorname{div} p_t^n - h_t^{k+1}/\theta)}{1 + \frac{\delta_t}{g_t} \| \nabla (\operatorname{div} p_t^n - h_t^{k+1}/\theta) \|},$$

with $\|.\|$ the Euclidean norm. After enough iterations, we set $f_t^{k+1} = f_t^{n+1}$.

**Sub-problem 5: Optimisation over $u$.** Finally, using the same change of variables as in sub-problem 2, the problem in $u$ reads

$$\min_u \frac{\gamma_2}{2T} \sum_i^T \| h_t \circ \phi_t - (\mathcal{C} u) \|_2^2 + \alpha \operatorname{TV}(u),$$

and we solve it with a primal-dual algorithm [CP11a]:

$$y^{k+1} = \frac{y^k + \sigma \nabla u^k}{\max(1, \| y^k + \sigma \nabla u^k \|)}, \\ u^{k+1} = \left( \frac{\gamma_2}{T} \mathcal{C}^* \mathcal{C} + \mathrm{Id} \right)^{-1} \left( u^k + \tau \nabla \cdot y^{k+1} + \frac{\gamma_2}{T} \mathcal{C}^* \sum_{t=1}^T h_t^{k+1} \circ \phi_t^{k+1} \right).$$

We remark that, in this work, we solve the registration problem in $z_t$ and $\phi_t$ in a multi-scale framework from coarser to finer grids and using a regridding technique [CRM96a] described in Algorithm 2. The latter ensures topology preservation even though theoretically the design of the regulariser guarantees positivity of the Jacobian determinant. Finally, our proposed algorithm is illustrated in Algorithm 3.

**Algorithm 2:** Regridding algorithm

**Input:** $z^0 = 0$, $\phi^0 = \mathrm{Id}$, $regrid\_count = 0$.
**for** $n = 1, \cdots, N$ **do**
  Update $z^n$ and $\phi^n$.
  **if** $det \nabla \phi^n < tol$ **then**
    $regrid\_count = regrid\_count + 1$.
    $h = h \circ \phi^{n-1}$.
    Save $tab\_phi(regrid\_count) = \phi^{n-1}$.
    $\phi^n = \mathrm{Id}$, $z^n = 0$.
  **end if**
**end for**
**if** $regrid\_count > 0$ **then**
  $\phi^{final} = tab\_phi(1) \circ \cdots \circ tab\_phi(regrid\_count)$.
**end if**

**Algorithm 3:** Our Proposed Multi-task Method

**Input:** $\phi_t = Id$, $z_t = 0$, $h_t = u$, $f_t = u$, $t = 1, \cdots, T$, $u = \mathcal{F}^* x_1$.
**for** $k = 1, \cdots, nbIter$ **do**
  **for** $t = 1, \cdots, T$ **do**
    **for** *scale=coarse to fine* **do**
      Solve sub-problems 1 and 2 for $z_{t,scale}^{k+1}$ and $\phi_{t,scale}^{k+1}$ including the regridding step.
    **end for** Solve sub-problem 3.
    Solve sub-problem 4.
  **end for**
  Solve sub-problem 5.
**end for**

### 5.3.1 Parameters Reasoning

In this section, we discuss the influence of each parameter. The parameters $a_1$ and $a_2$ control the regularisation of the deformations. Whilst the former acts on the smoothness of the deformations, the latter can be seen as a measure of rigidity. That is- the bigger $a_2$ is, the more rigid the deformations are and the less accurate the registration becomes. It thus behaves as a trade-off between the ability to handle large and nonlinear deformations, and topology preservation.

Moreover, $\gamma_1$ and $\gamma_2$ are chosen big, to ensure the closeness of the auxiliary variables to the original ones, and $\theta$ is set small for the same purpose. $\gamma_3$ weights the fidelity term joining the three tasks, and it is often chosen to be close to 1. Finally, $\alpha$ offers a balance between regularity and fidelity to the data for the super-resolved reconstructed image $u$.

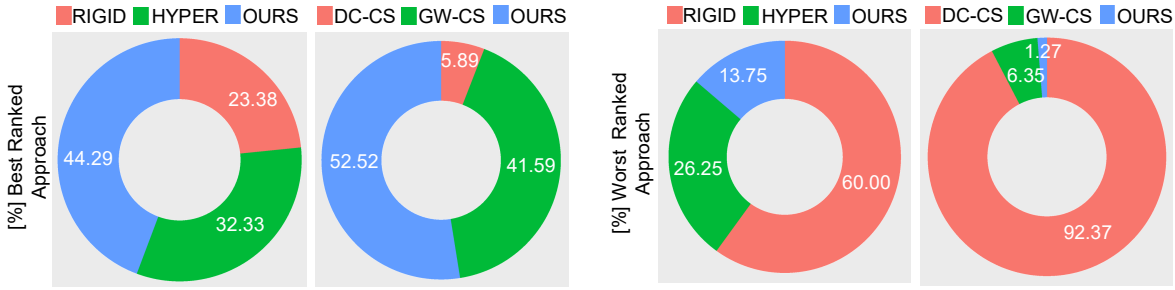


**(a)** % Best ranked approach **(b)** % Worst ranked approach

**Figure 5.2:** User study results (in %) indicating the level of agreement of clinicians for sequential and multi-task comparisons. (a) The majority indicates that our proposed reconstructions ranked the best. (b) Plot displays the percentage of responses indicating the worst ranked approach. This further supports the overall agreement of clinicians, favouring our approach.

## 5.4 Numerical Results

In this section, we present the experimental results performed to validate our proposed approach.

### 5.4.1 Data Description

We evaluate our framework on five publicly available datasets.

- **Dataset 1,2 & 3**[1]. These datasets are 2D T1-weighted data [BKM+17] acquired during free breathing of the entire thorax. It was acquired with a 3T Philips Achieva system with matrix size = $215 \times 173$, slice thickness=8mm, TR=3.1ms and TE=1.9ms. We remark that each dataset refers to three different patients.
- **Dataset 4 & 5**[2]. The datasets are 4DMRI data acquired during free-breathing of the right liver lobe [vSSG+07]. It was acquired on a 1.5T Philips Achieva system, TR = 3.1 ms, coils =4, slices =25, matrix size = $195 \times 166$, over roughly one hour on 22 to 30 sagittal slices and a temporal resolution of $2.6 - 2.8$ Hz.

### 5.4.2 Evaluation Protocol

To validate our theory, we expensively evaluate our model as follows.

**Comparison against Sequential Models.** For the first part of our evaluation, we compared our variational multi-task approach against two well-known models, *rigid*

[1] https://zenodo.org/record/55345#.XBOkvi2cbUZ
[2] http://www.vision.ee.ethz.ch/~organmot/chapter_download.shtml

(RIGID), and *hyperelastic* (HYPER), for deformations. To run this comparison, we solve the CS reconstruction model with TV, and then register all the frames to a reference frame used as initialisation in our proposed approach. For this, we use the well-established FAIR toolbox [Mod09], where we select rigid and hyperelastic transformations. Finally, we perform the super-resolution task with TV.

**Comparison against other Multi-task Approaches.** As to the best of our knowledge, this is the first variational model joining three tasks, we compare our model against two models that only joints two tasks- reconstruction and the motion estimation. More precisely, we compared our method against DC-CS [LDJ15] and GW-CS [RdVCGSW+16]:

- DC-CS: This approach solves a CS reconstruction and performs an elastic deformation Demons registration. After reconstructing the full sequence, we compute the average image for our analysis.
- GW-CS: this approach solves a CS reconstruction and performs a non-rigid group wise registration (GW) based on B-splines. After reconstructing the full sequence, we compute the average image for our analysis.

To show robustness and generalisation capabilities of our approach, we ran the comparisons using fully sampled data and acceleration factors $= \{2, 4, 5, 6, 8\}$.

**Metrics Evaluation.** As we seek to recover a single high resolved and motion corrected image, there is not ground truth for this task. Therefore, our evaluation is based on a standard protocol for evaluating MRI reconstruction, that is a user-study (expert scoring). For this, we design a a three-point Likert rating scale in which experts were asked to indicate the level of agreement, ranging from *best reconstruction to worst reconstruction*. The study is also supported by a nonparametric statistical test. Detailed protocol can be found in Section C.2. Moreover, to further support our multi-task model, we also offer CPU time comparison against all the compared approaches.

The experiments reported in this section were run under the same conditions in a CPU-based Matlab implementation. We used an Intel core i7 with 4GHz and a 16GB RAM.

### 5.4.3 Parameter Selection

In our experiments, we set the parameter of our approach and the compared ones as described next. For our experiments, we set the parameters as displayed in Table 5.1. Whilst for the sequential approaches, based on the FAIR implementation, we set the

| | $a_1$ | $a_2$ | $\gamma_1$ | $\gamma_2$ | $\gamma_3$ | $\theta$ | $\sigma$ | $k$ | $N$ | $n$ | $\alpha$ |
|---|---|---|---|---|---|---|---|---|---|---|---|
| D1 | 1 | 50 | 5 | $10^5$ | 15 | 5 | 1.5 | 2 | 500 | 500 | 0.01 |
| D2 | 1 | 50 | 5 | $10^5$ | 15 | 5 | 1.5 | 2 | 500 | 500 | 0.01 |
| D3 | 1 | 50 | 5 | $10^5$ | 15 | 5 | 1.5 | 2 | 500 | 500 | 0.01 |
| D4 | 1 | 100 | 1 | $10^5$ | 1 | 5 | 2 | 2 | 500 | 500 | 0.001 |
| D5 | 1 | 100 | 1 | $10^5$ | 1 | 5 | 2 | 2 | 500 | 500 | 0.001 |

**Table 5.1:** Parameter values used for our model and for all datasets. In this table, "D" stands for Dataset.

hyperelastic regularisation parameter for Datasets 1,2 & 3 = 1 and for Datasets 4 & 5 = 0.1.

### 5.4.4 Results and Discussion

We evaluate our proposed approach following the scheme described in Subsection 5.4.2. For the sake of compactness, we show results for Dataset 4 in Appendix C.

▷ **Is our Multi-tasking Approach Better than a Sequential one?**

We start evaluating our approach against two sequential models. We remark to the reader that sequential means to execute tasks (reconstruction registration and super-resolution) one after another. In particular, we compared our approach against two well-known models for deformations: rigid (RIGID) and hyperelastic (HYPER). Results of this comparison are displayed in Figure 5.6-5.9, and using different acceleration factors.

In a closer look at those Figures, one can see that our reconstructions have better sharp edges and retrieve fine details, in the heart and below the lung areas, than the sequential approaches. Particularly, the rigid transformation is not able to compensate for the whole motion and thus blurring effects are visible, especially under the lungs, for all acceleration factors. Hyperelastic deformations however, have more degrees of freedom and are capable of better compensating for motion which is manifested as sharp edges in the HYPER reconstruction. Moreover, the darker structure, at the center bottom of the heart, disappears or is much less visible in the HYPER reconstructions than in our approach. This effect is observed for all acceleration factors.

Besides, as the acceleration factor increases, the HYPER reconstruction loses the initial contrast, which is particularly visible for the acceleration factor of 8. In constrast our multi-task framework is able to preserve it nicely. This shows the robustness of our method to noise and corrupted data. The benefits of our multi-task framework is prevalent to all datasets.

Figure 5.6-5.9 show that hyperelastic deformations are better suited to deal with complex physiological motions, as the RIGID reconstructions exhibits strong blurring artefacts, this, due to residual movements amplified as the acceleration factor increases. Also, our method is able to preserve small structures in the kidney and the white blood vessels in the liver even for large acceleration factors contrary to the sequential HYPER approach. For the acceleration factor of 8, the HYPER reconstruction suffers more from staircaising effects than our approach and loses the initial contrast.

Overall, we can show that sharing representation between tasks (i.e. our multi-task approach) leads to better MRI reconstructions than if one perform the task separately. This is strongly supported by two factors, the computational time and the expert agreement. Following common protocol for MRI evaluation, we performed a user-study, in which we asked twelve experts (radiologist trainees and experienced) to evaluate reconstructions with all acceleration factors Figure 5.6 - 5.9.

The outcome is displayed in Figure 5.2. At left side of Figure 5.2a, one can see that overall (i.e. for all reconstruction/all acceleration factors) our approach was ranked best, with a 44.29% of agreement, in comparison with the output from the other methods. We also ran the nonparametric Friedman test, per acceleration and therefore accounting for FDR, and we found that there is significant statistical difference- that is, our approach offered the best reconstructions. Additionally, in Figure 5.2b, we display the results in terms of % worst ranked for all compared approaches.

▷ **Is it Three-Task Better Than Two-Task Framework?** In a multi-task framework a key factor is to assess if the tasks are not affecting negatively the final MRI reconstruction. To evaluate this factor, we ran a set of experiments of our approach against two multi-task frameworks DC-CS [LDJ15] and GW-CS [RdVCGSW+16]. These approaches perform only two-tasks (reconstruction and motion estimation), these approaches are our baselines as, to the best of our knowledge, there exist no approaches that joint three tasks.

The MRI reconstruction from our model against DC-CS and GW-CS can be seen in Figure 5.10-5.13. In a closer look at these figures, one can observe very blurred reconstructions from DC-CS, which can be interpreted as a failure of the model to capture the complex intrinsic nature of physiological motions. In contrast, GW-CS and our reconstructions are sharper even for very low undersampling factors and compensate well for motion.

However, our method is more robust to noise and outliers (as displayed in the compared reconstructions). Although, the GW-CS reconstructions preserve fine textures

and small structures, they are noisier than ours. That is, our approach preserve improves in terms of preserving information whilst removing noise in comparison with GW-CS. This effect is elevated even more as the acceleration factor increases. For example, for an acceleration factor of 8, artefacts and noise are visible in the heart and under the lungs in the GW-CS reconstruction whereas ours is clearer.

Another example of the good performance of our approach can be seen in Figure 5.10-5.12, in which we are able to retrieve more clinically useful texture and fine details than the GW-CS technique. This is particularly visible in the central part of the heart where noise is visible in the GW-CS reconstructions especially as the acceleration factor increases.

To further support our results, we display, at the right side of Figure 5.2a, the overall outcome of the user-study. From this plot, we can see that the majority of the expert agreed that our reconstructions are better than the compared approaches. Although, the second best ranked is GW-CS, it fails to correct for noise which compromises the readability of the underlying texture. Moreover, as soon as the acceleration factor increases, the noise level jumps, reducing drastically the readability and interpretability of the GW-CS reconstructions whereas our method retrieves relevant small structures and denoises the reconstruction. Again, we also report for the comparison to joint approach the results of the user study for the worst ranked approach in Figure 5.2b (right), which further supports the agreement to favour our proposed method.

▷ **The CPU Cost of Our Multi-Tasking Approach - Does It Pay Off?**
From previous sections, we demonstrated that our approach achieves a better reconstruction in comparison with other approaches, however, does it improvement come to pay off in terms of computationa time? Therefore, in this section, we highlight the computational advantages of our model. We remark to the reader that all comparisons were run under the same conditions.

The CPU time, for all approaches, is displayed at Figure 5.3 for several acceleration factors. Firstly, we observe that, in terms of sequential models, our model outperforms RIGID and HYPER reporting the lower CPU time. However and in terms of the other multi-task methods, the computational time for GW-CS is much longer compared to our method (and only performing two-tasks). Whilst the DC-CS approach readily competes with our approach, from the image quality standpoint our method offers by far better results in terms of reconstruction. We emphasise that the CPU times for our model and DC-CS are still on the same range, but the proposed method is performing three-tasks instead of two like the DC-CS. These advantages highlight our optimisation scheme that allows computing a complex problem in a very computational tractable form.

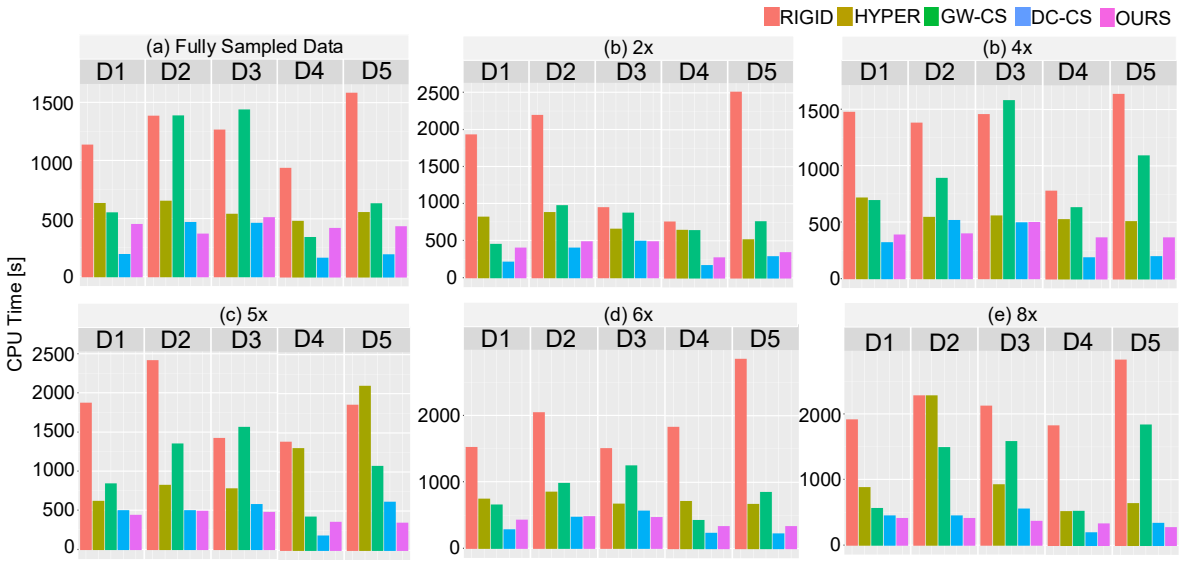


**Figure 5.3:** Computational performance comparison between sequential (three tasks), joint (two tasks) and our approach. Elapsed time in seconds. The sequential approaches are definitely much slower than our proposed method. We can see that our approach is comparable and competitive with joint approaches although slightly slower than the DC-CS, which, however, only computes two tasks.

### ▷ Further Analysis of Our Approach

To further support our model performance, we also analyse the difference maps to assess the quality of our registration, and therefore, its motion correction potential. To do this, we inspect the uncorrected average of the difference image, between a reference frame and each individual one, which is displayed at the left side of Figure 5.4. From this column, we can observe that the motion is significant in both the datasets. However, when we inspect the mean difference between our reconstruction and the individual registered acquisitions ($h_t \circ \phi_t$), at the middle and right sides of Figure 5.4, one can see that the structures are very well-aligned resulting in a much smaller range in difference maps. Overall, our approach successfully corrects for motion even at low undersampling rates, and this effect is preserved for all datasets. Moreover, we present for two datasets the estimated motion $\phi_t$ and its inverse $\phi_t^{-1}$ for a given time frame in Figure 5.5. We can see that our proposed approach produces a reasonable estimation of the motion, where the motion fields are visualised by a deformation grid. Additionally, we show the corresponding Jacobian determinant maps for the deformations. In these plots, we can see that the determinants remain positive meaning that our model ensures topology preservation both from a mathematical and practical point of view. The values are interpreted as follows: small deformations when values are closer to 1, big expansions

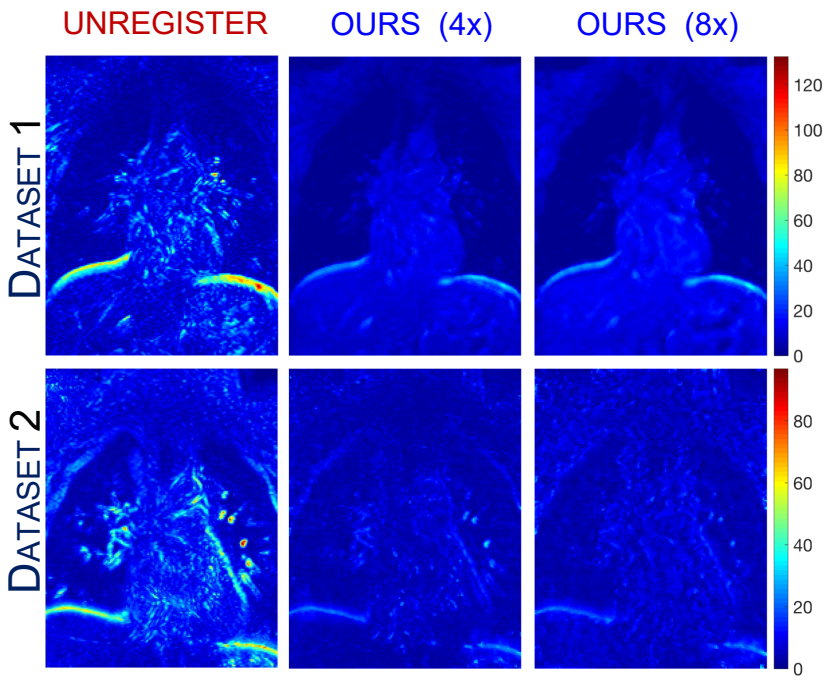


**Figure 5.4:** Difference maps. From left to right: average difference maps of the unregistered sequence, average difference map of the corrected sequence for an acceleration factor of 4 and 8 and the colorbar for Datasets 1 and 2.

when values are greater than 1, and big contractions when values are smaller than 1. Moreover, one can observe that the determinants remain positive in all cases, that is to say, our estimated deformations are physically meaningful and preserve the topology as required in a registration framework.

## 5.5 Conclusion and Outlook

In this chapter, we proposed a novel variational multi-task framework to achieve higher quality and super-resolved reconstructions. Our method compensates for motion due to breathing in undersampled data. To the best of our knowledge, it is the first variational framework that allows computing three tasks jointly.

In particular, our multi-task framework is composed of four major components: an $L^2$ fidelity term intertwining MRI reconstruction, super-resolution and registration; a weighted TV ensuring robustness of our method to intensity changes by promoting edge alignment; a TV regulariser of the super-resolved reconstruction; and a hyperelasticity-based regulariser modelling biological tissue behaviour and allowing for large and smooth deformations. With our model, we exploit the temporal redundancy to correct for blurring

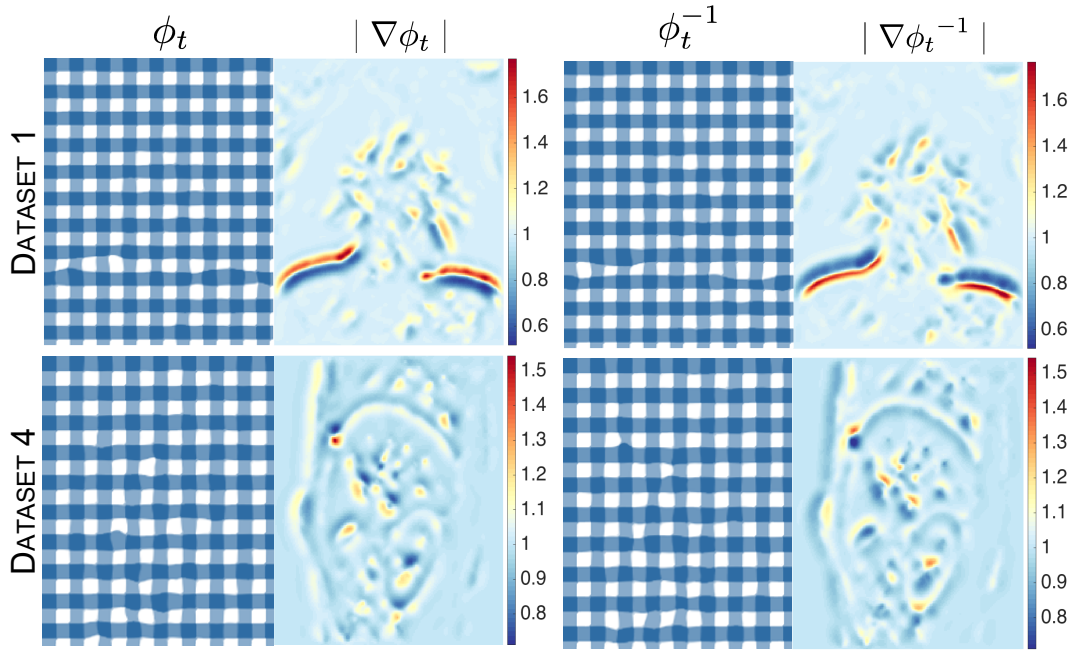


**Figure 5.5:** Estimated motion and determinant maps of the deformation Jacobian. This is shown for the transformation $\phi_i$ and its inverse $\phi_i^{-1}$ for two datasets (1 and 4).

artefacts and increase image quality. As a result, we obtain a single highly resolved and clear image reconstruction representing the true underlying anatomy.

The advantages of our model is that we guarantee preservation of anatomical structures whilst keeping fine details and producing less blurry and noise artefacts in the final reconstructions. We extensively evaluated our method against sequential and another multi-task methods from the body of literature. We demonstrated that our method achieves the best results whilst demanding low CPU time. Our method was further supported by a user-study (experts), favouring our solutions among other state of the art methods. This suggests the potential of our approach for clinical applications.

**Future work.** This multi-task framework is indeed very well-suited for the plug-and-play setting when one (or more) imaging tasks could be replaced by different algorithms. For instance, the modelling of the regularisation functional for the high resolution image reconstruction could be replaced in a plug-and-play fashion. It opens the door to hybrid methods as deep-learning can be used for the super-resolution tasks.

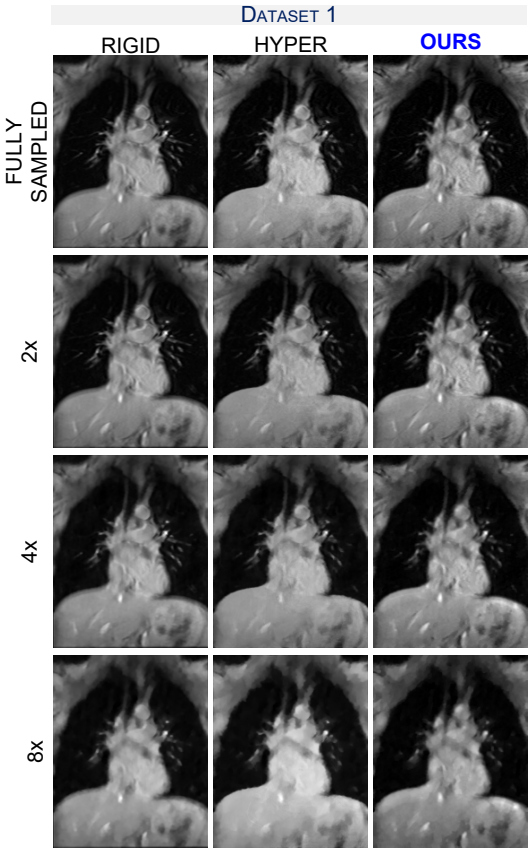


**Figure 5.6:** Reconstruction results for Dataset 1 compared to sequential approaches based on rigid and hyperelastic registration, for different acceleration factors. Our proposed reconstruction results in sharp edges and retrieves fine details especially for higher acceleration factors.

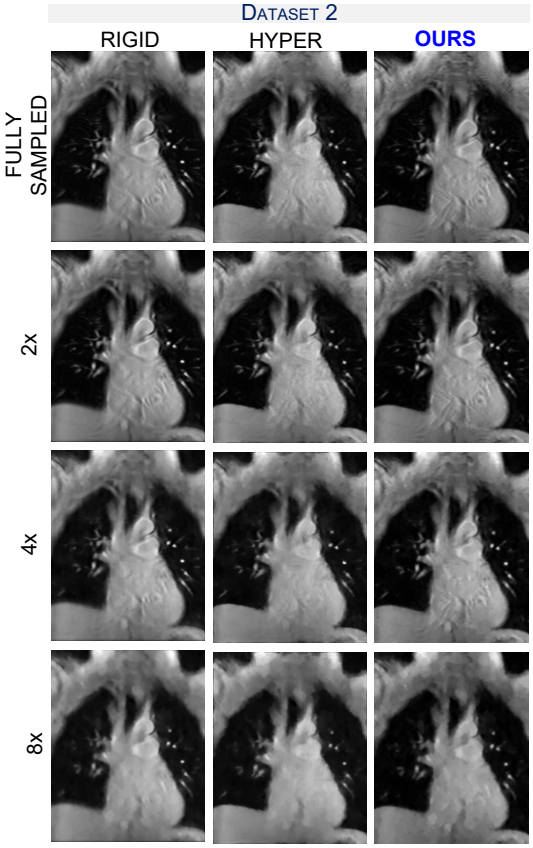


**Figure 5.7:** Reconstruction results for Dataset 2 compared to sequential approaches based on rigid and hyperelastic registration, for different acceleration factors. Our proposed reconstructions preserve fine structures and better correct for motion, thus resulting in sharper edges compared to the sequential reconstructions.

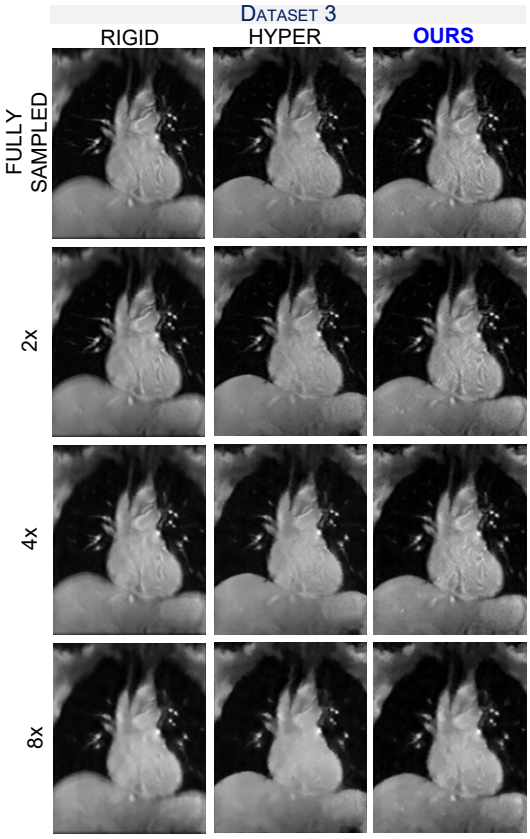


**Figure 5.8:** Reconstruction results for Dataset 3 compared to sequential approaches based on rigid and hyperelastic registration, for different acceleration factors. Our reconstruction results in sharp edges and retrieves fine details especially for higher acceleration factors.

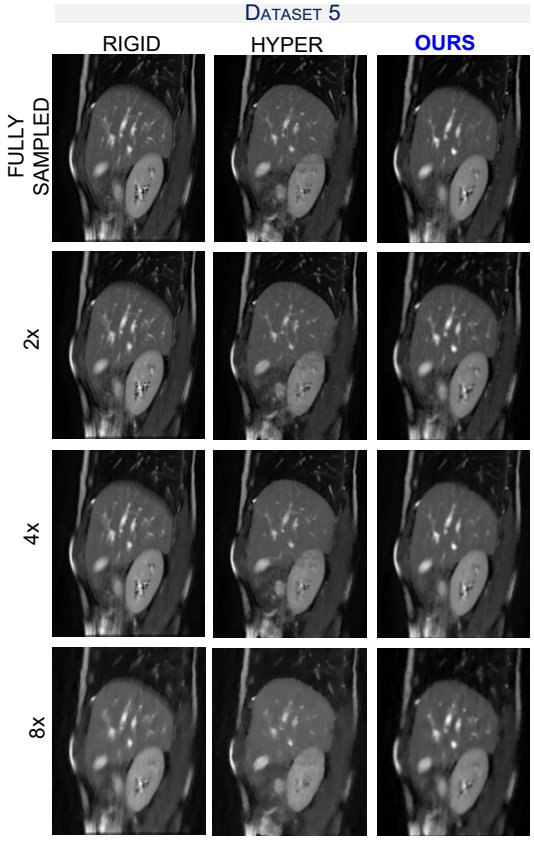


**Figure 5.9:** Reconstruction results for Dataset 5 compared to sequential approaches based on rigid and hyperelastic registration, for different acceleration factors. Our reconstructions show sharper edges and finer details especially for higher acceleration factors. Additionally, we can also notice a better contrast preservation in our results.

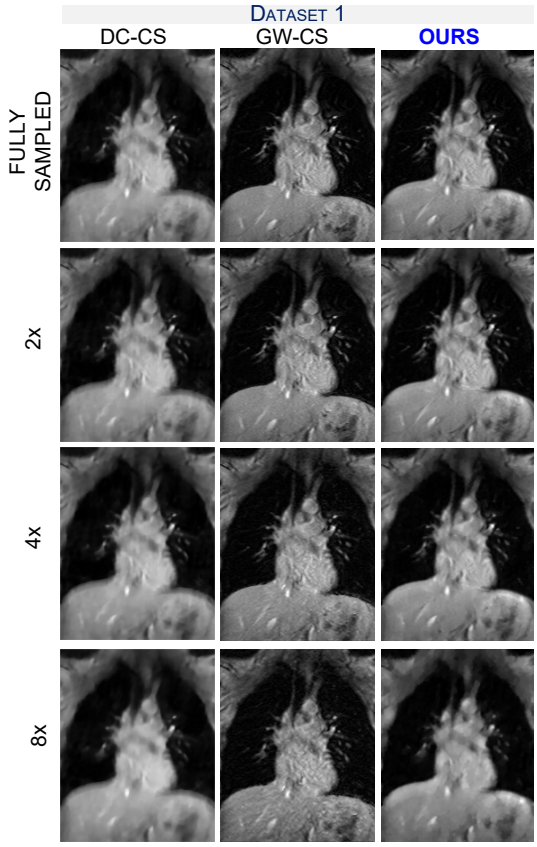


**Figure 5.10:** Reconstruction results for Dataset 1 for different acceleration factors and different joint approaches in comparison to our proposed method. We can clearly see that our approach provides the best results in terms of sharp structures and fine texture, while DC-CS results very blurry and GW-CS very noisy. This is particularly accentuated for high undersampling factors.

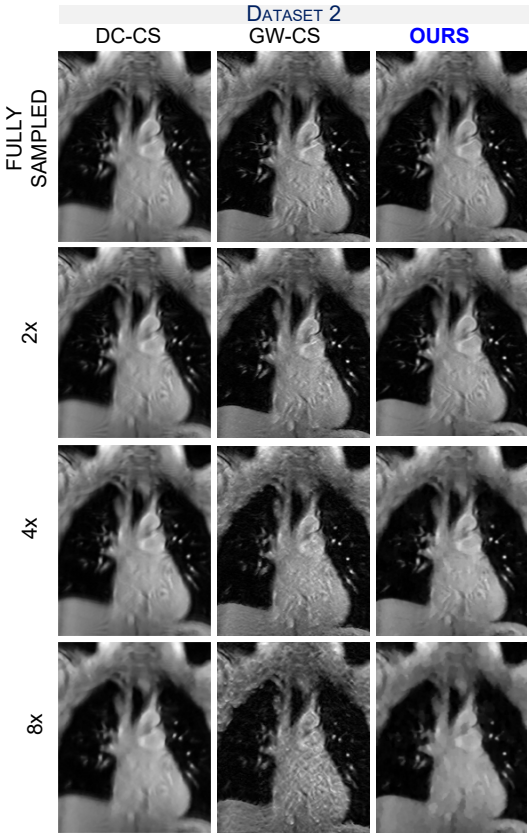


**Figure 5.11:** Reconstruction results for Dataset 2 for different acceleration factors and different joint approaches in comparison to our proposed method. Our approach results in very sharp edges and in particular we retrieve fine texture, while DC-CS results are very blurry and GW-CS very noisy (especially for high undersampling factors).

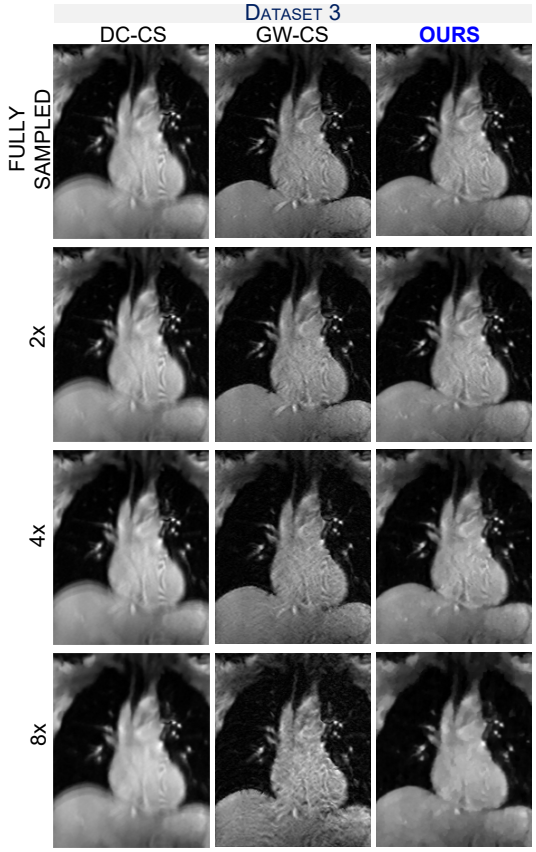


**Figure 5.12:** Comparison of our multi-task framework vs other bi-task approaches on Dataset 3. We note that our approach can preserve fine detail and sharp edges whilst DC-CS fail to compensate for motion, yielding blurring artefacts. We can also note the GW-CS approach highly amplifies the noise. This is more visible for high undersampling factors.

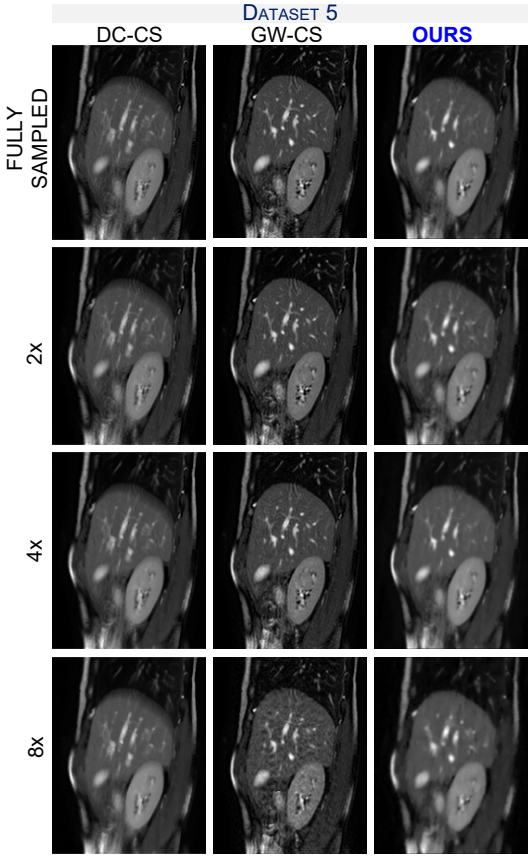


**Figure 5.13:** Comparison of our multi-task framework vs other bi-task approaches on Dataset 4. We can clearly see that our approach provides the best results in terms of sharp structures and fine texture, while DC-CS results very blurry and GW-CS very noisy. This is particularly accentuated for high undersampling factors.

# Chapter 6

# Conclusion and Outlook

In this thesis, we dealt with variational multi-task models for image analysis. Through three research projects, we have proposed novel solutions and demonstrated that by sharing information across tasks, we can exploit the correlative and complementary information of the data and improve overall performance.

By looking at different challenging imaging problems, such as image reconstruction, segmentation, registration and super-resolution, and by carefully intertwining them through unified variational formulations, we went beyond existing solutions from the state of the art and presented alternatives in a multi-task framework in which we can exploit redundancy and structure in the data to boost the final outcome. Our solutions were strongly evaluated through theoretical analysis and numerical experiments on simulated and real MRI data, showing the potentials of our models for applications.

## 6.1 Concluding Remarks

For each research topic discussed in Chapters 3, 4 and 5, in this section we summarise the conclusions by highlighting outcomes and the possible future research directions.

### 6.1.1 Multi-Task Model for Reconstruction and Segmentation with Non-Convex Bregman Iteration.

In Chapter 3, we introduced a novel mathematical approach to jointly perform image reconstruction and segmentation with applications to undersampled MRI data. The main idea was to inform the reconstruction with prior knowledge of the object of interest

(e.g. tumour and healthy tissue, air and water), and simultaneously update this belief according to the actual measurements.

With this in mind, we proposed a variational formulation that by interconnecting the reconstruction and the segmentation tasks, yields significant improvement upon both tasks compared to the traditional sequential approach and another popular joint model, i.e. the Potts model. This suggests that, with our model, it is possible to reduce error propagations that occur in the sequential analysis and to obtain sharper reconstructions and more accurate segmentations. Our joint variational optimisation scheme is based on Bregman iteration, for which we provide its convergence properties. Furthermore, we have assessed the performance of our approach for two different application, which are bubbly flow and cancer imaging. In both cases, our model compensates for error propagation yielding to sharper reconstructions and detection of finer structures, while the segmentations also benefit from the improvement in the reconstructions.

✓ Our proposed approach provides a robust tool to achieve sharp reconstructions by using the segmentation task as additional prior. This result motivated us to expand this current model to the case of velocity-encoded MRI, where we are not only interested in the magnitude image, but as well in the phase image.

### 6.1.2 Multi-Task Model for Phase Reconstruction and Magnitude Segmentation in Velocity-encoded MRI

In Chapter 4, we transitioned to dynamic MRI data and in particular to velocity-encoded MRI, where now we are also interested in retrieving velocity information from the phase images. Based on this, we extended our joint reconstruction and segmentation to also tackle phase reconstruction. This leads to a non-convex and non-linear problem for which we presented a joint optimisation scheme based on Bregman iteration.

We demonstrated that the joint model exploits the correlation and redundancy in the data, yielding accurate estimations of the velocities, as well as an enhanced magnitude reconstruction with sharp edges, thanks to the joint segmentation term. Furthermore, we assessed the performance of our joint approach on synthetic and real velocity-encoded MRI data and we show that our joint model improves the performances of the different imaging tasks compared to the classical sequential approach. This result shows that our proposed method is promising and can be used for real undersampled MRI data. Future work includes the investigation of the full joint temporal and spatial optimisation. By extending the model to the full 4D setting, we believe the performance would be further enhanced. The current limitation is the lack of such fully 4D data.

✓ Our solution can be used in different scenarios such as cardiovascular blood flow analysis in medical imaging and assessment of complex hydrodynamics as in the case of bubbly flow in chemical engineering.

### 6.1.3 Multi-Task model for motion-compensated MRI: Joint Reconstruction, Registration and Super-resolution

In Chapter 5, we presented for the first time a multi-task framework that integrates, in a single model, three relevant tasks, that is reconstruction, registration and super-resolution. We went beyond bi-task models and proposed, to the best of our knowledge, the first variational framework that allows computing three tasks jointly. Our model exploits the temporal redundancy to correct for blurring artefacts and to increase image quality. As a result, we obtain a single highly resolved and clear image reconstruction representing the true underlying anatomy. Furthermore, the significance of our model is that we guarantee preservation of anatomical structures whilst keeping fine details and reducing blurring and noise artefacts in the final reconstruction. From a clinical point of view, this is particularly important as we want to ensure that the biological tissues are not deformed in unrealistic ways. We extensively evaluated our method against sequential and other multi-task methods from the body of literature. We demonstrated that our method achieves the best results whilst demanding low CPU time. Our method was further supported by a user-study involving experts from the area of radiology.

✓ Our model shows promising results from a clinical perspective by producing high quality, motion-compensated reconstructions that exhibit fine structures, while also being computationally tractable.

## 6.2 Future Work

In this thesis, we have assessed the potentials and the benefit of multi-task models to solve inverse imaging problems. Through these solutions, we set the basis for the development of various tools that can be further investigated. Future projects and extensions related to our proposed approaches in the thesis are discussed next.

▷ **Hybrid Model for Multi-Task Reconstruction and Motion Estimation**
In Chapter 5, we have presented a plug & play framework for motion correction in MRI, where one or more tasks can be replaced by different algorithms. It has been showed in [ARWGS18] that, in dynamic MRI, that final reconstruction positively benefits from computing simultaneously the physical motion. With this in mind, we now pose the

question of how to improve the motion estimation with the aim of improving the MRI reconstruction. Motivated by the successful approaches in the field of machine learning, we propose to join variational methods and learning solutions in a unified hybrid model, and in particular, using dictionary learning to improve motion estimation. In this context, we start exploring a joint reconstruction and motion estimation framework with Timothée Schmoderer, visiting the group during the summer from Normandie Université, INSA de Rouen, France. In this project, we are interested in performing motion estimation through optical flow improved by dictionary learning. Our proposed hybrid model reads

$$\begin{aligned} E(u,v,D,a) = \int_0^T & \underbrace{\frac{1}{2}\left\|\mathcal{A}u - f\right\|^2 + \lambda_1 \left\|\nabla u\right\|_1 + \lambda_2 \left\|\Psi u\right\|_1}_{\text{reconstruction}} \\ & + \underbrace{\lambda_3 \left\| \frac{\partial u}{\partial t} + \nabla u \cdot v \right\|_1 + \lambda_4 \|\nabla v\|_1}_{\text{optical flow}} \\ & + \lambda_5 \underbrace{\|\mathcal{T}v - Da\|_F^2 + \lambda_6 \|a\|_1}_{\text{dictionary learning}} \end{aligned}$$

where $\Psi$ is the wavelet operator, the image sequence is denoted by $u$, the optical flow is $v$ and $f$ are the given data. The optical flow formulation is now linked to the reconstruction (where the image sequence $u$ is regularised using TV and wavelet transforms) and to a dictionary learning. Here, we assume that $u$ admits a sparse decomposition $a$ in some dictionary $D$, finally we impose some regularity on the flow. To obtain better learning we use the operator $\mathcal{T}$ that extractd overlapping patches of the flow. Moreover we add the constraint that the dictionary atoms (the column of $D$) to have norm less than 1 for well-posedness purpose.

▷**Regularisation-based Plug-and-Play Compression Approach for MRI Data** In this thesis, we have proposed several multi-task models to improve the reconstruction task through exploiting complementary information and outcomes from correlative tasks. This led to another collaboration with Yehuda Dar, post-doc at the Computer Science Department at Technion, Israel, in the context of optimising MRI processing through a compression framework.

Acquisition and compression are two crucial stages in imaging systems. The acquired data, describing the visual scene in a degraded form depending on the specific settings,

is further processed to form images that can be compressed for storage or transmission. The decompressed images are the important outcome of this overall process, and ideally should be of a good quality (with respect to the original visual scene) considering the bit-rate required for their binary compressed representations. However, this ultimate goal of optimising the entire processing chain is often neglected and the individual tasks of reconstruction and compression, do not interact with each other, leading to sub-optimal overall performance. This problem is central in medical imaging, where thousands of images are acquired every day with the need to be transferred and stored in an efficient way. Here, we focus once again on MRI.

The MRI processing chain starts with a critical acquisition stage, providing data for reconstruction of images required for medical diagnosis. In this project, we propose a framework for joint optimisation of the MRI reconstruction and lossy compression, producing medical images with an improved trade-off between quality and bit-rate. Suppose $u$ is the image reconstruction associated with the measurements $f$ in the MRI reconstruction setting that we have seen in this thesis (i.e., $f = \mathcal{A}u + \eta$). Now we denote by $v$ the output of the compression/decompression of the original image $u$. Ideally, we want to minimise the loss $\|u - v\|_2^2$, where $u$ is unknown. Following [DEB18], we formulate a new compression procedure in order to optimize the end-to-end rate-distortion performance of the MRI processing system. Specifically, we want the system output $v$ to be the best approximation of the source signal $u$ under the bit-budget constraint. Our proposed model reads

$$v^* = \arg\min_{v \in S} R(v) + \frac{1}{2}\|\mathcal{A}v - f\|_2^2 + \mathrm{TV}(v)$$

where we seek a solution $v \in S$, where $S$ is a discrete set of decompressed signals and $R(v)$ evaluates the bit-cost of the binary compressed representation associated with $v$. Our method has the contemporary plug-and-play structure, implemented using the alternating direction method of multipliers (ADMM) and the state-of-the-art standard image compression as a module, iteratively applied. The significance of the proposed algorithm is that, by joining the reconstruction task to the compression stage, the multi-task process improves the decompressed images without any post-decompression processing. Our preliminary experimental results show that our regularisation-based approach for joint MRI reconstruction and compression significantly outperforms non-regularised solutions to the joint task. Moreover, our approach is promising for clinical practice, allowing low bit-cost for highly undersampled-data.

# Appendix A

# Mathematical preliminaries

In this chapter we recall some mathematical tools, notions, definitions and properties which will be useful in this thesis. We start by recalling the notion of Lebesgue and Sobolev space. Then, we give a brief summary of concepts and definitions from convex analysis optimisation. We assume that the reader is familiar with basic real and functional analysis, measure theory and Sobolev space theory, convex analysis and optimisation. We refer the reader to [AFP00a, Bre10, EG91, Giu84, Rud87, ET99, BV04, Roc70].

We start by recalling the definitions of Lebesgue and Sobolev spaces, where we denote by $X$ an arbitrary measure space with measure $\mu$.

**Definition A.1.** *(Lebesgue space $L^p$, $L^p$-norm, $0 < p < \infty$) If $f$ is a measurable function on $X$, we define the $L^p$-norm of $f$ as*

$$\|f\|_p = \left(\int_X |f|^p d\mu\right)^{\frac{1}{p}}.$$

*The space $L^p(\mu)$ consists of all $f$ for which*

$$\|f\|_p < \infty.$$

**Definition A.2.** *(Lebesgue space $L^\infty$, $L^\infty$-norm) If $f$ is a measurable function on $X$, we define $\|f\|_\infty$ to be the essential supremum of $|f|$. The space $L^\infty(\mu)$ consists of all $f$ for which*

$$\|f\|_\infty < \infty.$$

In this thesis, when considering $n$-dimensional vector space $\mathbb{R}^n$ with Lebesgue measure $\mu$ (see e.g. [Rud87, Chapter 2]), we write $L^p(\mathbb{R}^n)$ instead of $L^p(\mu)$, and use the short notation $\|\cdot\|_p$ instead of the $L^p$-norm for a discrete $p$-norm.

The definition of Sobolev spaces (see e.g. [Eva98, Chapter 5]) will also be used in Chapter 5.

**Definition A.3.** *(Sobolev space $W^{k,p}$) Let $1 \leq p \leq \infty$ and $k \in \mathbb{Z}^{\geq 0}$. The Sobolev space $W^{k,p}(\Omega)$ is the set of $L^p$ functions with weak derivatives of order $k$, i.e. it consists of all locally summable functions $u\colon \Omega \to \mathbb{R}$ such that for each multi-index $\alpha$ with $|\alpha| \leq k$, the weak derivative $D^\alpha u$ exists and belongs to $L^p(\Omega)$.*

From now on, we denote by $X$ a finite-dimensional real vector space and recall the notion of inner product.

**Definition A.4.** *(Inner product) The inner product of two vectors $v, w \in X \subset \mathbb{R}^n$ is defined as*

$$\langle v, w \rangle = \sum_{i=1}^{n} v_i w_i.$$

## A.1 Convex Analysis

We now state some basic definitions from convex analysis that we will used in the rest of this thesis. We refer the reader to [ET99, BV04, Roc70] for more details.

**Definition A.5** (Convex set)**.** *A subset $C$ of $\mathbb{R}^n$ is called convex if*

$$(1 - \lambda)\, x + \lambda y \in C$$

*for all $x, y \in C$ and $0 < \lambda < 1$.*

**Definition A.6** (Epigraph)**.** *The epigraph of a function $f : X \to \mathbb{R}^n \cup \{+\infty, -\infty\}$ is defined as*

$$epif = \{(x, \mu) \in X \times \mathbb{R}, \mu \geq f(x)\}.$$

**Definition A.7** (Convex function)**.** *The function $f$ is convex on $X$ if $epif$ is convex as a subset of $\mathbb{R}^{n+1}$.*

**Definition A.8** (Effective domain)**.** *Let $f$ be a convex function on $X$. Then, its effective domain is defined as*

$$domf = \{x \mid \exists\, \mu\colon (x, \mu) \in epif\} = \{x \mid f(x) < +\infty\}$$

*and is the projection on $\mathbb{R}^n$ of the epigraph of $f$.*

**Definition A.9** (Proper function)**.** *A convex function $f$ is said to be proper if*

$$\exists\, x\colon f(x) < +\infty \quad \textit{and} \quad \forall\, x\colon f(x) > -\infty.$$

**Definition A.10** (Lower semi-continuous (l.s.c.))**.** *A proper function $f : X \to \mathbb{R}$ is said to be l.s.c. at a point $x \in X$ if*

$$f(x) \leq \lim_{i\to\infty} f(x_i)$$

*for every sequence $x_1, x_2, \ldots$ in $X$ such that $x_i$ converges to $x$ and the limit of $f(x_1), f(x_2), \ldots$ exists in $[-\infty, +\infty]$.*

**Theorem A.11.** *For $f\colon \mathbb{R}^n \to [-\infty, +\infty]$ the following conditions are equivalent:*

*(a) $f$ is l.s.c. throughout $\mathbb{R}^n$,*

*(b) $\{x \mid f(x) \leq \alpha\}$ is closed for every $\alpha \in \mathbb{R}$,*

*(c) epif is a closed set in $\mathbb{R}^{n+1}$.*

*Proof.* The proof can be found in [Roc70]. □

Now, let $X$ and $Y$ be two finite-dimensional real vector spaces equipped with an inner product $\langle\cdot,\cdot\rangle$ and a norm $\|\cdot\| = \langle\cdot,\cdot\rangle^{\frac{1}{2}}$and let $X^*$ and $Y^*$ be their dual space. Let us consider $\mathcal{K} : X \to Y$ to be a bounded continuous linear operator with operator norm defined as

$$\|\mathcal{K}\| = \sup\{\|\mathcal{K}x\| : x \in X,\ \|x\| \leq 1\} \tag{A.1}$$

and let $\mathcal{K}^* : Y^* \to X^*$ be its adjoint operator. Let us denote with $\overline{\mathbb{R}} := \mathbb{R} \cup \{\pm\infty\}$ the set of extended real numbers. Now, let $f : Y \to \overline{\mathbb{R}}$ and $g : X \to \overline{\mathbb{R}}$ be proper, convex and lower semi-continuous functions. We denote as $\mathrm{dom}(f)$ the domain of $F$ as the set of points where $f$ is finite, i.e.

$$\mathrm{dom}(f) = \{x \in X : f(x < \infty\} \tag{A.2}$$

A function $f$ is called proper if $\mathrm{dom}(f) \neq \emptyset$. The Legendre–Fenchel conjugate of $f$ is defined as follows.

**Definition A.12** (Legendre-Fenchel conjugate (convex conjugate))**.** *For a proper, convex and l.s.c. function $f$ on $X$, its Legendre-Fenchel conjugate is defined as*

$$f^*(y) = \sup_{x\in X} \langle x, y\rangle - f(x) \quad \forall x^* \in X^*$$

We can now introduce the concept of subdifferential.

**Definition A.13** (Subgradient, subdifferential)**.** *A subgradient of a convex function $f$ at a point $x \in X$ is a vector $y$ in the dual space of $X$ such that*

$$f(z) \geq f(x) + \langle y, z - x \rangle \ \forall \ z.$$

*The set of all subgradients of $f$ at $x$ is called the subdifferential of $f$ at $x$ and is denoted by $\partial f(x)$.*

## A.2 Primal Dual Hybrid Gradient Method

The above definitions are fundamental to describe the primal-dual hybrid gradient (PDHG) method, proposed in [CP11a, CP16, EZC10, PCBC09] and used throughout this thesis to solve convex problems and sub-problems. Here, we give a brief summary.

We consider the general *primal* problem

$$\min_{x \in X} F(\mathcal{K}x) + G(x)$$

and of the corresponding dual problem

$$\max_{y \in Y} - \left(G^*(-\mathcal{K}^* y) + F^*(y)\right),$$

making use of the definition of convex conjugate. We now write the correspondent saddle-point problem

$$\min_{x \in X} \max_{y \in Y} \langle \mathcal{K}x, y \rangle + G(x) - F^*(y), \tag{A.3}$$

where $G \colon X \to [0, \infty]$ and $F^* \colon Y \to [0, \infty]$ are proper, convex, l.s.c. functions. Now we can definte the proximity operator. or resolvent operator.

**Definition A.14** (Proximity operator (resolvent))**.** *If $f$ is a convex, proper and l.s.c. function, then*

$$\hat{z} = prox_{\tau f}(x) = \arg\min_z \left\{ f(z) + \frac{1}{2\tau} \|z - x\|^2 \right\} = (I + \tau \partial f)^{-1}(x),$$

*where $\tau > 0$, is the proximity operator or resolvent of $f$.*

When the proximity operators are easy to compute, one can solve (A.3) as follows [CP11a]

**Algorithm 4:** Primal-Dual Algorithm by Chambolle and Pock [CP11a]

**Input:** $\tau, \sigma > 0$, $\theta \in [0,1]$, $x^0$, $y^0$, $\bar{x}^0 = x^0$
**for** $k \geq 0$ **do**
  $y^{k+1} = (I + \sigma \partial F^*)^{-1}(y^k + \sigma \mathcal{K} \overline{x}^k)$
  $x^{k+1} = (I + \tau \partial G)^{-1}(x^k + \tau(-\mathcal{K}^* y^{k+1}))$
  $\overline{x}^{k+1} = x^{k+1} + \theta(x^{k+1} - x^k)$
**end for**
**Output:** $\hat{x}, \hat{y}$.

$$\begin{cases} y^\star = \underset{y \in Y}{\arg\min} \left( \dfrac{\|y - z_2\|_2^2}{2\sigma} + F^*(y) \right) = (I + \sigma \partial F^*)^{-1}(z_2), \\ x^\star = \underset{x \in X}{\arg\min} \left( \dfrac{\|x - z_1\|_2^2}{2\tau} + G(x) \right) = (I + \tau \partial G)^{-1}(z_1). \end{cases} \tag{A.4}$$

where $z_1$ and $z_2$ are the input of the proximal operators. By setting $z_1$ and $z_2$ as in the explicit gradient descent method

$$\begin{cases} z_2 = y^k + \sigma q, \quad q \in \partial F^*, \\ z_1 = x^k + \tau p, \quad p \in \partial G. \end{cases} \tag{A.5}$$

and from the optimality conditions of (A.3) , $q = \mathcal{K} x^\star$ and $p = -\mathcal{K}^* y^\star$, the alternating iterative scheme reads

$$\begin{cases} y^{k+1} = (I + \sigma \partial F^*)^{-1}(y^k + \sigma \mathcal{K} \overline{x}^k), \\ x^{k+1} = (I + \tau \partial G)^{-1}(x^k + \tau(-\mathcal{K}^* y^{k+1})), \\ \overline{x}^{k+1} = x^{k+1} + \theta(x^{k+1} - x^k), \end{cases} \tag{A.6}$$

where $\overline{x}$ is the primal variable accelerated by the acceleration parameter $\theta \in [0,1]$.

# Appendix B

# Appendix of Chapter 3

## B.1 Numerical Results on Phantoms

In this subsection, we present additional results of our joint approach compared to the sequenatial cases for phantoms.

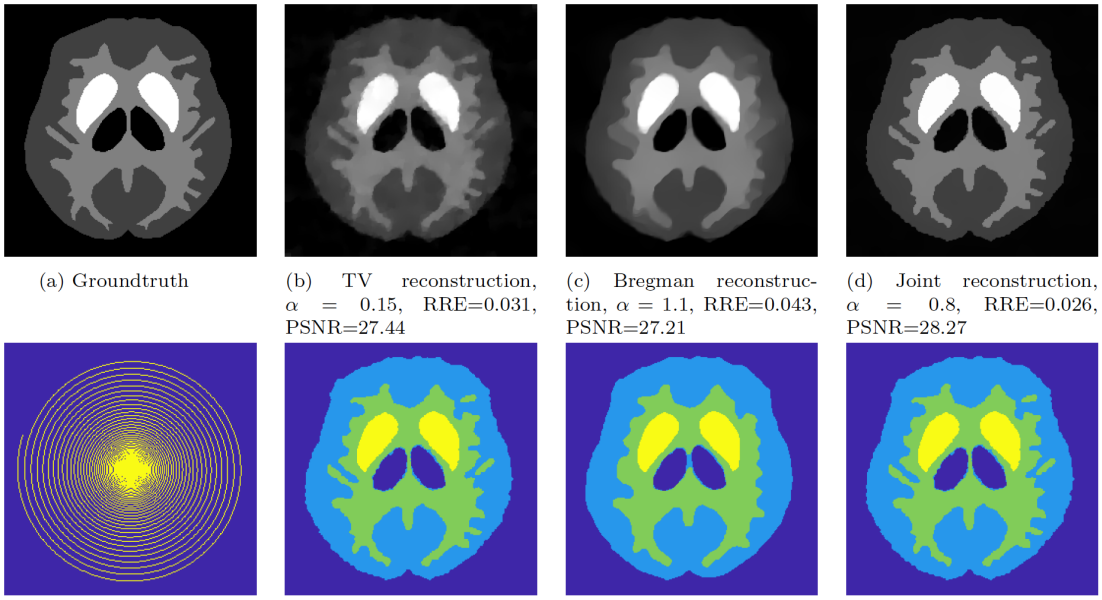

(a) Groundtruth

(b) TV reconstruction, $\alpha = 0.15$, RRE=0.031, PSNR=27.44

(c) Bregman reconstruction, $\alpha = 1.1$, RRE=0.043, PSNR=27.21

(d) Joint reconstruction, $\alpha = 0.8$, RRE=0.026, PSNR=28.27

(e) Sampling matrix, 15%

(f) Segmentation, $\beta = 0.001$ RSE=0.022

(g) Bregman segmentation, $\beta = 0.001$ RSE=0.040

(h) Joint segmentation, $\beta = 0.001$, $\delta = 2$, RSE=0.022

**Figure B.1:** This example shows clearly the effect of the parameter $\delta$ in the joint model. The segmentation is easy to achieve and we do not see a significant improvement in joint segmentation compared to the TV sequential segmentation, but there is a small gain compared to the sequential Bregman segmantation. However, the joint reconstruction results improved thanks to the parameter $\delta$ which biases the reconstruction to be closer to the segmentation.

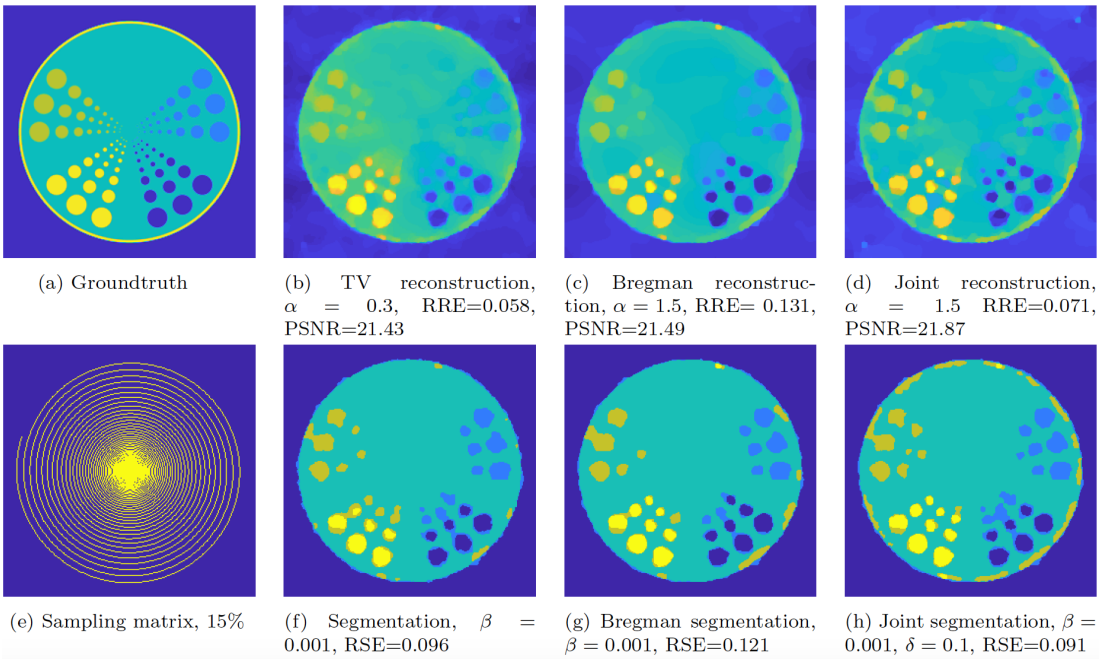

(a) Groundtruth

(b) TV reconstruction, $\alpha = 0.3$, RRE=0.058, PSNR=21.43

(c) Bregman reconstruction, $\alpha = 1.5$, RRE= 0.131, PSNR=21.49

(d) Joint reconstruction, $\alpha = 1.5$ RRE=0.071, PSNR=21.87

(e) Sampling matrix, 15%

(f) Segmentation, $\beta = 0.001$, RSE=0.096

(g) Bregman segmentation, $\beta = 0.001$, RSE=0.121

(h) Joint segmentation, $\beta = 0.001$, $\delta = 0.1$, RSE=0.091

**Figure B.2:** In this example, we can see that the reconstructions are quite similar. However in the joint reconstruction, the outer yellow circle, which is completely ignored by the sequential reconstructions, is partially detected. This is also the case for the joint segmenation.

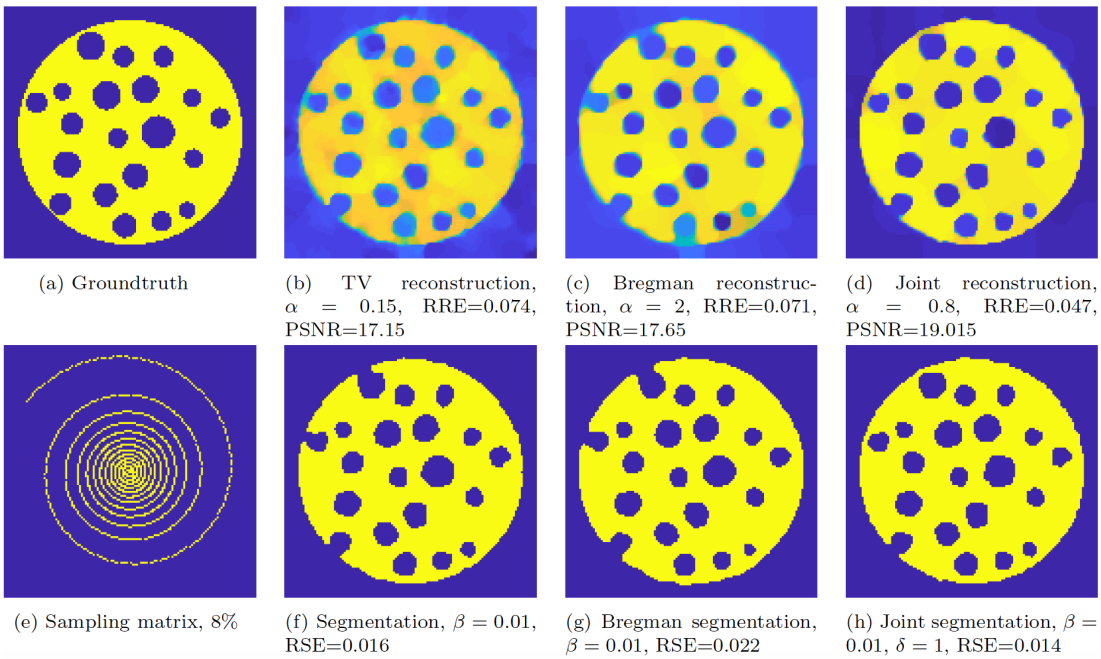

(a) Groundtruth

(b) TV reconstruction, $\alpha = 0.15$, RRE=0.074, PSNR=17.15

(c) Bregman reconstruction, $\alpha = 2$, RRE=0.071, PSNR=17.65

(d) Joint reconstruction, $\alpha = 0.8$, RRE=0.047, PSNR=19.015

(e) Sampling matrix, 8%

(f) Segmentation, $\beta = 0.01$, RSE=0.016

(g) Bregman segmentation, $\beta = 0.01$, RSE=0.022

(h) Joint segmentation, $\beta = 0.01$, $\delta = 1$, RSE=0.014

**Figure B.3:** In this example for the bubbly flow, we can see clearly an improvement for both joint reconstruction and joint segmentation. The contrast in the joint reconstruction is better recovered and the segmentation is more accurate, especially for the bubbles close to the edge of the pipe. The joint method results particularly useful for the bubbly flow application.

# Appendix C

# Appendix of Chapter 5

This appendix extends the experimental results and theoretical analysis of Chapter 5 to further support our proposed multi-task framework.

## C.1 Further Visual Assessment of Our Proposed Approach

In this section, we extend the reconstruction comparisons from the main chapter and provide results for Dataset 4.

## C.2 Further Details on the User-Study

To further support our results, we performed a user-study following standard protocol in clinical settings. That is- to ask experts and trainees to evaluate the reconstructions based on a scoring system. For this study, we had twelve experts and trainees from the area of radiology.

**Scoring Procedure.** We create an electronic survey in which, after giving the instructions to the users, they were provided with two-part evaluation. For the first part, they evaluated the reconstructions related to sequential models. To do this, they were provided with the reconstructions of the five dataset, for acceleration factor ={fully sampled, 2x, 4x, 6x, 8x}, and for the approaches ={RIGID, HYPER, OURS} (see Chapter 5 for description on these models). With the purpose of capturing they scores, we design a three-point Likert rating scale in which experts were asked to indicate the level of agreement, ranging from best reconstruction to worst reconstruction. Similarly, this protocol was followed to evaluate other multi-task methods = {DC-CD, GW-CS,

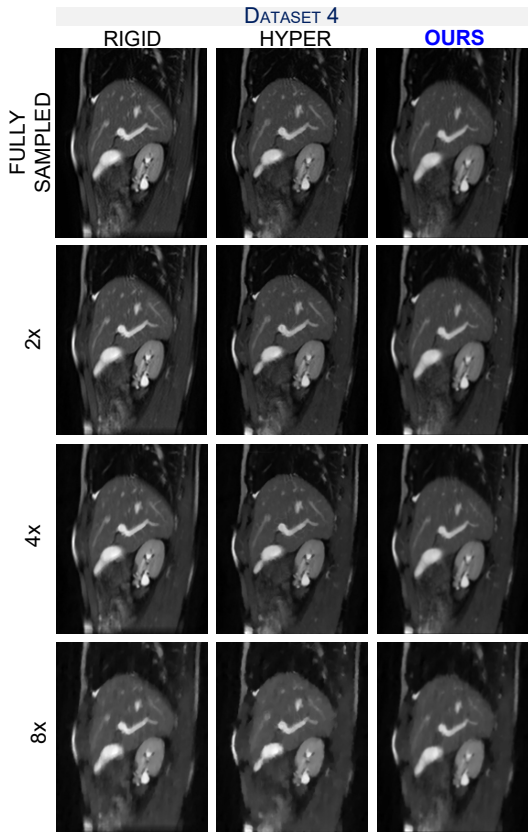


**Figure C.1:** Reconstruction results for Dataset 4 compared to sequential approaches based on rigid and hyperelastic registration, for different acceleration factors.

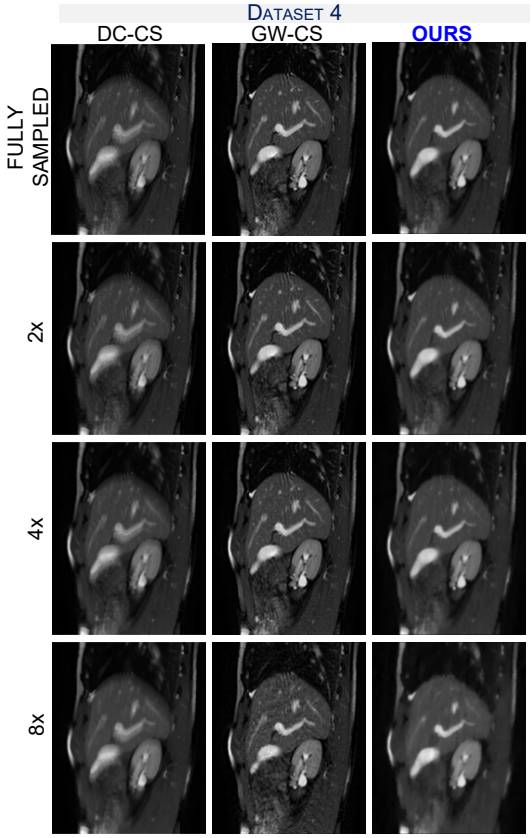


**Figure C.2:** Reconstruction results for Dataset 4 for different acceleration factors and different joint approaches in comparison to our proposed method.

OURS}. Fig. 1 displays the results in terms of % the worst ranked for all compared approaches.

**Statistical Analysis.** The circle plots displayed in Figure 5.2b and 5.2b, reflects the averaged results of all scoring (i.e. for all acceleration and all reconstructions). However, to test if there was statistical significant difference between the approaches we took into account the the scoring per each reconstruction, and ran the nonparametric Friedman test to compare the three approaches (for both sequential and multi-task frameworks). We also applied corrections for multiple comparisons during the statistical analysis. Overall, we found statistical significant difference between our approach and the compared ones. This support our previous discussions on our model offer the best reconstruction in comparison to the compared approached for both sequential and joint models.

## C.3 Proof of Theorem 5.1

*Proof.* The proof is based on arguments coming from the calculus of variations and is divided into three steps. We recall the assumptions on $g_t$: $g_t : \mathbb{R}^+ \to \mathbb{R}^+$, $g_t(0) = 1$, $g_t$ is strictly decreasing, $\lim_{r\to+\infty} g(r) = 0$, and there exists $c > 0$ such that $c \leq g_t \leq 1$ everywhere. We also have $\phi_t : \bar{\Omega} \to \bar{\Omega}$ thanks to Ball's results [Bal81a] as seen later.

**Coercivity inequality**: We first have that $G(0, (\mathrm{Id})_{t=1,\cdots,T}) = 4a_1\mathrm{meas}(\Omega) + \frac{1}{2T}\sum_{t=1}^{T}\|x_t\|^2_{L^2(\mathbb{R}^2)} < +\infty$. Let $u \in BV(\Omega')$, $\phi_t \in \mathscr{W}$, $\forall t \in \{1, \cdots, T\}$ such that $(\mathcal{C}u)\circ\phi_t \in BV_{g_t,0}(\Omega), \forall t \in \{1, \cdots, T\}$, we then derive a coercivity inequality:

$$
\begin{aligned}
G(u, (\phi_t)_{t=1,\cdots,T}) \geq \frac{1}{T}\sum_{t=1}^{T}(a_1\|\nabla\phi_t\|^4_{L^4(\Omega,M_2(\mathbb{R}))} \\
+ \frac{a_2}{2}\|\det\nabla\phi_t\|^4_{L^4(\Omega)} + \frac{a_2}{2}\|\frac{1}{\det\nabla\phi_t}\|^4_{L^4(\Omega)} \\
+ \frac{1}{4}\|(\mathcal{C}u)\circ\phi_t^{-1}\|^2_{L^2(\Omega)} + \delta\,\mathrm{TV}_{g_t}((\mathcal{C}u)\circ\phi_t^{-1}) + \alpha\,\mathrm{TV}(u) \\
- \frac{1}{2}\|x_t\|^2_{L^2(\mathbb{R}^2)} - 3a_2\mathrm{meas}(\Omega)).
\end{aligned}
$$

Indeed, $((\mathcal{C}u)\circ\phi_t^{-1}) \in BV_{g_t,0}(\Omega) \subset BV(\Omega) \subset L^2(\Omega)$ ([Bal01]) with continuous embedding, and $((\mathcal{C}u)\circ\phi_t^{-1})_e$ is the extension by 0 outside the domain $\Omega$ of $(\mathcal{C}u)\circ\phi_t^{-1}$, then $\|((\mathcal{C}u)\circ\phi_t^{-1})_e\|_{L^2(\mathbb{R}^2)} = \|(\mathcal{C}u)\circ\phi_t^{-1}\|_{L^2(\Omega)} < +\infty$, and finally Plancherel's theorem gives us $\|\mathcal{A}((\mathcal{C}u)\circ\phi_t^{-1})_e\|^2_{L^2(\mathbb{R}^2)} \leq \|\mathcal{F}((\mathcal{C}u)\circ\phi_t^{-1})_e\|^2_{L^2(\mathbb{R}^2)} = \|((\mathcal{C}u)\circ\phi_t^{-1})_e\|^2_{L^2(\mathbb{R}^2)} = \|(\mathcal{C}u)\circ\phi_t^{-1}\|^2_{L^2(\Omega)}$.
The infimum is thus finite. Let $(u_n, (\phi_{t,n})_{t=1,\cdots,T})_n \in \{u \in BV(\Omega'), \phi_t \in \mathscr{W}, \forall t = 1, \cdots, T \,|\, (\mathcal{C}u)\circ\phi_t^{-1} \in BV_{g_t,0}(\Omega), \forall t \in \{1, \cdots, T\}\}$ be a minimizing sequence such that $\lim_{n\to+\infty} G(u_n, (\phi_{t,n})_{t=1,\cdots,N}) = \inf_{(u,(\phi_t)_{t=1,\cdots,T})\in\mathscr{U}} G(u, (\phi_t)_{t=1,\cdots,T})$.

**Extraction of converging subsequences**: From the previous coercivity inequality and the finiteness of the infimum we deduce that:

- $(\phi_{t,n})_n$ is uniformly bounded according to $n$ in $W^{1,4}(\Omega, \mathbb{R}^2)$ for each $t = 1, \cdots, T$ by using the generalized Poincaré's inequality and the fact that $\phi_{t,n}$ is equal to the identity on the boundary $\partial\Omega$.
- $(\det\nabla\phi_{t,n})_n$ is uniformly bounded according to $n$ in $L^4(\Omega)$ for each $t = 1, \cdots, T$.
- $((\mathcal{C}u_n)\circ\phi_{t,n})_n$ is uniformly bounded according to $n$ in $BV_{g_t}(\Omega)$ and thus in $BV(\Omega)$ since $c \leq g_t \leq 1$ everywhere for each $t = 1, \cdots, T$.

Therefore we can extract subsequences (but for the sake of conciseness we keep the same notations) such that :

- $\phi_{t,n} \underset{n\to+\infty}{\rightharpoonup} \bar{\phi}_t$ in $W^{1,4}(\Omega,\mathbb{R}^2)$ for each $t=1,\cdots,T$ and by continuity of the trace operator, we deduce that $\bar{\phi}_t \in \mathrm{Id} + W_0^{1,4}(\Omega,\mathbb{R}^2)$.
- $\det \nabla\phi_{t,n} \underset{n\to+\infty}{\rightharpoonup} \delta_t$ in $L^4(\Omega)$ for all $t=1,\cdots,T$.
- $((\mathcal{C}u_n)\circ\phi_{t,n}^{-1}) \underset{n\to+\infty}{\longrightarrow} \alpha_t$ in $L^q(\Omega)$ for $q\in[1,2[$ and thus in $L^1(\Omega,g_t)$ with $\alpha_t \in BV(\Omega)\subset BV_{g_t}(\Omega)$. By continuity of the trace operator, we deduce that $\alpha_t \in BV_{g_t,0}(\Omega)$.
- $((\mathcal{C}u_n)\circ\phi_{t,n}^{-1}) \underset{n\to+\infty}{\rightharpoonup} \alpha_t$ in $L^2(\Omega)$ for each $t=1,\cdots,T$ by uniqueness of the weak limit in $L^1(\Omega)$ and the continuous embedding of $L^2(\Omega)\subset L^1(\Omega)$. Also, since $\alpha_t \in BV_{g_t,0}(\Omega)$, we can extend it by 0 outside the domain $\Omega$ and we have $((\mathcal{C}u_n)\circ\phi_{t,n}^{-1})_e \underset{n\to+\infty}{\rightharpoonup} (\alpha_t)_e$ in $L^2(\mathbb{R}^2)$, for each $t=1,\cdots,T$.

Also, from [Dac08, Theorem 8.20], we have that $\det\nabla\phi_{t,n} \underset{n\to+\infty}{\rightharpoonup} \det\nabla\bar{\phi}_t$ in $L^2(\Omega)$ for each $t=1,\cdots,T$, and by uniqueness of the weak limit in $L^2(\Omega)$ and the continuous embedding $L^4(\Omega)\subset L^2(\Omega)$, we deduce that $\delta_t = \det\nabla\bar{\phi}_t$ for each $t=1,\cdots,T$. Also, since we have for $\tilde{q}=2+\frac{1}{2}>2$ :

$$\begin{aligned}
&\int_\Omega \|(\nabla\phi_{t,n})^{-1}(x)\|_F^{\tilde{q}} \det\nabla\phi_{t,n}(x)\,dx\\
&= \int_\Omega \|\nabla\phi_{t,n}(x)\|_F^{\tilde{q}} (\det\nabla\phi_{t,n})^{1-\tilde{q}}\,dx,\\
&\le \|\nabla\phi_{t,n}\|_{L^4(\Omega,M_2(\mathbb{R}))}^{\tilde{q}} \Big\|\frac{1}{\det\nabla\phi_{t,n}}\Big\|_{L^4(\Omega)}^{\tilde{q}-1},
\end{aligned}$$

using Hölder's inequality with $\tilde{p}=\frac{4}{\tilde{q}}$, $r=\frac{4}{\tilde{q}-1}$ and noticing that $\frac{4(\tilde{q}-1)}{4-\tilde{q}}=4$. This quantity is uniformly bounded according to $n$ from what precedes and we deduce from [Bal81b, Theorem 1 and 2] that $(\phi_{t,n})$ are bi-Hölder's homeomorphisms and therefore $\phi_{t,n}^{-1}$ exists.

**Weak lower semi-continuity**: $W_{Op}$ is convex and continuous. If $\psi_n \underset{n\to+\infty}{\longrightarrow} \bar{\psi}$ in $W^{1,4}(\Omega,\mathbb{R}^2)$, then $\nabla\psi_n \underset{n\to+\infty}{\longrightarrow} \nabla\bar{\psi}$ in $L^4(\Omega,M_2(\mathbb{R}))$ and we can extract a subsequence still denoted $(\nabla\psi_n)$ such that $\nabla\psi_n \underset{n\to+\infty}{\longrightarrow} \nabla\bar{\psi}$ almost everywhere in $\Omega$. If $\delta_n \underset{n\to+\infty}{\longrightarrow} \bar{\delta}$ in $L^4(\Omega)$, then we can extract a subsequence still denoted $(\delta_n)$ such that $\delta_n \underset{n\to+\infty}{\longrightarrow} \bar{\delta}$ almost everywhere in $\Omega$. Then, by continuity of $W_{Op}$, we get that $W_{Op}(\nabla\psi_n(x),\delta_n(x)) \underset{n\to+\infty}{\longrightarrow} W_{Op}(\nabla\bar{\psi}(x),\bar{\delta}(x))$ almost everywhere in $\Omega$. Finally, by applying Fatou's lemma, we have that $\liminf_{n\to+\infty}\int_\Omega W_{Op}(\nabla\psi_n(x),\delta_n(x))\,dx \ge \int_\Omega W_{Op}(\nabla\bar{\psi}(x),\bar{\delta}(x))\,dx$. Since $W_{Op}$ is

convex, so is $\int_\Omega W_{Op}(\xi(x),\delta(x))\,dx$, and we can apply [Bré83, Corollaire III.8] to get that $\int_\Omega W_{Op}(\xi(x),\delta(x))\,dx$ is lower semicontinuous in $L^4(\Omega,M_2(\mathbb{R}))\times L^4(\Omega)$. We deduce that $\liminf_{n\to+\infty}\int_\Omega W_{Op}(\nabla\phi_{t,n}(x),\det\nabla\phi_{t,n}(x))\,dx \geq \int_\Omega W_{Op}(\nabla\bar{\phi}_t(x),\det\nabla\bar{\phi}_t(x))\,dx$.
Also since $(\mathcal{C}u_n)\circ\phi_{t,n}^{-1}\underset{n\to+\infty}{\longrightarrow}\alpha_t$ in $L^1(\Omega)$ and so in $L^1(\Omega,g_t)$, then by the semi-continuity theorem from [Bal01, Theorem 3.2], we conclude that $\mathrm{TV}_{g_t}(\alpha_t)\leq\liminf_{n\to+\infty}\mathrm{TV}_{g_t}((\mathcal{C}u_n)\circ\phi_{t,n}^{-1})$ for all $t=1,\cdots,T$.
$\mathcal{A}$ is a linear and operator and continuous for the strong topology from $L^2(\mathbb{R}^2)$ to $L^2(\mathbb{R}^2)$. Therefore, by applying [Bré83, Theorem III.9], $\mathcal{A}$ is continuous from the weak topology of $L^2(\mathbb{R}^2)$ to the weak topology of $L^2(\mathbb{R}^2)$. As $((\mathcal{C}u_n)\circ\phi_{t,n})_e\underset{n\to+\infty}{\rightharpoonup}(\alpha_t)_e$ in $L^2(\mathbb{R}^2)$, we deduce that $\mathcal{F}((\mathcal{C}u_n)\circ\phi_{t,n})_e\underset{n\to+\infty}{\rightharpoonup}\mathcal{A}(\alpha_t)_e$ and thus $\mathcal{A}((\mathcal{C}u_n)\circ\phi_{t,n})_e-x_t\underset{n\to+\infty}{\rightharpoonup}\mathcal{A}(\alpha_t)_e-x_t$ in $L^2(\mathbb{R}^2)$. By the lower semi-continuity of the norm, we deduce that $\liminf_{n\to+\infty}\|\mathcal{A}((\mathcal{C}u_n)\circ\phi_{t,n})_e-x_t\|^2_{L^2(\mathbb{R}^2)}\geq\|\mathcal{A}(\alpha_t)_e-x_t\|^2_{L^2(\mathbb{R}^2)}$.
We now need to prove that $(\mathcal{C}u_n)\circ\phi_{t,n}^{-1}\circ\phi_{t,n}=\mathcal{C}u_n\underset{n\to+\infty}{\longrightarrow}\alpha_t\circ\bar{\phi}_t=\bar{U}$ in $L^p(\Omega)$ for all $t=1,\cdots,T$. We first have :

$$\begin{aligned}&\|(\mathcal{C}u_n)\circ\phi_{t,n}^{-1}\circ\phi_{t,n}-\alpha_t\circ\bar{\phi}_t\|_{L^p(\Omega)}\\&\leq\|(\mathcal{C}u_n)\circ\phi_{t,n}^{-1}\circ\phi_{t,n}-\alpha_t\circ\phi_{t,n}\|_{L^p(\Omega)}\\&+\|\alpha_t\circ\phi_{t,n}-\alpha_t\circ\bar{\phi}_t\|_{L^p(\Omega)}.\end{aligned}$$

We now focus on the first term and make the change of variable $y=\phi_{t,n}(x)\Leftrightarrow x=\phi_{t,n}^{-1}(y)$ and $dy=\det\nabla\phi_{t,n}(x)\,dx$, $dx=\frac{1}{\det\nabla\phi_{t,n}(\phi_{t,n}^{-1}(y))}\,dy$ :

$$\begin{aligned}&\int_\Omega|(\mathcal{C}u_n)\circ\phi_{t,n}^{-1}\circ\phi_{t,n}-\alpha_t\circ\phi_{t,n}|^p\,dx\\&=\int_\Omega|(\mathcal{C}u_n)\circ\phi_{t,n}^{-1}-\alpha_t|^p\frac{1}{|\det\nabla\phi_{t,n}(\phi_{t,n}^{-1}(y))|}\,dy,\\&\leq\|(\mathcal{C}u_n)\circ\phi_{t,n}^{-1}-\alpha_t\|^p_{L^{\frac{5p}{4}}(\Omega)}\left(\int_\Omega\frac{1}{|\det\nabla\phi_{t,n}(\phi_{t,n}^{-1}(y))|^5}\,dy\right)^{\frac{1}{5}},\\&\leq\|(\mathcal{C}u_n)\circ\phi_{t,n}^{-1}-\alpha_t\|^p_{L^{\frac{5p}{4}}(\Omega)}\left(\int_\Omega\frac{1}{|\det\nabla\phi_{t,n}(x))|^4}\,dx\right)^{\frac{1}{5}},\end{aligned}$$

using Hölder's inequality and making another change of variable. Since $(\mathcal{C}u_n)\circ\phi_{t,n}^{-1}\underset{n\to+\infty}{\longrightarrow}\alpha_t$ in $L^{\frac{5p}{4}}(\Omega)$, as $\frac{5p}{4}<2$, and $\|\frac{1}{\det\nabla\phi_{t,n}}\|_{L^4(\Omega)}$ is uniformly bounded, we deduce that $\int_\Omega|(\mathcal{C}u_n)\circ\phi_{t,n}^{-1}\circ\phi_{t,n}-\alpha_t\circ\phi_{t,n}|\,dx\underset{n\to+\infty}{\longrightarrow}0$.
According to [DDE12, Theorem 6.70], there exists a sequence $(\xi_t^k)_k$ of functions in $\mathcal{C}_c^\infty(\Omega)$ such that $\|\alpha_t-\xi_t^k\|_{L^1(\Omega)}\underset{k\to+\infty}{\longrightarrow}0$ and $\int_\Omega|\nabla\xi_t^k|\underset{k\to+\infty}{\longrightarrow}\int_\Omega|\nabla\alpha_t|+\int_{\partial\Omega}|\alpha_t|\,dx$ with

$\int_{\partial\Omega} |\alpha_t|\, dx = 0$ since $\alpha_t = 0$ on $\partial\Omega$, for all $t = 1, \cdots, T$. Thus $(\xi_t^k)$ is uniformly bounded according to $k$ in $BV(\Omega) \underset{c}{\subset} L^q(\Omega)$, for $q \in [1, 2[$, and therefore $\xi_t^k \underset{k\to+\infty}{\longrightarrow} \alpha_t$ in $L^q(\Omega)$ for $q \in [1, 2[$. Let $\varepsilon > 0$. Thus we fix $N \in \mathbb{N}^*$ such that $\|\xi_t^N - \alpha_t\|_{L^{\frac{5p}{4}}(\Omega)} \leq \frac{\varepsilon}{3}$. We now have :

$$\begin{aligned}
&\|\alpha_t \circ \phi_{t,n} - \alpha_t \circ \bar{\phi}_t\|_{L^p(\Omega)} \leq \|\alpha_t \circ \phi_{t,n} - \xi_t^N \circ \phi_{t,n}\|_{L^p(\Omega)} \\
&+ \|\xi_t^N \circ \phi_{t,n} - \xi_t^N \circ \bar{\phi}_t\|_{L^p(\Omega)} + \|\xi_t^N \circ \bar{\phi}_t - \alpha_t \circ \bar{\phi}_t\|_{L^p(\Omega)}, \\
&\leq \Big(\int_\Omega |\alpha_t - \xi_t^N|^p \frac{1}{|\det \nabla\phi_{t,n}(\phi_{t,n}^{-1}(y))|}\, dy\Big)^{\frac{1}{p}} \\
&+ L_\varepsilon \|\phi_{t,n} - \bar{\phi}_t\|_{L^p(\Omega,\mathbb{R}^2)} \\
&+ \Big(\int_\Omega |\xi_t^N - \alpha_t|^p \frac{1}{|\det \nabla\bar{\phi}_t(\bar{\phi}_t^{-1}(y))|}\, dy\Big)^{\frac{1}{p}},
\end{aligned}$$

with $L_\varepsilon$ the Lipschitz constant of $\xi_t^N$ since it belongs to $\mathcal{C}_c^\infty(\Omega)$ and so is Lipschitz continuous, and using a change of variable. As $\phi_{t,n} \underset{n\to+\infty}{\rightharpoonup} \bar{\phi}_t$ in $W^{1,4}(\Omega) \underset{c}{\subset} L^p(\Omega, \mathbb{R}^2)$, there exists $K \in \mathbb{N}^*$ such that for any $n \geq K$, $\|\phi_{t,n} - \bar{\phi}_t\|_{L^p(\Omega,\mathbb{R}^2)} \leq \frac{\varepsilon}{3L_\varepsilon}$. From now on, we assume $n$ satisfies $n \geq K$, and we use Hölder's inequality :

$$\begin{aligned}
&\|\alpha_t \circ \phi_{t,n} - \alpha_t \circ \bar{\phi}_t\|_{L^p(\Omega)} \leq \|\alpha_t - \xi_t^N\|_{L^{\frac{5p}{4}}(\Omega)} \\
&\left(\int_\Omega \frac{1}{|\det \nabla\phi_{t,n}(\phi_{t,n}^{-1}(y))|^5}\, dy\right)^{\frac{1}{5p}} + \frac{\varepsilon}{3} \\
&+ \|\xi_t^N - \alpha_t\|_{L^{\frac{5p}{4}}(\Omega)} \left(\int_\Omega \frac{1}{|\det \nabla\bar{\phi}_t(\bar{\phi}_t^{-1}(y))|^5}\, dy\right)^{\frac{1}{5p}}, \\
&\leq \frac{\varepsilon}{3} \left\|\frac{1}{\det \nabla\phi_{t,n}}\right\|_{L^4(\Omega)}^{\frac{4}{5p}} + \frac{\varepsilon}{3} + \frac{\varepsilon}{3} \left\|\frac{1}{\det \nabla\bar{\phi}_t}\right\|_{L^4(\Omega)}^{\frac{4}{5p}},
\end{aligned}$$

with $\|\frac{1}{\det \nabla\phi_{t,n}}\|_{L^4(\Omega)}$ uniformly bounded according to $n$ and $\|\frac{1}{\det \nabla\bar{\phi}_t}\|_{L^4(\Omega)}$ bounded from what precedes. So by letting $\varepsilon$ tend to 0, we obtain that $\int_\Omega |\alpha_t \circ \phi_{t,n} - \alpha_t \circ \bar{\phi}_t|^p\, dx \underset{n\to+\infty}{\longrightarrow} 0$ and consequently $(\mathcal{C}u_n) \circ \phi_{t,n}^{-1} \circ \phi_{t,n} = \mathcal{C}u_n \underset{n\to+\infty}{\longrightarrow} \alpha_t \circ \bar{\phi}_t$ for all $t = 1, \cdots, N$. By uniqueness of the limit, we have that $\bar{U} = \alpha_t \circ \bar{\phi}_t \Leftrightarrow \alpha_t = \bar{U} \circ \bar{\phi}_t^{-1}$ for all $t = 1, \cdots, T$ in $L^p(\Omega)$, with $\bar{U} \in L^p(\Omega)$ and $\bar{U} \circ \bar{\phi}_t^{-1} \in BV_{g_t,0}(\Omega)$.

We now set $\tilde{u}_n = \frac{1}{|\Omega'|} \int_{\Omega'} u_n\, dx$, and $u_{0,n} = u_n - \tilde{u}_n$. We clearly have $\int_{\Omega'} u_{0,n}\, dx = 0$ for all $n$, and $\mathrm{TV}(u_{0,n}) = \mathrm{TV}(u_n)$ is uniformly bounded thanks to the coercivity inequality. We denote this uniform bound by $\nu$. Thus using Poincaré-Wirtinger's inequality we obtain

$$\|u_{0,n}\|_{L^1(\Omega')} \leq c_1\, \mathrm{TV}(u_{0,n}) \leq c_1 \nu,$$

with $c_1 > 0$. We now need a bound for $\|\mathcal{C}\tilde{u}_n\|_{L^p(\Omega)}$:

$$\begin{aligned}
&\|\mathcal{C}\tilde{u}_n\|^2_{L^p(\Omega)} - 2\|\mathcal{C}\tilde{u}_n\|_{L^p(\Omega)}\|\mathcal{C}\|_{\mathscr{L}(L^1(\Omega'),L^p(\Omega))}\|u_{0,n}\|_{L^1(\Omega')}\\
&\leq \|\mathcal{C}\tilde{u}_n\|^2_{L^p(\Omega)} - 2\|\mathcal{C}\tilde{u}_n\|_{L^p(\Omega)}\|\mathcal{C}u_{0,n}\|_{L^p(\Omega)},\\
&\leq (\|\mathcal{C}\tilde{u}_n\|_{L^p(\Omega)} - \|\mathcal{C}u_{0,n}\|_{L^p(\Omega)})^2,\\
&\leq \|\mathcal{C}(\tilde{u}_n + u_{0,n})\|^2_{L^p(\Omega)},\\
&\leq \|\mathcal{C}u_n\|^2_{L^p(\Omega)} \leq c_2^2 < +\infty,
\end{aligned}$$

as $\mathcal{C}u_n$ strongly converges in $L^p(\Omega)$. Besides, we have $\|\mathcal{C}\|_{\mathscr{L}(L^1(\Omega'),L^p(\Omega))}\|u_{0,n}\|_{L^1(\Omega')} \leq \|\mathcal{C}\|_{\mathscr{L}(L^1(\Omega'),L^p(\Omega))}c_1\nu = c_3 < +\infty$ and thus $\|\mathcal{C}\tilde{u}_n\|_{L^p(\Omega)} \leq 2\sqrt{c_3^2 + c_2^2}$. But we also know that $\|\mathcal{C}\tilde{u}_n\|_{L^p(\Omega)} = \frac{1}{|\Omega'|}|\int_{\Omega'} u_n\,dx|\|\mathcal{C}\mathbb{1}\|_{L^p(\Omega)} \leq 2\sqrt{c_2^2 + c_3^2}$. Since $\mathcal{C}\mathbb{1} \neq 0$, we have $\frac{1}{|\Omega'|}|\int_{\Omega'} u_n\,dx| \leq \frac{2\sqrt{c_2^2+c_3^2}}{\|\mathcal{C}\mathbb{1}\|_{L^p(\Omega)}} = c_4 < +\infty$. We therefore have

$$\begin{aligned}
\|u_n\|_{L^1(\Omega')} &\leq \|u_{0,n} + \frac{1}{|\Omega'|}|\int_{\Omega'} u_n\,dx|\|_{L^1(\Omega')},\\
&\leq \|u_{0,n}\|_{L^1(\Omega')} + |\int_{\Omega'} u_n\,dx|,\\
&\leq c_1\nu + c_4|\Omega'| < +\infty.
\end{aligned}$$

Thus $u_n$ is uniformly bounded according to $n$ in $BV(\Omega')$ and there exists a subsequence still denoted $(u_n)$ such that $u_n \underset{n\to+\infty}{\longrightarrow} \bar{u}$ in $L^1(\Omega')$ with $\bar{u} \in BV(\Omega')$. By continuity of the operator $\mathcal{C}$ and the uniqueness of the limit, we deduce that $\mathcal{C}u_n \underset{n\to+\infty}{\longrightarrow} \mathcal{C}\bar{u} = \bar{U}$ in $L^p(\Omega)$. By the semi-continuity theorem, we get $\mathrm{TV}(\bar{u}) \leq \liminf_{n\to+\infty} \mathrm{TV}(u_n)$.
By combining all the results, we obtain that $+\infty > \inf_{(u,(\phi_t)_{t=1,\cdots,T})\in\mathscr{U}} G(u,(\phi_t)_{t=1,\cdots,T}) = \liminf_{n\to+\infty} G(u_n,(\phi_{t,n})_{t=1,\cdots,T}) \geq \frac{1}{T}\sum_{t=1}^{T}\delta\,\mathrm{TV}_{g_t}((\mathcal{C}\bar{u})\circ\bar{\phi}_t^{-1}) + \frac{1}{2}\|\mathcal{A}((\mathcal{C}\bar{u})\circ\bar{\phi}_t^{-1})_e - x_t\|^2_{L^2(\mathbb{R}^2)} + \int_\Omega W_{Op}(\nabla\bar{\phi}_t)\,dx + \alpha\,\mathrm{TV}(\bar{u})$. It thus means that $\det\nabla\bar{\phi}_t \in L^4(\Omega)$, $\frac{1}{\det\nabla\bar{\phi}_t} \in L^4(\Omega)$, and $\det\nabla\bar{\phi}_t > 0$ almost everywhere in $\Omega$ for all $t = 1,\cdots,T$. Indeed, since $W_{Op}(\nabla\bar{\phi}_t(x), \det\nabla\bar{\phi}_t(x)) = +\infty$ when $\det\nabla\bar{\phi}_t(x) \leq 0$, it means that the set on which it happens must be of null measure otherwise we would have $\int_\Omega W_{Op}(\nabla\bar{\phi}_t, \det\nabla\bar{\phi}_t)\,dx = +\infty$. Also, by applying the same reasoning for each $\phi_{t,n}$, we prove that $\bar{\phi}_t$ is a bi-Hölder homeomorphism and have that $\bar{\phi}_t \in \mathscr{W}$ for each $t = 1,\cdots,T$.
We thus have proved the existence of minimisers for our problem (5.7).

□

# Bibliography


[AAF99] John Ashburner, Jesper LR Andersson, and Karl J Friston. High-dimensional image registration using symmetric priors. *NeuroImage*, 9(6):619–628, 1999. (Cited on page 20.)

[ABMB+15] Jalal B Andre, Brian W Bresnahan, Mahmud Mossa-Basha, Michael N Hoff, C Patrick Smith, Yoshimi Anzai, and Wendy A Cohen. Toward quantifying the prevalence, severity, and cost associated with patient motion during clinical mr examinations. *Journal of the American College of Radiology*, 12(7):689–695, 2015. (Cited on page 86.)

[ADS] Ganesh Adluru, Edward VR DiBella, and Matthias C Schabel. Model-based registration for dynamic cardiac perfusion MRI. *Journal of Magnetic Resonance Imaging. 2006;24(5):1062-70.* (Cited on page 88.)

[AEB06] Michal Aharon, Michael Elad, and Alfred Bruckstein. K-svd: An algorithm for designing overcomplete dictionaries for sparse representation. *IEEE Transactions on signal processing*, 54(11):4311–4322, 2006. (Cited on page 15.)

[AFP00a] L. Ambrosio, N. Fusco, and D. Pallara. *Functions of bounded variation and free discontinuity problems*. Oxford Mathematical Monographs. The Clarendon Press, Oxford University Press, New York, 2000. (Cited on pages 11 and 117.)

[AFP00b] Luigi Ambrosio, Nicola Fusco, and Diego Pallara. *Functions of bounded variation and free discontinuity problems*, volume 254. Clarendon Press Oxford, 2000. (Cited on page 31.)

[ARWGS18] Angelica I Aviles-Rivero, Guy Williams, Martin J Graves, and Carola-Bibiane Schönlieb. Compressed sensing plus motion (CS+M): A new perspective for improving undersampled MR image reconstruction. *arXiv preprint arXiv:1810.10828*, 2018. (Cited on pages 4, 87, 88, and 113.)

[AT90] Luigi Ambrosio and Vincenzo Maria Tortorelli. Approximation of functional depending on jumps by elliptic functional via t-convergence. *Communications on Pure and Applied Mathematics*, 43(8):999–1036, 1990. (Cited on page 30.)

[Axe84] L Axel. Blood flow effects in magnetic resonance imaging. *American Journal of Roentgenology*, 143(6):1157–1166, dec 1984. URL: https://doi.org/10.2214/ajr.143.6.1157, doi:10.2214/ajr.143.6.1157. (Cited on page 63.)

[Bal81a] J. M. Ball. Global invertibility of sobolev functions and the interpenetration of matter. *Proceedings of the Royal Society of Edinburgh: Section A Mathematics*, 88(3-4):315–328, 1981. (Cited on pages 91 and 127.)

[Bal81b] J. M. Ball. Global invertibility of Sobolev functions and the interpenetration of matter. *P Roy Soc Edinb A*, 88(3-4):315–328, 1981. (Cited on pages 92 and 128.)

[Bal01] A. Baldi. Weighted BV functions. *Houston Journal of Mathematics*, 27(3):683–705, 2001. (Cited on pages 93, 127, and 129.)

[BB01] Martin Benning and Martin Burger. Ground states and singular vectors of convex variational regularization methods. *Methods and Applications of Analysis*, 20(4):295–334, December 201. (Cited on page 29.)

[BB18] M. Benning and M. Burger. Modern regularization methods for inverse problems. *Acta Numerica*, 27:1–111, 2018. doi:10.1017/S0962492918000016. (Cited on page 12.)

[BBES17] Martin Benning, Marta M. Betcke, Matthias J. Ehrhardt, and Carola-Bibiane Schönlieb. Choose your path wisely: gradient descent in a Bregman distance framework. *arXiv preprint arXiv:1712.04045*, 2017. (Cited on pages 41, 47, 50, 74, and 76.)

[BC98] P. Blomgren and T. F. Chan. Color tv: total variation methods for restoration of vector-valued images. *IEEE Transactions on Image Processing*, 7(3):304–309, March 1998. doi:10.1109/83.661180. (Cited on page 13.)

[BCB04] Rasmus M Birn, Robert W Cox, and Peter A Bandettini. Experimental designs and processing strategies for fmri studies involving overt verbal responses. *Neuroimage*, 23(3):1046–1058, 2004. (Cited on page 86.)

[BCH+14] Robert W Brown, Y-C Norman Cheng, E Mark Haacke, Michael R Thompson, and Ramesh Venkatesan. *Magnetic resonance imaging: physical principles and sequence design*. John Wiley & Sons, 2014. (Cited on pages 14 and 23.)

[BDF+17] Martin Burger, Hendrik Dirks, Lena Frerking, Andreas Hauptmann, Tapio Helin, and Samuli Siltanen. A variational reconstruction method for undersampled dynamic x-ray tomography based on physical motion models. *Inverse Problems*, 33(12):124008, 2017. (Cited on page 4.)

[BDS18] M. Burger, H. Dirks, and C. Schönlieb. A variational model for joint motion estimation and image reconstruction. *SIAM Journal on Imaging Sciences*, 11(1):94–128, 2018. doi:10.1137/16M1084183. (Cited on pages 4 and 88.)

[BF02] J. Modersitzki B. Fischer. Fast Diffusion Registration. *AMS Contemporary Mathematics, Inverse Problems, Image Analysis and Medical Imaging*, 2002. (Cited on page 19.)

[BF03] J. Modersitzki B. Fischer. Curvature based Image Registration. *JMIV*, 2003. (Cited on page 19.)

[BGH+14] Martin Benning, Lynn Gladden, Daniel Holland, Carola-Bibiane Schönlieb, and Tuomo Valkonen. Phase reconstruction from velocity-encoded MRI measurements–a survey of sparsity-promoting variational approaches. *Journal of Magnetic Resonance*, 238:26–43, 2014. (Cited on pages 29, 30, and 72.)

[BK04] Y. Boykov and V. Kolmogorov. An experimental comparison of min-cut/max- flow algorithms for energy minimization in vision. *IEEE Transactions on Pattern Analysis and Machine Intelligence*, 26(9):1124–1137, Sep. 2004. doi:10.1109/TPAMI.2004.60. (Cited on page 16.)

[BKL+09] Leif Boysen, Angela Kempe, Volkmar Liebscher, Axel Munk, Olaf Wittich, et al. Consistencies and rates of convergence of jump-penalized least squares estimators. *The Annals of Statistics*, 37(1):157–183, 2009. (Cited on page 30.)

[BKM+17] Christian F. Baumgartner, Christoph Kolbitsch, Jamie R. McClelland, Daniel Rueckert, and Andrew P. King. Autoadaptive motion modelling for MR-based respiratory motion estimation. *Medical Image Analysis*, 35:83 – 100, 2017. (Cited on page 98.)

[BLMV10] A. Buades, T. M. Le, J. Morel, and L. A. Vese. Fast cartoon + texture image filters. *IEEE Transactions on Image Processing*, 19(8):1978–1986, Aug 2010. doi:10.1109/TIP.2010.2046605. (Cited on page 13.)

[Blo08] T Block. Advanced methods for radial data sampling in mri. *Georg-August-Universitaet Goettingen*, 2008. (Cited on page 15.)

[BLZ+08] Mario Bertero, Henri Lantéri, Luca Zanni, et al. Iterative image reconstruction: a point of view. *Mathematical Methods in Biomedical Imaging and Intensity-Modulated Radiation Therapy (IMRT)*, 7:37–63, 2008. (Cited on page 14.)

[BMMK+10] Moritz Blume, Axel Martinez-Moller, Andreas Keil, Nassir Navab, and Magdalena Rafecas. Joint reconstruction of image and motion in gated positron emission tomography. *IEEE Transactions on Medical Imaging*, 29(11):1892–1906, 2010. (Cited on pages 4, 87, and 88.)

[BMTV05] Dale L Bailey, Michael N Maisey, David W Townsend, and Peter E Valk. *Positron emission tomography*. Springer, 2005. (Cited on page 14.)

[BMTY05] M Faisal Beg, Michael I Miller, Alain Trouvé, and Laurent Younes. Computing large deformation metric mappings via geodesic flows of diffeomorphisms. *International journal of computer vision*, 61(2):139–157, 2005. (Cited on page 19.)

[Bre67] Lev M Bregman. The relaxation method of finding the common point of convex sets and its application to the solution of problems in convex programming. *USSR computational mathematics and mathematical physics*, 7(3):200–217, 1967. (Cited on pages 29 and 74.)

[Bré83] H. Brézis. *Analyse fonctionelle:*. Collection Mathématiques appliquées pour la maîtrise. 1983. (Cited on page 129.)

[Bre10] H. Brezis. *Functional Analysis, Sobolev Spaces and Partial Differential Equations*. Universitext. Springer New York, 2010. doi:10.1007/978-0-387-70914-7. (Cited on pages 11 and 117.)

[Bro81] C. Broit. *Optimal Registration of Deformed Images*. PhD thesis, Computer and Information Science, University of Pensylvania, 1981. (Cited on page 19.)

[BRZ16] Martin Burger, Carolin Rossmanith, and Xiaoqun Zhang. Simultaneous reconstruction and segmentation for dynamic SPECT imaging. *Inverse Problems*, 32(10):104002, 2016. URL: http://stacks.iop.org/0266-5611/32/i=10/a=104002. (Cited on pages 4, 35, and 37.)

[BSD15] Mark A Brown, Richard C Semelka, and Brian M Dale. *MRI: basic principles and applications*. John Wiley & Sons, 2015. (Cited on page 85.)

[BST14] Jérôme Bolte, Shoham Sabach, and Marc Teboulle. Proximal alternating linearized minimization for nonconvex and nonsmooth problems. *Mathematical Programming*, 146(1-2):459–494, 2014. (Cited on pages 47, 48, and 74.)

[BSW+11] Çağdaş Bilen, Ivan Selesnick, Yao Wang, Ricardo Otazo, and Daniel K Sodickson. A motion compensating prior for dynamic mri reconstruction using combination of compressed sensing and parallel imaging. In *2011 IEEE Signal Processing in Medicine and Biology Symposium (SPMB)*, pages 1–6. IEEE, 2011. (Cited on page 2.)

[BT09] A. Beck and M. Teboulle. Fast gradient-based algorithms for constrained total variation image denoising and deblurring problems. *IEEE Transactions on Image Processing*, 18(11):2419–2434, Nov 2009. doi:10.1109/TIP.2009.2028250. (Cited on page 13.)

[BUF07] Kai Tobias Block, Martin Uecker, and Jens Frahm. Undersampled radial mri with multiple coils. iterative image reconstruction using a total variation constraint. *Magnetic resonance in medicine.*, 57(6):1086–1098, 2007. (Cited on page 15.)

[Bur82] C.T. Burt. NMR measurements and flow. *Journal of Nuclear Medicine*, 23(11):1044–1045, 1982. cited By 6. URL: https://www.scopus.com/inward/record.uri?eid=2-s2.0-0020381764&partnerID=40&md5=73569943618e9eab0ca41607e12f8b4f. (Cited on page 63.)

[Buz08] Thorsten M. Buzug. Computed tomography from photon statistics to modern cone-beam ct, 2008. URL: http://www.amazon.de/Computed-Tomography-Photon-Statistics-Cone-Beam/dp/3540394079. (Cited on page 14.)

[BV04] Stephen Boyd and Lieven Vandenberghe. *Convex Optimization*. Cambridge University Press, New York, NY, USA, 2004. (Cited on pages 117 and 118.)

[BVZ01a] Y. Boykov, O. Veksler, and R. Zabih. Fast approximate energy minimization via graph cuts. *IEEE Transactions on Pattern Analysis and Machine Intelligence*, 23(11):1222–1239, Nov 2001. doi:10.1109/34.969114. (Cited on page 16.)

[BVZ01b] Yuri Boykov, Olga Veksler, and Ramin Zabih. Fast approximate energy minimization via graph cuts. *IEEE Transactions on pattern analysis and machine intelligence*, 23(11):1222–1239, 2001. (Cited on page 16.)

[Cal93] Paul T. Callaghan. *Principles of Nuclear Magnetic Resonance Microscopy*. Oxford science publications. Clarendon Press, 1993. URL: https://books.google.it/books?id=yjrjT_W5hygC. (Cited on page 65.)

[Cal99] Paul T Callaghan. Rheo-NMR: nuclear magnetic resonance and the rheology of complex fluids. *Reports on Progress in Physics*, 62(4):599, 1999. (Cited on page 64.)

[Cal11] P. T. Callaghan. *Translational Dynamics and Magnetic Resonance*. Oxford University Press, 2011. (Cited on page 63.)

[Car97] Rich Caruana. Multitask learning. *Machine learning*, 28(1):41–75, 1997. (Cited on page 4.)

[CARD+19a] Veronica Corona, Angelica I Aviles-Rivero, Noémie Debroux, Martin Graves, Carole Le Guyader, Carola-Bibiane Schönlieb, and Guy Williams. Multi-tasking to correct: Motion-compensated mri via joint reconstruction and registration. In *International Conference on Scale Space and Variational Methods in Computer Vision*, pages 263–274. Springer, 2019. (Cited on pages 7, 85, and 90.)

[CARD+19b] Veronica Corona, Angelica I Aviles-Rivero, Noémie Debroux, Carole Le Guyader, and Carola-Bibiane Schönlieb. Variational multi-task MRI reconstruction: Joint reconstruction, registration and super-resolution. *ArXiv e-prints*, 2019. arXiv:1908.05911. (Cited on pages 7 and 85.)

[CBE+19] Veronica Corona, Martin Benning, Matthias Joachim Ehrhardt, Lynn Faith Gladden, Richard Mair, Andi Reci, Andrew J Sederman, Stefanie Reichelt, and Carola-Bibiane Schönlieb. Enhancing joint reconstruction and segmentation with non-convex Bregman iteration. *Inverse Problems*, 2019. URL: http://iopscience.iop.org/10.1088/1361-6420/ab0b77. (Cited on pages 5, 25, 64, 72, 73, and 92.)

[CBG+19] Veronica Corona, Martin Benning, Lynn F. Gladden, Andi Reci, Andrew J Sederman, and Carola-Bibiane Schönlieb. Joint phase reconstruction and magnitude segmentation from velocity-encoded MRI data. *ArXiv e-prints*, 2019. arXiv:1908.05285. (Cited on pages 6 and 63.)

[CBP+14] Jose Caballero, Wenjia Bai, Anthony N. Price, Daniel Rueckert, , and Joseph V. Hajnal. Application-driven MRI: Joint reconstruction and segmentation from undersampled MRI data. *Med Image Comput Comput Assist Interv;17(Pt 1):106-13.*, 2014. (Cited on pages 4, 37, and 38.)

[CC98] T. F. Chan and Chiu-Kwong Wong. Total variation blind deconvolution. *IEEE Transactions on Image Processing*, 7(3):370–375, March 1998. doi:10.1109/83.661187. (Cited on page 13.)

[CCP12a] A. Chambolle, D. Cremers, and T. Pock. A convex approach to minimal partitions. *SIAM Journal on Imaging Sciences*, 5(4):1113–1158, 2012. URL: https://doi.org/10.1137/110856733, arXiv:https://doi.org/10.1137/110856733, doi:10.1137/110856733. (Cited on page 17.)

[CCP12b] Antonin Chambolle, Daniel Cremers, and Thomas Pock. A convex approach to minimal partitions. *SIAM Journal on Imaging Sciences*, 5(4):1113–1158, 2012. (Cited on page 39.)

[CDAR+19] Veronica Corona, Noémie Debroux, Williams Guy Aviles-Rivero, Angelica I, Martin Graves, Le Guyader, and Carola-Bibiane Carole Schönlieb. Motion correction resolved for mri via multi-tasking: A simultaneous reconstruction and registration approach. 27(4487), 2019. doi:https://doi.org/10.17863/CAM.41909. (Cited on pages 7, 85, and 90.)

[CEN06] Tony F. Chan, Selim Esedoglu, and Mila Nikolova. Algorithms for finding global minimizers of image segmentation and denoising models. *SIAM journal on applied mathematics*, 66(5):1632–1648, 2006. (Cited on pages 31 and 73.)

[Cha94] Jeffrey J. Chalmers. Cells and bubbles in sparged bioreactors. In *Cell Culture Engineering IV*, pages 311–320. Springer, 1994. (Cited on page 51.)

[Cha95] Antonin Chambolle. Image segmentation by variational methods: Mumford and shah functional and the discrete approximations. *SIAM Journal on Applied Mathematics*, 55(3):827–863, 1995. (Cited on page 30.)

[Cha04] Antonin Chambolle. An algorithm for total variation minimization and applications. *J Math Imaging Vis*, 20(1):89–97, 2004. (Cited on page 96.)

[Chr94] G.E. Christensen. *Deformable Shape Models for Anatomy*. PhD thesis, Sever Institute of Technology, Washington University, 1994. (Cited on page 19.)

[CKS97] Vicent Caselles, Ron Kimmel, and Guillermo Sapiro. Geodesic active contours. *International Journal of Computer Vision*, 22(1):61–79, Feb 1997. URL: https://doi.org/10.1023/A:1007979827043, doi:10.1023/A:1007979827043. (Cited on page 16.)

[CKS01] Tony F. Chan, Sung Ha Kang, and Jianhong Shen. Total variation denoising and enhancement of color images based on the cb and hsv color models. *Journal of Visual Communication and Image Representation*, 12(4):422 – 435, 2001. URL: http://www.sciencedirect.com/science/article/pii/S1047320301904912, doi:https://doi.org/10.1006/jvci.2001.0491. (Cited on page 13.)

[CL97] Antonin Chambolle and Pierre-Louis Lions. Image recovery via total variation minimization and related problems. *Numerische Mathematik*, 76(2):167–188, Apr 1997. URL: https://doi.org/10.1007/s002110050258, doi:10.1007/s002110050258. (Cited on page 13.)

[CP11a] Antonin Chambolle and Thomas Pock. A first-order primal-dual algorithm for convex problems with applications to imaging. *J Math Imaging Vis 40: 120. doi:10.1007/s10851-010-0251-1*, 2011. (Cited on pages 38, 39, 96, 120, and 121.)

[CP11b] Antonin Chambolle and Thomas Pock. A first-order primal-dual algorithm for convex problems with applications to imaging. *Journal of mathematical imaging and vision*, 40(1):120–145, 2011. (Cited on page 75.)

[CP14] H. Chavez-Roman and V. Ponomaryov. Super resolution image generation using wavelet domain interpolation with edge extraction via a sparse representation. *IEEE Geoscience and Remote Sensing Letters*, 11(10):1777–1781, October 2014. doi:10.1109/LGRS.2014.2308905. (Cited on page 21.)

[CP16] Antonin Chambolle and Thomas Pock. An introduction to continuous optimization for imaging. *Acta Numerica*, 25:161–319, 2016. (Cited on pages 12, 38, and 120.)

[CR03] Haili Chui and Anand Rangarajan. A new point matching algorithm for non-rigid registration. *Computer Vision and Image Understanding*, 89(2-3):114–141, 2003. (Cited on page 18.)

[CRM96a] G. E. Christensen, R. D. Rabbitt, and M. I. Miller. Deformable templates using large deformation kinematics. *IEEE Transactions on Image Processing*, 5(10):1435–1447, Oct 1996. doi:10.1109/83.536892. (Cited on pages 20 and 96.)

[CRM+96b] Gary E Christensen, Richard D Rabbitt, Michael I Miller, et al. Deformable templates using large deformation kinematics. *IEEE transactions on image processing*, 5(10):1435–1447, 1996. (Cited on page 18.)

[CRT04] Emmanuel Candes, Justin Romberg, and Terence Tao. Robust uncertainty principles: Exact signal reconstruction from highly incomplete frequency information. *arXiv preprint math/0409186*, 2004. (Cited on page 70.)

[CRT06a] Emmanuel J. Candès, Justin Romberg, and Terence Tao. Robust uncertainty principles: Exact signal reconstruction from highly incomplete frequency information. *IEEE Transactions on information theory*, 52(2):489–509, 2006. (Cited on pages 14 and 25.)

[CRT06b] Emmanuel J. Candès, Justin Romberg, and Terence Tao. Robust uncertainty principles: Exact signal reconstruction from highly incomplete frequency information. *IEEE Transactions on information theory*, 52(2):489–509, 2006. (Cited on page 14.)

[CS05] Tony F. Chan and Jianhong (Jackie) Shen. Variational image inpainting. *Communications on Pure and Applied Mathematics*, 58(5):579–619, 2005. URL: https://onlinelibrary.wiley.com/doi/abs/10.1002/cpa.20075, arXiv:https://onlinelibrary.wiley.com/doi/pdf/10.1002/cpa.20075, doi:10.1002/cpa.20075. (Cited on page 13.)

[CSB+05] Olivier Clatz, Maxime Sermesant, P-Y Bondiau, Hervé Delingette, Simon K Warfield, Grégoire Malandain, and Nicholas Ayache. Realistic simulation of the 3-d growth of brain tumors in mr images coupling diffusion with biomechanical deformation. *IEEE transactions on medical imaging*, 24(10):1334–1346, 2005. (Cited on page 18.)

[CT65] James W. Cooley and John W. Tukey. An algorithm for the machine calculation of complex fourier series. *Mathematics of Computation*, 19(90):297–301, 1965. URL: http://www.jstor.org/stable/2003354. (Cited on page 70.)

[CV01] Tony F. Chan and Luminita A. Vese. Active contours without edges. *IEEE Transactions on Image Processing*, 10(2):266–277, 2001. (Cited on pages 17, 30, and 73.)

[CZ00] D. P. Capel and A. Zisserman. Super-resolution enhancement of text image sequences. In *International Conference on Pattern Recognition*, pages 600–605, 2000. (Cited on page 21.)

[CZ03] D. Capel and A. Zisserman. Computer vision applied to super resolution. *IEEE Signal Processing Magazine*, 20(3):75–86, May 2003. doi:10.1109/MSP.2003.1203211. (Cited on page 21.)

[Dac08] B. Dacorogna. *Direct Methods in the Calculus of Variations, Second Edition*. Springer, 2008. (Cited on page 128.)

[DDE12] F. Demengel, G. Demengel, and R. Erné. *Functional Spaces for the Theory of Elliptic Partial Differential Equations*. Universitext. Springer London, 2012. (Cited on page 129.)

[DEB18] Yehuda Dar, Michael Elad, and Alfred M Bruckstein. Optimized pre-compensating compression. *IEEE Transactions on Image Processing*, 27(10):4798–4809, 2018. (Cited on page 115.)

[DF92] Wolf-Dieter Deckwer and Robert W. Field. *Bubble column reactors*, volume 200. Wiley New York, 1992. (Cited on page 51.)

[DG18] N. Debroux and C. Guyader. A joint segmentation/registration model based on a nonlocal characterization of weighted total variation and non-local shape descriptors. *SIAM Journal on Imaging Sciences*, 11(2):957–990, 2018. URL: https://doi.org/10.1137/17M1122906, arXiv:https://doi.org/10.1137/17M1122906, doi:10.1137/17M1122906. (Cited on page 4.)

[DKFH97] Malcolm H Davis, Alireza Khotanzad, Duane P Flamig, and Steven E Harms. A physics-based coordinate transformation for 3-d image matching. *IEEE transactions on medical imaging*, 16(3):317–328, 1997. (Cited on page 18.)

[DLG14] Ratiba Derfoul and Carole Le Guyader. A relaxed problem of registration based on the saint venant–kirchhoff material stored energy for the mapping of mouse brain gene expression data to a neuroanatomical mouse atlas. *SIAM Journal on Imaging Sciences*, 7(4):2175–2195, 2014. (Cited on page 18.)

[DM90] Bernard Dacorogna and Jürgen Moser. On a partial differential equation involving the jacobian determinant. In *Annales de l'Institut Henri Poincare (C) Non Linear Analysis*, volume 7, pages 1–26. Elsevier, 1990. (Cited on page 20.)

[DOLG17] Noémie Debroux, Solène Ozeré, and Carole Le Guyader. A non-local topology-preserving segmentation-guided registration model. *Journal of Mathematical Imaging and Vision*, 59(3):432–455, 2017. (Cited on page 4.)

[Don06] David L. Donoho. Compressed sensing. *IEEE Transactions on information theory*, 52(4):1289–1306, 2006. (Cited on pages 14, 25, and 70.)

[DRR+07] Olaf Dietrich, José G. Raya, Scott B. Reeder, Maximilian F. Reiser, and Stefan O. Schoenberg. Measurement of signal-to-noise ratios in mr images: Influence of multichannel coils, parallel imaging, and reconstruction filters. *Journal of Magnetic Resonance Imaging*, 26(2):375–385, 2007. URL: https://onlinelibrary.wiley.com/doi/abs/10.1002/jmri.20969, arXiv:https://onlinelibrary.wiley.com/doi/

pdf/10.1002/jmri.20969, doi:10.1002/jmri.20969. (Cited on page 14.)

[dVBV+17a] Bob D de Vos, Floris F Berendsen, Max A Viergever, Marius Staring, and Ivana Išgum. End-to-end unsupervised deformable image registration with a convolutional neural network. In *Deep Learning in Medical Image Analysis and Multimodal Learning for Clinical Decision Support*, pages 204–212. Springer, 2017. (Cited on page 18.)

[dVBV+17b] Bob D de Vos, Floris F Berendsen, Max A Viergever, Marius Staring, and Ivana Išgum. End-to-end unsupervised deformable image registration with a convolutional neural network. In *Deep Learning in Medical Image Analysis and Multimodal Learning for Clinical Decision Support*, pages 204–212. 2017. (Cited on page 89.)

[EA07] Christopher J. Elkins and Marcus T. Alley. Magnetic resonance velocimetry: applications of magnetic resonance imaging in the measurement of fluid motion. *Experiments in Fluids*, 43(6):823–858, Dec 2007. URL: https://doi.org/10.1007/s00348-007-0383-2, doi:10.1007/s00348-007-0383-2. (Cited on page 63.)

[EB16] Matthias J. Ehrhardt and Marta M. Betcke. Multi-contrast MRI reconstruction with structure-guided total variation. *SIAM Journal on Imaging Sciences*, 9(3):1084–1106, 2016. URL: http://arxiv.org/abs/1511.06631http://epubs.siam.org/doi/10.1137/15M1047325, arXiv:1511.06631, doi:10.1137/15M1047325. (Cited on pages 23 and 28.)

[EF97] Michael Elad and Arie Feuer. Restoration of a single superresolution image from several blurred, noisy, and undersampled measured images. *IEEE transactions on image processing*, 6(12):1646–1658, 1997. (Cited on page 21.)

[EG91] L.C. Evans and R.F. Gariepy. *Measure Theory and Fine Properties of Functions*. CRC Press, 1991. doi:10.1201/b18333. (Cited on pages 11 and 117.)

[EHN96] H.W. Engl, M. Hanke, and A. Neubauer. *Regularization of Inverse Problems*. Mathematics and Its Applications. Springer Netherlands, 1996. (Cited on pages 11 and 12.)

[EHO01] Michael Elad and Yacov Hel-Or. A fast super-resolution reconstruction algorithm for pure translational motion and common space-invariant blur. *IEEE Transactions on Image Processing*, 10(8):1187–1193, 2001. (Cited on page 21.)

[EK12] Yonina C Eldar and Gitta Kutyniok. *Compressed sensing: theory and applications*. Cambridge university press, 2012. (Cited on page 14.)

[EKR11] Ronny Ramlau Esther Klann and Wolfgang Ring. A Mumford-Shah level-set approach for the inversion and segmentation of SPECT/CT data. *Inverse Problems and Imaging, 5, 1, 137 - 166*, 2011. (Cited on page 34.)

[ET99] I. Ekeland and R. Témam. *Convex Analysis and Variational Problems*. Society for Industrial and Applied Mathematics, 1999. doi:10.1137/1.9781611971088. (Cited on pages 117 and 118.)

[Eva98] L.C. Evans. *Partial Differential Equations*, volume 19 of *Graduate studies in mathematics*. American Mathematical Society, 1998. doi:10.1090/gsm/019. (Cited on page 118.)

[EZC10] Ernie Esser, Xiaoqun Zhang, and Tony F. Chan. A general framework for a class of first order primal-dual algorithms for convex optimization in imaging science. *SIAM Journal on Imaging Sciences*, 3(4):1015–1046, 2010. (Cited on pages 38, 75, and 120.)

[Fes10] J. A. Fessler. Optimization transfer approach to joint registration / reconstruction for motion-compensated image reconstruction. In *2010 IEEE International Symposium on Biomedical Imaging: From Nano to Macro*, pages 596–599, April 2010. doi:10.1109/ISBI.2010.5490108. (Cited on page 89.)

[FH04] Pedro F Felzenszwalb and Daniel P Huttenlocher. Efficient graph-based image segmentation. *International journal of computer vision*, 59(2):167–181, 2004. (Cited on page 16.)

[FN04] J. A. Fessler and D. C. Noll. Iterative image reconstruction in MRI with separate magnitude and phase regularization. In *Proc. 2nd IEEE Int. Symp. Biomedical Imaging: Nano to Macro (IEEE Cat No. 04EX821)*, pages 209–212 Vol. 1, April 2004. doi:10.1109/ISBI.2004.1398511. (Cited on page 72.)

[FS03] J. A. Fessler and B. P. Sutton. Nonuniform fast fourier transforms using min-max interpolation. *IEEE Transactions on Signal Processing*, 51(2):560–574, Feb 2003. doi:10.1109/TSP.2002.807005. (Cited on page 70.)

[Fuk99] Eiichi Fukushima. Nuclear magnetic resonance as a tool to study flow. *Annual Review of Fluid Mechanics*, 31(1):95–123, 1999. URL: https://doi.org/10.1146/annurev.fluid.31.1.95, arXiv:https://doi.org/10.1146/annurev.fluid.31.1.95, doi:10.1146/annurev.fluid.31.1.95. (Cited on pages 63 and 64.)

[GAM02] B. K. Gunturk, Y. Altunbasak, and R. M. Mersereau. Multiframe resolution-enhancement methods for compressed video. *IEEE Signal Processing Letters*, 9(6):170–174, June 2002. doi:10.1109/LSP.2002.800503. (Cited on page 21.)

[GBK08] Urs Gamper, Peter Boesiger, and Sebastian Kozerke. Compressed sensing in dynamic mri. *Magnetic Resonance in Medicine*, 59(2):365–373, 2008. URL: https://onlinelibrary.wiley.com/doi/abs/10.1002/mrm.21477, arXiv:https://onlinelibrary.wiley.com/doi/pdf/10.1002/mrm.21477, doi:10.1002/mrm.21477. (Cited on page 22.)

[GC11] Jaideva C Goswami and Andrew K Chan. *Fundamentals of wavelets: theory, algorithms, and applications*. John Wiley & Sons, 2011. (Cited on page 15.)

[GDC05] Guofang Tu, Derong Liu, and Can Zhang. A new compression algorithm for medical images using wavelet transform. In *Proceedings. 2005 IEEE Networking, Sensing and Control, 2005.*, pages 84–89, March 2005. doi:10.1109/ICNSC.2005.1461166. (Cited on page 15.)

[GDCM17] Jonas Geiping, Hendrik Dirks, Daniel Cremers, and Michael Moeller. Multiframe motion coupling for video super resolution. In *International Workshop on Energy Minimization Methods in Computer Vision and Pattern Recognition*, pages 123–138. Springer, 2017. (Cited on page 21.)

[GDDM16] R. Girshick, J. Donahue, T. Darrell, and J. Malik. Region-based convolutional networks for accurate object detection and segmentation. *IEEE Transactions on Pattern Analysis and Machine Intelligence*, 38(1):142–158, Jan 2016. doi:10.1109/TPAMI.2015.2437384. (Cited on page 15.)

[GEO06] Audio-visual biofeedback for respiratory-gated radiotherapy: Impact of audio instruction and audio-visual biofeedback on respiratory-gated radiotherapy. *International Journal of Radiation Oncology*Biology*Physics*, 65(3):924 – 933, 2006. (Cited on page 86.)

[Gir15] Ross Girshick. Fast r-cnn. In *Proceedings of the 2015 IEEE International Conference on Computer Vision (ICCV)*, ICCV '15, pages 1440–1448, Washington, DC, USA, 2015. IEEE Computer Society. URL: http://dx.doi.org/10.1109/ICCV.2015.169, doi:10.1109/ICCV.2015.169. (Cited on page 15.)

[Giu84] E. Giusti. *Minimal Surfaces and Functions of Bounded Variation*. Birkhäuser Boston, Boston, MA, 1984. doi:10.1007/978-1-4684-9486-0. (Cited on page 117.)

[GJH+02] Mark A. Griswold, Peter M. Jakob, Robin M. Heidemann, Mathias Nittka, Vladimir Jellus, Jianmin Wang, Berthold Kiefer, and Axel Haase. Generalized autocalibrating partially parallel acquisitions (grappa). *Magnetic Resonance in Medicine*, 47(6):1202–1210, 2002. URL: https://onlinelibrary.wiley.com/doi/abs/10.1002/mrm.10171, arXiv:https://onlinelibrary.wiley.com/doi/pdf/10.1002/mrm.10171, doi:10.1002/mrm.10171. (Cited on page 24.)

[GKC+05] Peter D. Gatehouse, Jennifer Keegan, Lindsey A. Crowe, Sharmeen Masood, Raad H. Mohiaddin, Karl-Friedrich Kreitner, and David N. Firmin. Applications of phase-contrast flow and velocity imaging in cardiovascular mri. *European Radiology*, 15(10):2172–2184, Oct 2005. URL: https://doi.org/10.1007/s00330-005-2829-3, doi:10.1007/s00330-005-2829-3. (Cited on page 64.)

[GKHPU11] Matthieu Guerquin-Kern, M Haberlin, Klaas Paul Pruessmann, and Michael Unser. A fast wavelet-based reconstruction method for magnetic resonance imaging. *IEEE transactions on medical imaging*, 30(9):1649–1660, 2011. (Cited on page 15.)

[GP95] H Gudbjartsson and S Patz. The rician distribution of noisy mri data. *Magnetic resonance in medicine*, 34(6):910–914, 12 1995. URL: https://www.ncbi.nlm.nih.gov/pubmed/8598820. (Cited on page 14.)

[GS13] Lynn F. Gladden and Andrew J. Sederman. Recent advances in flow MRI. *Journal of Magnetic Resonance*, 229:2 – 11, 2013. Frontiers of In Vivo and Materials MRI Research. URL: http://www.sciencedirect.com/science/article/pii/S1090780712003667, doi:https://doi.org/10.1016/j.jmr.2012.11.022. (Cited on page 63.)

[GS17] Lynn F. Gladden and Andrew J. Sederman. Magnetic resonance imaging and velocity mapping in chemical engineering applications. *Annual Review of Chemical and Biomolecular Engineering*, 8(1):227–247, 2017. PMID: 28592175. URL: https://doi.org/10.1146/annurev-chembioeng-061114-123222, arXiv:https://doi.org/10.1146/annurev-chembioeng-061114-123222, doi:10.1146/annurev-chembioeng-061114-123222. (Cited on page 72.)

[GSB+03] Sandeep N Gupta, Meiyappan Solaiyappan, Garth M Beache, Andrew E Arai, and Thomas KF Foo. Fast method for correcting image misregistration due to organ motion in time-series MRI data. *Magn Reson Med*, 49(3):506–514, 2003. (Cited on page 88.)

[Had02] J. Hadamard. Sur les problèmes aux dérivés partielles et leur signification physique. *Princeton University Bulletin*, 13:49–52, 1902. (Cited on pages 2 and 11.)

[Had23] J. Hadamard. *Lectures on Cauchy's Problem in Linear Partial Differential Equations*. Yale University Press, New Haven, 1923. (Cited on pages 2 and 11.)

[HBT+12] Daniel J. Holland, Andrew Blake, Alexander B. Tayler, Andrew J. Sederman, and Lynn F. Gladden. Bubble size measurement using bayesian magnetic resonance. *Chemical engineering science*, 84:735–745, 2012. (Cited on page 51.)

[HBTV99] E.M. Haacke, R.W. Brown, M.R. Thompson, and R. Venkatesan. *Magnetic Resonance Imaging: Physical Principles and Sequence Design*. Wiley, 1999. URL: https://books.google.it/books?id=BnOvQgAACAAJ. (Cited on page 65.)

[HM04] Eldad Haber and Jan Modersitzki. Numerical methods for volume preserving image registration. *Inverse problems*, 20(5):1621, 2004. (Cited on page 18.)

[HMB+10] Daniel J. Holland, Dmitry M. Malioutov, Andrew Blake, Andrew J. Sederman, and L. F. Gladden. Reducing data acquisition times in phase-encoded velocity imaging using compressed sensing. *Journal of magnetic resonance*, 203(2):236–246, 2010. (Cited on pages 51, 64, and 70.)

[HMD+08] Daniel J Holland, Christoph R Müller, John S Dennis, Lynn F Gladden, and Andrew J Sederman. Spatially resolved measurement of anisotropic granular temperature in gas-fluidized beds. *Powder Technology*, 182(2):171–181, 2008. (Cited on page 64.)

[HOM+17] Inger Havsteen, Anders Ohlhues, Kristoffer H Madsen, Janus Damm Nybing, Hanne Christensen, and Anders Christensen. Are movement artifacts in magnetic resonance imaging a real problem?—a narrative review. *Frontiers in neurology*, 8:232, 2017. (Cited on page 86.)

[HSP+16] Mattias P Heinrich, Ivor JA Simpson, BartŁomiej W Papież, Michael Brady, and Julia A Schnabel. Deformable image registration by combining uncertainty estimates from supervoxel belief propagation. *Medical image analysis*, 27:57–71, 2016. (Cited on page 19.)

[HST+06] Jeremy D.P. Hoisak, Katharina E. Sixel, Romeo Tirona, Patrick C.F. Cheung, and Jean-Philippe Pignol. Prediction of lung tumour position based on spirometry and on abdominal displacement: Accuracy and reproducibility. *Radiotherapy and Oncology*, 78(3):339 – 346, 2006. URL: http://www.sciencedirect.com/science/article/pii/S0167814006000296, doi:https://doi.org/10.1016/j.radonc.2006.01.008. (Cited on page 86.)

[JBC18] Adam Johansson, James Balter, and Yue Cao. Rigid-body motion correction of the liver in image reconstruction for golden-angle stack-of-stars DCE MRI. *Magnetic Resonance in Medicine*, 79(3):1345–1353, 2018. (Cited on page 88.)

[JF03] M. W. Jacobson and J Fessler. Joint estimation of image and deformation parameters in motion-corrected PET. volume 5, pages 3290–3294 Vol.5, 2003. (Cited on pages 4, 87, and 88.)

[JHU+08] Bernd Jung, Matthias Honal, Peter Ullmann, Jürgen Hennig, and Michael Markl. Highly k-t-space–accelerated phase-contrast MRI. *Magnetic Resonance in Medicine: An Official Journal of the International Society for Magnetic Resonance in Medicine*, 60(5):1169–1177, 2008. (Cited on page 70.)

[JIA06] Technical aspects of image-guided respiration-gated radiation therapy. *Medical Dosimetry*, 31(2):141 – 151, 2006. (Cited on page 86.)

[JKV+17] MJA Jansen, HJ Kuijf, WB Veldhuis, FJ Wessels, MS Van Leeuwen, and JPW Pluim. Evaluation of motion correction for clinical dynamic contrast enhanced MRI of the liver. *Physics in Medicine & Biology*, 62(19):7556, 2017. (Cited on page 88.)

[Joh60] F. John. Continuous dependence on data for solutions of partial differential equations with a prescribed bound. *Communications on Pure and Applied Mathematics*, 13(4):551–585, 1960. doi:10.1002/cpa.3160130402. (Cited on page 11.)

[KBD17] András P Keszei, Benjamin Berkels, and Thomas M Deserno. Survey of non-rigid registration tools in medicine. *Journal of digital imaging*, 30(1):102–116, 2017. (Cited on page 18.)

[KBV90] SP Kim, Nirmal K Bose, and HM Valenzuela. Recursive reconstruction of high resolution image from noisy undersampled multiframes. *IEEE Transactions on Acoustics, Speech, and Signal Processing*, 38(6):1013–1027, 1990. (Cited on page 21.)

[KD04] Bilge Karaçali and Christos Davatzikos. Estimating topology preserving and smooth displacement fields. *IEEE Transactions on Medical Imaging*, 23(7):868–880, 2004. (Cited on page 18.)

[Kiw97] Krzysztof C. Kiwiel. Proximal minimization methods with generalized bregman functions. *SIAM journal on control and optimization*, 35(4):1142–1168, 1997. (Cited on pages 29 and 74.)

[KKVM00] P J Keall, V R Kini, S S Vedam, and R Mohan. Motion adaptive x-ray therapy: a feasibility study. *Physics in Medicine and Biology*, 46(1):1–10, nov 2000. (Cited on page 86.)

[Kla11] Esther Klann. A Mumford-Shah-like method for limited data tomography with an application to electron tomography. *SIAM J. Imaging Sci., 4(4), 1029–1048*, 2011. (Cited on pages 4 and 34.)

[KWT88] Michael Kass, Andrew Witkin, and Demetri Terzopoulos. Snakes: Active contour models. *International Journal of Computer Vision*, 1(4):321–331, Jan 1988. URL: https://doi.org/10.1007/BF00133570, doi:10.1007/BF00133570. (Cited on page 16.)

[KYK+01] Shuichiro Kaji, Philip C Yang, Adam B Kerr, WH Wilson Tang, Craig H Meyer, Albert Macovski, John M Pauly, Dwight G Nishimura, and Bob S Hu. Rapid evaluation of left ventricular volume and mass without breath-holding using real-time interactive cardiac magnetic resonance imaging system. *Journal of the American College of Cardiology*, 38(2):527–533, 2001. (Cited on page 86.)

[LCKAM] Maria J Ledesma-Carbayo, Peter Kellman, Andrew E Arai, and Elliot R McVeigh. Motion corrected free-breathing delayed-enhancement imaging of myocardial infarction using nonrigid registration. *Journal of Magnetic Resonance Imaging. 2007;26(1):184-90.* (Cited on page 88.)

[LCM07] Hsu LY Arai AE McVeigh ER. Ledesma-Carbayo MJ, Kellman P. Motion corrected free-breathing delayed-enhancement imaging of myocardial infarction using nonrigid registration. *J Magn Reson Imaging*, 26(1):184–90., July 2007. (Cited on page 88.)

[LDG+17] T. Lin, P. Dollár, R. Girshick, K. He, B. Hariharan, and S. Belongie. Feature pyramid networks for object detection. In *2017 IEEE Conference on Computer Vision and Pattern Recognition (CVPR)*, pages 936–944, July 2017. doi:10.1109/CVPR.2017.106. (Cited on page 15.)

[LDJ15] S. G. Lingala, E. DiBella, and M. Jacob. Deformation corrected compressed sensing (dc-cs): A novel framework for accelerated dynamic mri. *IEEE Transactions on Medical Imaging*, 34(1):72–85, Jan 2015. (Cited on pages 87, 88, 99, and 101.)

[LDP07] Michael Lustig, David Donoho, and John M. Pauly. Sparse MRI: The application of compressed sensing for rapid MR imaging. *Magnetic resonance in medicine*, 58(6):1182–1195, 2007. (Cited on pages 14, 15, 22, 25, 70, and 87.)

[LHDJ11a] Sajan Goud Lingala, Yue Hu, Edward DiBella, and Mathews Jacob. Accelerated dynamic mri exploiting sparsity and low-rank structure: kt slr. *IEEE Transactions on Medical Imaging*, pages 1042–1054, 2011. (Cited on pages 87 and 90.)

[LHDJ11b] Sajan Goud Lingala, Yue Hu, Edward DiBella, and Mathews Jacob. Accelerated dynamic mri exploiting sparsity and low-rank structure: kt slr. *IEEE transactions on medical imaging*, 30(5):1042–1054, 2011. (Cited on page 87.)

[Lia07] Zhi-Pei Liang. Spatiotemporal imagingwith partially separable functions. In *IEEE International Symposium on Biomedical Imaging: From Nano to Macro*, pages 988–991, 2007. (Cited on page 87.)

[LJF08] F. Li, X. Jia, and D. Fraser. Universal hmt based super resolution for remote sensing images. In *2008 15th IEEE International Conference on Image Processing*, pages 333–336, Oct 2008. doi:10.1109/ICIP.2008.4711759. (Cited on page 21.)

[LKS+09] Bo Liu, Kevin King, Michael Steckner, Jun Xie, Jinhua Sheng, and Leslie Ying. Regularized sensitivity encoding (sense) reconstruction using bregman iterations. *Magnetic Resonance in Medicine*, 61(1):145–152, 2009. URL: https://onlinelibrary.wiley.com/doi/abs/10.1002/mrm.21799, arXiv:https://onlinelibrary.wiley.com/doi/pdf/10.1002/mrm.21799, doi:10.1002/mrm.21799. (Cited on page 15.)

[LKY+09] Jan Lellmann, Jörg Kappes, Jing Yuan, Florian Becker, and Christoph Schnörr. Convex multi-class image labeling by simplex-constrained total variation. In *International conference on scale space and variational methods in computer vision*, pages 150–162. Springer, 2009. (Cited on pages 13 and 31.)

[LL14] Ka Chun Lam and Lok Ming Lui. Landmark-and intensity-based registration with large deformations via quasi-conformal maps. *SIAM Journal on Imaging Sciences*, 7(4):2364–2392, 2014. (Cited on page 19.)

[Llo06] S.P. Lloyd. Least squares quantization in pcm. *IEEE Trans. Inf. Theor.*, 28(2):129–137, 2006. doi:10.1109/TIT.1982.1056489. (Cited on page 16.)

[LLWS13] Jan Lellmann, Björn Lellmann, Florian Widmann, and Christoph Schnörr. Discrete and continuous models for partitioning problems. *International journal of computer vision*, 104(3):241–269, 2013. (Cited on page 31.)

[LMGCCV12] Jose M Leiva-Murillo, Luis Gómez-Chova, and Gustavo Camps-Valls. Multitask remote sensing data classification. *IEEE transactions on geoscience and remote sensing*, 51(1):151–161, 2012. (Cited on page 4.)

[Loj63] Stanislaw Lojasiewicz. Une propriété topologique des sous-ensembles analytiques réels. *Les équations aux dérivées partielles*, 117:87–89, 1963. (Cited on page 40.)

[LQP17] François Lauze, Yvain Quéau, and Esben Plenge. Simultaneous reconstruction and segmentation of CT scans with shadowed data. In *International Conference on Scale Space and Variational Methods in Computer Vision*, pages 308–319. Springer, 2017. (Cited on pages 35, 37, and 38.)

[LSD14] Jonathan Long, Evan Shelhamer, and Trevor Darrell. Fully convolutional networks for semantic segmentation. Technical report, 2014. (Cited on page 15.)

[LTC+15] Zhang Li, Jeroen A. W. Tielbeek, Matthan W. A. Caan, Carl A. J. Puylaert, Manon L. Ziech, C. Yung Nio, Jaap Stoker, Lucas J. van Vliet, and Frans M. Vos. Expiration-phase template-based motion correction of free-breathing abdominal dynamic contrast enhanced mri. *IEEE Transactions on Biomedical Engineering*, 62:1215–1225, 2015. (Cited on page 88.)

[LV08a] C. Le Guyader and L. A. Vese. Self-repelling snakes for topology-preserving segmentation models. *IEEE Transactions on Image Processing*, 17(5):767–779, May 2008. doi:10.1109/TIP.2008.919951. (Cited on page 16.)

[LV08b] Linh H. Lieu and Luminita A. Vese. Image restoration and decomposition via bounded total variation and negative hilbert-sobolev spaces. *Applied Mathematics and Optimization*, 58(2):167, May 2008. URL: https://doi.org/10.1007/s00245-008-9047-8, doi:10.1007/s00245-008-9047-8. (Cited on page 13.)

[Mac67] J.B. MacQueen. Some methods for classification and analysis of multivariate observations. In *Proceedings of the Fifth Berkeley Symposium on Mathematical Statistics and Probability, Volume 1: Statistics*, pages 281–297, Berkeley, California, 1967. University of California Press. (Cited on page 16.)

[Mac96] Albert Macovski. Noise in mri. *Magnetic Resonance in Medicine*, 36(3):494–497, 1996. (Cited on pages 14 and 28.)

[Mar06] Michael Markl. Velocity encoding and flow imaging. 2006. (Cited on page 69.)

[Mey01] Yves Meyer. *Oscillating patterns in image processing and nonlinear evolution equations: the fifteenth Dean Jacqueline B. Lewis memorial lectures*, volume 22. American Mathematical Soc., 2001. (Cited on pages 13 and 29.)

[MGS06] Bernard Anthony Mair, David R Gilland, and Jing Sun. Estimation of images and nonrigid deformations in gated emission CT. *IEEE Transactions on Medical Imaging*, 25(9):1130–1144, 2006. (Cited on page 88.)

[MO08] Antonio Marquina and Stanley J. Osher. Image super-resolution by tv-regularization and bregman iteration. *Journal of Scientific Computing*, 37(3):367–382, Dec 2008. doi:10.1007/s10915-008-9214-8. (Cited on page 21.)

[Mod04] Jan Modersitzki. *Numerical methods for image registration*. Oxford science publications. Oxford Univ Press, Oxford [u.a.], 2004. (Cited on page 19.)

[Mod09] J. Modersitzki. *FAIR: Flexible Algorithms for Image Registration*. SIAM, Philadelphia, 2009. (Cited on page 99.)

[Mor66] Vladimir Alekseevich Morozov. On the solution of functional equations by the method of regularization. In *Soviet Math. Dokl*, volume 7, pages 414–417, 1966. (Cited on page 30.)

[MRI08] Mri from picture to proton: 2nd ed. *American Journal of Neuroradiology*, 29(6):e50–e50, 2008. URL: http://www.ajnr.org/content/29/6/e50, arXiv:http://www.ajnr.org/content/29/6/e50.full.pdf, doi:10.3174/ajnr.A0980. (Cited on page 21.)

[MS89] David Mumford and Jayant Shah. Optimal approximations by piecewise smooth functions and associated variational problems. *Communications on pure and applied mathematics*, 42(5):577–685, 1989. (Cited on pages 16 and 30.)

[MSMM08] Masao Shimizu, Shin Yoshimura, Masayuki Tanaka, and Masatoshi Okutomi. Super-resolution from image sequence under influence of hot-air optical turbulence. In *2008 IEEE Conference on Computer Vision and Pattern Recognition*, pages 1–8, June 2008. doi:10.1109/CVPR.2008.4587525. (Cited on page 21.)

[MW12] Angshul Majumdar and Rabab K Ward. Exploiting rank deficiency and transform domain sparsity for mr image reconstruction. *Magnetic Resonance Imaging*, pages 9–18, 2012. (Cited on page 90.)

[MY01] Michael I. Miller and Laurent Younes. Group actions, homeomorphisms, and matching: A general framework. *International Journal of Computer Vision*, 41(1-2):61–84, 2001. (Cited on page 19.)

[MY10] S. Mallat and G. Yu. Super-resolution with sparse mixing estimators. *IEEE Transactions on Image Processing*, 19(11):2889–2900, November 2010. doi:10.1109/TIP.2010.2049927. (Cited on page 21.)

[Nik04] Mila Nikolova. A variational approach to remove outliers and impulse noise. *Journal of Mathematical Imaging and Vision*, 20(1):99–120, Jan 2004. URL: https://doi.org/10.1023/B:JMIV.0000011326.88682.e5, doi:10.1023/B:JMIV.0000011326.88682.e5. (Cited on page 13.)

[NM14] Kamal Nasrollahi and Thomas B. Moeslund. Super-resolution: a comprehensive survey. *Machine Vision and Applications*, 25(6):1423–1468, Aug 2014. URL: https://doi.org/10.1007/s00138-014-0623-4, doi:10.1007/s00138-014-0623-4. (Cited on page 20.)

[OBG+05] Stanley Osher, Martin Burger, Donald Goldfarb, Jinjun Xu, and Wotao Yin. An iterative regularization method for total variation-based image restoration. *Multiscale Modeling & Simulation*, 4(2):460–489, 2005. (Cited on page 29.)

[OCS15] Ricardo Otazo, Emmanuel Candès, and Daniel K Sodickson. Low-rank plus sparse matrix decomposition for accelerated dynamic mri with separation of background and dynamic components. *Magnetic Resonance in Medicine*, pages 1125–1136, 2015. (Cited on pages 87 and 90.)

[OF97] J. M. Ollinger and J. A. Fessler. Positron-emission tomography. *IEEE Signal Processing Magazine*, 14(1):43–55, Jan 1997. doi:10.1109/79.560323. (Cited on page 14.)

[OGLG15] Solene Ozeré, Christian Gout, and Carole Le Guyader. Joint Segmentation/Registration Model by Shape Alignment via Weighted Total Variation Minimization and Nonlinear Elasticity. *SIAM Journal on Imaging Sciences*, 8(3):1981–2020, 2015. (Cited on page 4.)

[OLG15] Solene Ozere and Carole Le Guyader. Topology preservation for image-registration-related deformation fields. *Communications in Mathematical Sciences*, 13(5):1135–1161, 2015. (Cited on pages 18 and 20.)

[OME+16] Freddy Odille, Anne Menini, Jean-Marie Escanyé, Pierre-André Vuissoz, Pierre-Yves Marie, Marine Beaumont, and Jacques Felblinger. Joint reconstruction of multiple images and motion in MRI: Application to free-breathing myocardial T2 quantification. *IEEE Transactions on Medical Imaging*, 35(1):197–207, 2016. (Cited on pages 4, 87, and 89.)

[OS88] Stanley Osher and James A Sethian. Fronts propagating with curvature-dependent speed: Algorithms based on hamilton-jacobi formulations. *Journal of Computational Physics*, 79(1):12 –

49, 1988. URL: http://www.sciencedirect.com/science/article/pii/0021999188900022, doi:https://doi.org/10.1016/0021-9991(88)90002-2. (Cited on page 16.)

[Ots79] N. Otsu. A threshold selection method from gray-level histograms. *IEEE Transactions on Systems, Man, and Cybernetics*, 9(1):62–66, 1979. doi:10.1109/TSMC.1979.4310076. (Cited on page 15.)

[PB11] Eva Paciok and Bernhard Blümich. Ultrafast microscopy of microfluidics: compressed sensing and remote detection. *Angewandte Chemie International Edition*, 50(23):5258–5260, 2011. (Cited on page 70.)

[PBP10] Jeffrey Paulsen, Vikram S Bajaj, and Alexander Pines. Compressed sensing of remotely detected MRI velocimetry in microfluidics. *Journal of Magnetic Resonance*, 205(2):196–201, 2010. (Cited on page 70.)

[PCBC09] Thomas Pock, Daniel Cremers, Horst Bischof, and Antonin Chambolle. An algorithm for minimizing the Mumford-Shah functional. In *Computer Vision, 2009 IEEE 12th International Conference on*, pages 1133–1140. IEEE, 2009. (Cited on pages 38, 39, 75, and 120.)

[PCCB09] Thomas Pock, Antonin Chambolle, Daniel Cremers, and Horst Bischof. A convex relaxation approach for computing minimal partitions. In *2009 IEEE Conference on Computer Vision and Pattern Recognition*, pages 810–817, June 2009. doi:10.1109/CVPR.2009.5206604. (Cited on page 30.)

[PCD15] Pedro O. Pinheiro, Ronan Collobert, and Piotr Dollár. Learning to segment object candidates. In *Proceedings of the 28th International Conference on Neural Information Processing Systems - Volume 2*, NIPS'15, pages 1990–1998, Cambridge, MA, USA, 2015. MIT Press. URL: http://dl.acm.org/citation.cfm?id=2969442.2969462. (Cited on page 15.)

[PMS+09] P Parasoglou, D Malioutov, AJ Sederman, J Rasburn, H Powell, LF Gladden, A Blake, and ML Johns. Quantitative single point imaging with compressed sensing. *Journal of Magnetic resonance*, 201(1):72–80, 2009. (Cited on page 70.)

[PSR+01] Sven Plein, William HT Smith, John P Ridgway, Andrea Kassner, David J Beacock, Timothy N Bloomer, and Mohan U Sivananthan. Qualitative and quantitative analysis of regional left ventricular wall dynamics using real-time magnetic resonance imaging: comparison with conventional breath-hold gradient echo acquisition in volunteers and patients. *Journal of Magnetic Resonance Imaging: An Official Journal of the International Society for Magnetic Resonance in Medicine*, 14(1):23–30, 2001. (Cited on page 86.)

[PST94] Andrew J Patti, M Ibrahim Sezan, and A Murat Tekalp. High-resolution image reconstruction from a low-resolution image sequence in the presence of time-varying motion blur. In *Proceedings of 1st International*

*Conference on Image Processing*, volume 1, pages 343–347. IEEE, 1994. (Cited on page 21.)

[PWSB99] Klaas P Pruessmann, Markus Weiger, Markus B Scheidegger, and Peter Boesiger. Sense: sensitivity encoding for fast mri. *Magnetic resonance in medicine*, 42(5):952–962, 1999. (Cited on page 24.)

[QGN+12] Xiaobo Qu, Di Guo, Bende Ning, Yingkun Hou, Yulan Lin, Shuhui Cai, and Zhuotong Chen. Undersampled mri reconstruction with patch-based directional wavelets. *Magnetic resonance imaging*, 30 7:964–77, 2012. (Cited on page 15.)

[RB10] Saiprasad Ravishankar and Yoram Bresler. Mr image reconstruction from highly undersampled k-space data by dictionary learning. *IEEE transactions on medical imaging*, 30(5):1028–1041, 2010. (Cited on page 15.)

[RC01] D. Rajan and S. Chaudhuri. Generation of super-resolution images from blurred observations using Markov random fields. In *Proc. (Cat. No.01CH37221) and Signal Processing 2001 IEEE Int Conf. Acoustics, Speech*, volume 3, pages 1837–1840 vol.3, May 2001. doi:10.1109/ICASSP.2001.941300. (Cited on page 21.)

[RDDH15] Mikhail Romanov, Anders Bjorholm Dahl, Yiqiu Dong, and Per Christian Hansen. Simultaneous tomographic reconstruction and segmentation with class priors. *Inverse Problems in Science and Engineering, 24,8, 1432-1453*, 2015. (Cited on pages 36 and 38.)

[RdVCGSW+16] Javier Royuela-del Val, Lucilio Cordero-Grande, Federico Simmross-Wattenberg, Marcos Martín-Fernández, and Carlos Alberola-López. Nonrigid groupwise registration for motion estimation and compensation in compressed sensing reconstruction of breath-hold cardiac cine mri. *Magnetic resonance in medicine*, 75(4):1525–1536, 2016. (Cited on pages 87, 88, 99, and 101.)

[Rec19] Andi Reci. *Signal sampling and processing inmagnetic resonance applications*. PhD thesis, University of Cambridge, 2019. (Cited on pages 75, 76, 77, and 78.)

[RFB15] Olaf Ronneberger, Philipp Fischer, and Thomas Brox. U-net: Convolutional networks for biomedical image segmentation. In Nassir Navab, Joachim Hornegger, William M. Wells, and Alejandro F. Frangi, editors, *Medical Image Computing and Computer-Assisted Intervention – MICCAI 2015*, pages 234–241, Cham, 2015. Springer International Publishing. (Cited on page 15.)

[Roc70] R Tyrrell Rockafellar. *Convex analysis*, volume 28. Princeton university press, 1970. (Cited on pages 117, 118, and 119.)

[ROF92] L. Rudin, S. Osher, and E. Fatemi. Nonlinear total variation based noise removal algorithms. *Physica D: Nonlinear Phenomena*, 60(1):259–268, 1992. doi:10.1016/0167-2789(92)90242-F. (Cited on pages 12 and 90.)

[RR07] Ronny Ramlau and Wolfgang Ring. A Mumford-Shah level-set approach for the inversion and segmentation of X-ray tomography data. *Journal of Computational Physics, 221, 2, 539 - 557*, 2007. (Cited on pages 4, 34, and 37.)

[RSH+99] D. Rueckert, L. I. Sonoda, C. Hayes, D. L. G. Hill, M. O. Leach, and D. J. Hawkes. Nonrigid registration using free-form deformations: application to breast mr images. *IEEE Transactions on Medical Imaging*, 18(8):712–721, Aug 1999. doi:10.1109/42.796284. (Cited on page 19.)

[RSK+14] Tiago B. Rodrigues, Eva M. Serrao, Brett W. C. Kennedy, De-En Hu, Mikko I. Kettunen, and Kevin M. Brindle. Magnetic resonance imaging of tumor glycolysis using hyperpolarized 13 c-labeled glucose. *Nature medicine*, 20(1):93, 2014. (Cited on page 54.)

[Rud87] W. Rudin. *Real and complex analysis*. McGraw-Hill Book Co., New York, third edition, 1987. (Cited on pages 11 and 117.)

[SC02] J. Shen and T. Chan. Mathematical models for local nontexture inpaintings. *SIAM Journal on Applied Mathematics*, 62(3):1019–1043, 2002. URL: https://doi.org/10.1137/S0036139900368844, arXiv:https://doi.org/10.1137/S0036139900368844, doi:10.1137/S0036139900368844. (Cited on page 13.)

[SC03] David Strong and Tony Chan. Edge-preserving and scale-dependent properties of total variation regularization. *Inverse problems*, 19(6):S165, 2003. (Cited on page 29.)

[SDP13a] A. Sotiras, C. Davatzikos, and N. Paragios. Deformable Medical Image Registration: A Survey. *IEEE Transactions on Medical Imaging*, 32(7):1153–1190, July 2013. doi:10.1109/TMI.2013.2265603. (Cited on pages 17 and 19.)

[SDP13b] A. Sotiras, C. Davatzikos, and N. Paragios. Deformable medical image registration: A survey. *IEEE Transactions on Medical Imaging*, 32(7):1153–1190, 2013. (Cited on page 18.)

[SdVB+17] Hessam Sokooti, Bob de Vos, Floris Berendsen, Boudewijn PF Lelieveldt, Ivana Išgum, and Marius Staring. Nonrigid image registration using multi-scale 3d convolutional neural networks. In *International Conference on Medical Image Computing and Computer-Assisted Intervention*, pages 232–239. Springer, 2017. (Cited on page 19.)

[SF06] F. Sroubek and J. Flusser. Resolution enhancement via probabilistic deconvolution of multiple degraded images. *Pattern Recognition Letters*, 27(4):287 – 293, 2006. Pattern Recognition in Remote Sensing

(PRRS 2004). URL: http://www.sciencedirect.com/science/article/pii/S0167865505002230, doi:https://doi.org/10.1016/j.patrec.2005.08.010. (Cited on page 21.)

[SFL00] Randy M Setser, Stefan E Fischer, and Christine H Lorenz. Quantification of left ventricular function with magnetic resonance images acquired in real time. *Journal of magnetic resonance imaging*, 12(3):430–438, 2000. (Cited on page 86.)

[SGG+09] O. Scherzer, M. Grasmair, H. Grossauer, M. Haltmeier, and F. Lenzen. *Variational Methods in Imaging*, volume 167 of *Applied Mathematical Sciences*. Springer, New York, 2009. (Cited on page 12.)

[SHSG09] Mark H. Sankey, Daniel J. Holland, Andrew J. Sederman, and Lynn F. Gladden. Magnetic resonance velocity imaging of liquid and gas two-phase flow in packed beds. *Journal of Magnetic Resonance*, 196(2):142–148, 2009. (Cited on page 64.)

[SJAG98] Andrew J. Sederman, Michael L. Johns, Paul Alexander, and Lynn F. Gladden. Structure-flow correlations in packed beds. *Chemical Engineering Science*, 53(12):2117–2128, 1998. (Cited on page 64.)

[SM00] Jianbo Shi and Jitendra Malik. Normalized cuts and image segmentation. *Departmental Papers (CIS)*, page 107, 2000. (Cited on page 16.)

[SMF09] H. Schumacher, J. Modersitzki, and B. Fischer. Combined reconstruction and motion correction in SPECT imaging. *IEEE Transactions on Nuclear Science*, 56(1):73–80, Feb 2009. doi:10.1109/TNS.2008.2007907. (Cited on pages 4, 88, and 89.)

[SMI+95] Todd S Sachs, Craig H Meyer, Pablo Irarrazabal, Bob S Hu, Dwight G Nishimura, and Albert Macovski. The diminishing variance algorithm for real-time reduction of motion artifacts in mri. *Magnetic resonance in medicine*, 34(3):412–422, 1995. (Cited on page 85.)

[SPSM18] Piotr Swierczynski, Bartłomiej W Papież, Julia A Schnabel, and Colin Macdonald. A level-set approach to joint image segmentation and registration with application to ct lung imaging. *Computerized Medical Imaging and Graphics*, 65:58–68, 2018. (Cited on page 4.)

[Ste56] H. Steinhaus. Sur la division des corp materiels en parties. *Bull. Acad. Polon. Sci*, 1:801–804, 1956. (Cited on page 16.)

[SW14] M. Storath and A. Weinmann. Fast partitioning of vector-valued images. *SIAM Journal on Imaging Sciences*, 7(3):1826–1852, 2014. (Cited on page 17.)

[SWFU15] Martin Storath, Andreas Weinmann, Jürgen Frikel, and Michael Unser. Joint image reconstruction and segmentation using the Potts model. *Inverse Problems 31 (2015) 025003 (29pp)*, 2015. (Cited on pages 15, 37, and 58.)

[SYC09] Jeffrey A. Fessler Se Young Chun. Joint image reconstruction and nonrigid motion estimation with a simple penalty that encourages local invertibility. volume 7258, 2009. URL: https://doi.org/10.1117/12.811067, doi:10.1117/12.811067. (Cited on page 89.)

[TC07] Tommy WH Tang and Albert CS Chung. Non-rigid image registration using graph-cuts. In *International Conference on Medical Image Computing and Computer-Assisted Intervention*, pages 916–924. Springer, 2007. (Cited on page 19.)

[Ter86] D. Terzopoulos. Regularization of inverse visual problems involving discontinuities. *IEEE Transactions on Pattern Analysis and Machine Intelligence*, PAMI-8(4):413–424, July 1986. doi:10.1109/TPAMI.1986.4767807. (Cited on page 2.)

[THSG12a] Alexander B. Tayler, Daniel J. Holland, Andrew J. Sederman, and Lynn F. Gladden. Applications of ultra-fast MRI to high voidage bubbly flow: measurement of bubble size distributions, interfacial area and hydrodynamics. *Chemical engineering science*, 71:468–483, 2012. (Cited on pages 51, 64, and 70.)

[THSG12b] Alexander B. Tayler, Daniel J. Holland, Andrew J. Sederman, and Lynn F. Gladden. Exploring the origins of turbulence in multiphase flow using compressed sensing MRI. *Physical review letters*, 108(26):264505, 2012. (Cited on pages 51 and 77.)

[Tik63] Andrei Nikolaevich Tikhonov. Regularization of incorrectly posed problems. In *Soviet Mathematics Doklady*, volume 4, pages 1624–1627, 1963. (Cited on page 2.)

[Tsa89] RY Tsai. Multiple frame image restoration and registration. *Advances in Computer Vision and Image Processing*, 1:1715–1989, 1989. (Cited on page 21.)

[TYO08] M. Tanaka, Y. Yaguchi, and M. Okutomi. Robust and accurate estimation of multiple motions for whole-image super-resolution. In *2008 15th IEEE International Conference on Image Processing*, pages 649–652, Oct 2008. doi:10.1109/ICIP.2008.4711838. (Cited on page 21.)

[UAO+13] Muhammad Usman, David Atkinson, Freddy Odille, Christoph Kolbitsch, Ghislain Vaillant, Tobias Schaeffter, Philip G Batchelor, and Claudia Prieto. Motion corrected compressed sensing for free-breathing dynamic cardiac mri. *Magnetic resonance in medicine*, 70(2):504–516, 2013. (Cited on page 2.)

[UPWB10] Markus Unger, Thomas Pock, Manuel Werlberger, and Horst Bischof. A convex approach for variational super-resolution. In *Joint pattern recognition symposium*, pages 313–322. Springer, 2010. (Cited on page 21.)

[Val14] Tuomo Valkonen. A primal–dual hybrid gradient method for nonlinear operators with applications to mri. *Inverse Problems*, 30(5):055012, 2014. (Cited on page 72.)

[VdSB08] Dominique Van de Sompel and Michael Brady. Simultaneous reconstruction and segmentation algorithm for positron emission tomography and transmission tomography. *5th IEEE International Symposium on Biomedical Imaging: From Nano to Macro, 1035-1038*, 2008. (Cited on pages 36 and 38.)

[Ves01] Luminita A. Vese. A study in the bv space of a denoising—deblurring variational problem. *Applied Mathematics and Optimization*, 44:131–161, 2001. (Cited on page 13.)

[VMA+11] S. Vasanawala, M. Murphy, M. Alley, P. Lai, K. Keutzer, J. Pauly, and M. Lustig. Practical parallel imaging compressed sensing mri: Summary of two years of experience in accelerating body mri of pediatric patients. In *2011 IEEE International Symposium on Biomedical Imaging: From Nano to Macro*, pages 1039–1043, March 2011. doi:10.1109/ISBI.2011.5872579. (Cited on page 22.)

[VO03] Luminita A. Vese and Stanley J. Osher. Modeling textures with total variation minimization and oscillating patterns in image processing. *Journal of Scientific Computing*, 19(1):553–572, Dec 2003. URL: https://doi.org/10.1023/A:1025384832106, doi:10.1023/A:1025384832106. (Cited on page 13.)

[VO04] Luminita A Vese and Stanley J Osher. Image denoising and decomposition with total variation minimization and oscillatory functions. *Journal of Mathematical Imaging and Vision*, 20(1-2):7–18, 2004. (Cited on page 13.)

[vO06] J.D. van Ouwerkerk. Image super-resolution survey. *Image and Vision Computing*, 24(10):1039 – 1052, 2006. URL: http://www.sciencedirect.com/science/article/pii/S0262885606001089, doi:https://doi.org/10.1016/j.imavis.2006.02.026. (Cited on page 20.)

[vSSG+07] Martin von Siebenthal, Gabor Szekely, Urs Gamper, Peter Boesiger, Antony Lomax, and Ph Cattin. 4D MR imaging of respiratory organ motion and its variability. *Physics in Medicine & Biology*, 52(6):1547, 2007. (Cited on page 98.)

[WCH19] Zhihao Wang, Jian Chen, and Steven CH Hoi. Deep learning for image super-resolution: A survey. *arXiv preprint arXiv:1902.06068*, 2019. (Cited on page 21.)

[WIVA+96] William M Wells III, Paul Viola, Hideki Atsumi, Shin Nakajima, and Ron Kikinis. Multi-modal volume registration by maximization of mutual information. *Medical image analysis*, 1(1):35–51, 1996. (Cited on page 19.)

[WVRE08] Fei Wang, Baba C Vemuri, Anand Rangarajan, and Stephan J Eisenschenk. Simultaneous nonrigid registration of multiple point sets and atlas construction. *IEEE transactions on pattern analysis and machine intelligence*, 30(11):2011–2022, 2008. (Cited on page 19.)

[WYW+08] Kelvin K Wong, Edward S Yang, Ed X Wu, Hung-Fat Tse, and Stephen T Wong. First-pass myocardial perfusion image registration by maximization of normalized mutual information. *Journal of Magnetic Resonance Imaging*, 27(3):529–537, 2008. (Cited on page 88.)

[WYZ07] Yilun Wang, Wotao Yin, and Yin Zhang. A fast algorithm for image deblurring with total variation regularization", caam. Technical report, 2007. (Cited on page 13.)

[XY13] Yangyang Xu and Wotao Yin. A block coordinate descent method for regularized multiconvex optimization with applications to nonnegative tensor factorization and completion. *SIAM Journal on imaging sciences*, 6(3):1758–1789, 2013. (Cited on page 74.)

[XYM+12] Qiong Xu, Hengyong Yu, Xuanqin Mou, Lei Zhang, Jiang Hsieh, and Ge Wang. Low-dose x-ray ct reconstruction via dictionary learning. *IEEE transactions on medical imaging*, 31(9):1682–1697, 2012. (Cited on page 15.)

[YKSN17] Xiao Yang, Roland Kwitt, Martin Styner, and Marc Niethammer. Quicksilver: Fast predictive image registration–a deep learning approach. *NeuroImage*, 158:378–396, 2017. (Cited on page 89.)

[YSG+10] A. Yoshikawa, S. Suzuki, T. Goto, S. Hirano, and M. Sakurai. Super resolution image reconstruction using total variation regularization and learning-based method. In *2010 IEEE International Conference on Image Processing*, pages 1993–1996, Sep. 2010. doi:10.1109/ICIP.2010.5649059. (Cited on page 21.)

[YZS12] Q. Yuan, L. Zhang, and H. Shen. Multiframe super-resolution employing a spatially weighted total variation model. *IEEE Transactions on Circuits and Systems for Video Technology*, 22(3):379–392, March 2012. doi:10.1109/TCSVT.2011.2163447. (Cited on page 21.)

[ZC08] Mingqiang Zhu and Tony Chan. An efficient primal-dual hybrid gradient algorithm for total variation image restoration. *UCLA CAM Report*, 34, 2008. (Cited on page 75.)

[ZD10] M. V. W. Zibetti and A. R. De Pierro. Separate magnitude and phase regularization in MRI with incomplete data: Preliminary results. In *Proc. IEEE Int. Symp. Biomedical Imaging: From Nano to Macro*, pages 736–739, April 2010. doi:10.1109/ISBI.2010.5490069. (Cited on page 72.)

[ZM07] M. V. W. Zibetti and J. Mayer. A robust and computationally efficient simultaneous super-resolution scheme for image sequences. *IEEE Transactions on Circuits and Systems for Video Technology*, 17(10):1288–1300, Oct 2007. doi:10.1109/TCSVT.2007.903801. (Cited on page 21.)

[ZMCL16] Hongyuan Zhu, Fanman Meng, Jianfei Cai, and Shijian Lu. Beyond pixels: A comprehensive survey from bottom-up to semantic image segmentation and cosegmentation. *Journal of Visual Communication and Image Representation*, 34:12–27, 2016. (Cited on page 15.)

[ZMH15] Maxim Zaitsev, Julian Maclaren, and Michael Herbst. Motion artifacts in MRI: a complex problem with many partial solutions. *Journal of Magnetic Resonance Imaging,*, 42(4), 2015. (Cited on page 85.)

[ZNNF12] F. Zhao, D. C. Noll, J. Nielsen, and J. A. Fessler. Separate magnitude and phase regularization via compressed sensing. *IEEE Transactions on Medical Imaging*, 31(9):1713–1723, September 2012. doi:10.1109/TMI.2012.2196707. (Cited on page 72.)

[ZP17] Marcelo V. Zibetti and Alvaro R. Pierro. Improving compressive sensing in mri with separate magnitude and phase priors. *Multidimensional Syst. Signal Process.*, 28(4):1109–1131, October 2017. URL: https://doi.org/10.1007/s11045-016-0383-6, doi:10.1007/s11045-016-0383-6. (Cited on page 72.)

[ZPB07] Christopher Zach, Thomas Pock, and Horst Bischof. A duality based approach for realtime tv-l 1 optical flow. In *Joint pattern recognition symposium*, pages 214–223. Springer, 2007. (Cited on page 13.)

[ZPL15] Tao Zhang, John M Pauly, and Ives R Levesque. Accelerating parameter mapping with a locally low rank constraint. *Magnetic resonance in medicine*, 73(2):655–661, 2015. (Cited on page 87.)

[ZvDT+17] Leonie Zeune, Guus van Dalum, Leon W. M. M. Terstappen, Stephan A. van Gils, and Christoph Brune. Multiscale segmentation via bregman distances and nonlinear spectral analysis. *SIAM journal on imaging sciences*, 10(1):111–146, 2017. (Cited on page 33.)